Arts and Crafts of particle phenomenology: a journey through analytical methods and applications



Federica Devoto

Merton College

University of Oxford

A thesis submitted for the degree of

Doctor of Philosophy

Trinity 2024

To Paolo, Nicolina, Marisa and Gianfranco,
my very own Standard Model of fundamental interactions.

Acknowledgements

It is an extremely hard endevour to fit in one page my gratefulness to all the people that played a major role in accompanying me throughout these four year, but I will do my best to make this happen. Above all, I wish to express my heartfelt gratitude to my supervisor, Fabrizio, who has been the greatest source of inspiration throughout these years. As both a physicist and a person, you have continually motivated me to explore new horizons and turned every conversation into an opportunity for growth. I will never forget our discussions that effortlessly transitioned into physics dialogues, as well as your unparalleled commitment to both your research and my development as a young researcher.

Secondly, I extend my gratitude to all my collaborators. I wish to particularly acknowledge Federico, who has been a guiding light for me, offering support whenever I faced obstacles and motivating me to excel in my endeavors. Thank you for supporting me throughout emotional breakdowns and joys, I have always known where you stand. Additionally, I am indebted to Giulio, with whom I have shared the academic journey since our undergraduate days in Genova, all the way to being my officemate during these four years. Thanks for always being patient when I used to throw to you my unicorn Frilla, distracting you from work. I also want to thank Chiara, my partner in subtraction, whose collaboration transformed the initial challenges of my first year of PhD, haunted by the presence of the pandemic, into a period of fruitful and productive work. I will never forget our endless Skype calls from the couch wearing my pyjamas. I also want to thank Lorenzo, Kirill, Raoul and Davide for being amazing collaborators. I really learnt a lot from all of you and will always be grateful.

I want to thank Andrea, for his persistent presence in my life. We have been through both amazing and rough times, but I always knew where to find you. Thank you for all your patience, love and support, I will keep it in my heart forever. A huge thank goes also to my best friends Elisa, Elisa and Valentina. I cannot express how much I love you and how grateful I am for being close to me and never giving up on me even when I could not be there for you as much as I would have wanted to. Thanks to Jasmine, who made my last year in Oxford absolutely wonderful. I am so glad and lucky to have found a life-time friend in you. Thanks Melissa, for being an absolute source of inspiration both on a personal and professional level,

and for being an amazing friend. I also want to thank my family, whose support has been absolutely crucial. I could not have made it without all of you by my side.

Finally, I want to express gratitute to myself. This has been the hardest albeit most rewarding experience of my life. This is for every bite that would not go down and that I could not swallow. I dedicate all this to that side of me, that took me so far, but that I hope will also take me closer. Maybe, at some point. And to what, I do not know.

Abstract

In this thesis we set on a journey through modern techniques for the calculation of higher order corrections to key collider processes and their applications in the context of precision physics at the Large Hadron Collider (LHC). In particular, we will focus on the description of the highest energy stage of the particles collision, that goes under the name of "hard process", in the context of the Standard Model (SM) of fundamental interactions.

We identify two of the main ingredients that are needed for precision calculations of the hard process: scattering amplitudes and infrared subtraction. The two concepts are much intertwined, since infrared subtraction has the aim of organizing the cancellation of infrared divergences arising from loop amplitudes and phase space integrals in such a way that the two ingredients can be combined to give well-defined predictions for physical observables.

On the amplitude front, we offer an overview of contemporary techniques employed for multiloop amplitude calculations. Specifically, we undertake a computation of five-point two-loop scattering amplitudes in massless Quantum Chromodynamics (QCD) beyond the so-called large-N_c limit. These amplitudes, demanding cutting-edge computational methodologies, present avenues for exploring the non-planar sector of QCD and are ingredients e.g. for predictions that would facilitate the extraction of the strong coupling at very high energy scales.

In addressing infrared divergences, we present the challenges and frontiers of next-to-next-to-leading order (NNLO) subtraction schemes, with a focus on the Nested Soft-Collinear subtraction (NSC) scheme. By applying it to the case of mixed NNLO QCD-electroweak (EW) corrections to dilepton production at the LHC, we navigate through the intricacies of NNLO calculations within a simplified framework. Furthermore, we touch upon ongoing efforts towards extending the NSC scheme to address generic high-multiplicity NNLO processes.

Lastly, we apply these methodologies to phenomenological applications. We delve into the analysis of NNLO soft-virtual corrections to interference effects in the $H \to \gamma\gamma$ decay channel, as well as NLO corrections to the rare $H \to Z\gamma$ decay, the former playing a role in constraining the Higgs boson decay width. Additionally, we present a comprehensive analysis of mixed QCD-EW corrections to dilepton production at the LHC in the high-invariant mass region, where the role of EW corrections is enhanced by the presence of Sudakov logarithms.

Contents

1 Introduction **1**

1.1 The Standard Model of particle physics 1

1.1.1 Electroweak sector 3

1.1.2 Strong sector 15

1.2 Testing the SM: the Large Hadron Collider 23

1.3 Mastering precision: the What, How and Why 28

2 Scattering amplitudes **44**

2.1 Introduction 44

2.2 Full colour five-point two-loop amplitudes in massless QCD 48

2.2.1 Kinematics of five particles scattering 50

2.2.2 Colour and helicity decomposition 51

2.2.3 Reduction to master integrals 56

2.2.4 UV renormalization and IR subtraction 60

2.2.5 Final checks and results 62

3 Infrared divergences and subtraction **65**

3.1 Introduction 65

3.2 NSC subtraction at NLO EW 68

3.3 NSC at NNLO mixed QCD-EW 75

3.4 A new perspective on the NSC: towards high multiplicity processes 85

3.4.1 NLO 87

3.4.2 NNLO 90

4 Bounding the Higgs width at the LHC **95**

4.1 Motivation 95

4.2 Interference effects in $H \to \gamma\gamma$ 99

4.2.1 Theoretical background 99

4.2.2 Higher-order QCD calculation and results 104

4.3 Interference effects in $H \to Z\gamma$ 118

4.3.1 The $gg \to Z\gamma$ process 119

4.3.2 Interference effects at NLO QCD 122

5 Mixed QCD-EW corrections to dilepton production at the LHC 127
5.1 Introduction 127
5.2 Details of the calculation 130
5.2.1 Analytic results for the $q\bar{q}$ channel 130
5.2.2 Virtual contributions 132
5.3 Phenomenological results 136

6 Conclusions 148

Appendices

A Feynman rules 153

B Splitting functions 156

C Spinor helicity formalism 160

D RR contribution to the SV cross section 163
D.1 Three body phase space 163
D.2 Double real cross section in the soft limit 166

E Phase space integration of the triple color-correlated one-loop soft current 170

References 176

In so far as a scientific statement speaks about reality, it must be falsifiable: and in so far as it is not falsifiable, it does not speak about reality.

— Karl Popper's *The Logic of Scientific Discovery*

1 Introduction

Contents

1.1 The Standard Model of particle physics 1
1.1.1 Electroweak sector 3
1.1.2 Strong sector 15
1.2 Testing the SM: the Large Hadron Collider 23
1.3 Mastering precision: the What, How and Why 28

1.1 The Standard Model of particle physics

The aim of fundamental physics is to study and understand natural phenomena. It is perhaps the most ancient discipline that men have undertaken, although the concept of what is fundamental and what is not has changed dramatically over the centuries. Nowadays we know that nature is inherently quantum and that its fundamental constituents interact via four different forces: gravity, weak, strong and electromagnetic. From the perspective of theoretical physics, fundamental particles are nothing but irreducible representations of the symmetry group describing our spacetime: the Poincaré group. The Standard Model (SM) of particle theory is the framework that describes three out of the four forces mentioned above, all but gravity. A schematic depiction of its particle content can be found in Fig. 1.1.

It includes both fermions, the actual constituents of matter, and bosons, the carriers of the interactions. Fermions are further split into quarks and leptons. Leptons interact via the weak and electromagnetic forces, whereas quarks also interact via the strong force. The weak and electric interaction carriers are the W and Z bosons, and the photon. In the following sections we will give an overview of both the so-called electroweak sector of the SM (the one describing the electromagnetic and weak forces) and of the strong sector (describing the strong force). Interactions are mathematically described in the context of Quantum Field Theory (QFT). The QFT describing strong interactions is called Quantum Chromodynamics, and it was developed as a mathematically consistent theory in the 1970s[1]. The electroweak theory, on the other hand, originated from the Weinberg-Salam theory developed around the same period.

It was clear from the very beginning that the SM as composed by quarks, leptons and gauge bosons could not be a consistent theory. The simplest model that could be built in order to make the SM consistent is the *Higgs model*, that we will briefly describe in the following sections. Such model predicts the existence of a scalar particle in the spectrum, the Higgs boson. Although the existence of the Higgs was conjectured since the 1960s, it is only in 2012 that it has been discovered experimentally at the Large Hadron Collider (LHC) [2, 3]. It is the only scalar particle of the SM spectrum and its properties are linked to many open questions in high-energy physics such as the stability of the electroweak vacuum, the naturalness problem, its fundamental versus composite nature, and many others.

The SM has been and is currently being tested at an unprecedented level of precision at particle colliders. The range of energy scales at which one finds agreement between data and theoretical predictions is stunning and makes it the most successful theory in describing nature. However, as more and more data are being collected and experiments are able to provide very precise measurements, theoretical predictions need to be reliable at a comparable level of precision. How to make precise theoretical predictions in the Standard Model is the main topic of this thesis.

[1] for an historical perspective on the developments of QCD from its foundations up to this date see e.g. [1]

The rest of this chapter is organized as follows: in the next two subsections we will review both the electroweak and the strong sectors of the SM, as they lay the theoretical foundations for the rest of the thesis. In Section 1.2, we will give an overview of the tools that are available to test the Standard Model from a theoretical perspective. We will introduce perturbative calculations and factorization theorems, that allow us to describe very complicated collider events from first principles. Finally, in Section 1.3, we will try to argue in a more quantitative way that higher order calculations are actually important to give an accurate description of collider events, and give a broad brush introduction to the many difficulties that one encounters when performing them.

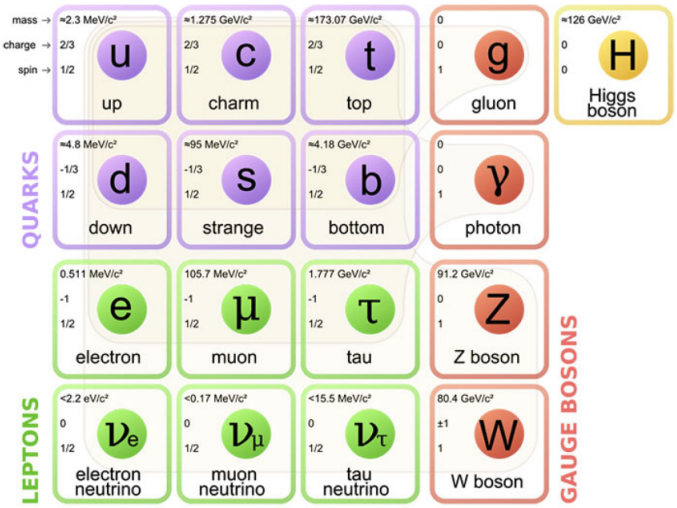


Figure 1.1: The Standard Model of Particle Physics [4]

1.1.1 Electroweak sector

The electroweak theory is a *gauge theory*, that is a theory built on local invariance under the action of some group of field transformations, the latter being $SU(2)_L \times U(1)_Y$. It is meant to describe both the electromagnetic and the weak interactions at high energies. The subscripts L and Y refer to "left" and "hypercharge" respectively. The word "left" comes from the fact that the weak interactions violate parity symmetry. Loosely speaking, what this means is that the physics of weak interactions is different if seen from a mirror. The violation of parity has been discovered experimentally by

Chien-Shiung Wu in 1956 [5], causing much astonishment amongst the community, as it was the first theory of nature found to violate such symmetry. The word "hypercharge", on the other hand, refers to the conserved charged associated with the abelian part of the symmetry group. We will expand on it later in this section.

Weak interactions are therefore said to be *chiral*, as they distinguish left and right components of a particle polarization. It is then useful to introduce left- and right-handed projectors as follows

$$\gamma_L = \frac{1}{2}\left(1-\gamma_5\right) , \quad \gamma_R = \frac{1}{2}\left(1+\gamma_5\right) , \tag{1.1}$$

such that $\gamma_R^2 = \gamma_R$, $\gamma_L^2 = \gamma_L$, and $\gamma_R\gamma_L = 0$. Furthermore, $\gamma_5 = i\,\gamma_0\gamma_1\gamma_2\gamma_3$, and γ^μ are the standard Dirac gamma matrices [6]. We can then project the fermion fields into right-handed and left-handed components, which in the massless limits correspond to positive and negative helicity states. The weak interactions will treat such components differently. More specifically, the left-handed component will be charged under the $SU(2)$ part of the gauge group, while the right-handed one will be a singlet. This explains the meaning of the subscript L in the gauge group, that we will simple denote $SU(2)$ from now on.

Let us begin the discussion on the SM electroweak sector by considering leptons. We take the left-handed electron and neutrino as part of a $SU(2)$ doublet, whereas their right-handed counterpart are assigned to a singlet representation, given the chiral nature of the weak interaction mentioned above. More specifically, the gauge transformation yields

$$\begin{aligned} &\begin{pmatrix}\nu_{e_L}\\ e_L\end{pmatrix} \to \exp\left[ig\alpha_i\frac{\tau_i}{2}\right]\begin{pmatrix}\nu_{e_L}\\ e_L\end{pmatrix}, \\ &\nu_{e_R} \to \nu_{e_R}\,, \\ &e_R \to e_R\,, \end{aligned} \tag{1.2}$$

where e_L and ν_{e_L} denote the left-handed electron and neutrino, whereas e_R and ν_{e_R} are their right-handed counterpart. In the above equation, the τ_i denote the Pauli matrices, i.e. the generators of $SU(2)$ in the fundamental representation. To each

generator T_i of the symmetry group corresponds a gauge field W_i. As is customary in gauge theories, we can define a covariant derivative as follows

$$D^\mu = \partial^\mu + igW_i^\mu T_i, \tag{1.3}$$

where g is the coupling constant and T_i are the gauge group generators in the appropriate representation. The covariant derivative encapsulates the interaction between matter and gauge fields, and transforms in the same way as the fields themselves under the action of the gauge group. We also define the field strength tensor associated to gauge fields as

$$W_{\mu\nu} = \frac{1}{i\,g}\Big[D_\mu, D_\nu\Big]\,. \tag{1.4}$$

The lagrangian describing the lepton fields is then given by

$$\begin{aligned}\mathcal{L} &= i\bar{L}\not{D}L + i\bar{\nu}_{e_R}\not{D}\nu_{e_R} + i\bar{e}_R\not{D}e_R \\ &= \mathcal{L}_{kin} + \mathcal{L}_c + \mathcal{L}_n.\end{aligned} \tag{1.5}$$

In the first line of the above equation, L denotes the $SU(2)$ left-handed doublet $L = \binom{\nu_{e_L}}{e_L}$. In the second line of the above equation we have also rearranged the lagrangian in three separate contributions: the kinetic term, the charged current term and the neutral current term. These are given by the following expressions

$$\begin{aligned}\mathcal{L}_{kin} &= i\bar{L}\not{\partial}L + i\bar{\nu}_{e_R}\not{\partial}\nu_{e_R} + i\bar{e}_R\not{\partial}e_R\,, \\ \mathcal{L}_c &= -g\,W_1^\mu\bar{L}\gamma_\mu\frac{\tau_1}{2}L + g\,W_2^\mu\bar{L}\gamma_\mu\frac{\tau_2}{2}L\,, \\ \mathcal{L}_n &= -g\,W_3^\mu\bar{L}\gamma_\mu\frac{\tau_3}{2}L\,,\end{aligned} \tag{1.6}$$

where τ_i are, again, the Pauli matrices. The first term in the above equation describes the usual kinetic term for massless fermions, whereas the second and third terms describe charged current and neutral current interactions respectively. The charged current term is usually expressed in terms of the following rotated fields

$$W_\mu^\pm = \frac{1}{\sqrt{2}}(W_\mu^1 \mp iW_\mu^2) \tag{1.7}$$

so that the charged current lagrangian becomes

$$\mathcal{L}_c = \frac{g}{\sqrt{2}}\Big(\bar{L}\gamma^\mu\tau^+LW_\mu^+ + \bar{L}\gamma^\mu\tau^-LW_\mu^-\Big). \tag{1.8}$$

Up to now we have discussed the weak sector, i.e. the $SU(2)$ part of the gauge group. However, we still need to introduce electromagnetism. The neutral current associated to τ_3, cannot be naively assigned to the electromagnetic current, since it includes neutrinos and since electromagnetic interactions do not distinguish between left and right particles. In order to include the photon in the theory, we need to enlarge the gauge group adding a $U(1)$ local symmetry, giving the enlarged gauge group $SU(2) \times U(1)$ mentioned at the beginning of the section. Such enlarged gauge symmetry implies the invariance of the lagrangian under a phase rotation of the field ψ as follows

$$\psi \to \psi' = \exp\left[ig'\alpha\frac{Y_\psi}{2}\right]\psi\,, \tag{1.9}$$

where Y_ψ is a quantum number usually referred to as the *weak hypercharge*, that was briefly mentioned above. Hence, note that as this point the abelian part of the gauge group is not yet the one associated to the electric charge, rather to the weak hypercharge. The abelian part of the gauge group introduces a new field B_μ, so that the covariant derivative becomes

$$D^\mu = \partial^\mu + igW_i^\mu T_i + ig'\frac{Y}{2}B^\mu\,, \tag{1.10}$$

where Y is a diagonal matrix whose eigenvalues are the hypercharges. Note that the fact that Y is diagonal implies that only the neutral current term of the lagrangian gets modified. In particular the latter can be written as follows

$$\mathcal{L}_n = -g\bar{\Psi}\gamma_\mu T_3 \Psi W_3^\mu - g'\bar{\Psi}\gamma_\mu\frac{Y}{2}\Psi B^\mu\,, \tag{1.11}$$

where Ψ is a column vector containing all the left-handed and right-handed fermionic fields of the theory, i.e.

$$\Psi = \begin{bmatrix} \nu_{e_L} \\ e_L \\ \nu_{e_R} \\ e_R \end{bmatrix}\,. \tag{1.12}$$

Furthermore, $T_3 = \mp 1/2$ for left-handed electron and neutrino fields respectively, and $T_3 = 0$ for their right-handed counterparts.

By rotating the fields B^μ and W_3^μ by an angle θ_W one obtains the usual fields A^μ and Z^μ associated with the photon and the Z boson respectively. The neutral current term of the lagrangian takes the following form

$$\begin{aligned}\mathcal{L}_n = &\bar{\Psi}\gamma_\mu \left(g \sin\theta_W T_3 + \frac{Y}{2} g' \cos\theta_W\right) \Psi A^\mu \\ &+ \bar{\Psi}\gamma_\mu \left(g \cos\theta_W T_3 - \frac{Y}{2} g' \sin\theta_W\right) \Psi Z^\mu \,.\end{aligned}$$

More specifically, in order for A^μ to represent the photon field, we need to choose $Y_L, Y_{\nu_{e_R}}$ and Y_{e_R} so that A^μ couples to the well known electromagnetic current

$$J^\mu_{em} = -e\left(\bar{e}_R \gamma^\mu e_R + \bar{e}_L \gamma^\mu e_L\right) \equiv eQ\bar{\Psi}\gamma^\mu\Psi, \tag{1.13}$$

where Q is the electromagnetic charge matrix per unit of positron charge e. Comparing the expressions we get

$$g \sin\theta_W T_3 + \frac{Y}{2} g' \cos\theta_W = eQ \,. \tag{1.14}$$

We can fix the value of one of the hypercharges, since they always appear in the combination $Y\,g'$. We choose $Y_L = -1$, which in turn implies the following two important relations

$$\begin{aligned} &g \sin\theta_W = g' \cos\theta_W = e \\ &T_3 + \frac{Y}{2} = Q \,. \end{aligned} \tag{1.15}$$

Note that the last equation is valid for any fermion and also implies $Y_{e_R} = -2$ and $Y_{\nu_{e_R}} = 0$, confirming the fact that the right-handed neutrino does not take part to electroweak interactions. Note that so far we have only discussed one family of leptons, the electron family. In the Standard Model there are three leptonic families, as can be seen from Fig. 1.1. In particular, we should have also included in our discussion the muon and the tau lepton, together with their corresponding neutrinos. We refrain from doing so since the extension of the theory to three families is straightforward.

We now move to the discussion of the quark sector. In the SM there are six quark flavours: up (u), down (d), charm (c), strange (s), top (t) and bottom (b). Once again, given the chirality of weak interactions, left components of the quark

fields are assigned to $SU(2)$ doublets, whereas their right-handed component are in a singlet representation. The gauge transformation on the $SU(2)$ quark doublet is the same as the one in Eq. (1.2). In the following we only consider the lightest quark family since the generalization to the other two families is straightforward. We will denote the quark doublet as $Q_L = \binom{u_L}{d_L}$. Using the second line of Eq. (1.15) one finds the following hypercharge values

$$Y_{Q_L} = \frac{1}{6}, \qquad Y_{u_R} = \frac{2}{3}, \qquad Y_{d_R} = -\frac{1}{3}\,. \tag{1.16}$$

The full lagrangian takes the form

$$\begin{aligned}\mathcal{L} = &-\frac{1}{4}W^a_{\mu\nu}W^{\mu\nu,a} - \frac{1}{4}B_{\mu\nu}B^{\mu\nu} + i\bar{L}\not{D}L + i\bar{e}_R\not{D}e_R \\ &+ i\bar{Q}_L\not{D}Q_L + i\bar{u}_R\not{D}u_R + i\bar{d}_R\not{D}d_R\,,\end{aligned} \tag{1.17}$$

where we can once again identify a kinetic, charged current and neutral current term defined as follows

$$\begin{aligned}\mathcal{L}_{kin} = &-\frac{1}{4}W^a_{\mu\nu}W^{\mu\nu,a} - \frac{1}{4}B_{\mu\nu}B^{\mu\nu} + i\bar{L}\not{\partial}L + i\bar{e}_R\not{\partial}e_R \\ &+ i\bar{Q}_L\not{\partial}Q_L + i\bar{u}_R\not{\partial}u_R + i\bar{d}_R\not{\partial}d_R \\ \mathcal{L}_n = &\frac{g}{2}W^\mu_3\left(\bar{\nu}_{e_L}\gamma_\mu\nu_{e_L} - \bar{e}_L\gamma_\mu e_L + \bar{u}_L\gamma_\mu u_L - \bar{d}_L\gamma_\mu d_L\right) \\ &+ \frac{g'}{2}B^\mu(-\frac{1}{2}\left(\bar{\nu}_{e_L}\gamma_\mu\nu_{e_L} + \bar{e}_L\gamma_\mu e_L\right) - \bar{\nu}_{e_R}\gamma_\mu\nu_{e_R} \\ &+ \frac{1}{6}\left(\bar{u}_L\gamma_\mu u_L + \bar{d}_L\gamma_\mu d_L\right) + \frac{2}{3}\bar{u}_R\gamma_\mu u_R - \frac{1}{3}\bar{d}_R\gamma_\mu d_R)\,, \\ \mathcal{L}_c = &\frac{g}{\sqrt{2}}\left(W^{\mu,+}\left(\bar{\nu}_{e_L}\gamma_\mu e_L + \bar{u}_L\gamma_\mu d_L\right) + W^{\mu,-}\left(\bar{e}_L\gamma_\mu\nu_{e_L} + \bar{d}_L\gamma_\mu u_L\right)\right)\,.\end{aligned}$$

We have reviewed the construction of a $SU(2) \times U(1)$ gauge theory describing electroweak interactions. Gauge invariance guarantees renormalizability of the theory. However, let us note that the fermions and gauge bosons that we have introduced so far need to be massless, since a mass term in the lagrangian would spoil gauge invariance, as we will show in the next section. This is in contradiction with experiments, since we know that particles such as the electron and the W and Z bosons have a mass. This so-called "mass problem" is solved in the Standard Model via the *Higgs mechanism*, that we will now briefly outline.

The Higgs mechanism in the Standard Model

In this section we will outline how the Standard Model gauge bosons and fermions acquire a mass, without spoiling gauge invariance. This is possible with the so-called *spontaneous symmetry breaking* (SSB) mechanism. Spontaneous symmetry breaking is a field-theoretical phenomenon characterized by the fact that the Lagrangian of a system displays a symmetry (global or local) but the quantum theory, instead of having a unique vacuum state which respects the symmetry, has a family of degenerate vacua that transform into each other under the action of the symmetry group. In the SM, a simple implementation of SSB requires the presence of a scalar field, that we will call the Higgs field, which needs to transform non-trivially under the part of the gauge group that we want to spontaneously break. We also want the theory to retain a $U(1)$ invariance corresponding to electrodynamics; in other words, the photon needs to stay massless. SSB must then take place in three of the four "directions" of the gauge group, the fourth one being the one corresponding to electric charge. Let us start by assigning the scalar field ϕ to the fundamental representation of $SU(2)$:

$$H = \begin{pmatrix} \phi_1 \\ \phi_2 \end{pmatrix}. \tag{1.18}$$

The most general scalar potential consistent with gauge invariance and renormalizability is

$$V(H) = m^2 \left(H^\dagger H\right) + \lambda \left(H^\dagger H\right)^2. \tag{1.19}$$

Let us now consider the case $m^2 < 0$. In this case, $V(H)$ is minimum for $H^\dagger H = -\frac{m^2}{2\lambda} \equiv \frac{v^2}{2}$. Indeed, the minimum configuration can be written as

$$H = \frac{1}{\sqrt{2}} \begin{pmatrix} v_1 \\ v_2 \end{pmatrix}, \qquad |v_1|^2 + |v_2|^2 = v^2 \tag{1.20}$$

and we require it to be left unchanged by electromagnetic gauge transformations, which correspond to the abelian subgroup $U(1)_{\text{em}}$. This corresponds to the requirement

$$e^{ie\alpha Q} \frac{1}{\sqrt{2}} \begin{pmatrix} v_1 \\ v_2 \end{pmatrix} = \frac{1}{\sqrt{2}} \begin{pmatrix} v_1 \\ v_2 \end{pmatrix}. \tag{1.21}$$

Using the relation between electric charge and weak hypercharge, $Q = T_3 + \frac{Y}{2}$, we can fix the hypercharge of the scalar doublet. We have

$$\begin{pmatrix} Q_1 & 0 \\ 0 & Q_2 \end{pmatrix} \begin{pmatrix} v_1 \\ v_2 \end{pmatrix} = \begin{pmatrix} \frac{1}{2} + \frac{Y}{2} & 0 \\ 0 & -\frac{1}{2} + \frac{Y}{2} \end{pmatrix} \begin{pmatrix} v_1 \\ v_2 \end{pmatrix} = \begin{pmatrix} 0 \\ 0 \end{pmatrix}, \tag{1.22}$$

where Q_1 and Q_2 are the electric charges of ϕ_1 and ϕ_2. There are two solutions to Eq. (1.22):

$$1) \quad v_1 = 0, \quad |v_2| = v, \quad Y = +1 \tag{1.23}$$

$$2) \quad v_2 = 0, \quad |v_1| = v, \quad Y = -1. \tag{1.24}$$

We will adopt the first choice, $Y_H = +1$, and therefore $Q_1 = 1$ and $Q_2 = 0$.

We can reparametrize H as follows:

$$H = \frac{1}{\sqrt{2}} e^{\frac{i\tau^i \theta^i(x)}{v}} \begin{pmatrix} 0 \\ v + h(x) \end{pmatrix}, \tag{1.25}$$

with $\theta^i(x)$ and $h(x)$ real. This parametrization is non-linear and contains all powers of the fields θ_i, but it's convenient if we work in unitary gauge since with this choice we can get rid of the θ_i fields by means of a gauge transformation. This is the choice we make from now on.

The scalar potential in Eq. (1.19) takes the form

$$V = \frac{1}{2}(2\lambda v^2)h^2 + \lambda v h^3 + \frac{1}{4}\lambda h^4 \tag{1.26}$$

from which we can see that the Higgs scalar has a mass $m_H^2 = 2\lambda v^2$ as well as cubic and quartic self interactions.

From the covariant derivative we get:

$$(D^\mu H)^\dagger (D_\mu H) = \frac{1}{2}\partial^\mu h \partial_\mu h + \left[\frac{1}{4}g^2 W^{\mu,+} W_\mu^- + \frac{1}{8}(g^2 + g'^2) Z^\mu Z_\mu\right](h + v)^2 . \tag{1.27}$$

We see that the W and Z bosons have acquired masses

$$\begin{aligned} m_W^2 &= \frac{1}{4} g^2 v^2 \\ m_Z^2 &= \frac{1}{4}\left(g^2 + g'^2\right) v^2. \end{aligned} \tag{1.28}$$

while the photon stays massless. We also observe that a kinetic term for the Higgs field has appeared as well as interactions between the Higgs boson and the gauge bosons W and Z.

Up to this point we have four free parameters: v, λ, g and g'. From Fermi's constant G_F we can evaluate v; we get

$$v = \sqrt{\frac{1}{G_F\sqrt{2}}} \approx 246 \text{ GeV}. \tag{1.29}$$

The Higgs boson has been discovered at the LHC in 2012 and its mass has the experimental value $m_H = 125.18$ GeV. This measure allows us to extract the value of the Higgs quartic coupling λ, which turns out to be $\lambda \approx 0.13$. The couplings g and g' are also as small as λ, therefore making possible a perturbative approach even in presence of the Higgs boson.

We now turn to the fermion masses. Let us recall the form of a Dirac mass term:

$$-m\bar{\psi}\psi = -m\left(\bar{\psi}_L\psi_R + \bar{\psi}_R\psi_L\right). \tag{1.30}$$

As we have seen in the previous section, the gauge transformations of the Standard Model act differently on left-handed and right-handed fields due to the chirality of electroweak interactions. It is immediate to observe how the mass term in Eq.(1.30) cannot be invariant upon such a transformation. However, reality tells us that fermions are massive and our theory needs to be consistent with it. Once again, the Higgs mechanism allows us to solve the puzzle, as we shall now see.

Let us start with leptons. We introduce a Yukawa term in the Lagrangian that has the following form

$$\mathcal{L}_Y^l = -y_e\bar{L}He_R + \text{h.c.}. \tag{1.31}$$

This term is gauge invariant, since, as mentioned above, H transforms as a $SU(2)$ doublet. Using the reparametrized field of Eq. (1.25) with $\theta_i = 0$, Eq. (1.31) becomes

$$\mathcal{L}_Y^l = -y_e\frac{v}{\sqrt{2}}\left(\bar{e}_Re_L + \bar{e}_Le_R\right) - y_e\frac{h}{\sqrt{2}}\left(\bar{e}_Re_L + \bar{e}_Le_R\right). \tag{1.32}$$

We obtained an interaction term with the Higgs field as well as a mass for the electron, while the neutrino remains massless.

We can apply the same procedure to quarks. By adding to the Lagrangian the term

$$\mathcal{L}_Y^d = -y_d \bar{Q}_L H d_R + \text{h.c.} \tag{1.33}$$

we find a mass term for the down quark, while the up quark remains massless. This can be seen by plugging into Eq. (1.33) the reparametrized expression for H, thus obtaining

$$\mathcal{L}_Y^d = -y_d \frac{v}{\sqrt{2}} \left(\bar{d}_R d_L + \bar{d}_L d_R \right) - y_d \frac{h}{\sqrt{2}} \left(\bar{d}_R d_L + \bar{d}_L d_R \right). \tag{1.34}$$

In order to obtain a massive up quark let us introduce the conjugate scalar field $\tilde{H} = i\tau_2 H^*$, where τ_2 is the second Pauli matrix and H^* is the complex conjugate field. It is easy to show that $\tilde{H}$ transforms as a doublet under $SU(2)$ and has hypercharge -1. The gauge invariant Yukawa term responsible for the up quark mass will then have the form:

$$\mathcal{L}_Y^u = -y_u \bar{Q}_L \tilde{H} u_R + \text{h.c.} \tag{1.35}$$

which, after SSB occurs, becomes

$$\mathcal{L}_Y^u = -y_u \frac{v}{\sqrt{2}} \left(\bar{u}_R u_L + \bar{u}_L u_R \right) - y_u \frac{h}{\sqrt{2}} \left(\bar{u}_R u_L + \bar{u}_L u_R \right). \tag{1.36}$$

Therefore, what we need to do to get a mass term for fermions is add to the Standard Model Lagrangian a *Yukawa term* of the form

$$\mathcal{L}_Y = -y_e \bar{L} H e_R - y_d \bar{Q}_L H d_R - y_u \bar{Q}_L \tilde{H} u_R + \text{h.c.} \tag{1.37}$$

which, via the mechanism of SSB, leads to the following masses for the electron as well as up and down quarks:

$$m_e = y_e \frac{v}{\sqrt{2}}, \qquad m_u = y_u \frac{v}{\sqrt{2}}, \qquad m_d = y_d \frac{v}{\sqrt{2}}. \tag{1.38}$$

The same picture is readily generalized to the other two families of the SM.

The coupling between fermions and the Higgs boson is proportional to the fermion mass; the greater the fermion mass, the stronger the interaction with the Higgs will be. In particular, the strongest coupling will be the top quark Yukawa, the

top being the heaviest quark in the SM with a mass of approximately $m_t \approx 173$ GeV. Note that, in general, while the kinetic terms of the Lagrangian are diagonal in terms of fields with definite flavour, the interaction Lagrangian is not. In other words, the basis of interaction eigenstates, that is built with the physical states in which interactions are diagonal, do not correspond to mass eigenstates.

To take this into account we can write the Yukawa couplings as constant matrices in the generation space, thus allowing flavour mixing:

$$\mathcal{L}_Y = -(Y_e)_{ij}\,\bar{L}_i H e_{R_j} - (Y_d)_{ij}\,\bar{Q}_{L_i} H d_{R_j} - (Y_u)_{ij}\,\bar{Q}_{L_i} H^* u_{R_j} + \text{h.c.}, \tag{1.39}$$

where i, j run over the different families and Y_{ij} are 3×3 complex matrices whose entries have to be measured by looking at decay processes. The mass matrix $M_{ij} = \frac{Y_{ij} v}{\sqrt{2}}$ is therefore not diagonal. We want to write the Lagrangian in terms of mass eigenstates, which means diagonalize the mass matrix. To accomplish this task, we use the fact that any matrix M can be diagonalized by means of a *bi-unitary transformation*

$$U^\dagger M V = M_{diag} \tag{1.40}$$

where U, V are unitary matrices and M_{diag} has real non negative eigenvalues. Let us now introduce the following vectors in flavour space:

$$E_{L,R} = \begin{pmatrix} e_{L,R} \\ \mu_{L,R} \\ \tau_{L,R} \end{pmatrix}, \quad N_L = \begin{pmatrix} \nu_{e_L} \\ \nu_{\mu_L} \\ \nu_{\tau_L} \end{pmatrix}, \quad U_{L,R} = \begin{pmatrix} u_{L,R} \\ c_{L,R} \\ t_{L,R} \end{pmatrix}, \quad D_{L,R} = \begin{pmatrix} d_{L,R} \\ s_{L,R} \\ b_{L,R} \end{pmatrix}. \tag{1.41}$$

Note that we did not include the right-handed neutrino since it is not involved in electroweak processes.

We can redefine the fields (except for the neutrinos, we will redefine those fields later on) via the action of unitary matrices, as follows:

$$\begin{aligned} E_L &= V_e E'_L \qquad D_L = V_d D'_L \qquad U_L = V_u U'_L \\ E_R &= U_e E'_R \qquad D_R = U_d D'_R \qquad U_R = U_u U'_R \end{aligned} \tag{1.42}$$

so that the Yukawa Lagrangian will contain terms such as:

$$\begin{aligned} \mathcal{L}_Y &\supset -\bar{E}'_R U_e^\dagger M_e V_e E'_L - \bar{D}'_R U_d^\dagger M_d V_d D'_L - \bar{U}'_R U_u^\dagger M_u V_u U'_L \\ &= -\bar{E}'_R M_e^{diag} E'_L - \bar{D}'_R M_d^{diag} D'_L - \bar{U}'_R M_u^{diag} U'_L, \end{aligned} \tag{1.43}$$

where we have used Eq. (1.40). The fields with primes are mass eigenstates, while $M_e^{diag}, M_d^{diag}, M_u^{diag}$ are diagonal matrices whose entries are the fermions masses.

We now want to see what happens to the other terms of the SM Lagrangian when we use the basis of mass eigenstates. It is easy to verify that the kinetic, neutral current and electromagnetic current terms are not affected by the field redefinition of Eq. (1.42). In fact, we can write the kinetic part of the Lagrangian as follows:

$$\mathcal{L}^{kin} = \sum_f i\bar{f}\partial\!\!\!/ f \tag{1.44}$$

where the sum is over all the fermionic fields of the theory. The γ^μ matrices commute with the unitary matrices V_f and U_f, since they act on different spaces. Hence

$$\begin{aligned} i\bar{f}_L\partial\!\!\!/ f_L &= i\bar{f}'_L V_f^\dagger \partial\!\!\!/ V_f f'_L = i\bar{f}'_L \partial\!\!\!/ V_f^\dagger V_f f'_L = i\bar{f}'_L \partial\!\!\!/ \mathbb{1} f'_L \\ i\bar{f}_R\partial\!\!\!/ f_R &= i\bar{f}'_R U_f^\dagger \partial\!\!\!/ U_f f'_R = i\bar{f}'_R \partial\!\!\!/ U_f^\dagger U_f f'_R = i\bar{f}'_R \partial\!\!\!/ \mathbb{1} f'_R, \end{aligned} \tag{1.45}$$

where f_L and f_R stand for the left and right components of the fermionic fields in the theory. The same proof holds for the neutral current and electromagnetic current terms of the SM Lagrangian.

Something interesting happens with the charged current term, since it involves the coupling between different components of the same $SU(2)$ doublet. Let us see it in some detail. We have

$$\mathcal{L}^c = \frac{g}{\sqrt{2}}\left(W_{\mu,-}J^{\mu,+} + W_\mu^+ J^{\mu,-}\right), \tag{1.46}$$

where, using the vector notation of Eq. (1.41) and Eq. (1.42),

$$J_\mu^+ = \bar{E}_L\gamma_\mu N_L + \bar{D}_L\gamma_\mu U_L \to \bar{E}'_L V_e^\dagger \gamma_\mu N_L + \bar{D}'_L V_d^\dagger \gamma_\mu V_u U'_L. \tag{1.47}$$

Since we are working with massless neutrinos we can rotate them (leaving everything else unchanged) by redefining their associate fields as follows

$$N_L = V_e N'_L. \tag{1.48}$$

Equation (1.47) becomes

$$J_\mu^+ = \bar{E}'_L\gamma_\mu N'_L + \bar{D}'_L V_d^\dagger V_u \gamma_\mu U'_L. \tag{1.49}$$

The first term is diagonal in flavour space, while there is nothing we can do for the quark part. In the base of mass eigenstates, the interactions between charged quarks are not diagonal. The matrix $V_d^\dagger V_u \equiv V_{\text{CKM}}$ is known as the *Cabibbo-Kobayashi-Maskawa* matrix and it contains information on the strength of flavour-changing weak decays. It is a unitary 3×3 matrix and all its entries are fundamental parameters of the SM, whose values are extracted from experiments.[2]

We have now completed our brief review of the SM electroweak sector. The concepts above will be important in order to understand and follow the notation employed in Chapter 5, where we will be interested in electroweak corrections to dilepton production at the LHC. We now turn to a discussion of the strong sector of the Standard Model.

1.1.2 Strong sector

The strong sector of the SM describes the interactions between quarks and gluons. In particular it describes how they bind together to form protons, neutrons and more generally hadrons. Indeed, although the proton is the only stable hadron in nature, at colliders many more, albeit unstable, are produced. These include baryons and mesons, the former being bound states of three quarks and the latter being bound states of quark anti-quark pairs.

The strong interaction finds its theoretical framework within the realm of Quantum Chromodynamics, a non-Abelian gauge theory based on $SU(3)$. While we won't delve into the historical evolution of QCD as the theory of strong interactions, our focus here is to elucidate its modern understanding, particularly emphasizing its perturbative regime.

The main difference with respect to the electroweak sector of the SM, is that hadrons, the particles that are actually detected at colliders, are not elementary; rather, they are composed of fundamental constituents, quarks, which we previously introduced when discussing the particle spectrum of the SM as well as in the discussion of the EW sector. Quarks, akin to leptons, are fermions but possess

[2]Unitarity also guarantees the suppression of flavour-changing neutral currents (FCNC).

an additional quantum property known as *color*, which is the degree of freedom responsible for strong interactions. The introduction of an additional quantum number became imperative to reconcile the fully symmetric wave function of observed excited states of nucleons with the Fermi-Dirac statistics that fermions are expected to adhere to. Nowadays experiments firmly substantiate the presence of color. Quarks then arise as irreducible representations of the gauge group $SU(3)$. More specifically they transform in the fundamental representation, usually denoted with "3", whereas antiquarks transform in the complex conjugate representation, denoted by "$\bar{3}$". The gauge bosons of $SU(3)$ are called *gluons*, and they transform in the eight-dimensional adjoint representation.

The two most striking features of QCD are its asymptotic behaviours, i.e. the low energy and high energy behaviour. In the high energy regime, the coupling constant governing the interactions of quarks and gluons becomes smaller and smaller, making a perturbative approach feasible (see e.g. [7]). This phenomenon goes under the name of *asymptotic freedom*, and it is a consequence of the non-Abelian nature of QCD. On the other hand, at low energies, the coupling grows larger and larger, leaving to *confinement* of quarks and gluons inside hadrons. The low energy regime is therefore strongly coupled and not suited for perturbation theory, which requires the coupling to be small. As a consequence of confinement, color is not an observable degree of freedom, and physical hadrons only appear as color singlets. We will not focus here on the non-perturbative regime of QCD, but rather only focus on the high energy behaviour.

As we have done in the case of the EW sector, we define the covariant derivative as

$$D_\mu = \partial_\mu + i g_s T^c G^c_\mu \,, \tag{1.50}$$

where g_s denotes the strong coupling constant and G^c_μ denotes the gluon gauge field. In analogy with what has been done in the EW sector, we define the gluon field strength tensor by means of Eq. (1.4), provided we substitute the correct coupling constant and covariant derivative. The gluon field strength tensor can

be written in terms of the gluon field G^a_μ as follows

$$G^a_{\mu\nu} = \partial_\mu G^a_\nu - \partial_\nu G^a_\mu - g_s f^{abc} G^b_\mu G^c_\nu \,. \tag{1.51}$$

Furthermore, in Eq. (1.50) the matrices T^c are the generators of $SU(3)$ in a generic representation (which will correspond to the fundamental when D_μ acts on quark fields and to the adjoint when it acts on gluon fields). The generators of $SU(3)$ satisfy the commutation relations $[T^a, T^b] = if^{abc}T^c$ in any representation, and they are normalised as $\mathrm{Tr}\left[T^a, T^b\right] = T_R\,\delta^{ab}$. We find it convenient to choose $T_R = 1/2$. The $SU(3)$ generators in the fundamental representation are related to the well known Gell-Mann matrices λ_i by $T_i = \lambda_i/2$, whereas in the adjoint representation they are related to the structure constants as $(T^a)_{bc} = -if^{abc}$. Important invariants of $SU(3)$ are the quadratic Casimirs of a representation, defined as $T^a_{ij}T^a_{jk} = C_R\delta_{ik}$. The quadratic Casimirs of $SU(3)$ in the fundamental and adjoint representation are denoted with C_F and C_A respectively, and their value can be shown to be

$$C_F = \frac{4}{3}\,, \quad C_A = 3\,.$$

It is sometimes useful to think in terms of a generic number of dimensions of the gauge group, that we denote with N_c, although in QCD we know that $N_c = 3$. This may seem to be unnecessary now, but it will prove useful when discussing the large-N_c limit of scattering amplitudes in Chapter 2. In this generalized case, the quadratic Casimirs are given by $C_A = N_c$ and $C_F = (N_c^2 - 1)/(2N_c)$. For future convenience, we also define color operators $\mathbf{T}_i$ related to the $SU(N_c)$ generators associated with particle i. More specifically

$$\begin{aligned}
&(\mathbf{T}_i)^a_{b_i c_i} = -if^a_{b_i c_i} \quad \text{if } i \text{ is a gluon,} \\
&(\mathbf{T}_i)^a_{i_i j_i} = +T^a_{i_i j_i} \quad \text{if } i \text{ is a final(initial) state quark(anti-quark),} \\
&(\mathbf{T}_i)^a_{i_i j_i} = -T^a_{j_i i_i} \quad \text{if } i \text{ is an initial(final) state quark(anti-quark).}
\end{aligned} \tag{1.52}$$

The square of the color charge operator yields the Casimir operator, i.e. $\mathbf{T}_i^2 = C_i$, where $C_g = C_A$ and $C_q = C_F$.

The lagrangian of QCD is given by

$$\mathcal{L}_{QCD} = \mathcal{L}_{cl} + \mathcal{L}_{gf} + \mathcal{L}_{gh} \tag{1.53}$$

where $\mathcal{L}_{cl}$ is the classical lagrangian, $\mathcal{L}_{gf}$ is the gauge fixing term necessary to quantize the theory, and $\mathcal{L}_{gh}$ is the ghost contribution, necessary in the quantization of a non-abelian theory (see e.g.[6] for a review on the quantization of non-abelian gauge theories). The classical lagrangian is given by

$$\mathcal{L}_{cl} = \mathcal{L}_{\rm YM} + \mathcal{L}_{\rm quarks} \tag{1.54}$$

where $\mathcal{L}_{\rm YM}$ is the Yang-Mills lagrangian, whose explicit expression is given by

$$\mathcal{L}_{\rm YM} = -\frac{1}{4} G^a_{\mu\nu} G^{\mu\nu}_a \tag{1.55}$$

and $\mathcal{L}_{\rm quarks}$ describes the quarks and their interactions with gluons and is given by

$$\mathcal{L}_{\rm quarks} = \sum_{\rm flavours} \bar{q}_i \left(i \not{D} - m \right)_{ij} q_j \,, \tag{1.56}$$

where the sum runs over n_f different flavours. Regarding the gauge-fixing term, we choose a class of covariant gauges characterized by the parameter ξ. The gauge fixing term of the Lagrangian can then be written as

$$\mathcal{L}_{gf} = -\frac{1}{2\xi} \left(\partial^\mu G^a_\mu \right)^2 . \tag{1.57}$$

Two common choices of covariant gauges are the so-called *Laundau gauge*, achieved by setting $\xi = 0$, and the so-called *Feynman gauge*, where $\xi = 1$. Note that in all the relevant computations reported in this thesis we will use the Feynman gauge. In such a gauge, the gluon propagator acquires a particularly simple form, reducing the number of terms one needs to compute. However, the price to pay is that ghost fields are required with this gauge choice in order to cancel unphysical degrees of freedom that would otherwise propagate. The ghost part of the Lagrangian reads

$$\mathcal{L}_{gh} = \partial_\mu \eta^{a,\dagger} D^\mu_{ab} \eta^b \,. \tag{1.58}$$

One of the consequences of the non-Abelian nature of QCD is that the field strength tensor $G^a_{\mu\nu}$ is not gauge invariant. It is only its trace that satisfies this requirement. This is due to the fact that the gluon itself is "colored", unlike the photon which is electrically neutral. As in the case of photons, gluons are

massless. Any explicit gluon mass terms in the QCD lagrangian would break gauge invariance. The quark mass term in Eq. (1.56), instead, is perfectly allowed, since QCD is a non-chiral theory. The Feynman rules that follow from the lagrangian of QCD are reported in Appendix A and will be extensively used for the calculations performed in the rest of this thesis.

We will now conclude this section emphasising the concepts of perturbative QCD, running strong coupling and asymptotic freedom, which will lay the foundations for the main chapters of this thesis.

Towards perturbative QCD

It is well known (see e.g.[6]) that the parameters that appear in the lagrangian of a QFT are not in one to one correspondence to the physical quantities that are measured in experiments. Examples of such parameters are the coupling constants as well as the masses of the particles. In order to connect the lagrangian parameters with the physical quantities, a *renormalization* procedure is required. In a renormalizable theory, as is the case of QCD, this procedure is enough to make all the $n-$point Green functions finite, therefore reabsorbing the UV divergences that are usually encountered when computing loop amplitudes. In the case of QCD, however, this notion of perturbative renormalizability, makes sense when working in the high energy regime, where the coupling constant is small.

The renormalization procedure introduces an additional energy scale, that we will denote with μ. We will refer to this parameter as the renormalization scale. However, physical observables should not depend on an arbitrary scale that we introduced by renormalizing the parameters of the lagrangian. To see this in practice, we consider the case of a physical dimensionless observable O that we assume for simplicity to only depend on one scale Q^2 as well as on the strong coupling $\alpha_s = g_s^2/(4\pi)$. Being dimensionless, the only μ dependence can be through the ration Q^2/μ^2. The requirement that the physical observable should not depend

on the scale can be expressed through the following equation[3]

$$\mu^2 \frac{d}{d\mu^2} O(Q^2/\mu^2; \alpha_s) = \mu^2 \Big[\frac{\partial}{\partial \mu^2} + \frac{\partial \alpha_s}{\partial \mu^2} \frac{\partial}{\partial \alpha_s} \Big] O = 0 \,. \tag{1.59}$$

We define the so-called β-*function* as

$$\beta(\alpha_s) = \mu^2 \frac{\partial \alpha_s}{\partial \mu^2} \,, \tag{1.60}$$

and rewrite the differential equation in Eq. (1.59) as follows

$$\Big[- \frac{\partial}{\partial t} + \beta(\alpha_s) \frac{\partial}{\partial \alpha_s} \Big] O(e^t; \alpha_s) = 0 \,, \tag{1.61}$$

with $t = \log \frac{Q^2}{\mu^2}$, which is solved by defining a new function, the running coupling $\alpha_s(Q^2)$ such that

$$\log \frac{Q^2}{\mu^2} = \int_{\alpha_s(\mu^2)}^{\alpha_s(Q^2)} \frac{du}{\beta(u)} \,. \tag{1.62}$$

This implies that the only dependence of our observable O on the energy scale derives from the running of the coupling. Remarkably, this also means that if we can compute the value of the observable at some energy scale by means of perturbation theory, we can derive its value at a different energy scale by solving Eq. (1.62). The $\beta-$function, at weak coupling, can be expanded in perturbation theory as follows

$$\beta(\alpha_s) = -\alpha_s \left(\beta_0 \frac{\alpha_s}{2\pi} + \beta_1 \left(\frac{\alpha_s}{2\pi} \right)^2 + \beta_2 \left(\frac{\alpha_s}{2\pi} \right)^3 + \mathcal{O}(\alpha_s^4) \right) \,. \tag{1.63}$$

The β function coefficients can be obtained by computing higher-order corrections to the correlation functions of the theory. We will only report the result for β_0 and β_1 here

$$\beta_0 = \frac{11}{6} C_A - \frac{1}{3} n_f \,, \quad \beta_1 = 17 C_A - \frac{19}{3} n_f \,. \tag{1.64}$$

We note that for $n_f \leq 33/2$ the β coefficients are positive (since we collected an overall minus sign). This behaviour is the opposite as the one the we find in QED, and the difference is due to the non-Abelian nature of QCD. Going back to Eq. (1.60),

[3]Here we are not considering quark masses, that would introduce anomalous dimensions. We are also neglecting scale dependence arising from the renormalization of parton distribution functions, since this will be treated later in the section.

in the perturbative region we can truncate the series on the right hand side and solve the equation for the running of the strong coupling to its first order as follows

$$\alpha_s(Q^2) = \frac{\alpha_s(\mu^2)}{1 + (\alpha_s(\mu^2)/2\pi)\beta_0 \log(Q^2/\mu^2)} \,. \tag{1.65}$$

From the above equation it is clear that as Q^2 becomes large the strong coupling decreases, as shown in Fig. 1.2. This is the property of asymptotic freedom, that was already mentioned when introducing the strong sector. On the other hand, at low energies, the strong coupling becomes large, thus endangering the validity of perturbative methods. To see this more closely, let us introduce a dimensionful parameter, that we denote $\Lambda_{\rm QCD}$, defined as the scale at which α_s, if extrapolated outside the perturbative domain, i.e. from Eq. (1.62)

$$\log \frac{Q^2}{\Lambda^2_{\rm QCD}} = \int_\infty^{\alpha_s(Q^2)} \frac{du}{\beta(u)} \,. \tag{1.66}$$

In terms of this scale, Eq. (1.65) becomes

$$\alpha_s(Q^2) = \frac{2\pi}{\beta_0 \log\left(\frac{Q^2}{\Lambda^2_{\rm QCD}}\right)} \,. \tag{1.67}$$

It is clear from the equation above that $\alpha_s(Q^2)$ decreases as $\log\left(Q^2\right)^{-1}$ as Q^2 increases. Using $Q^2 = m_Z^2$ and $\alpha_s(m_Z^2) = 0.118$, we find $\Lambda_{\rm QCD} \sim 200\,\text{MeV}$. Perturbation theory is valid only for Q larger than this value, say around 1 GeV.

When renormalizing a theory, one needs to define a renormalization scheme. In QCD, it is customary to renormalize the strong coupling in the so-called $\overline{\rm MS}$ scheme, defined as

$$\alpha_{s,b}\ S_\epsilon = \alpha_s(\mu)\, \mu^{2\epsilon}\, Z\left[\alpha_s(\mu)\right] , \tag{1.68}$$

where μ is the renormalization scale, and $S_\epsilon = (4\pi)^\epsilon e^{-\epsilon\gamma_E}$, with $\gamma_E \approx 0.5772$ the Euler constant. Up to two loops, the renormalization factor Z reads

$$Z[\alpha_s] = 1 - \frac{\alpha_s}{2\pi}\frac{\beta_0}{\epsilon} + \left(\frac{\alpha_s}{2\pi}\right)^2 \left(\frac{\beta_0^2}{\epsilon^2} - \frac{\beta_1}{2\epsilon}\right) , \tag{1.69}$$

with the β-function coefficients defined in Eq. (1.64).

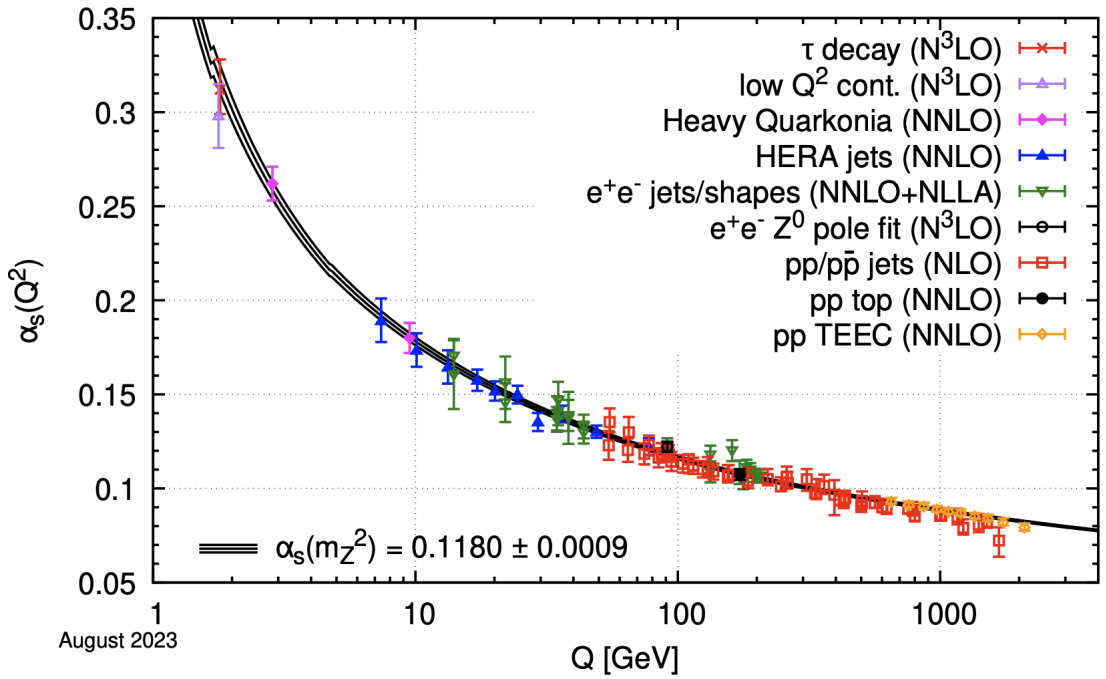


Figure 1.2: Running of the strong coupling [8].

It is important to mention that the renormalization group equation Eq. (1.60), only gives us information on the running of the coupling, but not on its value at a given scale. The latter needs to be extracted from experiments. Figure 1.2 shows different values of the coupling extracted by means of a number of observables. Indeed, there are various methods that can be used to extract values of the strong coupling from experiments, although a dedicated discussion goes beyond the scope of this thesis. For a review on the measurements of the strong coupling, see e.g. [9]. In the context of the running of α_s, it is interesting to note that the LHC is able to provide very hard probes, e.g. the production of very energetic partons in the final state (jets), bringing sensitivity to the strong coupling at very high energy scales. This in principle allows us to test the evolution of the coupling in the TeV region. One observable that could be used for this purpose is the three-to-two jets ratio. Therefore, theoretical predictions involving jets are quite important[4]. These require many ingredients, including the scattering amplitudes. In Chapter 2, we will present the calculation of three-jets scattering amplitudes at two loops in massless QCD.

[4]Jet observables are important in many other contexts, we only mention this here since it is related to the computation of jet amplitudes reported later in this thesis

1.2 Testing the SM: the Large Hadron Collider

We have provided an overview of the Standard Model of particle physics, covering both the electroweak and strong sectors. Our focus now shifts to the central theme of this thesis: the precision testing of the Standard Model through collider phenomenology. It is fair to say that the Standard Model is a story of success. Measurements are in agreement with theoretical predictions over many order of magnitudes, to the point that - if we lived inside a collider - we could claim that we fully understand fundamental physics. However, there are still several puzzles that the SM cannot solve in its present form: the oscillation of neutrinos, the matter/anti-matter asymmetry, the presence of dark matter, etc. Collider physics has the unique ability to recreate early-Universe conditions with enough statistics so that we can actually try to understand at least some of these problems. The search of physics "beyond the Standard Model" (BSM) at colliders usually follows two distinct yet complimentary paths. One is the so-called *direct searches*, where one looks for bumps in the measured spectrum as to indicate the presence of a new particle, as was the case for the discovery of the Higgs boson in 2012 for instance. Another search strategy is the so-called *indirect search*, where one tries to improve the accuracy of measurements as much as possible. By comparing such precise measurements with theoretical predictions (that will also need to be as accurate as possible), one tries to look for deviations that could be attributed to New Physics effects. Although many different colliders contributed to the discovery of SM particles over the last 60 years, we now mainly work with the Large Hadron Collider (LHC), operational at CERN since 2008. The LHC is a hadron collider, mainly used as a proton-proton collider but also employed for the collision of heavy ions. The collider consists of a tunnel ring of 27 km in circumference, where two beams of protons circulate in opposite directions. The beams are scattered at extremely high energies, reaching the maximum of 13.6 TeV. The LHC is able to provide a billion collisions per second, and provides enough statistics to observe rare processes such as the ones involving the Higgs boson. Indeed, in 2012, the long-seeked Higgs boson was discovered at the LHC, therefore confirming the last

missing evidence of the SM particle content. The Higgs boson was discovered by two different experiments at the LHC, ATLAS and CMS [2, 3], at first in the diphoton and 4−leptons decay channels, see Fig. 1.3. Indeed, since it is not a stable particle,

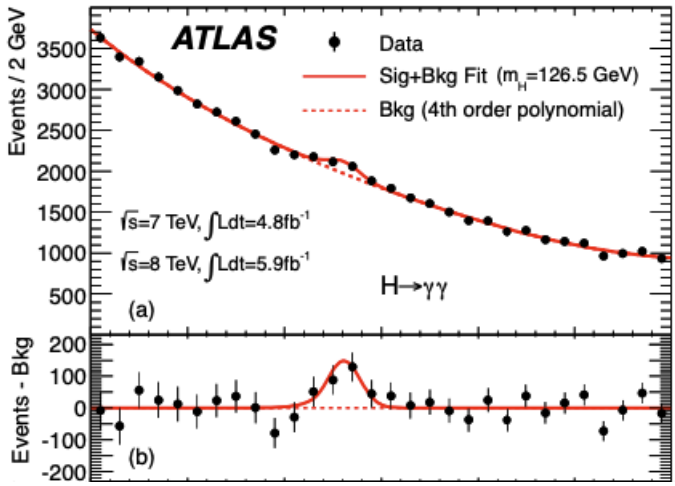


Figure 1.3: Higgs boson discovery by ATLAS in the diphoton decay channel

it cannot be detected directly at a collider and needs to be reconstructed through its decay products. The lifetime of the Higgs boson is approximately $10^{-22}s$, and it is related by the uncertainty principle to the decay width, which is predicted by the Standard Model to be around 4 MeV. The width of the Higgs boson and its measurement at a hadron collider will be thoroughly discussed in Chapter 4. Ever since the Higgs boson discovery, the LHC has entered the so-called precision era. No new fundamental particles have been discovered, and a significant effort is devoted to indirect searches. This requires theoretical predictions to be at least as precise as the experimental measurements, in order to establish whether BSM effects are present in a given measurement, as well as to allow the study of SM phenomena at high precision. Theoretical predictions for high-energy scattering are made in the context of perturbation theory. This is made possible by the property of asymptotic freedom of QCD, that we discussed in the previous section. However the LHC is a proton collider and protons are not elementary particles. We therefore need to understand what happens to the proton when probed at such high energies and what the actual high-energy degrees of freedom of QCD are, in order to describe a collision from first principle. This is done in the context of the so-called *parton model*. We

will only briefly discuss it here, leaving the details to the rich literature. The parton model has been formulated by Richard Feynman between the '60s and the '70s, and confirmed experimentally by means of deep-inelastic scattering (DIS) experiments performed at the Stanford Linear Accelerator (SLAC) around the same years [10]. These were fixed target collisions, where a high energetic electron beam is fired towards protons and neutrons in atomic nuclei. The result of these experiments was that at high energies the components of the proton (quarks and gluons) behave as free particles. The scattering can therefore be described in terms of the elementary scattering of an electron with a quark (or a gluon). QCD is therefore such that its degrees of freedom change from the low- energy non-perturbative regime (hadrons) to the high-energy regime (quarks and gluons behaving as free particles). A proton-proton high-energy collision can therefore be interpreted, in the light of the parton model, as an elementary collision between massless quarks and gluons, weighted by the 'probability' of extracting a quark or a gluon from the proton. In other words, the cross section for a proton-proton scattering to produce a generic final state X can be written by means of the following *factorization formula* (see e.g. [7])

$$\begin{aligned}\sigma_{pp\to X} = &\sum_{i_1,i_2}\int dx_1 dx_2 f_{i_1}(x_1,\mu_F^2) f_{i_2}(x_2,\mu_F^2)\hat{\sigma}_{i_1 i_2\to X} \\ &\times\left(1+\mathcal{O}\left(\frac{\Lambda_{\rm QCD}^n}{Q^n}\right)\right), \quad n\geq 1\,,\end{aligned} \tag{1.70}$$

where the sum runs over different parton flavours, $x_{1,2}$ are fractions of incoming hadrons longitudinal energies carried by partons i_1, i_2, whose distribution in the hadron is encoded in the so-called parton distribution functions $f_{i_{1,2}}$. The latter are inherently non-perturbative objects, whose dependence on x_i need to be extracted from data. The crucial point, however, is that they are universal objects and their evolution is governed by DGLAP equations (see e.g. [7]). This universality makes it possible to extract them from one experiment and use them for all the others. The DGLAP evolution introduces a dimensionful parameter μ_F^2, the so-called factorization scale, in a similar fashion to what RGE does in the renormalization procedure discussed in the previous section. As we have seen there, a physical observable will be independent of the factorization scale. Furthermore, $\hat{\sigma}_{i_1 i_2\to X}$

denotes the *partonic cross section*, meaning the cross section for the elementary scattering $i_1 i_2 \to X$, which can be computed with perturbative techniques. The correction $\mathcal{O}\left(\Lambda^n_{\rm QCD}/Q^n\right)$ measures the error that we make by employing this factorization formula. It takes into account non-perturbative effects that may spoil the validity of factorization, such as hadronization, mass effects etc. The suppression of such non-perturbative effects is usually quadratic and therefore negligible, although it has been proven that for some observables it could also be linear, making these effects relevant for precise phenomenology (see e.g. [11] for a recent phenomenological study).

We want to emphasize the importance of Eq. (1.70), that allows us to describe a very complicated collision event in terms of well-defined ingredients. Note also that a factorized approach is possible due to the large separation of scales between the so-called *hard process*, describing the highest momentum-transfer event in the collision and that usually happens at scales $Q \gtrsim \mathcal{O}(100)\,\text{GeV}$ and low energy effects such as hadronization, where $Q \sim 1\,\text{GeV}$. The evolution from the high energy to the low energy regime happens through the emission of mostly collinear streams that lose energy, until they reach low-enough energy to hadronize. These subsequent collinear parton branchings are described by so-called *parton showers* and an accurate description of them is crucial in order to obtain results that can be meaningfully compared with experiments. A discussion of parton showers and hadronization models goes beyond the scope of this thesis, and we refer to e.g. [12] for a review of their status and theoretical developments.

In this thesis we will focus on the theoretical description of the hard process. Higher order corrections to the hard process are very often required to make adequate predictions for collider phenomenology. The strong coupling at the energy scale of the Z boson mass is $\alpha_s(Q^2 = m_Z^2) \sim 0.118$, which means that - loosely speaking - if we are interested in 1% precision physics at the LHC, we would need to expand to at least $\mathcal{O}(\alpha_s^2)$. A different situation holds for electroweak corrections. Indeed, the electromagnetic coupling at the same energy scale is roughly 10% of the strong coupling. This means that usually $\mathcal{O}(\alpha)$ predictions will be enough

for the same precision target. However, in some situations, electroweak effects can be enhanced. In such a situation, higher-order EW corrections, as well mixed QCD-EW corrections are also important to control. We will see an example of this scenario in Chapter 5, where we will be interested in the mixed QCD-EW corrections to dilepton production at the LHC.

We write the perturbative expansion of the partonic cross section as follows

$$\begin{aligned}\hat{\sigma} = \alpha_s^q \alpha^r \Bigg(\hat{\sigma}_0 + \left(\frac{\alpha_s}{2\pi}\right)\hat{\sigma}_{1,\mathrm{QCD}} + \left(\frac{\alpha_{ew}}{2\pi}\right)\hat{\sigma}_{1,\mathrm{EW}} + \\ \left(\frac{\alpha_s}{2\pi}\right)^2 \hat{\sigma}_{2,\mathrm{QCD}} + \left(\frac{\alpha_s}{2\pi}\right)\left(\frac{\alpha_{ew}}{2\pi}\right)\hat{\sigma}_{2,\mathrm{QCD}\otimes\mathrm{EW}} + \dots\Bigg),\end{aligned} \tag{1.71}$$

where $\hat{\sigma}_0$ denotes the *leading order* (LO) prediction, $\hat{\sigma}_{1,\mathrm{QCD(EW)}}$ the *next-to-leading order* (NLO) QCD(EW) prediction, and $\hat{\sigma}_{2,\mathrm{QCD}}$ the *next-to-next-to-leading order* (NNLO) QCD prediction. For future convenience we have also included the NNLO-like mixed QCD-EW correction $\hat{\sigma}_{2,\mathrm{QCD}\otimes\mathrm{EW}}$. It is worth mentioning here that the perturbative series on the right hand side of Eq. (1.71), both in the strong and electroweak coupling, is an asymptotic series - therefore not convergent. We expect the perturbative convergence to break down at sufficiently high perturbative orders, although well beyond the first two orders which are the focus of this thesis[5].

The cross section is related to the *scattering amplitude* in the following way

$$\hat{\sigma} = \mathrm{Flux}\int d\Phi |\mathcal{M}|^2\,, \tag{1.72}$$

where the flux factor, in the case of a massless two particle initial state, is given by $\mathrm{Flux} = 1/(2s)$, s being the partonic center of mass energy. Furthermore, $d\Phi$ denotes the Lorentz-invariant phase space associated with the production of a given final state. The scattering amplitude $\mathcal{M}$ is the central ingredient and its calculation in the context of perturbative QFT will be discussed at length in Chapter 2.

In the next section, we will try to motivate and present in a more physical way the concepts that we introduced above. We will also try to argue why it is important to perform higher order calculations and why we actually care about %-level precision for collider phenomenology. We will do this by considering the important case of Higgs production at the LHC.

[5]We will not deal with this problem here, but only mention that the effect of breaking of the perturbative series is partially reflected in the $\Lambda^n_{\mathrm{QCD}}/Q^n$ terms in Eq. (1.70).

1.3 Mastering precision: the What, How and Why

As previously mentioned, one of the main missions of the LHC is to "stress-test" the SM and look for physics beyond it. In the SM with minimal assumptions, New Physics (NP) effects are governed by the ratio Q^2/Λ^2, where Q^2 is the typical energy scale of the probe, and Λ^2 is the energy scale at which NP degrees of freedom live. At the LHC, direct searches (see e.g. [13]) constrain Λ to be heavier than $\mathcal{O}(1\,\text{TeV})$, whereas the typical energy of the probe is $Q \sim 100\,\text{GeV}$. This implies that in order to get a handle on NP at the LHC we need to control the SM at the %-level precision. In the context of NP searches, the Higgs sector plays a fundamental role. Indeed, many open questions in high-energy physics are related to the knowledge of its properties. Furthermore, since it is a new fundamental particle, we want to study it as precisely as possible. Since, as we will argue shortly, Higgs production is mainly gluon induced, its production rate is dependent on the gluon color charge C_A. In QCD, $\alpha_s \sim 0.1$ and $C_A = 3$, which means that in order to reach %-level precision we need to compute higher order terms in the perturbative series. This is what we will do in the rest of this section, where we will sketch the computation of NLO QCD corrections to Higgs production at the LHC. In doing so, we will introduce most of the concepts that will be the main characters of the following chapters.

In Section 1.1.1 we have seen how in the SM the Higgs boson couples to quarks via Yukawa coupling, which is proportional to the mass of the quarks. For this reason, the preferred coupling will be to the heaviest fermion in the SM, the top quark. Recall that the LHC is a proton-proton collider and that we can associate to the proton the energy scale of hadrons $\Lambda_{\text{QCD}} \sim 1\,\text{GeV}$, while the Higgs boson lives at the EW scale $v \sim \mathcal{O}(100\,\text{GeV})$. As a consequence, $t_{\text{proton}} = 1/\Lambda_{\text{QCD}} \gg t_{\text{EW}} = 1/v$, which means that the Higgs sees the proton as a static object. This large separation of scales result in the factorization formula presented in Eq. (1.70). In this respect it is worth mentioning that a generic proof of factorization for hadron collisions is still not entirely available, whereas it is present in the case of hadron-lepton collisions (DIS) (see e.g. [14]). We will make use of it anyhow for LHC processes

since its validity has been continuously confirmed by experiments, besides having been proved up to NNLO by explicit calculations (see Chapter 3).

In order to produce Higgs bosons, we need to extract high energy particles from the proton. At center of mass energies that are relevant for this process, the LHC behaves mostly as a gluon collider. The diagram giving the largest contribution to this process is therefore a one-loop diagram rather than a tree diagram, where gluons interact with a virtual top quark that is in turn coupled to the Higgs, see left pane of Fig. 1.4[6].

We now want to compute this diagram. The Higgs boson is lighter than the top quark so we might think of treating the latter as a heavy degree of freedom that decouples from the SM at the energies that are relevant for Higgs production. This way, we can see an example of the "decoupling" of heavy degrees of freedom that is at the basis of the Q^2/Λ^2 behaviour discussed at the beginning of this section[7]. Let us write down the contribution associated with the triangle diagram in the left pane of Fig. 1.4

$$I = \quad \sim y_t \int \frac{d^4k}{(2\pi)^4} \frac{\mathrm{Tr}\left[\gamma^\mu \left(\not{k} + m_t\right) \gamma^\nu \left(\not{p}_2 + \not{k} + m_t\right) \left(\not{k} - \not{p}_1 + m_t\right)\right]}{\left(k^2 - m_t^2\right) \left((k+p_2)^2 - m_t^2\right) \left((k-p_1)^2 - m_t^2\right)} \,, \tag{1.73}$$

where y_t is the top quark Yukawa. Formally, we then take $m_t \gg m_H$. By looking at the numerator of the equation above, one can see that the trace is non zero provided that the fermion circulating in the propagators is massive. Indeed, by taking $m_t \to 0$ inside the trace, one is left with the trace of an odd number of gamma matrices which, as it is well known, vanishes. The mass inside the propagator provides the *helicity flip*, necessary for the Higgs, which is a scalar particle, to couple to back-to-back gluons. Also, note that this integral is superficially divergent in the UV region since at large values of the loop momentum it scales as d^4k/k^4. For this reason we need to regulate the integral: this can be done in many ways but for simplicity we choose

[6] An analogous diagram with the two gluons exchanged is implicitly assumed.

[7] Note that the top quark is not much heavier that the Higgs boson, so one could argue that this is not a justified expansion. It can be proven however that the relevant expansion is in $m_H^2/4m_t^2 \ll 1$

dimensional regularization [15], which means that we integrate in a generic number of spacetime dimensions $d = 4 - 2\epsilon$, and then take the limit $\epsilon \to 0$ at the end of the calculation. This is the first example of a non convergent integral that we encounter, but we will familiarise ourselves more with divergences in the rest of this section.

Consider now the denominator of the integral in Eq. (1.73). As mentioned above, we are only interested in the heavy top mass limit. However, we need to keep in mind that we are integrating from zero to infinity in the loop momentum, so the latter can be small but can also be large. In the case of small loop momentum, the denominators become constants and we are left with a scaleless integral that can be proven to vanish in dimensional regularization, as we will see later on[8]. We therefore only need to care about the large loop momentum region. In this region we have

$$\left(k^2 - m_t^2\right)\left((k+p_2)^2 - m_t^2\right)\left((k-p_1)^2 - m_t^2\right) \to \left(k^2 - m_t^2\right)^3 . \tag{1.74}$$

The trace will give rise to tensor structures proportional to $k^\mu p_i^\nu$, $k^\mu k^\nu$, $g^{\mu\nu}$,and $p_1^\nu p_2^\mu$. However, it is easy to see that the structure $k^\mu p_i^\nu$ leads to a vanishing integral, since we are integrating an odd function over an even domain. On the other hand, the integral is rotationally invariant, so we can write the structure $k^\mu k^\nu$ as $(k^2/d)\, g^{\mu\nu}$. Note that by doing this, we have effectively turned a tensor integral into a scalar one, which is easier to compute. It is a first example of a *projection* operation that we will see in detail in Chapter 2 and that allows one to turn tensor integrals into scalar ones, even for more complicated kinematics.

We can now write $k^2 = (k^2 - m_t^2) + m_t^2$ in the numerator, so that some terms will cancel against one power of the denominator, leaving us with the combination

$$I = I_2\, 4y_t\, g^{\mu\nu} m_t \left(\frac{4}{d} - 1\right) + I_3\, y_t \left[g^{\mu\nu} m_t \left(\frac{16}{d} m_t^2 - 4p_1 \cdot p_2\right) + 4p_1^\nu p_2^\mu m_t\right] , \tag{1.75}$$

[8] One may ask whether this still applies if we integrate over a restricted loop momentum region. In principle the answer is negative, but it is known that, as it is formalized in the method of *expansion by region* [16], in order to find the asymptotic behaviour of the integrals one should expand the integrand over relevant small/large loop momentum regions, and integrate each of them over the *whole* space. Although the details go outside the scope of this thesis, it turns out that the double counting terms that one get lead to scaleless integrals, which vanish in dimensional regularization.

where

$$I_n = \int \frac{d^d k}{(2\pi)^d} \frac{1}{(k^2 - m_t^2)^n} \propto \frac{\Gamma(n - d/2)}{\Gamma(n)} \left(m_t^2\right)^{d/2-n} , \tag{1.76}$$

are the so-called tadpole integrals. Note that I_2 has a pole in the dimensional regulator ϵ, while I_3 yields a finite result. However, upon substituting the expressions of the integrals in Eq. (1.75) we get the following finite result

$$I = 2\frac{y_t}{m_t^2} m_t \left(p_1 \cdot p_2 \, g^{\mu\nu} - p_1^\nu p_2^\mu\right) + \mathcal{O}(1/m_t^2) \, . \tag{1.77}$$

From the equation above it is clear that the top quark does not decouple in the Standard Model. Recall that the Yukawa is proportional to the mass, and $y_t/m_t^2 = 1/(v m_t)$, where v is the vacuum expectation value, and the m_t in the numerator of the above equation is the helicity flip discussed above.



Figure 1.4: Higgs production via gluon fusion in the Standard Model (left pane), and in the large top mass EFT (right pane)

Note that we could have obtained the same result of Eq. (1.77) by taking the Higgs to gluons interaction to be a point-like interaction with a tensor structure of the type described in the above equation. It is easy to see that such a Feynman rule arises from a theory described by the following gauge invariant Lagrangian

$$\mathcal{L} = -\frac{\lambda}{4} H \, G^a_{\mu\nu} G^{\mu\nu,a} \, , \tag{1.78}$$

where H and $G^a_{\mu\nu}$ are the Higgs field and the gluon field strength tensor already introduced in Sec. 1.1.2, and λ is an effective coupling given by

$$\lambda = -\frac{\alpha_s}{3\pi v} C(\alpha_s) Z_\lambda(\alpha_s) \, . \tag{1.79}$$

This is indeed a simple example of the construction of an *effective field theory* (EFT), where one sets the symmetries of the theory and writes down all the possible operators that are compatible with them. Such a theory will be valid up to a

certain cut-off, above or below which the effective description breaks down. The effective theory is matched to the "true" theory by means of an *a priori* unknown coefficient, called the *Wilson coefficient*. In our simple example, the large top mass EFT, one can compute the Wilson coefficient since it arises by matching the effective theory described by the lagrangian in Eq. (1.78) to the full SM. Such a coefficient is denoted as $C(\alpha_s)$ in Eq. (1.79)[9]. In the above equation, $Z_\lambda(\alpha_s)$ is the renormalization factor relative to the effective coupling λ. The perturbative expansions of $C(\alpha_s)$ and $Z_\lambda(\alpha_s)$ in the $\overline{\text{MS}}$ scheme are given by (see e.g. [17])

$$\begin{aligned} Z_\lambda(\alpha_s) &= 1 - \frac{\beta_0}{\epsilon}\left(\frac{\alpha_s(\mu)}{2\pi}\right) + \mathcal{O}(\alpha_s^2) \\ C(\alpha_s) &= 1 + \left[\frac{5}{2}C_A - \frac{3}{2}C_F\right]\left(\frac{\alpha_s(\mu)}{2\pi}\right) + \mathcal{O}(\alpha_s^2)\,. \end{aligned} \tag{1.80}$$

Note that in this case the Wilson coefficient is of $\mathcal{O}(1)$ instead of being suppressed by powers of the cut-off scale (the top mass in this example). This is a consequence of the fact that the top quark does not actually decouple in the SM, as already mentioned above.

We can now use the EFT tools described above to compute radiative corrections to Higgs production. Higher order corrections consist of *virtual contributions*, coming from loop diagrams, as well as *real contributions*, coming from leading order diagrams with the emission of extra radiation. We begin by considering the virtual corrections to the leading order process in the large top mass EFT framework. In this framework, the triangle diagram that we considered before reduces to a point-like interaction, as shown in the right pane of Fig. 1.4. There are four diagrams that contribute to this process at one-loop; we show them in Figure 1.5. The one loop amplitude is obtained upon summing the four different diagrams.

As in the case of the triangle diagram that we considered above, the one loop amplitude will be a Lorentz tensor depending on two indices. The most generic structure it can have, after integration over the loop momentum, that is compatible

[9] In general, for physics beyond the SM, in the absence of a known UV theory the Wilson coefficient has to be extracted from data.

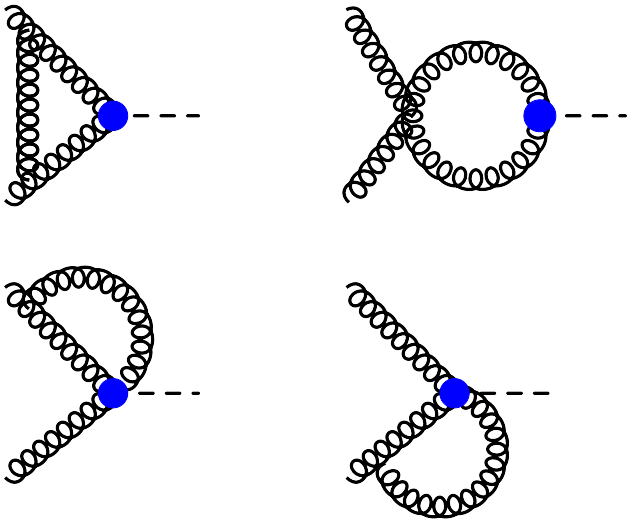


Figure 1.5: One-loop Feynman diagrams for Higgs production in gluon fusion in the large top mass EFT

with Lorentz and gauge symmetry is the following

$$\mathcal{M}^{(1),\mu\nu} = A\ (g^{\mu\nu}\, p_1 \cdot p_2 - p_1^\nu p_2^\mu) + B\, p_1^\mu p_2^\nu\,. \tag{1.81}$$

Because of the transversality of the external gluons' polarization vectors, i.e. $p_{1,2}^\mu \epsilon_\mu(p_{1,2}) = 0$, we can set $B = 0$. As a consequence, we only consider

$$\mathcal{M}^{(1),\mu\nu} = \mathcal{F}\ (g^{\mu\nu} p_1 \cdot p_2 - p_1^\nu p_2^\mu)\ , \tag{1.82}$$

where $\mathcal{F}$ is a scalar *form factor*. It is clear from the equation above that the one loop amplitude fully factorizes into the leading order tensor structure times a coefficient, the form factor, which is now a scalar object. The latter can only be a combination of two different scalar Feynman integrals, the triangle and the bubble integral, that we report in Fig. 1.6. Their expression reads

$$\begin{aligned} \text{Bub} &= \int \frac{d^dk}{(2\pi)^d} \frac{1}{k^2(k+p_1+p_2)^2}\,, \\ \text{Tri} &= \int \frac{d^dk}{(2\pi)^d} \frac{1}{k^2(k+p_2)^2(p_1-k)^2}\,. \end{aligned} \tag{1.83}$$

Let us look at these integrals more closely. We emphasize that the loop integrals need to be performed over the whole space. If we now take the limit $k \to \infty$ in both integrands we obtain

$$\text{Bub} \to \int \frac{|k|^{d-1} d|k| d\Omega}{(2\pi)^d} \frac{1}{|k|^4}\,, \qquad \text{Tri} \to \int \frac{|k|^{d-1} d|k| d\Omega}{(2\pi)^d} \frac{1}{|k|^6}\,, \tag{1.84}$$

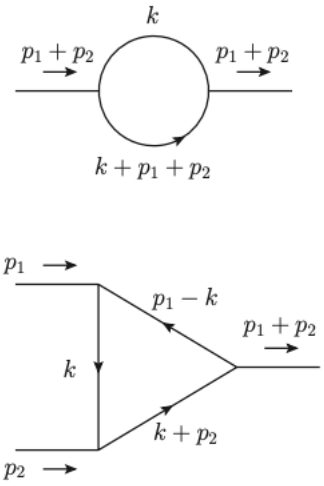


Figure 1.6: Bubble and triangle scalar integrals

where we employed the standard polar coordinates for the loop momentum after performing the standard Wick rotation (see below for a concrete example). It is clear from the above equation that the bubble integral is not convergent in the ultraviolet (UV) region in $d = 4$, as in this case the integrand scales as $1/|k|$, therefore leading to a logarithmic divergence. On the other hand, the triangle integral is perfectly convergent in $d = 4$ in the UV region, as it scales as $1/|k|^3$. We therefore say that the bubble is UV-*divergent*, and the triangle is UV-*finite*. Ultraviolet divergences in QFT are well understood, and cured via renormalization of the parameters entering the lagrangian of the theory. In the case of massless QCD ultraviolet divergences are removed by renormalization of the strong coupling α_s, which is usually performed in the $\overline{\text{MS}}$ scheme.

UV divergences, however, are not the only kind of divergences one finds in Feynman integrals. Indeed, let us now take the limit $|k| \to 0$ in the triangle and bubble integrands above. We get

$$\text{Bub} \to \int \frac{|k|^{d-1} d|k| d\Omega}{(2\pi)^d} \frac{1}{k^2}\,, \qquad \text{Tri} \to \int \frac{|k|^{d-1} d|k| d\Omega}{(2\pi)^d} \frac{1}{k^2\,(k \cdot p_2)\,(k \cdot p_1)}\,, \quad (1.85)$$

so it is clear that in four dimensions the triangle integral diverges in the limit $|k| \to 0$, which corresponds to the configuration where the particle with momentum k becomes *soft*. Although it is not as straightforward to see this just by looking

at the integrand in this parametrization, it turns out that the triangle integral also diverges in the *collinear limit*, corresponding to configurations where the loop momentum becomes collinear to either p_1 or p_2[10]. Note that the bubble integral, on the other hand, is fully convergent in the soft and collinear limits. Soft and collinear divergences go under the name of *infrared divergences* (IR). These will be the main topic of Chapter 3. As we will shortly see, infrared divergences cancel out when one combines loop contributions with real emission matrix elements. This is guaranteed by the Kinoshita–Lee–Nauenberg (KLN) theorem [18, 19], which states that the SM as a whole is infrared finite. However, one still needs a regularization procedure that allows to perform Feynman integrals (and phase space integrals as we will shortly see). We would like to adopt a regularization procedure that is gauge invariant and that makes calculations simple. We therefore choose dimensional regularization, that was already briefly introduced when dealing with the superficially divergent triangle integral of Eq. (1.73). As explained above, in this framework one performs the integrals in a generic number of spacetime dimensions $d = 4 - 2\epsilon$. At the end of the calculation, the limit $\epsilon \to 0$ yields the physical, four dimensional result. Note that this procedure regulates both UV and IR divergences for opposite signs of the dimensional regulator ϵ.

The use of dimensional regularization has a number of consequences. First, it makes scaleless integrals vanish. As an example, consider the integral $\int d^dk/k^4$, which is divergent both in the UV and in the IR. Let us introduce a parameter Λ to separate the two regions

$$\int \frac{d^dk}{(2\pi)^d}\frac{1}{k^4} \propto \int_0^\Lambda \frac{dk}{k^{4-d+1}} + \int_\Lambda^\infty \frac{dk}{k^{4-d+1}} \sim \frac{1}{\epsilon_{\rm UV}} - \frac{1}{\epsilon_{\rm IR}}\,, \tag{1.86}$$

where one has $\epsilon_{\rm UV} > 0$ and $\epsilon_{\rm IR} < 0$. However, after analytic continuation, the only possibility is $\epsilon_{\rm IR} = \epsilon_{\rm UV}$, hence the integral above vanishes.[11] Dimensional regularization has also the advantage of not introducing extra parameters such

[10] This can be seen for instance by employing the standard Sudakov parametrization for the loop momentum.

[11] Note that the fact that scaleless integrals vanish has the advantage of making the massless wavefunction renormalization trivial.

as masses[12], therefore not increasing the complexity of the integrals. Finally, dimensional regularization preserves the infinitesimal shift symmetry of Feynman integrals. This symmetry lies at the very heart of the so-called *integration by parts* (IBPs) procedure, that is needed when computing multiloop amplitudes in order to write a large number of linearly dependent Feynman integrals into a minimal set of independent *master integrals*. To see how this comes about, note that by using the infinitesimal shift symmetry of Feynman integrals, we can write

$$I(k) = \int \frac{d^d k}{(2\pi)^d} f(k + \alpha\, q) = I(k) + \alpha \int \frac{d^d k}{(2\pi)^d} \frac{\partial}{\partial k^\mu} \left(q^\mu f(k)\right) + \mathcal{O}(\alpha^2)\,, \tag{1.87}$$

where in the second step we Taylor-expanded the integrand. Note that q^μ is a generic external momentum. The equation above therefore implies

$$\int \frac{d^d k}{(2\pi)^d} \frac{\partial}{\partial k^\mu} \left[q^\mu f(k)\right] = 0\,. \tag{1.88}$$

It turns out, although we do not show it here, that the same identity is valid also if $q^\mu = k^\mu$. The equation above is the definition of an IBP identity. As a practical example, let us consider the scalar triangle in the second line of Eq. (1.83) and apply the IBP identity of Eq. (1.88) with the choice $q = k$. We get

$$\begin{aligned} 0 &= \int \frac{d^d k}{(2\pi)^d} \frac{\partial}{\partial k^\mu} \frac{k^\mu}{k^2 (k+p_2)^2 (p_1-k)^2} \\ &= \int \frac{d^d k}{(2\pi)^d} \Big[\frac{(d-4)}{k^2 (k+p_2)^2 (p_1-k)^2} - \frac{1}{\left((k+p_2)^2\right)^2 (p_1-k)^2} \\ &\quad - \frac{1}{\left((p_1-k)^2\right)^2 (k+p_2)^2} \Big]\,, \end{aligned} \tag{1.89}$$

which means that the triangle can actually be reduced to a sum of bubble integrals, with one denominator squared. A double propagator is usually called a *dotted* propagator. The dotted bubble can then further be reduced to the usual bubble integral by applying the IBP identities one more time. In passing, we note that the IBP procedure has then the feature of mixing the IR and the UV, since it reduces the triangle (only IR divergences) to a bubble (only UV divergences). Note that this case is particularly simple, but in general the IBP reduction procedure

[12] As for instance the Pauli-Villars regularization scheme would do.

produces rational functions as coefficients of the master integrals that, in the case of multiloop amplitudes, conspire to the swelling of intermediate expressions of the scattering amplitude.

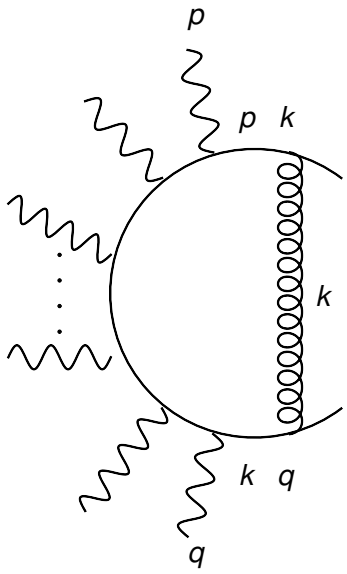
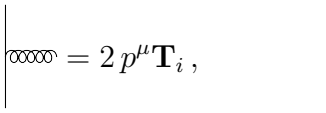


Figure 1.7: Generic one loop $n-$point amplitude. External lines are generic particles and the internal particle with momentum k is a gluon.

We have seen how the virtual contributions to the Higgs cross section lead to divergences that are made explicit by computing Feynman integrals. Since the UV divergences are taken care of upon renormalization, we will mainly be interested in infrared divergences. We have seen how in this example all the infrared divergences are contained in the triangle scalar integral. It can be shown that this is actually the case for any $n-$point one loop amplitude. We will sketch the argument below in the case of soft divergences. Consider the generic $n-$point one loop amplitude depicted in Fig. 1.7, where the internal particle with momentum k is a gluon. Let us now consider the situation where k becomes soft. The only three propagators that survive are k^2 and the two immediately adjacent to it, since the others reduce to constants in this limit. We are therefore left with a triangle topology, that can be projected into a scalar triangle integral as we have seen previously. On the other hand, in the soft limit, the Feynman rule for the vertex involving the hard external

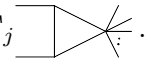
line and the soft gluon reduces to the *eikonal vertex* (see e.g. [6]) that reads



$$= 2\,p^{\mu}\mathbf{T}_i\,, \tag{1.90}$$

where p is the four-momentum of the hard particle i, and $\mathbf{T}_i$ is its associated color charge operator, as defined in Eq. (1.52). Since the soft gluon is then attached to another hard particle j, the Feynman rules give the factor $-(p_i \cdot p_j)\ \mathbf{T}_i\mathbf{T}_j$. The soft divergences associated with the one loop amplitude in Fig. 1.7 can therefore be schematically written as

$$\mathcal{M}^{(1)}_{\text{soft}} \sim \sum_{i\neq j} (p_i \cdot p_j)\ \mathbf{T}_i\mathbf{T}_j$$



. (1.91)

Similar considerations can be done for collinear configurations, that however turn out to be dependent on the square of single color charge operators rather than giving rise to color correlations amongst external particles. Infrared divergences of loop amplitudes are in fact universal and predicted, up to two loops, by the so-called Catani's formula [20] (see also [21]). While the explicit formula will be given later in Chapter 2 when describing multiloop scattering amplitudes and their divergences, here we want to emphasize that the structure of soft and collinear divergences turns out to be largely process independent. They only depend on the color and nature of the external partons.

Going back to our calculation, we report below the result for the one-loop amplitude interfered with the tree level one, since this is the combination that enters the virtual cross section. It reads

$$2\text{Re}\left(\mathcal{M}^{(1)}\mathcal{M}^{(0)\,*}\right) = \frac{\alpha_s(\mu^2)}{2\pi}\left[-\frac{2C_A}{\epsilon^2}+\frac{-2\beta_0}{\epsilon}+\left(5C_A-3C_F+\frac{7}{6}\pi^2 C_A\right)+\mathcal{O}(\epsilon)\right]|\mathcal{M}_0^{gg\to H}|^2\,, \tag{1.92}$$

where $|\mathcal{M}^{(0)}|^2$ is the leading order squared matrix element, averaged over initial state spin and color degrees of freedom, and summed over final state ones. Its explicit expression is given by

$$|\mathcal{M}_0^{gg\to H}|^2 = \frac{1}{(d-2)}\frac{1}{N_c^2-1}\alpha_s^2\frac{2m_H^4}{36\pi^2 v^2}\,., \tag{1.93}$$

and the leading order cross section is given by

$$\sigma_{\rm LO} = \frac{1}{2m_H^2}|\mathcal{M}_0^{gg\to H}|^2 2\pi\delta(1-z) \equiv \sigma_0\delta(1-z)\,, \tag{1.94}$$

with $z = m_H^2/s_{12}$ and s_{12} the partonic center of mass energy squared. Also, we have set $\mu^2 = m_H^2$ for simplicity. If we then integrate the tree level-one loop interference in Eq. (1.92) over the Higgs boson phase space we find the virtual contribution to the total cross section. If we write the virtual contribution as $\sigma^{\rm V} = (\alpha_s(\mu)/2\pi)\sigma_0\eta^{\rm V}$, with σ_0 defined in Eq. (1.94), we obtain

$$\begin{aligned}\eta^{\rm V} = \delta(1-z)\Bigg[&-\frac{2C_A}{\epsilon^2} - \frac{2\beta_0}{\epsilon} - 2\frac{C_A}{\epsilon}\log\left(\frac{\mu^2}{m_H^2}\right) \\ &+ 5C_A - 3C_F + \frac{7}{6}\pi^2 C_A - 2\beta_0\log\left(\frac{\mu^2}{m_H^2}\right) - C_A\log^2\left(\frac{\mu^2}{m_H^2}\right)\Bigg]\,.\end{aligned} \tag{1.95}$$

We now move to the discussion of the real emission contributions to the Higgs cross section. This means we need to compute the leading order cross section for the process[13]

$$g(p_1) + g(p_2) \to H(p_3) + g(p_4)\,. \tag{1.96}$$

Indeed, such contribution is also of order $\mathcal{O}(\alpha_s)$ and need to be added to the virtual corrections. Physically, this is justified by the fact that when a particle becomes soft and/or collinear, it cannot be resolved. The final state becomes indistinguishable from that of virtual contributions. Quantum Mechanics then tells us to sum such contributions. We proceed with the calculation of the scattering amplitude for the process in Eq. (1.96). There are four Feynman diagrams that contribute to the process in the EFT framework. Upon writing down the Feynman rules, summing up the diagrams and squaring to get the amplitude squared one obtains

$$|\mathcal{M}_0^{gg\to Hg}|^2 \sim C_A \frac{(m_H^8 + s_{12}^4 + s_{14}^4 + s_{24}^4)(1-2\epsilon) + (\epsilon/2)\left(m_H^4 + s_{12}^2 + s_{14}^2 + s_{24}^2\right)^2}{s_{12}\,s_{14}\,s_{24}}\,, \tag{1.97}$$

[13]We do not consider here the other partonic channels since they do not contain both real and virtual contributions at NLO

where $s_{ij} = 2(p_i \cdot p_j)$ and $m_H^2 = s_{12} + s_{14} + s_{24}$ by momentum conservation. We then need to integrate this matrix element squared over the phase space of the final state particles. We denote the phase space of a particle with momentum p as $[p] = d^3p/\left((2\pi)^3 2p_0\right)$. Let us start with the gluon's phase space and focus on the energy integral. The phase space scales as

$$[p_4] \propto \frac{dE_4\, E_4^2}{E_4} = dE_4\, E_4\,. \tag{1.98}$$

The matrix element squared in Eq. (1.97), on the other hand, completely factorises in the $E_4 \to 0$ soft limit as follows

$$|\mathcal{M}_0^{gg\to Hg}|^2 \sim g_s^2\, C_A \left(\frac{s_{12}}{s_{14}s_{24}}\right) s_{12}^2 \sim g_s^2\, C_A\, \mathrm{Eik}\,(p_1,p_2,p_4)\, |\mathcal{M}_0^{gg\to H}|^2\,, \tag{1.99}$$

where $\mathrm{Eik}\,(p_1,p_2,p_4) = 2s_{12}/(s_{14}s_{24})$ is the so-called *eikonal* factor, capturing the soft behaviour of the matrix element. The latter scales as E_4^{-2} so that the energy integral diverges logarithmically. We are facing another example of a soft divergence, although in the case of real emission matrix elements it only arises when integrating over the phase space of the extra radiation in the soft configuration.

A similar situation arises in the collinear $p_4||p_1$ and $p_4||p_2$ configurations. Let us consider the collinear limit $p_4||p_1$. The angular phase space of the emitted gluon scales as $[dp_4] \sim \theta_{14} d\theta_{14}$, where θ_{14} is the polar angle between p_1 and p_4. It is also clear by looking at Eq. (1.97) that the limit $\theta_{14} \to 0$ also leads to a logarithmic divergence since the matrix element squared scales as θ_{14}^{-2}. Note that the matrix element squared factorises in the collinear limit as well. Indeed, if we define $z = (E_1 - E_4)/E_1$, we obtain the following factorization formula

$$\lim_{\theta_{14}\to 0} |\mathcal{M}_0^{gg\to Hg}|^2 \sim \frac{g_s^2}{(p_1-p_4)^2} P_{gg}\left(\frac{1}{z}\right) |\tilde{\mathcal{M}}_0{}^{gg\to Hg}|^2\,, \tag{1.100}$$

where $|\tilde{\mathcal{M}}_0{}^{gg\to H}|^2$ is the Born-level matrix element squared for gluon induced Higgs production where the four momentum p_1 is shifted as $p_1 \to p_1 - p_4$. Moreover, the splitting function $P_{gg}(z)$ can be found in e.g. Ref. [22][14] and reads

$$P_{gg}(z) = 2C_A \left(\frac{z}{1-z} + \frac{1-z}{z} + z(1-z)\right)\,. \tag{1.101}$$

[14] In principle the gluon-gluon splitting produces spin correlations. However, in this process they are not present because of the scalar nature of the Higgs boson.

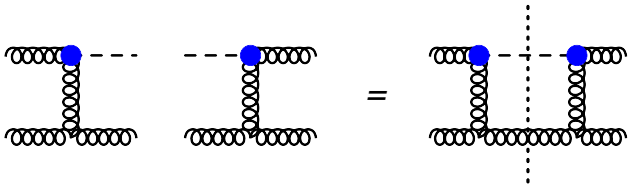


Figure 1.8

We will study the factorization properties of matrix elements in the infrared limits in detail in Chapter 3. Infrared divergences of real emission matrix elements can also be regulated via dimensional regularization, as we already did for loop amplitudes. The poles in the dimensional regulator ϵ will cancel against those arising from loop integrals to yield a finite result for physical observables.

If one is interested in so-called *inclusive* observables, such as the total cross section, then the matrix elements can be integrated over the full final-state particles' phase space, irrespectively of whether the final state particle is resolved or not. In our case, instead of computing the phase space integral directly, we use the method of *reverse unitarity* [23], which allows one to compute the phase space integral as a loop integral with cut propagators.

Let us see this more closely. We have

$$\int |\mathcal{M}_0^{gg\to Hg}|^2 d\Phi_2 \sim \int \frac{d^d p_4 \delta(p_4^2)\delta(p_3^2 - m_H^2)}{((p_1 - p_4)^2)^2((p_2 - p_4)^2)^2}[\dots]\,, \tag{1.102}$$

where $[\dots]$ denote the remaining parts of the amplitude squared, and by using the Cutkosky rules [24] one can write the delta functions in the numerator as a difference of two propagators as follows

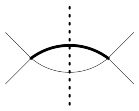
$$-2\pi i\delta(p^2 - m^2) = \frac{1}{p^2 - m^2 + i0} - \frac{1}{p^2 - m^2 - i0}\,. \tag{1.103}$$

By doing so, we have traded a tree level amplitude squared with a one loop amplitude, as depicted in Figure 1.8.

One can then compute the phase space integral by means of the standard techniques used in multiloop scattering amplitudes, which will be discussed at length in Chapter 2. The crucial part is that the IBP reduction procedure commutes with the application of the Cutkosky rules. The real emission cross section, after

IBP reduction, can be written in terms of one single integral, the two body phase space integral, which is given by the following expression

$$\Phi_2 = \quad = r_\Gamma (4\pi)^\epsilon \frac{\sin(\pi\epsilon)}{8\pi^2(1-2\epsilon)\epsilon} \left(\frac{\mu^2}{m_H^2}\right)^\epsilon (1-z)^{1-2\epsilon} z^\epsilon \,, \tag{1.104}$$



where we recall that $z = m_H^2/s_{12}$ and define $r_\Gamma = \Gamma^2(1-\epsilon)\Gamma(1+\epsilon)/\Gamma(1-2\epsilon)$. Upon combining the real and virtual contributions to the cross section one gets

$$\eta^{\rm V} + \eta^{\rm R} = \frac{1}{\epsilon}\frac{\alpha_s(\mu)}{2\pi}\left(-2\beta_0\delta(1-z) - 4C_A\frac{(1-z+z^2)^2}{(1-z)_+}\right) + \mathcal{O}(\epsilon^0)\,, \tag{1.105}$$

where $\eta^{\rm R}$ denotes the NLO correction to the total cross section normalised by the leading order cross section. We also have that $1/(1-z)_+ \equiv \mathcal{D}_0(z)$ is a *plus distribution*, defined by its action on a test function as follows

$$\int_0^1 \mathcal{D}_n(z)\, g(z) = \int_0^1 \frac{\log^n(1-z)}{1-z}\left(g(z) - g(1)\right)\,. \tag{1.106}$$

As one can see from Eq. (1.105), there is still a leftover single pole in the dimensional regulator.

The latter can be absorbed into the definition of the parton distribution functions. The procedure is similar to standard ultraviolet renormalization in QFT, and amounts, in the $\overline{\rm MS}$ scheme, to the following replacement

$$f_i^{\rm bare} \to \left[\delta_{ij} + \frac{\alpha_s(\mu)}{2\pi\epsilon}\hat{P}_{ij}^{(0)} + \mathcal{O}(\alpha_s)^2\right] \otimes f_j(\mu)\,, \tag{1.107}$$

where i, j are flavour indices and $\hat{P}_{ij}^{(0)}$ are the Altarelli-Parisi splitting functions [25]. In our case, $i = j = g$, and

$$\hat{P}_{gg}^{(0)}(z) = 2N_c\left(\mathcal{D}_0(z) + \frac{1}{z} + z(1-z) - 2\right) + \beta_0\delta(1-z)\,. \tag{1.108}$$

We can implement the renormalization of parton distribution functions as an additive counterterm in our partonic cross section, that can be obtained by convoluting the Altarelli-Parisi splitting kernel with the leading order cross section. Its expression, normalized to the leading order cross section, reads

$$\eta^{\rm PDFs} = \frac{2}{\epsilon} z\hat{P}_{gg}^{(0)}(z)\,. \tag{1.109}$$

Putting all the contributions together we obtain the finite prediction for the NLO Higgs production cross section in gluon fusion. It reads

$$\begin{aligned}\eta^{(1)} \equiv \eta^{\mathrm{V}} + \eta^{\mathrm{R}} + \eta^{\mathrm{PDFs}} &= \left(\frac{3}{2N_c} + \frac{1}{6}N_c\left(21 + 4\pi^2\right)\right)\delta(1-z) \\ &+ N_c\Bigg(-\frac{11}{3}(1-z)^3 + 8\mathcal{D}_1(z) - 8z(2-z+z^2)\log(1-z) \\ &- 4\frac{(1-z+z^2)^2}{1-z}\log(z) + \log\left(\frac{\mu^2}{m_H^2}\right)\left(-4\mathcal{D}_0(z) + 4z(2-z+z^2)\right)\Bigg).\end{aligned} \tag{1.110}$$

Let us recap what we have accomplished so far: we have computed the NLO inclusive cross section for Higgs production in gluon fusion. We saw how we needed to combine virtual and real emission contributions (as well as PDF renormalization) in order to get rid of unphysical infrared divergences arising from loop integration and phase space integration of soft and collinear configurations of unresolved particles. Note that the cancellation of divergences that one has when combining real and virtual contributions is guaranteed by the KLN theorem, as we already mentioned at the beginning of the section. However, for phenomenological applications, more *differential* observables are also crucial. In practice, this implies that we would like to extract and cancel divergences, without actually integrating over the resolved phase space of final state particles. This can be achieved with different methods, usually classified into two categories: *slicing* and *subtraction*. In Chapter 3 we will focus on a particular subtraction scheme to tackle this problem at NNLO. This, together with the computation of scattering amplitudes, will allow us to give a complete description of the hard process in the context of perturbation theory.

Rust in the mountains
Rust in the brain
The air is sacred here
In spite of your claim

— Radiohead *The Trickster*

2 Scattering amplitudes

Contents

2.1 Introduction 44
2.2 Full colour five-point two-loop amplitudes in massless QCD 48
2.2.1 Kinematics of five particles scattering 50
2.2.2 Colour and helicity decomposition 51
2.2.3 Reduction to master integrals 56
2.2.4 UV renormalization and IR subtraction 60
2.2.5 Final checks and results 62

2.1 Introduction

In this section we will present a brief overview of scattering amplitudes. As we have already seen in Chapter 1, they stand at the very core of the hard process description. They are not only fundamental objects in particle phenomenology, as they allows one to link experiments with theoretical predictions, but also very interesting objects in the broader and more formal context of QFT. The aim of this chapter is twofold: we want to briefly present the techniques that are currently used to compute multiloop amplitudes that are relevant for collider phenomenology, as well as present the calculation of the five-points two loops scattering amplitudes

in massless QCD. The latter is based on the publication Ref. [26].

Before delving into the details, let us give a brief introduction on scattering amplitudes as fundamental objects in QFT. We stress that the following introduction does not aim to be self-contained and complete. We refer the reader to the rich literature for further details (see e.g. [6]). In the Schroedinger picture of quantum mechanics, we can consider a quantum state $|i\rangle$ at time T_i, evolving into another quantum state $|f\rangle$ at time T_f. The amplitude for such time evolution is schematically given by

$$\langle f| e^{-iH(T_f-T_i)} |i\rangle \ . \tag{2.1}$$

The scattering $S-$matrix is defined as the time evolution operator reported above, in the limit $T_f - T_i \to \infty$ and where H is the second-quantized hamiltonian of the theory. The $S-$matrix has the important property of being unitary, i.e. $SS^\dagger = 1$. Such property expresses the conservation of probability. In our definition of scattering amplitude, we want to separate the identity operator in order to only deal with the interaction part as follows

$$S = I + i\,\mathcal{M}\,. \tag{2.2}$$

When we refer to scattering amplitudes from here on, we will refer to $\mathcal{M}$ defined as in the above equation.

We now want to understand how to compute scattering amplitudes in QFT. It is well known that the scattering amplitude can be related to the vacuum expectation value of a time-ordered product of fields via the famous Lehmann-Symanzik-Zimmermann (LSZ) reduction formula (see e.g. [6]). In order to highlight the meaning of the formula without running into unnecessary complications, we write it for the case of free real scalar fields. Assume we have m particles in the initial state labeled by momenta $k_1 \dots k_n$ evolving into n particles in the final state labeled by $p_1 \dots p_m$. The LSZ reduction formula reads

$$\begin{aligned}
&\prod_{i=1}^{m} \int d^4x_i e^{-ik_i x_i} \prod_{j=1}^{n} \int d^4y_j e^{ip_j y_j} \langle 0| T\{\phi(x_i) \dots \phi(x_m)\phi(y_1) \dots \phi(y_m)\} |0\rangle \\
&= \left(\prod_{i=1}^{m} \frac{i\sqrt{Z}}{k_i^2 - m^2}\right) \left(\prod_{j=1}^{n} \frac{i\sqrt{Z}}{p_j^2 - m^2}\right) \langle p_1 \dots p_n| \, i\mathcal{M} \, |k_1 \dots k_m\rangle \ ,
\end{aligned} \tag{2.3}$$

where Z is the wave-function renormalization factor, and T denotes the time-ordered product operator. Computing the time-ordered products of fields in a generic interacting theory can become extremely difficult. Whenever applicable, the perturbative approach is by far the most successful approach to compute scattering amplitudes, and it has a very intuitive diagrammatic expansion in terms of Feynman diagrams. The perturbative approach, however, holds meaningful results only in the presence of a small parameter. In the case of quantum electrodynamics, this is never a problem, since the electromagnetic coupling remains small for the relevant energy scales covered by experiments. The case of QCD is more complicated, since as we have already seen in Chapter 1 QCD is an asymptotically free theory. Another complication that arises in QCD is relative to asymptotic states. Indeed, the $S-$matrix formalism requires to take the limit $T_f - T_i \to \infty$ which makes sense if the quantum mechanical states are still defined at infinite times. In the case of QCD, however, the degrees of freedom used to perform calculations for hard scatterings are quarks and gluons, but they do not coincide with the asymptotic states at large times, which have to be color singlets due to confinement. Nevertheless, factorization still allows us to compute the hard process by means of a perturbative approach, as we discussed in Chapter 1. We write the perturbative expansion of the amplitude as follows

$$\mathcal{M} = \sum_n \left(\frac{\alpha}{4\pi}\right)^n \mathcal{M}^{(n)}\,, \tag{2.4}$$

where $\alpha = g^2/(4\pi)$ denotes the bare coupling relative to the theory at hand. In Chapter 1 we have already computed both tree level and one loop amplitudes in the context of the inclusive Higgs cross section calculation at NLO. Tree level and loop amplitudes, as already mentioned, are generally computed as sums of Feynman diagrams. It is important to highlight, however, some limitations of the Feynman diagrams approach. First of all, individual diagrams are not gauge invariant and therefore not physical. In general, there are large cancellations happening when summing together all the diagrams, hiding the structures and simplicity of the amplitude. Furthermore, the number of Feynman diagrams

contributing to the amplitude grows beyond factorial level as the number of loops and external legs increase.

At tree level and one loop, different methods are available that make the structures amplitude more explicit. For example in the case of tree level amplitudes the so-called Britto-Cachazo-Feng-Witten (BCFW) recursion [27] allows to compute higher point amplitudes in terms of lower point ones. It does so by exploiting unitarity and factorisation property of the amplitudes when momenta go on-shell. Details on BCFW recursion can be found in e.g. Ref. [28]. At one loop level, unitarity provides a powerful method to compute scattering amplitude without going through the redundant description of Feynman diagrams. The original idea dates back to the work of Cutkosky [29] and the analytic $S-$matrix [30]. The main idea is that one can obtain the full one-loop amplitude by the knowledge of its *discontinuities*. Indeed, Feynman integrals lead to the presence of transcendental functions such as logarithms and polylogarithms. These functions display branch cuts in the complex plane associated to the kinematic invariants that the amplitude depends on. The discontinuity of an amplitude, that we denote Disc, is then given by the difference between the value of the amplitude that one obtains when crossing a branch cut. At one loop, once we identify the discontinuities of the transcendental functions, we can recover the full analytic structure of the amplitude by means of the following relation

$$\mathcal{M}^{(1)}(s_1, \dots s_n) = \sum_i \int \frac{ds_i'}{s_i' - s_i} \text{Disc}_{s_i} \mathcal{M}^{(1)} \,, \tag{2.5}$$

where s_i are a set of invariants. The modern implementation of unitarity is due to the work by Bern, Dixon, Dunbar, Kosower (BDK) [31], as well as Ref. [32] and many others (see Ref. [33] for a thorough introduction on unitarity methods). In these approaches, the authors use both the cut knowledge and factorisation properties in infrared limits to constrain the amplitude. Many efforts have been and are currently being made to extend the idea of unitarity beyond one-loop level, see e.g. [34] and references therein. However, the method is not fully mature yet, so that in the following we will restrict ourselves to more standard techniques for multiloop

amplitude calculations. In particular, we will present a calculation of five-point two-loop scattering amplitudes in massless QCD based on a traditional Feynman diagram approach. Although we will focus on one specific example, it will be enough to show all the state-of-the-art technology which is nowadays used in multiloop calculations.

2.2 Full colour five-point two-loop amplitudes in massless QCD

In this section, we present the calculation of two-loop five-point scattering amplitudes in massless QCD. As one may have noticed, the denomination "full colour" also appear in the title of the section. Let us now explain what it means, although a more detailed explanation will be given later in the chapter.

In Chapter 1, when reviewing the strong sector of the SM, we mentioned how in many cases it is convenient to keep the dimensionality of the gauge group associated with colour generic, i.e. work in $SU(N_c)$ rather than $SU(3)$. The reason for this is that in many cases the structure of QCD is largely simplified in the *large* N_c limit (see e.g. [35]), the latter being a parametric expansion in $1/N_c$ at fixed $g_s^2 N_c$. Although we refrain from giving a full description of the large N_c limit, we only mention here that the computation of multiloop scattering amplitude is largely simplified in this limit, since in QCD the so-called *leading color* diagrams have a simpler topology, as they turn out to be *planar*. Let us briefly explain what the words "topology" and "planar" (and therefore also "non-planar") mean in the context of Feynman integrals, as they will play a crucial role in what follows. In a Feynman diagram, the topology refers to the arrangement of the lines and vertices. A planar topology is one where all the lines and vertices can be drawn on a single plane without any lines crossing over each other. Non-planar topologies, on the other hand, involve lines crossing over each other and therefore cannot be drawn on a single plane. In general, the leading-color approximation already gives precious information on the structure of QCD amplitudes, and it turns out to be sufficient in most phenomenological applications. However, if one wants to get an insight on the non-planar structure of QCD, it becomes necessary to go beyond the large-N_c

limit, performing a "full colour" calculation. This is what we do here in the case of five-point two-loop amplitudes in massless QCD.

Before delving into the details of the calculation, let us briefly highlight the relevance of such amplitudes. The calculation of scattering amplitudes for n partons in perturbative QCD has attracted much attention since the discovery of the ubiquitous role of Yang-Mills theories in the description of particle interactions. These amplitudes constitute the building blocks for the calculation of cross sections for processes involving jets at hadron colliders, which have played a crucial role in providing direct experimental access to fundamental parameters of QCD such as the number of colours and the strong coupling constant. At the LHC, the measurement of multi-jet cross sections at large transverse momenta constitutes a unique opportunity to explore QCD dynamics in extreme regimes [36–39]. Such high-precision analyses need to be matched by accurate theoretical predictions which as of today have been carried out to an impressive second order in perturbative QCD [40–44]. In addition, analytic calculations of n-parton scattering amplitudes provide important insights into the fundamental properties of Yang-Mills theories, such as their high-energy (Regge) limit (see *e.g.* [45]) or the universal structure of infrared divergences and factorization in soft and collinear limits (see *e.g.* [46]). Very interestingly, in both of these cases new interesting structures appear beyond one loop in the non-planar sector, thus also motivating the calculation presented here.

We consider the following all-outgoing processes

$$0 \to gggg\,, \quad 0 \to q\bar{q}gg\,, \quad 0 \to q\bar{q}q'\bar{q}'g\,, \tag{2.6}$$

where q' denotes a different quark flavour. From these, results for all relevant partonic channels relevant for the production of three jets (including contributions from identical quark flavours) can be obtained. For simplicity, we will illustrate the details of the calculation for the process $0 \to q\bar{q}q'\bar{q}'g$, although the framework remains the same for all partonic channels. The calculation of scattering amplitudes via Feynman diagrams becomes quite complex at higher loops, due to the large number of diagrams involved and a swelling in the size of intermediate expressions.

It is mandatory to decompose the amplitude into simpler building blocks that make it possible to keep the complexity under control. To this end, we will decompose the amplitude in colour space and we will work with the coefficients of the colour basis, the so-called *partial amplitudes*. These objects have the good property of being gauge invariant, thus limiting redundancies and preventing cancellations among diagrams. We will then be interested in the calculation of *helicity amplitudes*, which means that we will fix the helicity of the external partons. By doing so, we will be left with tensor structures that can be projected into scalar form factors with a procedure that will be illustrated later on. At that point, the helicity amplitude will be a linear combination of rational functions multiplying a large number of scalar Feynman integrals. As we have already anticipated in Chapter 1, such integrals are not linearly independent, and can be reduced to an independent set of master integrals through IBP reduction, which in the case of five particles' scattering take the name of *Pentagon Functions* (see e.g. [47]). We will explain in some details all these steps in the following sections. To set the stage, let us begin with a preliminary discussion on the kinematics of five particles scattering.

2.2.1 Kinematics of five particles scattering

For the sake of definiteness, we consider the process

$$0 \to \bar{q}(p_1) + q(p_2) + \bar{q}'(p_3) + q'(p_4) + g(p_5)\,, \tag{2.7}$$

although the same arguments can be applied to the all-gluon process and the two-quark three-gluon process. The five external momenta are all outgoing and massless

$$p_1^\mu + p_2^\mu + p_3^\mu + p_4^\mu + p_5^\mu = 0\,, \quad p_i^2 = 0\,. \tag{2.8}$$

The five-point kinematics can be parametrized by means of five independent invariants, as a result of momentum conservation and Poincaré symmetry. We choose the cyclic set $s_{12}, s_{23}, s_{34}, s_{45}, s_{51}$, with $s_{ij} = (p_i + p_j)^2$. Note that in a four point scattering, the number of independent invariants is 2. The rapidly growing number of scales as the number of external particles increases is one of the main obstacles in the calculation of higher-multiplicity scattering amplitudes.

The physical scattering process will correspond to the configuration $12 \to 345$. We therefore define the *physical region* of the scattering as follows

$$s_{12}, s_{34}, s_{45} > 0 \quad s_{23}, s_{51} < 0\,, \tag{2.9}$$

together with the conditions

$$s_{12} \geq s_{34}\,, \quad s_{12} - s_{34} \geq s_{45}\,, \quad 0 \geq s_{23} \geq s_{45} - s_{12}\,, \quad s_{51}^{-} \leq s_{51} \leq s_{51}^{+}\,, \tag{2.10}$$

where

$$\begin{aligned} s_{51}^{\pm} = \frac{1}{(s_{12}-s_{45})^2}\Big[s_{12}^2 s_{23} + s_{34}s_{45}(s_{45}-s_{23}) - s_{12}\left(s_{34}s_{45} + s_{23}s_{34} + s_{23}s_{45}\right)\Big] \\ \pm \sqrt{s_{12}s_{23}s_{34}s_{45}\left(s_{12}+s_{23}-s_{45}\right)\left(s_{34}+s_{45}-s_{12}\right)}\,. \end{aligned} \tag{2.11}$$

In order to fully describe the helicity amplitudes for these processes, we also need to introduce the following parity-odd invariant

$$\mathrm{tr}_5 = 4i\epsilon_{\mu\nu\rho\sigma}p_1^\mu p_2^\nu p_3^\rho p_4^\sigma\,, \tag{2.12}$$

where $\epsilon_{\mu\nu\rho\sigma}$ is the fully antisymmetric Levi-Civita tensor. Note that $\mathrm{tr}_5^2 = \Delta$, with

$$\begin{aligned} \Delta = &-4s_{12}s_{23}s_{34}\left(s_{23}-s_{45}-s_{51}\right) \\ &+\left(s_{12}s_{23}+s_{23}s_{34}-s_{34}s_{45}+s_{45}s_{51}-s_{51}s_{12}\right)^2 \end{aligned} \tag{2.13}$$

the so-called *Gram determinant*, i.e. the determinant of the Gram matrix $G_{ij} = 2p_ip_j$. Note that, in the physical region, $\Delta < 0$.

2.2.2 Colour and helicity decomposition

We now proceed with the colour and helicity decomposition of the scattering amplitude for the process in Eq. (2.7). We start by decomposing the amplitude in colour space as follows

$$\mathcal{M} = (4\pi\alpha_{s,b})^{\frac{3}{2}}\mathcal{M}_c\,\mathcal{C}_c\,, \tag{2.14}$$

where $\alpha_{s,b}$ is the bare strong coupling, $\mathcal{M}_c$ are the partial amplitudes, and $\mathcal{C}_c$ are the element of the colour basis. For the process under consideration they are given by

$$\begin{aligned} \mathcal{C}_1 = \delta_{i_2i_3}T^{a_5}_{i_4i_1}\,, \quad \mathcal{C}_2 = \delta_{i_1i_2}T^{a_5}_{i_4i_3}\,, \\ \mathcal{C}_3 = \delta_{i_3i_4}T^{a_5}_{i_2i_1}\,, \quad \mathcal{C}_4 = \delta_{i_1i_4}T^{a_5}_{i_2i_3}\,. \end{aligned} \tag{2.15}$$

where the $SU(N_c)$ adjoint index a_5 is associated with the external gluon, while the (anti-)fundamental index i_n with the corresponding (anti-)quark state. The matrices T^a_{ij} are generators of $SU(N_c)$ in the fundamental representation that were already introduced in Section 1.1.2. Note that for this particular process the dimension of the color basis remain unchanged beyond tree level. However, this is not the case for the other two processes in Eq. (2.6). There, the dimensionality of the colour basis increases when moving to one-loop amplitudes. More details regarding the all-gluonic and the two-quark three-gluon processes can be found in Refs. [26, 48, 49].

Note that at two loops there are a total of 28020, 9136, and 2129 diagrams for the three channels in Eq. (2.6) respectively. We generate them using `QGRAF` [50]. However, not all of them contribute to the independent color structures described above. The relevant diagrams can be selected by repeated application of the color identities

$$\begin{aligned} \mathrm{Tr}\, T^a = 0, \quad T^a_{ij} T^a_{kh} &= \frac{1}{2}\left(\delta_{ih}\delta_{kj} - \frac{1}{N_c}\delta_{ij}\delta_{kh}\right), \\ f^{abc} &= -2i\mathrm{Tr}(T^a[T^b, T^c]), \end{aligned} \tag{2.16}$$

which reduce their color structure to a linear combination of the basis elements. From here, one can easily read off the contribution of the corresponding diagram to each element of the vectors. The partial amplitudes are polynomials in the variables N_c and n_f. At two loops they can be written as follows

$$\mathcal{M}_c = b_c^{(2,0)} N_c^2 + b_c^{(1,0)} N_c + b_c^{(0,0)} + b_c^{(-1,0)} N_c^{-1} + b_c^{(-2,0)} N_c^{-2} + b_c^{(1,1)} N_c^2 \frac{n_f}{N_c} + \dots . \tag{2.17}$$

The coefficients of the highest powers of Nc are the leading color part of the amplitude. The remaining terms are said to be sub-leading color, since they are suppressed by appropriate powers of N_c and n_f/N_c. As we already mentioned at the beginning of this section, the leading color part of the amplitude is not only dominant but also easier to compute. In this thesis, however, we will present the full colour calculation of the amplitude, which means that we will retain both leading and subleading structures.

We now proceed with the helicity decomposition of the amplitude. As we already argued, we are interested in computing the amplitudes for fixed helicity configurations of the external particles. To do so, it is convenient to work in the spinor-helicity formalism[1]. We choose the polarization vectors for gluons as follows

$$\epsilon^{\mu}_{i,-} = \frac{[i+1|\gamma^{\mu}|i\rangle}{\sqrt{2}[i|i+1]}, \qquad \epsilon^{\mu}_{i,+} = \frac{[i|\gamma^{\mu}|i+1\rangle}{\sqrt{2}\langle i+1|i\rangle}\,, \tag{2.18}$$

where $i = 1, \dots 5$ and $|5+1\rangle \equiv |1\rangle$, $|5+1] \equiv |1]$. The spinors for (anti-)quarks are defined as

$$\overline{u}_{i,+} = \langle i|, \quad \overline{u}_{i,-} = [i|, \quad u_{i,-} = |i\rangle, \quad u_{i,+} = |i]\,. \tag{2.19}$$

Helicities are given in the all-outgoing convention. We define spinor-stripped helicity amplitudes $\mathcal{H}_c(\boldsymbol{\lambda})$ as

$$\mathcal{M}_c(\boldsymbol{\lambda}) = \sqrt{2}\,\Phi_c(\boldsymbol{\lambda})\,\mathcal{H}_c(\boldsymbol{\lambda})\,, \tag{2.20}$$

where $\Phi_c(\boldsymbol{\lambda})$ is a colour and helicity dependent spinor factor that fully accounts for the spinor weight of the corresponding amplitude. We choose the spinor factors Φ_c in such a way that the tree level spinor-stripped helicity amplitude is equal to unity. The specific choice for each independent colour vector is reported in Table 2.1. The scalar quantities $\mathcal{H}_c(\boldsymbol{\lambda})$ can be further split into their parity even and odd parts

$$\mathcal{H}_c(\boldsymbol{\lambda}) = \mathcal{H}^E_c(\boldsymbol{\lambda}) + \mathrm{tr}_5\,\mathcal{H}^O_c(\boldsymbol{\lambda}) \tag{2.21}$$

that are individually gauge invariant and can be computed independently. For the process under consideration, there are four different colour vectors and eight different helicity configurations. However, we can compute a minimal set of helicities and colour structures, and obtain all the remaining ones by means of crossings of the external states. More specifically, we can consider the first two elements of the colour basis in Eq. (2.15), and obtain the remaining two by sending $1 \to 3, 2 \to 4$. In a similar manner, we can select only four out of eight helicity configurations, such that the remaining four can be obtained via parity transformation.

[1]Details on the spinor-helicity formalism can be found in Appendix C

$\bar{q}q\bar{q}'q'g$	$\Phi(\boldsymbol{\lambda})$	$\mathcal{M}_c$	$\Phi(\boldsymbol{\lambda})$	$\mathcal{M}_c$
$-+-+-$	$\frac{[14][42]^2}{[12][43][51][54]}$	1	$\frac{[42]^2}{[12][53][54]}$	2
$-+-++$	$\frac{\langle 41\rangle\langle 13\rangle^2}{\langle 15\rangle\langle 21\rangle\langle 34\rangle\langle 45\rangle}$	1	$\frac{\langle 13\rangle^2}{\langle 21\rangle\langle 35\rangle\langle 45\rangle}$	2
$-++--$	$\frac{[32]^2[41]}{[12][43][51][54]}$	1	$\frac{[32]^2}{[21][53][54]}$	2
$-++-+$	$\frac{\langle 14\rangle^3}{\langle 15\rangle\langle 21\rangle\langle 34\rangle\langle 45\rangle}$	1	$\frac{\langle 14\rangle^2}{\langle 12\rangle\langle 35\rangle\langle 45\rangle}$	2

Table 2.1: Definition of the minimal set of helicity and color configurations for the process of Eq. (2.7). The list of helicity configuration is given in the left-most column of each table. The middle columns contain our definition of the spinor factors $\Phi_c(\boldsymbol{\lambda})$ for the different color factors. The right columns give the list of partial amplitudes we computed analytically for the corresponding helicity configuration. Spinor factors are chosen to set the corresponding tree-level to 1.

Each partial amplitude can be further decomposed into a linear combination of tensor structures as follows

$$\mathcal{M}_c(\boldsymbol{\lambda}) = \sum_{i=1}^{N} \mathcal{F}_{i,c}\, T_i(\boldsymbol{\lambda})\,, \tag{2.22}$$

where the T_i are a set of tensor structures containing all polarization vectors, and the $F_{i,c}$ are scalar form factors for the different color structures. The form factors have a perturbative expansion and, at a given perturbative order, are linear combinations of scalar Feynman integrals. As we have already seen in Chapter 1, Feynman integrals are generally divergent both in the UV and in the IR. We therefore work in dimensional regularization, setting $d = 4 - 2\epsilon$. However, in this case, since we are interested in helicity amplitudes, we employ the so-called *'t Hooft-Veltman scheme*, which means that we treat all external particles in $d = 4$ dimensions, whereas all the internal ones are in generic d dimensions.

Let us now briefly discuss the tensor structure decomposition of the amplitude, i.e. the choice of $T_i(\boldsymbol{\lambda})$ in Eq. (2.22). In general, one should write down all the possible independent Lorentz structures compatible with the amplitude, starting from the metric, the fully antisymmetric Levi-Civita tensor, the external momenta, the gluon

polarization vectors and the external spinors.[2] The number of these independent structures in d dimensions is in general very large and therefore complicated to handle. In the case of the four-quark one-gluon amplitude at hand, however, the situation is even worse. More specifically, the number of tensors increases with the number of loops, since every vertex contributes a Dirac gamma function to the tensor structure. In 4 dimensions, one can repeatedly use the Fierz identity to reduce contracted strings of γ-matrices to obtain simpler strings. However, since the Dirac algebra does not close in d dimensions, these manipulations are not allowed in a generic number of dimensions and one is left with a growing number of tensors. Most of these structures, however, turn out to not contribute to the final $4-$dimensional helicity amplitudes, the latter being the actual objects we want to compute.

A solution to this problem was given in Refs. [51, 52], where the authors prove that only a subset of all the possible Lorentz structures spans the whole space of purely four-dimensional tensors, therefore making it possible to project out the unphysical -2ϵ dimensional part through a simple Gram-Schmidt orthogonalization procedure. It turns out that indeed that the number of independent Lorentz structures is the same as the number of independent helicity configurations, that in the case of the process in Eq. (2.7) is equal to eight.

In practice this means that after numbering the helicity configurations $\boldsymbol{\lambda}_1, \boldsymbol{\lambda}_2, \ldots$ for our process, we can change to a new basis of tensors $\overline{T}_{i,c}(\boldsymbol{\lambda})$, which satisfy

$$\overline{T}_{i,c}(\boldsymbol{\lambda} = \boldsymbol{\lambda}_j) = \delta_{ij}\Phi_c(\boldsymbol{\lambda}_j)\,. \tag{2.23}$$

This allows us to define the helicity projectors $P_{\boldsymbol{\lambda},c}$ by requiring

$$P_{\boldsymbol{\lambda},c} \circ \overline{T}_{i,c}(\boldsymbol{\lambda}') = \delta_{\boldsymbol{\lambda},\boldsymbol{\lambda}'}\,. \tag{2.24}$$

We can therefore compute the projectors and apply them to our partial amplitudes in order to obtain the helicity amplitudes. We perform these steps using `FORM` [53, 54]. At this point, the spinor-stripped helicity amplitudes $\mathcal{H}(\boldsymbol{\lambda})$ in (2.20) are expressed as linear combination of scalar Feynman integrals.

[2] In the case at hand, the number of external momenta is large enough to span the whole $4-$dimensional space, so that one does not need neither the Levi-Civita tensor nor the metric tensor.

2.2.3 Reduction to master integrals

We are now at a stage where the helicity amplitudes are written as a sum of scalar Feynman integrals. It is convenient to express the latter in the following form

$$\mathcal{I}^{\text{fam}}_{n_1,\ldots,n_N} = \mu_0^{2L\epsilon} e^{L\epsilon\gamma_E} \int \prod_{i=1}^{L} \left(\frac{\mathrm{d}^d k_i}{i\pi^{\frac{d}{2}}} \right) \frac{1}{D_1^{n_1} \ldots D_N^{n_N}} \,, \tag{2.25}$$

where the loop momenta are labeled by k_i, and L denotes the number of loops. Note that the measure is not the standard measure for Feynman integrals that we have encountered so far, i.e. $d^d k/(2\pi)^{d3}$, but it is modified in a way that is particularly convenient for the $\overline{\text{MS}}$ renormalization. The label "fam" represents a particular integral family, that in our language corresponds to a topology as we have defined it at the beginning of the main section. In our case there are two integral families that we denote with $\{A, B\}$. Every integral family specifies the list of inverse propagators $D_e = q_e^2 + i\varepsilon$ in Eq. (2.25), where ε implements the Feynman prescription. The propagators for the different integral families (see *e.g.* refs. [55–57]) are given by

[3] In particular, Eq. (2.25) implicitly assumes factoring out a factor of $i(4\pi)^{\epsilon} e^{-\epsilon\gamma_E}/(4\pi)^2$ per loop.

Prop. den.	Family A	Family B
D_1	k_1^2	k_1^2
D_2	$(k_1+p_1)^2$	$(k_1-p_1)^2$
D_3	$(k_1+p_1+p_2)^2$	$(k_1-p_1-p_2)^2$
D_4	$(k_1+p_1+p_2+p_3)^2$	$(k_1-p_1-p_2-p_3)^2$
D_5	k_2^2	k_2^2
D_6	$(k_2+p_1+p_2+p_3)^2$	$(k_2-p_1-p_2-p_3-p_4)^2$
D_7	$(k_2+p_1+p_2+p_3+p_4)^2$	$(k_1-k_2)^2$
D_8	$(k_1-k_2)^2$	$(k_1-k_2+p_4)^2$
D_9	$(k_1+p_1+p_2+p_3+p_4)^2$	$(k_2-p_1)^2$
D_{10}	$(k_2+p_1)^2$	$(k_2-p_1-p_2)^2$
D_{11}	$(k_2+p_1+p_2)^2$	$(k_2-p_1-p_2-p_3)^2$

where we suppressed the $+i\varepsilon$ from Feynman's prescription everywhere. Note that we have eleven propagators even though one would only expect eight two appear, given the five-point two-loop kinematics. However, we want to express also scalar products appearing in the numerator as linear combinations of propagators, and this is only possible by adding three extra propagators (although these would not naturally appear in the diagrams as denominators). All required crossed families are obtained from the two reference families above by permutations of the external momenta. Note that collectively, across the various primitive amplitudes for the processes in Eq. (2.6), we are left with $\sim \mathcal{O}(10^6)$ different scalar integrals.

Luckily, one does not need to compute such a huge number of Feynman integrals. This is because, as we already discussed in Chapter 1, Feynman integrals satisfy many linear relations that can be obtained via IBPs (see Eq. (1.88)). Exploiting

all the linear relations amongst Feynman integrals makes it possible to reduce them to a set of independent master integrals. This step of the calculation, despite sounding simple, represents one of the main bottlenecks of modern multiloop scattering amplitudes calculations. This is because all the linear relations between the integrals build up a very large system that becomes computationally very hard to solve. Moreover, one needs to also make sure that the system generated via IBP reduction is closed, i.e. there are enough equations for the number of the given number of unknowns. This is guaranteed in the so-called *Laporta algorithm* [58], which is nowadays implemented in many dedicated public codes. For the calculation under consideration, we perform the IBP reduction using the public code `Kira` [59, 60] and, specifically for the non-planar topologies (which are the hardest to reduce), the code `Finred`. The latter is an in-house implementation of Laporta's algorithm which employs finite field techniques [61–64] enhanced with denominator guessing from a rational sample [65] (see [66] for an alternative approach) for an efficient reconstruction of multivariate rational functions and syzygy algorithms [67–72].

We observe that the multi-scale kinematics of five-point amplitudes causes a large swell in intermediate expressions. In fact in the course of this calculation one encounters individual IBP identities with disk-sizes of up to 3GB. Our approach to this computational problem is based on the observation that partial fraction decomposition can reduce the expression size for single IBPs by various orders of magnitude. We perform IBP reduction for a minimal subset of integrals and decompose the resulting integral coefficients into multivariate partial fractions. Reduction identities for all integrals contributing to the amplitudes are then obtained using crossings of external invariants. To perform the partial-fraction decomposition, we utilize `MultivariateApart` [65] augmented by `Singular` [73]. This step requires first defining an appropriate ordering among the denominator factors that appear in the individual color factors of each helicity amplitudes. As expected, the complexity of the final expressions depends greatly on this choice of monomial ordering. We find it beneficial, in particular, to choose an ordering that avoids as much as possible the appearance of spurious singularities in the denominators, for more details

see Refs. [56, 57]. Once the simplified reduction identities are inserted into the amplitude, we perform an additional partial-fraction decomposition to simplify the resulting expressions further; in addition to the IBP reduction, this proves to be the step with the highest computational cost in our framework.

Once the obstacles of IPB reduction are overcome and the integrals are reduced, one is left with the computation of master integrals. For the process under consideration, the master integrals were computed in Refs. [55, 74–78] via the *method of differential equations*. Three different classes of master integrals can be identified: the pentagon box, belonging to the planar topology, and the hexagon box and double pentagon, that both belong to the non-planar topology (see e.g. [47] for details). The main idea of the method of differential equations is to solve Feynman integrals by means of differentiation rather than direct integration over the loop momenta. To do this, one differentiates the set of master integrals with respect to the different kinematic invariants. At this point, one can apply the IBP reduction procedure to the derivatives of the master integrals in order to write them as a linear combination of the master themselves

$$\partial_{s_{ij}} M_l(s_{ij}, \epsilon) = r_{lk}(s_{ij}, \epsilon) M_k(s_{ij}, \epsilon)\,. \tag{2.26}$$

In other words, the master integrals satisfy a first-order homogeneous linear differential equation (DEQ). Note that the matrix r in the above equation, depend both on the kinematic invariants and on the spacetime dimensions d. This makes the DEQ very hard to solve analytically. A solution to this problem was suggested in Ref. [79], where it is observed that finding a solution becomes simple if one can write the system in a $\epsilon-$factorized form, also called *canonical system*, that takes the form

$$\partial_{s_{ij}} M_l(s_{ij}, \epsilon) = \epsilon\, r_{lk}(s_{ij}) M_k(s_{ij}, \epsilon)\,. \tag{2.27}$$

However, finding such a canonical form is not always straightforward and in many cases not algorithmic. The power of this approach is that, if a canonical form can be found, than the system becomes solvable analytically order by order in

the dimensional regulator. In such cases, there is a special class of functions that solve canonical DEQs: *Chen's iterated integrals* [80]

$$G(a_n, \ldots, a_1; z) = \int_{z_n}^{z} dx f_n(x) G(a_{n-1}, \ldots, a_1; x)\,, \quad G(z) = 1\,, \tag{2.28}$$

defined recursively with a kernel function $f_i(z)$. The solution of the canonical differential equations for our five point master integrals is indeed written in terms of Chen's iterated integrals, and the full set is made available in Ref. [47].

Having discussed the integral reduction and the calculation of master integrals, we can now go back to our calculation and discuss the final result. After including the IBP reduction in the amplitude, having performed partial fractioning and having used the known results for the master integrals the calculation of the bare amplitude is essentially complete. We have already seen in Chapter 1 that Feynman integrals develop both UV and IR singularities. Therefore, the bare amplitude will display poles in the dimensional regulator. In order to obtain the finite remainder, which captures the non-trivial hard physics, we need to perform UV renormalization and IR subtraction, which will be discussed in the next section.

2.2.4 UV renormalization and IR subtraction

UV divergences can be removed by expressing the amplitudes in terms of the $\overline{\text{MS}}$ renormalized strong coupling $\alpha_s(\mu)$ [4]. The renormalized helicity amplitudes can be expanded as a perturbative series in the renormalized strong coupling

$$\boldsymbol{\mathcal{M}}(\boldsymbol{\lambda}) = \sum_{\ell=0}^{2} \left(\frac{\alpha_s}{4\pi}\right)^{\ell} \boldsymbol{\mathcal{M}}^{(\ell)}_{\boldsymbol{\lambda},\text{ren}} + \mathcal{O}(\alpha_s^3), \tag{2.29}$$

where $\boldsymbol{\mathcal{M}}^{(\ell)}_{\boldsymbol{\lambda},\text{ren}}$ is the renormalized ℓ-loop contribution. These still contain IR singularities that need to be extracted. In our fully inclusive Higgs cross section calculation, we did not need to extract IR singularities, since we added the real emission contribution that automatically regulates them. In this case, however, we want to exploit the universality of IR singularities to extract them and provide a

[4] Note that the $\beta-$function coefficients here differ of a factor of 2 with respect to the ones used in Chapter 1. This is due to the fact that the natural expansion parameter for loop amplitudes is $\alpha_s/(4\pi)$, whereas for cross sections it is $\alpha_s/(2\pi)$.

finite remainder. Indeed, the infrared structure of two-loop QCD amplitudes is well known [20, 21], and we can use this knowledge to define the finite remainders of the amplitudes at each loop order as

$$\begin{aligned}
&\boldsymbol{\mathcal{M}}^{(0)}_{\boldsymbol{\lambda},\,\mathrm{fin}} = \boldsymbol{\mathcal{M}}^{(0)}_{\boldsymbol{\lambda}} \,, \quad \boldsymbol{\mathcal{M}}^{(1)}_{\boldsymbol{\lambda},\,\mathrm{fin}} = \boldsymbol{\mathcal{M}}^{(1)}_{\boldsymbol{\lambda},\,\mathrm{ren}} - \boldsymbol{\mathcal{I}}_1 \, \boldsymbol{\mathcal{M}}^{(0)}_{\boldsymbol{\lambda},\,\mathrm{ren}} \,, \\
&\boldsymbol{\mathcal{M}}^{(2)}_{\boldsymbol{\lambda},\,\mathrm{fin}} = \boldsymbol{\mathcal{M}}^{(2)}_{\boldsymbol{\lambda},\,\mathrm{ren}} - \boldsymbol{\mathcal{I}}_2 \, \boldsymbol{\mathcal{M}}^{(0)}_{\boldsymbol{\lambda},\,\mathrm{ren}} - \boldsymbol{\mathcal{I}}_1 \, \boldsymbol{\mathcal{M}}^{(1)}_{\boldsymbol{\lambda},\,\mathrm{ren}} \,,
\end{aligned} \tag{2.30}$$

where

$$\begin{aligned}
\boldsymbol{\mathcal{I}}_1(\epsilon) &= \frac{e^{\epsilon\gamma_E}}{\Gamma(1-\epsilon)} \sum_i \left(\frac{1}{\epsilon^2} - \frac{\gamma_0^i}{2\epsilon} \frac{1}{\mathbf{T}_i^2} \right) \sum_{i \neq j} \frac{\mathbf{T}_i \cdot \mathbf{T}_j}{2} \left(\frac{\mu^2}{-s_{ij}} \right)^{\epsilon} \,, \\
\boldsymbol{\mathcal{I}}_2(\epsilon) &= \frac{e^{-\epsilon\gamma_E}\Gamma(1-2\epsilon)}{\Gamma(1-\epsilon)} \left(\frac{\gamma_1^{\mathrm{cusp}}}{8} + \frac{\beta_0}{2\epsilon} \right) \boldsymbol{\mathcal{I}}_1(2\epsilon) - \frac{1}{2} \boldsymbol{\mathcal{I}}_1(\epsilon) \left(\boldsymbol{\mathcal{I}}_1(\epsilon) + \frac{\beta_0}{\epsilon} \right) + \frac{1}{\epsilon} \boldsymbol{\mathcal{H}}_2 \,,
\end{aligned} \tag{2.31}$$

and "fin" denotes terms that are finite in four dimensions. In the above equation, the quantities $\mathbf{T}_i$ are color operators related to the $\mathrm{SU}(N_c)$ generators associated with particle i, as already defined in Eq. (1.52). The operator $\boldsymbol{\mathcal{H}}_2$ is given by

$$\begin{aligned}
\boldsymbol{\mathcal{H}}_2 = &\frac{1}{16} \sum_i \left(\gamma_1^i - \frac{1}{4} \gamma_1^{\mathrm{cusp}} \gamma_0^i + \frac{\pi^2}{16} \beta_0 \gamma_0^{\mathrm{cusp}} C_i \right) \\
&+ \frac{i f^{abc}}{24} \sum_{(i,j,k)} \mathbf{T}_i^a \mathbf{T}_j^b \mathbf{T}_k^c \log \frac{-s_{ij}}{-s_{jk}} \log \frac{-s_{jk}}{-s_{ki}} \log \frac{-s_{ki}}{-s_{ij}} \\
&- \frac{i f^{abc}}{128} \gamma_0^{\mathrm{cusp}} \sum_{(i,j,k)} \mathbf{T}_i^a \mathbf{T}_j^b \mathbf{T}_k^c \left(\frac{\gamma_0^i}{C_i} - \frac{\gamma_0^j}{C_j} \right) \log \frac{-s_{ij}}{-s_{jk}} \log \frac{-s_{ki}}{-s_{ij}} \,,
\end{aligned} \tag{2.32}$$

where the cusp anomalous dimension reads

$$\begin{aligned}
\gamma_0^{\mathrm{cusp}} &= 4 \,, \\
\gamma_1^{\mathrm{cusp}} &= \left(\frac{268}{9} - \frac{4\pi^2}{3} \right) C_A - \frac{40}{9} N_f \,,
\end{aligned} \tag{2.33}$$

while the quark and gluon anomalous dimensions are given by

$$\begin{aligned}
&\gamma_0^q = -3 C_F \,, \\
&\gamma_1^q = C_F^2 \left(-\frac{3}{2} + 2\pi^2 - 24\zeta_3 \right) + C_A C_F \left(-\frac{961}{54} - \frac{11}{6}\pi^2 + 26\zeta_3 \right) + C_F N_f \left(\frac{65}{27} + \frac{\pi^2}{3} \right) \,, \\
&\gamma_0^g = -\beta_0 \,, \\
&\gamma_1^g = C_A^2 \left(-\frac{692}{27} + \frac{11}{18}\pi^2 + 2\zeta_3 \right) + C_A N_f \left(\frac{128}{27} - \frac{\pi^2}{9} \right) + 2 C_F N_f \,.
\end{aligned} \tag{2.34}$$

Note that the operator $\boldsymbol{\mathcal{H}}_2$, in this particular way of subtracting divergences, contains triple color correlators, i.e. structure of the type $\mathbf{T}_i^a\mathbf{T}_j^b\mathbf{T}_k^c$. The cancellation pattern of such structures in NNLO cross sections will be studied in some detail in Chapter 3.

A further level of simplification can be achieved by expressing the finite remainders in terms of a minimal set of independent rational functions. Following Refs. [56, 57], we start from a partial-fractioned form of the rational functions based on a fixed monomial ordering. We exploit the uniqueness of this representation in order to search for linear relations among the rational functions, which we solve using row reductions. As a measure of complexity we use the byte size of the rational functions and we reduce the system of linear relations to express more complicated functions in terms of simpler ones, see Ref. [57] for more details. This final step makes it possible for us to obtain an improvement of around one order of magnitude in the disk-size of independent color-ordered primitive helicity amplitudes.

2.2.5 Final checks and results

The color and helicity configurations listed in Table 2.1 for the processes in Eq. (2.7) are sufficient to reconstruct all possible partonic channels with four quarks and one gluon in total[5]. In particular, using parity and charge conjugation, as well as permutations of the external particles, one can obtain all amplitudes for the processes

$$q\bar{q} \to \bar{q}'q'g, \quad q\bar{q}' \to \bar{q}'qg, \quad \bar{q}'\bar{q} \to \bar{q}'\bar{q}g, \quad g\bar{q} \to \bar{q}'q'\bar{q}. \tag{2.35}$$

The same-flavor quark amplitudes

$$q\bar{q} \to \bar{q}qg, \quad qq \to qqg, \quad qg \to qq\bar{q} \tag{2.36}$$

can then be obtained as linear combinations of appropriate components of the different-flavor quark amplitudes. More specifically, in the notation of Eq. (2.20) we can write

$$\begin{aligned}
\boldsymbol{\mathcal{M}}_{q\bar{q}\to q\bar{q}g}(\boldsymbol{\lambda}) &= \boldsymbol{\mathcal{M}}_{q\bar{q}'\to q\bar{q}'g}(\boldsymbol{\lambda}) - \boldsymbol{\mathcal{M}}_{q\bar{q}\to q'\bar{q}'g}(\boldsymbol{\lambda}), \\
\boldsymbol{\mathcal{M}}_{qq\to qqg}(\boldsymbol{\lambda}) &= \boldsymbol{\mathcal{M}}_{qq'\to qq'g}(\boldsymbol{\lambda}) - \boldsymbol{\mathcal{M}}_{qq'\to q'qg}(\boldsymbol{\lambda}), \\
\boldsymbol{\mathcal{M}}_{qg\to qq\bar{q}}(\boldsymbol{\lambda}) &= \boldsymbol{\mathcal{M}}_{qg\to qq'\bar{q}'}(\boldsymbol{\lambda}) - \boldsymbol{\mathcal{M}}_{qg\to q'q\bar{q}'}(\boldsymbol{\lambda}),
\end{aligned} \tag{2.37}$$

[5]For a complete set of partonic channels see Ref. [26]

where all channels on the rhs of these identities are either in eq. (2.35) or can be obtained from them by crossings which do not require analytic continuation.

Crossings of rational functions and spinor factors amounts to a simple renumbering of momenta and their helicities (including flipping of helicities from incoming to outgoing states). Crossing of the transcendental functions, on the other hand, may require a dedicated analytic continuation. We note that the analytic continuation of each pentagon function individually is non-trivial but also not necessary. In fact, the information needed to perform the required continuation is available implicitly in the results provided by Ref. [47], where all master integrals are evaluated for all 120 permutations of the external invariants in terms of a minimal set of pentagon functions. In practice, we took every uncrossed master integral and applied the required crossing on its analytic expression by formally crossing all appearing pentagon functions. We then equated these formal expressions to the crossed master integrals available in Ref. [47], which are written in terms of uncrossed pentagon functions. Repeating this for all master integrals for a given crossing, we obtained a linear system of equations, which we solved using `FiniteFlow` [64] to express the crossed pentagon functions in terms of the uncrossed ones. Typically, the system is under-determined and some crossed pentagon functions remain unsolved for. Nevertheless, since the results in Ref. [47] are, by construction, sufficient to represent any crossing of the amplitudes, all remaining crossed pentagon functions must cancel upon inserting these relations in the amplitude. We verified this cancellation explicitly for each crossing required to obtain the helicity and color ordered amplitudes for all partonic sub-channels. This provided a strong check of the consistency of our procedure.

We performed numerous checks on our results. First, we observed full cancellation of UV and IR poles of the bare amplitudes after UV renormalization and IR subtraction. For the five-gluon channel, we also verified the one- and two-loop $U(1)$ decoupling identities as well as the generalized color-trace identities described in [81]. For the same channel, we also computed a redundant set of single-trace partial amplitudes; the crossing relations among them allowed us to verify the

	$\overline{\sum}2\mathrm{Re}[\boldsymbol{\mathcal{M}}^{0\dagger}\boldsymbol{\mathcal{M}}^{1}_{\mathrm{fin}}]$	$\overline{\sum}\lvert\boldsymbol{\mathcal{M}}^{1}_{\mathrm{fin}}\rvert^2$	$\overline{\sum}2\mathrm{Re}[\boldsymbol{\mathcal{M}}^{0\dagger}\boldsymbol{\mathcal{M}}^{2}_{\mathrm{fin}}]$
$q\bar{q} \to \bar{q}'q'g$	-101.6531	3271.088	2511.430
$q\bar{q}' \to \bar{q}'qg$	-82.09317	4338.144	-768.0230
$\bar{q}'\bar{q} \to \bar{q}'\bar{q}g$	-47.41403	769.2739	82.75641
$g\bar{q} \to \bar{q}'q'\bar{q}$	-57.86782	1181.730	1341.638
$q\bar{q} \to \bar{q}qg$	-88.39101	3926.462	379.8467
$qq \to qqg$	-45.63443	767.2815	94.00947
$qg \to qq\bar{q}$	-71.33829	1686.104	1626.085

Table 2.2: Benchmark results for the interference of the tree-level with the one- and two-loop finite remainders (first and third columns) and for the squared one-loop finite remainder (second column). $\overline{\sum}$ refers to summation over color and helicity states, and normalization over the corresponding leading order term.

consistency of our calculation at the level of finite remainders. We also compared our tree-level and one-loop results against existing analytic calculations [82, 83] as well as `OpenLoops2` [84], by numerically evaluating all helicity configurations of the channels listed in (2.35) and (2.36). Finally, we found perfect agreement with the analytic two-loop full-color all-plus gluon amplitude of Ref. [85] and with the numerical benchmarks in the leading-color approximation provided in Ref. [86] for all channels in (2.35). Furthermore, we found perfect agreement with numerical benchmarks provided by the authors of Refs. [48, 49], who performed an independent calculation of the same full colour amplitudes.

In Table 2.2 we present benchmark results for all the partonic channels under consideration. We provide the finite remainder of the squared matrix elements summed over color and helicities, normalized by the corresponding leading order term. We choose the kinematic configuration

$$\begin{aligned} &s_{12} = 10^6, && s_{23} = -761244.13, && s_{34} = 865719.14, \\ &s_{45} = 126204.05, && s_{51} = -29885.560, && \mu^2 = 10^4, \end{aligned} \tag{2.38}$$

and fix $N_c = 3$ and $N_f = 5$. To evaluate the pentagon functions we use the `PentagonMI` package [47]. All results in electronic format are available at [87].

3

Infrared divergences and subtraction

Contents

3.1 Introduction 65
3.2 NSC subtraction at NLO EW 68
3.3 NSC at NNLO mixed QCD-EW 75
3.4 A new perspective on the NSC: towards high multiplicity processes 85
3.4.1 NLO 87
3.4.2 NNLO 90

3.1 Introduction

In this chapter we want to deal with another major bottleneck of higher order calculations in particle phenomenology: the treatment of infrared singularities. At this point one might wonder why this is the case, since in Chapter 2 we claimed that infrared divergences of loop amplitudes are well known up to two loops, and in Chapter 1 we showed how they naturally cancel when combining real and virtual corrections in a NLO inclusive cross section calculation. However, as we have already mentioned at the very end of Chapter 1, there is more physical information enclosed in differential observables rather than very inclusive ones. For differential

observables, we need to find a way to extract and cancel the divergences coming from loops and phase space integrations without integrating over the *resolved* phase space, i.e. the phase space associated with the hard particles.

There are different ways one can achieve this goal. The two main approaches go under the name of *subtraction* and *slicing*. Although we will only deal with subtraction in the rest of the chapter, let us outline the main differences in the two approaches. In a subtraction scheme, one considers a matrix element that needs to be integrated over the real emission phase space, then subtracts and adds back the singular infrared configurations. By doing this, one ends up with a regulated matrix element, that can be computed directly in $d = 4$, and the integration of a singular counterterm. The latter contains the explicit singularities that will cancel against virtual contributions. Crucially, the counterterms can be constructed entirely from building blocks that are process independent. On the other hand, in a slicing scheme, one introduces a lower cutoff in the phase space integration, the slicing parameter, that separates resolved and unresolved configurations. The former are finite and can be directly integrated. For the latter, if the separation scale is very close to the unresolved configurations, one can substitute the actual radiation with its (universal) IR limit. The neglected terms vanish with power behaviour as the slicing parameter goes to zero, so one would need to choose small values for the latter. Unfortunately, both the resolved and unresolved configurations depend logarithmically on the slicing scale, and this dependence only cancels in their sum. One then has a "non-local" cancellation of IR singularities, where individual terms have a spurious dependence on the slicing scale, making the method numerically challenging. However, thanks to its approximate nature, slicing is easier to extend at higher orders.

It is important to point out that the subtraction procedure at NLO is a solved problem. There are two main different approaches that are implemented in public codes and fully automated. One approach is the so-called Frixione-Kunszt-Signer (FKS) subtraction [88], and another one is the Catani-Seymour subtraction [89]. Both of them are fully automated in public codes. A detailed discussion of the two approaches go beyond the scope of this thesis, although we will learn about the

FKS approach when dealing with the so-called Nested Soft-Collinear subtraction scheme in Section 3.2.

At NNLO the situation is quite different. The structure of infrared singularities becomes much more involved and a fully automated subtraction is still out of reach. There are many different slicing and subtraction schemes for NNLO calculations available nowadays. On the subtraction side they include the *Antenna subtraction* [90–96], the *Sector-improved residue subtraction* [97, 98], the *Nested Soft-Collinear subtraction scheme* [99–103](NSC), *Projection-to-Born* [104], the *Local analytic subtraction* [105–108], *Colourful subtraction* [109, 110] and the *Geometric subtraction* [111]. In this thesis we will focus on the Nested Soft-Collinear method. The NSC is designed by exploiting two properties of scattering amplitudes. The first one is their factorization in the soft and collinear limits into a product of universal kernels and lower-multiplicity on-shell amplitudes [25, 112–115]. The second one is QCD color coherence [116–118], which implies that soft and collinear limits of on-shell amplitudes are not entangled. One can use these features to set up an iterative subtraction procedure that starts with the subtraction of soft divergences. To regulate the remaining collinear singularities, one introduces a partitioning of the phase space to deal with a minimum number of collinear configurations at a time. This allows one to subtract collinear divergences in a relatively simple and modular way. This method was developed for NLO QCD computations in Ref. [88] and then extended to NNLO in Refs. [99–102]. Although the NSC was originally developed for NNLO QCD calculations, it can be easily generalized to the case of EW corrections, as we will see in the following sections.

We will start with a warm-up at NLO to fix the notation, and then we will move to NNLO and present the challenges and frontiers of its applications to phenomenology. We will do so by applying it to a specific case, the case of mixed QCD-EW corrections to dilepton production at the LHC. This part will be based on the publication Ref. [119]. The reason why we do this is not only to set the stage for the discussion in Chapter 5, where the phenomenological implications of these corrections will be discussed, but also because it allows us to introduce all

the relevant concepts in a simplified setting. Indeed, in the case of mixed QCD-EW corrections, we will need to introduce phase space partitions and angular sectoring, although the abelian nature of QED will make some structures, e.g. soft limits, easier to treat. We will devote the last part of this chapter to an extension of the NSC to more complicated processes at NNLO QCD, specifically those involving jets in the final state. There we will need to deal with the full complexity of a NNLO subtraction, and we will show how one can organise the cancellation of divergences in a transparent and physical way. This part is based on the publication Ref. [103]. We will then finally show how to obtain the simplified results of the mixed QCD-EW case starting from the fully general formulas in Sections 3.4.1 and 3.4.2.

3.2 NSC subtraction at NLO EW

Let us begin with a discussion of the NSC at NLO EW. Note that at this perturbative order, the scheme reduces to the well known FKS subtraction. We find it convenient to explain the method by going through an example in some detail: we will compute the NLO EW corrections to dilepton production at the LHC. We choose the case of EW rather than QCD since in the former case we can also have extra radiation emitted from the final state. This will force us to introduce partitions already at NLO, and therefore introduce concepts that will become crucial in the NNLO case.

We start by discussing real-emission corrections to the process $f_1(p_1) + f_2(p_2) \to \ell^-(p_3) + \ell^+(p_4)$, i.e. we consider the process

$$f_1(p_1) + f_2(p_2) \to \ell^-(p_3) + \ell^+(p_4) + f_3(p_5) \,, \tag{3.1}$$

where the label $f_i = \{\gamma, g, q, \bar{q}\}$ specifies the parton that participates in the hard scattering and p_i is the four-momentum of the parton i. Following Ref. [99] we define the function

$$F_{\rm LM}(1_{f_1}, 2_{f_2}, 3, 4|5_{f_5}) = \mathcal{N} \sum_{\rm col,\, pol} \int {\rm dLips}_{34}\, (2\pi)^d\, \delta^{(d)}\Big(p_{12} - \sum_{j=3}^{5} p_j\Big) \Big|\mathcal{M}(p_1 \dots p_5)\Big|^2 \,, \tag{3.2}$$

where $p_{12} = p_1 + p_2$, $\mathcal{M}$ is the matrix element of the process in Eq. (3.1), dLips_{34} is the Lorentz-invariant phase space of the two leptons and $\mathcal{N}$ is a quantity that includes spin- and color-averaging factors, if required.

The partonic cross section of the process Eq. (3.1) is obtained by integrating Eq. (3.2) over the phase space of parton f_5

$$2s \cdot d\hat{\sigma}_{\mathrm{r}}^{f_1 f_2} = \int [dp_5]\, F_{\mathrm{LM}}(1_{f_1}, 2_{f_2}, 3, 4|5_{f_5}) \equiv \Big\langle F_{\mathrm{LM}}(1_{f_1}, 2_{f_2}, 3, 4|5_{f_5}) \Big\rangle \,, \tag{3.3}$$

where $s = 2p_1 \cdot p_2$ is the partonic center-of-mass energy squared. In the nested soft-collinear subtraction framework, the phase space element $[dp]$ is assumed to include an upper bound on the parton energy E_{max} [99]

$$[dp] = \frac{d^{d-1}p}{(2\pi)^{d-1} 2E_p}\, \theta\Big(E_{\mathrm{max}} - E_p\Big) \,. \tag{3.4}$$

We note that the value for E_{max} can be chosen arbitrarily provided it exceeds the maximal energy that parton f_5 can reach in the process Eq. (3.1). The reason for introducing E_{max} will become clear momentarily.

For the sake of concreteness, we will now focus on NLO electroweak corrections to the $q\bar{q}$ production channel; then $f_1 = q$, $f_2 = \bar{q}$, $f_5 = \gamma$. The matrix element in Eq. (3.2) develops singularities when the photon becomes either soft or collinear to one of the four charged partons; we need to regulate these singularities and extract them without integrating over unresolved parts of the photon's phase space. To accomplish this, we follow Ref. [99] and introduce operators S_5 and C_{5i}, $i = 1, 2, 3, 4$, that extract leading singularities of the functions F_{LM} in the soft $p_5 \to 0$ and collinear $\vec{p}_5 || \vec{p}_i$ limits, respectively. These singular limits can be written as products of universal functions and lower-multiplicity matrix elements, as we have seen in Chapter 1 when dealing with our toy model calculation. More specifically, we have

$$S_5\, F_{\mathrm{LM}}(1_q, 2_{\bar{q}}, 3, 4|5_\gamma) = -2\, e^2 \sum_{j>i=1}^{4} \lambda_{ij}\, Q_i Q_j\, \frac{p_i \cdot p_j}{p_i \cdot p_5\; p_j \cdot p_5}\, F_{\mathrm{LM}}(1_q, 2_{\bar{q}}, 3, 4) \,, \tag{3.5}$$

where $e = \sqrt{4\pi\alpha}$ is the electric charge of the positron, Q_i is the physical electric charge of parton i in units of the positron charge, and λ_{ij} is equal to $+1$ if i, j are

both incoming or outgoing and -1 otherwise. For our process, $Q_1 = -Q_2 = Q_q$ and $Q_3 = -Q_4 = Q_{e^-} \equiv Q_e$.

To describe collinear limits, we need to distinguish between cases where the photon is collinear to an incoming QCD parton or to an outgoing lepton. The corresponding formulas read

$$C_{5i}\, F_{\rm LM}(1_q, 2_{\bar{q}}, 3, 4|5_\gamma) = e^2\, Q_i^2\, \frac{P_{qq}(z)}{p_i \cdot p_5} \cdot \begin{cases} \frac{F_{\rm LM}(\ldots z\cdot i \ldots)}{z}, & z = \frac{E_i - E_5}{E_i},\ i \in \{1,2\}, \\ F_{\rm LM}\left(\ldots \frac{i}{z} \ldots\right), & z = \frac{E_i}{E_i + E_5},\ i \in \{3,4\}, \end{cases} \tag{3.6}$$

where $P_{qq}(z)$ is the color-stripped quark splitting function

$$P_{qq}(z) = \frac{1+z^2}{1-z} - \epsilon(1-z), \tag{3.7}$$

and the notation $z \cdot i$ in Eq. (3.6) implies that the function $F_{\rm LM}$ has to be computed with the momentum of the parton i set to zp_i. Note that both soft and collinear limits also act on the momentum conserving δ-function, so they give rise to an on-shell reduced kinematics. With an abuse of notation, we will still call such reduced kinematics with the same labels of the full kinematics.

We can use soft and collinear operators to construct expressions that are finite in the corresponding limits. We start with the soft operator S_5 and write

$$\begin{aligned} \Big\langle F_{\rm LM}(1_q, 2_{\bar{q}}, 3, 4|5_\gamma)\Big\rangle = &\Big\langle S_5\, F_{\rm LM}(1_q, 2_{\bar{q}}, 3, 4|5_\gamma)\Big\rangle \\ &+ \Big\langle [I - S_5]\, F_{\rm LM}(1_q, 2_{\bar{q}}, 3, 4|5_\gamma)\Big\rangle\,, \end{aligned} \tag{3.8}$$

where I is an identity operator. The two terms in Eq. (3.8) have very different properties. Indeed, according to Eq. (3.5), in the first term of Eq. (3.8) the four-momentum p_5 factorizes from the function $F_{\rm LM}$. Hence, we can analytically integrate over p_5 without affecting the kinematics of other particles.[1] The result of such integration is well-known (see e.g. [120]) and can be written as follows

$$\begin{aligned} &\Big\langle S_5\, F_{\rm LM}(1_q, 2_{\bar{q}}, 3, 4|5_\gamma)\Big\rangle = \\ &-\frac{2[\alpha]}{\epsilon^2}\Big(2E_{\rm max}\Big)^{-2\epsilon} \sum_{j>i=1}^{4} \lambda_{ij}\, Q_i Q_j \Big\langle \eta_{ij}^{-\epsilon}\, \mathcal{F}(\eta_{ij})\, F_{\rm LM}(1_q, 2_{\bar{q}}, 3, 4)\Big\rangle\,. \end{aligned} \tag{3.9}$$

[1] We note that the integration over the photon energy becomes UV divergent once the soft limit is taken, since by construction S_5 removes p_5 from the momentum-conserving δ-function; this potential divergence is regulated by $E_{\rm max}$.

In Eq. (3.9) we introduced

$$\eta_{ij} = \frac{\rho_{ij}}{2} = \frac{1-\cos\theta_{ij}}{2}, \tag{3.10}$$

where θ_{ij} is the relative angle between the directions of partons i and j, and

$$\mathcal{F}(\eta) = \frac{\Gamma^2(1-\epsilon)}{\Gamma(1-2\epsilon)}\,\eta^{1+\epsilon}\,{}_2F_1(1,1,1-\epsilon;1-\eta). \tag{3.11}$$

We have also introduced the coupling $[\alpha]$, that reads[2]

$$[\alpha] = \frac{e^2}{8\pi^2}\frac{(4\pi)^\epsilon}{\Gamma(1-\epsilon)}\,. \tag{3.12}$$

The second term on the r.h.s. of Eq. (3.8) is regular in the soft $p_5 \to 0$ limit but it still contains collinear singularities that arise when the emitted photon is collinear to quarks or leptons. Since we would like to deal with one collinear singularity at a time, we introduce a partition of unity

$$1 = \omega^{51} + \omega^{52} + \omega^{53} + \omega^{54}\,, \tag{3.13}$$

where the partitions functions ω^{5i} are designed to have following property

$$C_{5i}\,\omega^{5j} = \delta_{ij}. \tag{3.14}$$

This implies that the function $\omega^{5i}[I - S_5]F_{\rm LM}(1_q, 2_{\bar q}, 3, 4|5_\gamma)$ is only singular in the limit $\vec{p}_5||\vec{p}_i$, while all other collinear singularities are damped. Our choice of partition functions reads

$$\omega^{5i} = \frac{1/\rho_{5i}}{\sum_{j=1}^4 1/\rho_{5j}}\,, \tag{3.15}$$

with ρ_{ij} defined in Eq. (3.10). It is straightforward to check that with this choice Eq. (3.14) is satisfied. We can use Eqs. (3.14, 3.15) to extract collinear singularities from the soft-regulated contribution in Eq. (3.8). We arrive at

$$\begin{aligned}\Big\langle F_{\rm LM}(1_q, 2_{\bar q}, 3, 4|5_\gamma)\Big\rangle &= \Big\langle S_5\, F_{\rm LM}(1_q, 2_{\bar q}, 3, 4|5_\gamma)\Big\rangle \\ &+ \sum_{i=1}^4 \Big\langle [I - S_5]\, C_{5i}\, F_{\rm LM}(1_q, 2_{\bar q}, 3, 4|5_\gamma)\Big\rangle + \Big\langle \mathcal{O}^\gamma_{\rm nlo}\, F_{\rm LM}(1_q, 2_{\bar q}, 3, 4|5_\gamma)\Big\rangle\,,\end{aligned} \tag{3.16}$$

[2] A similar definition is to be intended, *mutatis mutandis*, for the strong coupling $[\alpha_s]$ in the case of QCD corrections.

where

$$\Big\langle \mathcal{O}^{\gamma}_{\rm nlo}\, F_{\rm LM}(1_q, 2_{\bar{q}}, 3, 4|5_\gamma)\Big\rangle = \Big\langle [I - S_5] \sum_{i=1}^{4} [I - C_{5i}]\, \omega^{5i} F_{\rm LM}(1_q, 2_{\bar{q}}, 3, 4|5_\gamma)\Big\rangle \quad (3.17)$$

is fully regulated and can be numerically computed in four dimensions with any infra-red safe restriction on the phase space.

The only ingredients that we still require to compute the function $\langle F_{\rm LM}(1_q, 2_{\bar{q}}, 3, 4|5_\gamma)\rangle$ in Eq. (3.16) are the hard-collinear subtraction terms $(I - S_5)C_{5i}F_{\rm LM}$, $i = 1, .., 4$. They were calculated in Refs. [99, 101] and we do not report their calculation here. To get the soft-collinear counterterm one can start from the soft limit in Eq. (3.5) and take the collinear limit on top of it. For the collinear limit, it is sufficient to integrate over the phase space the collinear counterterm of Eq. (3.6). The results read

$$\Big\langle [1 - S_5]\, C_{5i}\, F_{\rm LM}(1_q, 2_{\bar{q}}, 3, 4|5_\gamma)\Big\rangle = \frac{[\alpha]\, Q_i^2}{\epsilon}\, \frac{\Gamma^2(1-\epsilon)}{\Gamma(1-2\epsilon)}\, \Big(2E_i\Big)^{-2\epsilon} \mathcal{HC}_i(L_i)\ , \quad (3.18)$$

where $L_i = \log\left(E_{\rm max}/E_i\right)$ and

$$\mathcal{HC}_i(L_i) = \begin{cases} -\int_0^1 dz \left\langle P^{\rm NLO}_{qq}(z, L_i)\, F^{(i)}_{\rm LM}(1_q, 2_{\bar{q}}, 3, 4; z)\right\rangle, & i \in \{1, 2\}\,, \\ \left\langle P^{\rm NLO}_{qq}(L_i)\ F_{\rm LM}(1_q, 2_{\bar{q}}, 3, 4)\right\rangle, & i \in \{3, 4\}\,. \end{cases} \quad (3.19)$$

Following Ref. [121] we have used the notation

$$F^{(i)}_{\rm LM}(1_q, 2_{\bar{q}}, 3, 4; z) = \begin{cases} F_{\rm LM}(z \cdot 1_q, 2_{\bar{q}}, 3, 4)/z\ , & i = 1\ , \\ F_{\rm LM}(1_q, z \cdot 2_{\bar{q}}, 3, 4)/z\ , & i = 2\ . \end{cases} \quad (3.20)$$

The splitting functions $P^{\rm NLO}_{qq}$ are defined in Eq. (B.1).

It is important to emphasize that the integration over z in Eq. (3.19) does not introduce additional $1/\epsilon$ singularities, since we have already regulated soft singularities. The explicit $1/\epsilon$ poles that appear in Eqs. (3.9, 3.18) have to cancel against similar poles in the one-loop EW corrections to $q\bar{q} \to \ell^+\ell^-$ and in contributions that describe collinear renormalization of PDFs. Infrared divergences that appear in one-loop virtual corrections can be written in a process-independent way, as we have already seen in Chapter 2. To do so, we introduce the function

$F_{\rm LV}$ that describes contributions of virtual electroweak corrections to the DY cross section and write

$$2s \cdot d\hat{\sigma}_{\rm v}^{q\bar{q}} = \Big\langle F_{\rm LV}(1_q, 2_{\bar{q}}, 3, 4) \Big\rangle = \\ \mathcal{N} \sum_{\rm col,\, pol} \int {\rm dLips}_{34}\, (2\pi)^d\, \delta^{(d)}\Big(p_{12} - \sum_{j=3}^{4} p_j\Big)\, 2{\rm Re}\Big[\, \mathcal{M}^{\rm 1loop}(p_1 \dots p_4) \mathcal{M}^{\dagger}(p_1 \dots p_4)\Big]\,. \tag{3.21}$$

This function can be written as a sum of divergent and finite terms

$$\Big\langle F_{\rm LV}(1_q, 2_{\bar{q}}, 3, 4) \Big\rangle = [\alpha]\, I_{EW}^{(1)} \, \langle F_{\rm LM}(1_q, 2_{\bar{q}}, 3, 4) \rangle + \Big\langle F_{\rm LV}^{\rm fin}(1_q, 2_{\bar{q}}, 3, 4) \Big\rangle\,, \tag{3.22}$$

with Catani's operator $I_{EW}^{(1)}$ defined as follows [20]

$$I_{EW}^{(1)} = \left(\frac{1}{\epsilon^2} + \frac{3}{2}\frac{1}{\epsilon}\right) \sum_{j>i=1}^{4} 2\, \tilde{\lambda}_{ij}\, Q_i Q_j \left(\frac{\mu^2}{s_{ij}}\right)^{\epsilon}, \tag{3.23}$$

where $s_{ij} = 2p_i \cdot p_j$ and $\tilde{\lambda}_{ij} = \cos(\pi\epsilon)$ if i, j are both incoming or outgoing and $\tilde{\lambda}_{ij} = -1$ otherwise. We note that the finite remainder of the virtual corrections $\Big\langle F_{\rm LV}^{\rm fin}(1_q, 2_{\bar{q}}, 3, 4) \Big\rangle$ can only be obtained through a dedicated computation; for the current discussion the only important point is that it contains no divergences, both explicit or implicit.

Finally, we note that collinear singularities related to the photon emission by incoming quarks are removed by re-defining parton distribution functions. The corresponding contribution to the cross section in the $\overline{\rm MS}$ scheme reads (see e.g. [121])

$$2s \cdot d\hat{\sigma}_{\rm pdf}^{q\bar{q}} = [\alpha] \frac{Q_q^2}{\epsilon} \frac{\Gamma(1-\epsilon)}{e^{\epsilon\gamma_E}} \sum_{i=1}^{2} \int_0^1 dz\, \bar{P}_{qq}^{\rm AP,0}(z) \Big\langle F_{\rm LM}^{(i)}(1_q, 2_{\bar{q}}, 3, 4; z) \Big\rangle\,, \tag{3.24}$$

where we used the fact that the absolute values of electric charges of incoming quark and anti-quark are equal. We also note that $\bar{P}_{qq}^{\rm AP,0}$ in Eq. (3.24) is the color-stripped leading order Altarelli-Parisi splitting function; it reads

$$\bar{P}_{qq}^{\rm AP,0}(z) = 2\mathcal{D}_0(z) - (1+z) + \frac{3}{2}\delta(1-z)\,, \tag{3.25}$$

To compute the NLO EW contribution to the partonic cross section $q\bar{q} \to \ell^+\ell^-$, we need to combine Eqs. (3.16, 3.22, 3.24) and expand the result up to

$\mathcal{O}(\epsilon^0)$. Working in the partonic center of mass frame, and choosing $E_{\rm max} = \sqrt{s}/2$, we obtain the following result

$$\begin{aligned} 2s \cdot d\hat{\sigma}^{q\bar{q}}_{\rm nlo,EW} &= \Big\langle \mathcal{O}^{\gamma}_{\rm nlo}\, F_{\rm LM}(1_q, 2_{\bar{q}}, 3, 4|5_\gamma)\Big\rangle + \Big\langle F^{\rm fin}_{\rm LV}(1_q, 2_{\bar{q}}, 3, 4)\Big\rangle \\ &+ \frac{\alpha}{2\pi}\Bigg\{ Q_q^2 \sum_{i=1}^{2} \int_0^1 dz \Big[\bar{P}^{\rm AP,0}_{qq}(z) \log\left(\frac{s}{\mu^2}\right) + P^{'}_{qq}(z)\Big]\Big\langle F^{(i)}_{\rm LM}(1_q, 2_{\bar{q}}, 3, 4; z)\Big\rangle \\ &\qquad + \Big\langle\, \mathcal{G}_{\rm EW}\, F_{\rm LM}(1_q, 2_{\bar{q}}, 3, 4)\Big\rangle\Bigg\}\,, \end{aligned} \tag{3.26}$$

where we have defined

$$\begin{aligned} \mathcal{G}_{\rm EW} &= Q_q^2\, \frac{2\pi^2}{3} + Q_e^2\Big(13 - \frac{2\pi^2}{3}\Big) \\ &\quad + 2\, Q_q Q_e \Big[3 \log\left(\frac{\eta_{13}}{\eta_{23}}\right) + 2\,{\rm Li}_2(1-\eta_{13}) - 2\,{\rm Li}_2(1-\eta_{23})\Big]\,, \end{aligned} \tag{3.27}$$

and

$$P^{'}_{qq}(z) = 4\,\mathcal{D}_1(z) + (1-z) - 2\,(1+z)\,\log(1-z)\,. \tag{3.28}$$

We note that in the chosen reference frame, the momentum conserving delta function included in $F_{\rm LM}(1_q, 2_{\bar{q}}, 3, 4)$ forces $\eta_{13} = \eta_{24}$ and $\eta_{23} = \eta_{14}$; we have used this fact to simplify Eq. (3.27).

Note that NLO QCD corrections to the $q\bar{q}$ channel can be easily obtained from the above formulas by replacing electric charges with QCD charges $Q_e \to 0$ and $Q_q^2 \to C_F$, and restricting the collinear subtractions in $\mathcal{O}^{\gamma}_{\rm nlo}$ to incoming partons only. We also note that the computations described above can be extended to other partonic channels with trivial modifications, and for this reason we do not consider them here. Their discussion in the case of the $W-$boson mediated dilepton production process can be found in Ref. [121].

We are now in the position of moving to the more involved case of NNLO subtraction. Note that we will present the mixed QCD-EW corrections to dilepton production rather than the pure NNLO QCD ones. This makes the subtraction simpler given the abelian nature of QED, although it still gives us the chance of explaining how the method works.

3.3 NSC at NNLO mixed QCD-EW

We continue with mixed QCD-EW corrections and focus on the $q\bar{q}$ partonic channel. To obtain a finite partonic cross section in this case, we need to combine the following contributions

$$d\hat{\sigma}^{q\bar{q}}_{\text{mix}} = d\hat{\sigma}^{q\bar{q}}_{\text{vv}} + d\hat{\sigma}^{q\bar{q}}_{\text{rv},\gamma} + d\hat{\sigma}^{q\bar{q}}_{\text{rv},g} + d\hat{\sigma}^{q\bar{q}}_{\text{rr},g\gamma} + d\hat{\sigma}^{q\bar{q}}_{\text{rr},q\bar{q}} + d\hat{\sigma}^{q\bar{q}}_{\text{pdf}} \,, \tag{3.29}$$

where $d\hat{\sigma}_{\text{vv}}$ is the double-virtual (two-loop) correction to the elastic process $q\bar{q} \to \ell^-\ell^+$, $d\hat{\sigma}_{\text{rv},\gamma}$ describes the one-loop QCD correction to the process with an additional photon in the final state, $d\hat{\sigma}_{\text{rv},g}$ is the one-loop EW correction to the process with an additional gluon, $d\hat{\sigma}_{\text{rr},ij}$ represents the tree-level double-real emission of partons i and j, and $d\hat{\sigma}_{\text{pdf}}$ describes collinear renormalization of PDFs.

We note that the singularity structure of the processes $q\bar{q} \to \ell_1\ell_2 + g\gamma$ and $q\bar{q} \to \ell_1\ell_2 + q\bar{q}$ are very different. Indeed, the latter only contains so-called *triple-collinear singularities*[3], which correspond to configurations where three partons become collinear to each other. This configuration arises at NNLO for the first time, and it is one of the most involved structures that appear in the NNLO subtraction, since it cannot be treated as an iteration of a NLO structure. Such singularities are removed through PDFs renormalization. Because of this, we find it convenient to treat the $g\gamma$ and $q\bar{q}$ final states separately. Hence, we write

$$d\hat{\sigma}^{q\bar{q}}_{\text{mix}} = d\hat{\sigma}^{q\bar{q}}_{\text{mix},g\gamma} + d\hat{\sigma}^{q\bar{q}}_{\text{mix},q\bar{q}} \,, \tag{3.30}$$

with

$$\begin{aligned} d\hat{\sigma}^{q\bar{q}}_{\text{mix},g\gamma} &= d\hat{\sigma}^{q\bar{q}}_{\text{vv}} + d\hat{\sigma}^{q\bar{q}}_{\text{rv},\gamma} + d\hat{\sigma}^{q\bar{q}}_{\text{rv},g} + d\hat{\sigma}^{q\bar{q}}_{\text{rr},g\gamma} + d\hat{\sigma}^{q\bar{q}}_{\text{pdf},g\gamma} \,, \\ d\hat{\sigma}^{q\bar{q}}_{\text{mix},q\bar{q}} &= d\hat{\sigma}^{q\bar{q}}_{\text{rr},q\bar{q}} + d\hat{\sigma}^{q\bar{q}}_{\text{pdf},q\bar{q}} \,. \end{aligned} \tag{3.31}$$

In this thesis, we only describe the infrared regularization of $d\hat{\sigma}^{q\bar{q}}_{\text{mix},g\gamma}$, since it is more instructive than $d\hat{\sigma}^{q\bar{q}}_{\text{mix},q\bar{q}}$.

[3]Note that in QCD there would also be double soft and double collinear configurations, that however vanish in this case due to color conservation.

We begin with the analysis of the double-real emission cross section. We write it as

$$2s \cdot d\hat{\sigma}^{q\bar{q}}_{\mathrm{rr},g\gamma} \equiv \int [dp_5][dp_6] F_{\mathrm{LM}}(1_q, 2_{\bar{q}}, 3, 4|5_g, 6_\gamma) \equiv \Big\langle F_{\mathrm{LM}}(1_q, 2_{\bar{q}}, 3, 4|5_g, 6_\gamma) \Big\rangle. \tag{3.32}$$

The phase space elements for the gluon and the photon are defined in Eq. (3.4) and the meaning of the function F_{LM} should be clear from the discussion in the previous section. In analogy to the NLO case, we first isolate soft singularities in Eq. (3.32). At NNLO, the so-called *double soft* singular configuration arises. In this configuration, both extra partons become soft at a comparable rate. Note that in the case of pure NNLO QCD corrections, the double soft contribution is much more involved given the non-abelian nature of the theory. In our example, however, this contribution is fully factorized into the product of two NLO-like eikonal currents, since gluons and photons do not interact with each other. We can therefore write

$$\begin{aligned}\Big\langle F_{\mathrm{LM}}(1_q, 2_{\bar{q}}, 3, 4|5_g, 6_\gamma) \Big\rangle &= \Big\langle S_g\, S_\gamma\, F_{\mathrm{LM}}(1_q, 2_{\bar{q}}, 3, 4|5_g, 6_\gamma) \Big\rangle \\ &+ \Big\langle \Big[(I - S_g)\, S_\gamma + (I - S_\gamma)\, S_g \Big] F_{\mathrm{LM}}(1_q, 2_{\bar{q}}, 3, 4|5_g, 6_\gamma) \Big\rangle \\ &+ \Big\langle (I - S_g)\, (I - S_\gamma)\, F_{\mathrm{LM}}(1_q, 2_{\bar{q}}, 3, 4|5_g, 6_\gamma) \Big\rangle\,.\end{aligned} \tag{3.33}$$

In Eq. (3.33), S_g and S_γ are operators that extract the leading soft behavior of the function F_{LM} in the limits $E_5 \to 0$ and $E_6 \to 0$ respectively. The first term on the right hand side of Eq. (3.33) corresponds to the double soft limit; as already mentioned it is equal to the product of two NLO soft factors (cf. Eq. (3.9))

$$\begin{aligned}\Big\langle S_g\, S_\gamma\, F_{\mathrm{LM}}(1_q, 2_{\bar{q}}, 3, 4|5_g, 6_\gamma) \Big\rangle &= 4\, \frac{[\alpha_s][\alpha]}{\epsilon^4}\, C_F \left(2E_{\max}\right)^{-4\epsilon} \eta_{12}^{-\epsilon}\, \mathcal{F}(\eta_{12}) \\ &\times \sum_{j>i=1}^{4} \lambda_{ij}\, Q_i Q_j \Big\langle \eta_{ij}^{-\epsilon}\, \mathcal{F}(\eta_{ij})\, F_{\mathrm{LM}}(1_q, 2_{\bar{q}}, 3, 4) \Big\rangle.\end{aligned} \tag{3.34}$$

The two contributions in the second line of Eq. (3.33) correspond to kinematic configurations where either a gluon or a photon is soft. These terms still contain single collinear singularities that need to be regulated. We follow the discussion

in the previous section and write

$$\begin{aligned}\langle S_g\,(I-S_\gamma)\,F_{\rm LM}(1_q,2_{\bar q},3,4|5_g,6_\gamma)\rangle &= \frac{2\,C_F[\alpha_s]\Big(2E_{\rm max}\Big)^{-2\epsilon}}{\epsilon^2}\,\Big\langle \eta_{12}^{-\epsilon}\,\mathcal{F}(\eta_{12})\\ \times\,\Big[\mathcal{O}^\gamma_{\rm nlo}\,F_{\rm LM}(1_q,2_{\bar q},3,4|6_\gamma) &- \frac{[\alpha]}{\epsilon}\,\frac{\Gamma^2(1-\epsilon)}{\Gamma(1-2\epsilon)}\,\sum_{i=1}^4 Q_i^2\,\Big(2E_i\Big)^{-2\epsilon}\,\mathcal{HC}_i(L_i)\Big]\Big\rangle\,,\end{aligned} \tag{3.35}$$

with $\mathcal{HC}_i(L_i)$ defined in Eq. (3.19), and

$$\begin{aligned}&\langle S_\gamma\,(I-S_g)\,F_{\rm LM}(1_q,2_{\bar q},3,4|5_g,6_\gamma)\rangle =\\ &2\,[\alpha]\,\frac{1}{\epsilon^2}\Big(2E_{\rm max}\Big)^{-2\epsilon}\Big\langle\sum_{j>i=1}^4\lambda_{ij}\,Q_iQ_j\,\eta_{ij}^{-\epsilon}\,\mathcal{F}(\eta_{ij})\,\Big[\mathcal{O}^g_{\rm nlo}\,F_{\rm LM}(1_q,2_{\bar q},3,4|5_g)\\ &-[\alpha_s]\frac{C_F}{\epsilon}\,\frac{\Gamma^2(1-\epsilon)}{\Gamma(1-2\epsilon)}\sum_{i=1}^2\Big(2E_i\Big)^{-2\epsilon}\int_0^1 dz\,P^{\rm NLO}_{qq}(z,L_i)\,F^{(i)}_{\rm LM}(1_q,2_{\bar q},3,4;z)\Big]\Big\rangle\,,\end{aligned} \tag{3.36}$$

where $\mathcal{O}^g_{\rm nlo}=(I-S_g)(I-C_{g1}-C_{g2})$, and $P^{\rm NLO}_{qq}(z,L_i)$ defined in Eq. (B.1). Eqs. (3.35, 3.36) provide formulas for $\langle S_g\,(I-S_\gamma)\,F_{\rm LM}\rangle$ and $\langle S_\gamma\,(I-S_g)\,F_{\rm LM}\rangle$ with all the $1/\epsilon$ singularities extracted and no implicitly divergent contributions left.

We now focus on the term in the last line of Eq. (3.33) which is soft-regulated. Unfortunately, it still contains multiple collinear singularities that need to be isolated. To do this, we partition the phase space in such a way that for each partition only a subset of kinematic configurations becomes singular. Using the η_{ij} defined in Eq. (3.10), we construct the partition functions

$$\omega^{\gamma i,gj}=\frac{\eta_{gj}^{-1}}{\sum\limits_{k=1}^2\eta_{gk}^{-1}}\times\frac{\eta_{\gamma i}^{-1}}{\sum\limits_{k=1}^4\eta_{\gamma k}^{-1}}\,, \tag{3.37}$$

with $i\in\{1,2,3,4\}$, $j\in\{1,2\}$. They clearly add up to unity

$$1=\sum_{i=1}^4\sum_{j=1}^2\omega^{\gamma i,gj}\,. \tag{3.38}$$

The partition functions $\omega^{\gamma i,gj}$ are designed in such a way that $\omega^{\gamma i,gj}\,F_{\rm LM}(1,2,3,4|5_g,6_\gamma)$ is only singular when the photon becomes collinear to parton i and/or the gluon becomes collinear to parton j. They also satisfy further relations:

$$\begin{aligned}&C_{g\gamma,i}\,\omega^{\gamma i,gi}=C_{g\gamma,i}\,, && i\in\{1,2\}\,,\\ &C_{\gamma i}\,C_{gj}\,\omega^{\gamma i,gj}=C_{\gamma i}\,C_{gj}\,, && i\in\{1,2,3,4\}\,,\qquad j\in\{1,2\}\,,\end{aligned} \tag{3.39}$$

where $C_{g\gamma,i}$ is the projection operator that describes the triple-collinear limit $\vec{p}_g||\vec{p}_\gamma||\vec{p}_i$.

Triple-collinear configurations, which correspond to the partition functions $\omega^{\gamma 1,g1}$ and $\omega^{\gamma 2,g2}$ in Eq. (3.38), are quite involved since they contain overlapping collinear limits. To disentangle them, we further split these partitions into sectors [121]

$$\omega^{\gamma i,gi} = \omega^{\gamma i,gi}\left(\theta_A^{(i)} + \theta_B^{(i)}\right) \equiv \omega^{\gamma i,gi}\left[\theta\Big(\eta_{\gamma i} - \eta_{gi}\Big) + \theta\Big(\eta_{gi} - \eta_{\gamma i}\Big)\right]. \tag{3.40}$$

We then write the soft-regulated term in Eq. (3.33) as follows

$$\begin{aligned}\Big\langle (I-S_g)\,(I-S_\gamma)\,F_{\rm LM}(1_q,2_{\bar q},3,4|5_g,6_\gamma)\Big\rangle = \Big\langle (I-S_g)\,(I-S_\gamma)\Big[\omega^{\gamma 1,g1}\left(\theta_A^{(1)}+\theta_B^{(1)}\right)\\ +\ \omega^{\gamma 2,g2}\left(\theta_A^{(2)}+\theta_B^{(2)}\right) + \sum_{i=1}^{4}\sum_{\substack{j=1\\ j\neq i}}^{2}\omega^{\gamma i,gj}\Big]F_{\rm LM}(1_q,2_{\bar q},3,4|5_g,6_\gamma)\Big\rangle,\end{aligned} \tag{3.41}$$

and note that each term that appears on the r.h.s in Eq. (3.41) is singular in one collinear configuration only. To simplify the analytic computation of the corresponding limits, we re-write Eq. (3.41) as follows

$$\begin{aligned}&\Big\langle (I-S_g)(I-S_\gamma)F_{\rm LM}(1_q,2_{\bar q},3,4|5_g,6_\gamma)\Big\rangle = \\ &\sum_{i=1}^{4}\Big\langle (I-S_g)(I-S_\gamma)\,\Omega_i^{q\bar q}\,F_{\rm LM}(1_q,2_{\bar q},3,4|5_g,6_\gamma)\Big\rangle,\end{aligned} \tag{3.42}$$

where the four operators $\Omega_i^{q\bar q}$ read

$$\begin{aligned}\Omega_1^{q\bar q} &= (1-C_{g\gamma,1})(1-C_{g1})\,\omega^{\gamma 1,g1}\,\theta_A^{(1)} + (1-C_{g\gamma,1})(1-C_{\gamma 1})\,\omega^{\gamma 1,g1}\,\theta_B^{(1)}\\ &+\ (1-C_{g\gamma,2})(1-C_{g2})\,\omega^{\gamma 2,g2}\,\theta_A^{(2)} + (1-C_{g\gamma,2})(1-C_{\gamma 2})\,\omega^{\gamma 2,g2}\,\theta_B^{(2)}\\ &+\ (1-C_{g2})(1-C_{\gamma 1})\,\omega^{\gamma 1,g2} + (1-C_{g1})(1-C_{\gamma 2})\,\omega^{\gamma 2,g1}\\ &+\ (1-C_{g2})(1-C_{\gamma 3})\,\omega^{\gamma 3,g2} + (1-C_{g2})(1-C_{\gamma 4})\,\omega^{\gamma 4,g2}\\ &+\ (1-C_{g1})(1-C_{\gamma 3})\,\omega^{\gamma 3,g1} + (1-C_{g1})(1-C_{\gamma 4})\,\omega^{\gamma 4,g1},\end{aligned} \tag{3.43}$$

$$\begin{aligned}\Omega_2^{q\bar q} &= C_{g\gamma,1}(1-C_{g1})\,\omega^{\gamma 1,g1}\,\theta_A^{(1)} + C_{g\gamma,1}(1-C_{\gamma 1})\,\omega^{\gamma 1,g1}\,\theta_B^{(1)}\\ &+\ C_{g\gamma,2}(1-C_{g2})\,\omega^{\gamma 2,g2}\,\theta_A^{(2)} + C_{g\gamma,2}(1-C_{\gamma 2})\,\omega^{\gamma 2,g2}\,\theta_B^{(2)}\,,\end{aligned} \tag{3.44}$$

$$\Omega_3^{q\bar q} = -\,C_{g2}\,C_{\gamma 1}\,\omega^{\gamma 1,g2} - C_{g1}\,C_{\gamma 2}\,\omega^{\gamma 2,g1} - C_{g2}\,C_{\gamma 3}\,\omega^{\gamma 3,g2}$$

$$- C_{g2}\, C_{\gamma 4}\, \omega^{\gamma 4,g2} - C_{g1}\, C_{\gamma 3}\, \omega^{\gamma 3,g1} - C_{g1}\, C_{\gamma 4}\, \omega^{\gamma 4,g1} \,, \tag{3.45}$$

$$\begin{aligned}
\Omega_4^{q\bar{q}} = {} & C_{g1} \left[\omega^{\gamma 1,g1}\, \theta_A^{(1)} + \omega^{\gamma 2,g1} + \omega^{\gamma 3,g1} + \omega^{\gamma 4,g1}\right] \\
& + C_{g2} \left[\omega^{\gamma 2,g2}\, \theta_A^{(2)} + \omega^{\gamma 1,g2} + \omega^{\gamma 3,g2} + \omega^{\gamma 4,g2}\right] \\
& + C_{\gamma 1} \left[\omega^{\gamma 1,g1}\, \theta_B^{(1)} + \omega^{\gamma 1,g2}\right] + C_{\gamma 2} \left[\omega^{\gamma 2,g2}\, \theta_B^{(2)} + \omega^{\gamma 2,g1}\right] \\
& + C_{\gamma 3} \left[\omega^{\gamma 3,g1} + \omega^{\gamma 3,g2}\right] + C_{\gamma 4} \left[\omega^{\gamma 4,g2} + \omega^{\gamma 4,g1}\right].
\end{aligned} \tag{3.46}$$

We now discuss the integrated subtraction terms for each of the four structures separately. The $\Omega_1^{q\bar{q}}$ contribution is fully regulated, i.e. all the soft and collinear limits have been extracted. Hence,

$$\left\langle (I - S_g)(I - S_\gamma)\, \Omega_1^{q\bar{q}} F_{\rm LM}(1_q, 2_{\bar{q}}, 3, 4|5_g, 6_\gamma) \right\rangle \tag{3.47}$$

can be numerically integrated in four space-time dimensions and does not require further discussion.

The operator $\Omega_2^{q\bar{q}}$ contains all triple-collinear limits. The corresponding integrated counterterm can be found in Refs. [121–123] and yields

$$\begin{aligned}
& \left\langle (I - S_g)(I - S_\gamma)\, \Omega_2^{q\bar{q}} F_{\rm LM}(1_q, 2_{\bar{q}}, 3, 4|5_g, 6_\gamma) \right\rangle = \\
& - 2[\alpha_s][\alpha]\, Q_q^2\, C_F \sum_{i=1}^{2} (2E_i)^{-4\epsilon} \int_0^1 dz\, P_{qq}^{TC}(z) \left\langle F_{\rm LM}^{(i)}(1_q, 2_{\bar{q}}, 3, 4; z) \right\rangle ,
\end{aligned} \tag{3.48}$$

where the function $P_{qq}^{TC}(z)$ is reported in Eq. (B.3).

We continue with the discussion of double-collinear terms which are contained in the operator $\Omega_3^{q\bar{q}}$. There are two types of such contributions that need to be considered separately: a contribution where a photon and a gluon are emitted by two different initial-state particles and a contribution where a gluon is emitted by one of the initial-state quarks and a photon is emitted by one of the final-state leptons. In both cases collinear limits are described by leading order splitting functions; the main difference between the two cases is the kinematics of the underlying Born process. Indeed, when both partons are emitted from initial state legs one obtains a *double boosted kinematics*, since as we have seen above each collinear final initial state limit boosts the kinematics with a z factor. In the case that

one collinear limit is in the initial state and the other one is in the final state, one ends up with a *single boosted kinematics*, since the final state collinear limit does not result in any z factor. We obtain [119]

$$\begin{aligned}\Big\langle (I-S_g)(I-S_\gamma)\,\Omega_3^{q\bar{q}} F_{\rm LM}(1_q,2_{\bar{q}},3,4|5_g,6_\gamma)\Big\rangle &= \frac{[\alpha_s][\alpha]C_F}{\epsilon^2}\Bigg\{-2Q_q^2\Big(4E_1E_2\Big)^{-2\epsilon}\\ &\times\int_0^1 dz_1\,dz_2\,P_{qq}^{\rm NLO}(z_1,L_1)\,P_{qq}^{\rm NLO}(z_2,L_2)\left\langle\frac{F_{\rm LM}(z_1\cdot 1_q,z_2\cdot 2_{\bar{q}}\cdot 2,3,4)}{z_1\,z_2}\right\rangle\\ &+Q_e^2\sum_{\substack{i=1,2\\ j=3,4}}\left\langle\Big(2E_j\Big)^{-2\epsilon}P_{qq}^{\rm NLO}(L_j)\Big(2E_i\Big)^{-2\epsilon}\int_0^1 dz\,P_{qq}^{\rm NLO}(z,L_i)\;F_{\rm LM}^{(i)}(1_q,2_{\bar{q}},3,4;z)\right\rangle\Bigg\}\,,\end{aligned} \tag{3.49}$$

where $P_{qq}^{\rm NLO}(z_i,L_i), P_{qq}^{\rm NLO}(L_i)$ are given in Eq. (B.1).

Finally we consider the operator $\Omega_4^{q\bar{q}}$ which contains all single-collinear singularities. It is convenient to split it into two terms

$$\Omega_4^{q\bar{q}} \equiv \Omega_4^{q\bar{q},\,\rm IS} + \Omega_4^{q\bar{q},\,\rm IS\times FS}\,, \tag{3.50}$$

defined as follows

$$\begin{aligned}\Omega_4^{q\bar{q},\,\rm IS} &= C_{g1}\Big[\omega^{\gamma 1,g1}\,\theta_A^{(1)}+\omega^{\gamma 2,g1}+\;C_{g2}\Big[\omega^{\gamma 2,g2}\,\theta_A^{(2)}+\omega^{\gamma 1,g2}\Big]\\ &+\;C_{\gamma 1}\Big[\omega^{\gamma 1,g1}\,\theta_B^{(1)}+\omega^{\gamma 1,g2}\Big]+C_{\gamma 2}\Big[\omega^{\gamma 2,g2}\,\theta_B^{(2)}+\omega^{\gamma 2,g1}\Big]\,,\\ \Omega_4^{q\bar{q},\,\rm IS\times FS} &= C_{g1}\Big[\omega^{\gamma 3,g1}+\omega^{\gamma 4,g1}\Big]+\;C_{g2}\Big[\omega^{\gamma 3,g2}+\omega^{\gamma 4,g2}\Big]\\ &+\;C_{\gamma 3}\Big[\omega^{\gamma 3,g1}+\omega^{\gamma 3,g2}\Big]+C_{\gamma 4}\Big[\omega^{\gamma 4,g2}+\omega^{\gamma 4,g1}\Big]\,.\end{aligned} \tag{3.51}$$

The $\Omega_4^{q\bar{q},\,\rm IS}$ operator accounts for the emission of collinear photons and gluons by the incoming quark and anti-quark. It is important that it contains partitions that only allow for initial state singularities. For this reason this contribution is closely related to similar contributions studied earlier in the context of NNLO QCD computations. The result can be extracted from Refs. [99, 100]. After obvious modifications that account for the fact that we deal with mixed QCD-EW rather

than NNLO QCD corrections, we find [119]

$$\begin{aligned}
&\Big\langle (I-S_g)(I-S_\gamma)\,\Omega_4^{q\bar{q},\,\mathrm{IS}}\,F_{\mathrm{LM}}(1_q,2_{\bar{q}},3,4|5_g,6_\gamma)\Big\rangle = \\
&-\frac{1}{\epsilon}\sum_{i=1}^{2}\Big\langle \Big(2E_i\Big)^{-2\epsilon}\int_0^1 dz\,P_{qq}^{\mathrm{NLO}}(z,L_i)\Big\{[\alpha_s]\,C_F\,\mathcal{O}^{\gamma}_{\mathrm{nlo}}\Big[\Delta_{\gamma i}\,F^{(i)}_{\mathrm{LM}}(1_q,2_{\bar{q}},3,4|6_\gamma;z)\Big] \\
&\qquad\qquad + [\alpha]\,Q_q^2\,\mathcal{O}^{g}_{\mathrm{nlo}}\Big[\Delta_{gi}\,F^{(i)}_{\mathrm{LM}}(1_q,2_{\bar{q}},3,4|5_g;z)\Big]\Big\}\Big\rangle \\
&+[\alpha_s][\alpha]\,\frac{C_F\,Q_q^2}{\epsilon^2}\,\frac{\Gamma(1-\epsilon)\,\Gamma(1-2\epsilon)}{\Gamma(1-3\epsilon)} \\
&\qquad\times\sum_{i=1}^{2}\Big\langle\Big(2E_i\Big)^{-4\epsilon}\int_0^1 dz\,\Big[P_{qq}^{\mathrm{NLO}}\otimes P_{qq}^{\mathrm{NLO}}\Big](z,E_i)\;F^{(i)}_{\mathrm{LM}}(1_q,2_{\bar{q}},3,4;z)\Big\rangle \\
&+4\,\frac{[\alpha_s][\alpha]C_F\,Q_q^2}{\epsilon^2}\,\frac{\Gamma^2(1-\epsilon)}{\Gamma(1-2\epsilon)}\Big(2E_1\Big)^{-2\epsilon}\Big(2E_2\Big)^{-2\epsilon} \\
&\qquad\times\Big\langle\int_0^1 dz_1dz_2\,P_{qq}^{\mathrm{NLO}}(z_1,L_1)\,P_{qq}^{\mathrm{NLO}}(z_2,L_2)\,\frac{F_{\mathrm{LM}}(z_1\cdot 1,z_2\cdot 2,3,4)}{z_1z_2}\Big\rangle\,.
\end{aligned}\tag{3.52}$$

The convolution $\Big[P_{qq}^{\mathrm{NLO}}\otimes P_{qq}^{\mathrm{NLO}}\Big]$ that appears in Eq. (3.52) is defined, with a slight abuse of notation, as (see Ref. [119] for details)

$$\Big[P_{qq}^{\mathrm{NLO}}\otimes P_{qq}^{\mathrm{NLO}}\Big](z,E_i)\equiv\int_0^1 dz_1dz_2\,z_1^{-2\epsilon}\,P_{qq}^{\mathrm{NLO}}(z_1,L_i)\,P_{qq}^{\mathrm{NLO}}(z_2,L_{iz_i})\,\delta(z-z_1z_2)\,,\tag{3.53}$$

with $L_{iz_i}=\log\left(E_{\max}/(z_iE_i)\right)$ and $P_{qq}^{\mathrm{NLO}}(z_1,L_i)$ in Eq. (B.1). It arises as a result of taking two successive collinear limits on the same hard leg. The quantities $\Delta_{\gamma(g)i}$ are remnants of the partition functions and the phase-space measure in relevant collinear limits. They read

$$\Delta_{\gamma i}=\tilde{\omega}^{\gamma i,gi}_{g\|i}\,\eta_{\gamma i}^{-\epsilon}+\tilde{\omega}^{\gamma j,gi}_{g\|i}\,,\qquad \Delta_{gi}=\tilde{\omega}^{\gamma i,gi}_{\gamma\|i}\,\eta_{gi}^{-\epsilon}+\tilde{\omega}^{\gamma i,gj}_{\gamma\|i}\,,\tag{3.54}$$

where we have introduced

$$\tilde{\omega}^{\gamma i,gj}_{g\|j}\equiv C_{gj}\,\omega^{\gamma i,gj},\qquad \tilde{\omega}^{\gamma i,gj}_{\gamma\|i}\equiv C_{\gamma i}\,\omega^{\gamma i,gj}.\tag{3.55}$$

The operator $\Omega_4^{q\bar{q},\,\mathrm{IS\times FS}}$ contains partition functions that only allow for initial-final state singularities. They can be computed following steps discussed in the context of NLO computations. We find

$$\Big\langle (I-S_g)(I-S_\gamma)\Omega_4^{q\bar{q},\,\mathrm{IS\times FS}}F_{\mathrm{LM}}(1_q,2_{\bar{q}},3,4|5_g,6_\gamma)\Big\rangle =$$

$$
\begin{aligned}
&- [\alpha_s]\frac{C_F}{\epsilon}\sum_{i=1}^{2}\left\langle \mathcal{O}^{\gamma}_{\rm nlo}\left(\tilde{\omega}^{\gamma 3,gi}_{g\|i}+\tilde{\omega}^{\gamma 4,gi}_{g\|i}\right)\left(2E_i\right)^{-2\epsilon}\int_0^1 dz\, P^{\rm NLO}_{qq}(z,L_i)\, F^{(i)}_{\rm LM}(1_q,2_{\bar q},3,4|6_\gamma;z)\right\rangle\\
&+ [\alpha]\frac{Q_e^2}{\epsilon}\sum_{i=3}^{4}\left\langle \mathcal{O}^{g}_{\rm nlo}\left(\tilde{\omega}^{\gamma i,g1}_{\gamma\|i}+\tilde{\omega}^{\gamma i,g2}_{\gamma\|i}\right)\left(2E_i\right)^{-2\epsilon}P^{\rm NLO}_{qq}(L_i)\, F_{\rm LM}(1_q,2_{\bar q},3,4|5_g)\right\rangle \quad (3.56)\\
&- 2\,\frac{[\alpha_s][\alpha]C_F\,Q_e^2}{\epsilon^2}\,\frac{\Gamma^2(1-\epsilon)}{\Gamma(1-2\epsilon)}\times\\
&\qquad\times\sum_{\substack{i=1,2\\ j=3,4}}\left\langle\left(2E_i\right)^{-2\epsilon}\left(2E_j\right)^{-2\epsilon}P^{\rm NLO}_{qq}(L_j)\int_0^1 dz\, P^{\rm NLO}_{qq}(z,L_i)\, F^{(i)}_{\rm LM}(1_q,2_{\bar q},3,4;z)\right\rangle .
\end{aligned}
$$

To compute the double-real emission contribution to the partonic channel $d\hat{\sigma}^{q\bar q}_{{\rm rr},g\gamma}$ we add Eqs. (3.34,3.36, 3.47, 3.48, 3.49, 3.52, 3.56) and expand in ϵ. It is straightforward to do this since there are no *implicit* singularities left. We do not show such an intermediate result here since it is not very illuminating.

We now proceed with the calculation of real-virtual contributions. As we have anticipated earlier, these contributions are generated in two different ways, either as QCD corrections to the process $q\bar q \to \ell^-\ell^+ + \gamma$ or as electroweak corrections to the process $q\bar q \to \ell^-\ell^+ + g$. We write

$$
2s\cdot\sum_{f=g,\gamma} d\hat{\sigma}^{q\bar q}_{{\rm rv},f} = \left\langle F^{(\rm EW)}_{\rm LRV}(1_q,2_{\bar q},3,4|5_g)\right\rangle + \left\langle F^{(\rm QCD)}_{\rm LRV}(1_q,2_{\bar q},3,4|5_\gamma)\right\rangle, \qquad (3.57)
$$

where the superscript on the r.h.s. specifies whether the loop correction involves a gluon or an electroweak boson. Since gluons and photons do not interact with each other, soft limits of loop corrections are trivial. In particular, the soft structure is identical to the tree level one, i.e. $S_5\, F^{(\rm EW,QCD)}_{\rm LRV} \sim {\rm Eik}(p_5) F^{(\rm EW,QCD)}_{\rm LV}$, where ${\rm Eik}(p_5)$ schematically denotes the eikonal NLO-like factorization discussed in Section 3.2. The collinear limit can be dealt with by adapting analogous QCD results [99]. At the end, we find

$$
\begin{aligned}
2s\cdot\sum_{f=g,\gamma} d\hat{\sigma}^{q\bar q}_{{\rm rv},f} &= 2C_F\frac{[\alpha_s]}{\epsilon^2}\left(2E_{\rm max}\right)^{-2\epsilon}\left\langle \eta_{12}^{-\epsilon}\,\mathcal{F}(\eta_{12})\, F^{(\rm EW)}_{\rm LV}(1_q,2_{\bar q},3,4)\right\rangle\\
&+ 2\frac{[\alpha]}{\epsilon^2}\left(2E_{\rm max}\right)^{-2\epsilon}\sum_{j>i=1}^{4}\lambda_{ij}\,Q_iQ_j\left\langle \eta_{ij}^{-\epsilon}\,\mathcal{F}(\eta_{ij})\, F^{(\rm QCD)}_{\rm LV}(1_q,2_{\bar q},3,4)\right\rangle\\
&- C_F\,\frac{[\alpha_s]}{\epsilon}\,\frac{\Gamma^2(1-\epsilon)}{\Gamma(1-2\epsilon)}\sum_{i=1}^{2}\left(2E_i\right)^{-2\epsilon}\int_0^1 dz\, P^{\rm NLO}_{qq}(z,L_i)\left\langle F^{(i),(\rm EW)}_{\rm LV}(1_q,2_{\bar q},3,4;z)\right\rangle
\end{aligned}
$$

$$
\begin{aligned}
&+ 2C_F \, \frac{[\alpha_s][\alpha]}{\epsilon} \, \frac{\Gamma^4(1-\epsilon)\,\Gamma(1+\epsilon)}{\Gamma(1-3\epsilon)} \\
&\qquad \times \sum_{i=1}^{2} (2E_i)^{-4\epsilon} \, Q_i^2 \int_0^1 dz \, \mathcal{P}_{qq}^{\text{loop},\,RV}(z) \left\langle F_{\text{LM}}^{(i)}(1_q, 2_{\bar{q}}, 3, 4; z) \right\rangle \\
&- \frac{[\alpha]}{\epsilon} \, \frac{\Gamma^2(1-\epsilon)}{\Gamma(1-2\epsilon)} \sum_{i=1}^{2} Q_i^2 \, (2E_i)^{-2\epsilon} \int_0^1 dz \, P_{qq}^{\text{NLO}}(z, L_i) \left\langle F_{\text{LV}}^{(i),(\text{QCD})}(1_q, 2_{\bar{q}}, 3, 4; z) \right\rangle \\
&+ \frac{[\alpha]}{\epsilon} \, Q_e^2 \, \frac{\Gamma^2(1-\epsilon)}{\Gamma(1-2\epsilon)} \left\langle \sum_{i=3}^{4} (2E_i)^{-2\epsilon} \, P_{qq}^{\text{NLO}}(L_i) F_{\text{LV}}^{(\text{QCD})}(1_q, 2_{\bar{q}}, 3, 4) \right\rangle \\
&+ \langle \mathcal{O}_{\text{nlo}}^{g} \, F_{\text{LRV}}^{(\text{EW})}(1_q, 2_{\bar{q}}, 3, 4|5_g) \rangle + \langle \mathcal{O}_{\text{nlo}}^{\gamma} \, F_{\text{LRV}}^{(\text{QCD})}(1_q, 2_{\bar{q}}, 3, 4|5_\gamma) \rangle \, ,
\end{aligned}
\tag{3.58}
$$

where $\mathcal{P}_{qq}^{\text{loop},\,RV}(z)$ is defined in Eq. (B.8). In Eq. (3.58), we have used the following parametrization for the explicit infrared $1/\epsilon$ poles that are present in both QCD and electroweak virtual amplitudes

$$
\left\langle F_{\text{LRV}}^{(\text{X})}(1_q, 2_{\bar{q}}, 3, 4|5_i) \right\rangle = [\alpha_X] \left\langle I_X^{(1)} F_{\text{LM}}(1_q, 2_{\bar{q}}, 3, 4|5_i) \right\rangle + \left\langle F_{\text{LV}}^{(\text{X}),\,\text{fin}}(1_q, 2_{\bar{q}}, 3, 4|5_i) \right\rangle , \tag{3.59}
$$

where $\{X, \alpha_X, i\} = \{\text{EW}, \alpha, g\}$ for EW and $\{X, \alpha_X, i\} = \{\text{QCD}, \alpha_s, \gamma\}$ for QCD corrections. In Eq. (3.59), $F_{\text{LV}}^{(\text{X}),\,\text{fin}}$ are one-loop finite remainders, $I_{EW}^{(1)}$ is the electroweak Catani's operator given in Eq. (3.23) and $I_{QCD}^{(1)}$ is the QCD one, defined as [20]

$$
I_{QCD}^{(1)} = -2C_F \left(\frac{1}{\epsilon^2} + \frac{3}{2\epsilon} \right) \cos(\pi\epsilon) \left(\frac{\mu^2}{s_{12}} \right)^{\epsilon} . \tag{3.60}
$$

Next, we consider the double-virtual mixed QCD-electroweak corrections. Their infrared singularities can be derived by abelianizing the NNLO QCD case in Ref. [20]. In particular, we neglect all soft-correlated emissions, and abelianize the triple collinear contributions by setting $C_A \, C_F \to 0, C_F^2 \to 2C_F \, Q_q$, where the factor of two accounts for the mismatch in the symmetry factors between the γg and the gg case. We find

$$
\begin{aligned}
2s \cdot d\hat{\sigma}_{\text{vv}}^{q\bar{q}} = [\alpha_s][\alpha] &\left[I_{QCD}^{(1)} \cdot I_{EW}^{(1)} + 2C_F \, Q_q^2 \, \frac{e^{\epsilon\,\gamma_E}}{\Gamma(1-\epsilon)} \frac{1}{\epsilon} \left(\frac{\pi^2}{2} - 6\zeta_3 - \frac{3}{8} \right) \right] \\
&\times \left\langle F_{\text{LM}}(1_q, 2_{\bar{q}}, 3, 4) \right\rangle + [\alpha_s] I_{QCD}^{(1)} \left\langle F_{\text{LV}}^{(\text{EW}),\,\text{fin}}(1_q, 2_{\bar{q}}, 3, 4) \right\rangle \\
&+ [\alpha] I_{EW}^{(1)} \left\langle F_{\text{LV}}^{(\text{QCD}),\,\text{fin}}(1_q, 2_{\bar{q}}, 3, 4) \right\rangle + \left\langle F_{\text{LVV+LV}^2}^{(\text{QCD}\times\text{EW}),\,\text{fin}}(1_q, 2_{\bar{q}}, 3, 4) \right\rangle .
\end{aligned}
\tag{3.61}
$$

The quantity $F^{(\mathrm{QCD}\times\mathrm{EW}),\,\mathrm{fin}}_{\mathrm{LVV+LV^2}}$ represents the finite remainder of two- and one-loop virtual corrections to the process $q\bar{q} \to \ell^+\ell^-$. It was recently calculated in Ref. [124], and we will not discuss the computation here.

The last ingredient that we require to obtain a finite partonic cross section comes from the renormalization of parton distribution functions. The latter, in the $\overline{\mathrm{MS}}$ scheme, amounts to the following replacement

$$\begin{aligned} f_{i,\mathrm{bare}} \to \Bigg[1 + \frac{\alpha_s(\mu)}{2\pi}\frac{\bar{P}^{\mathrm{AP},0}_{ij}}{\epsilon} + \left(\frac{\alpha_s(\mu)}{2\pi}\right)^2 \Bigg[\frac{1}{2\epsilon^2}\Big(\bar{P}^{\mathrm{AP},0}_{ik} \otimes \bar{P}^{\mathrm{AP},0}_{kj} \\ - \beta_0 \bar{P}^{\mathrm{AP},0}_{ij} \Big) + \frac{1}{2\epsilon}\bar{P}^{\mathrm{AP},1}_{ij} \Bigg] + \mathcal{O}(\epsilon^3) \Bigg] \otimes f_j(\mu)\,, \end{aligned} \tag{3.62}$$

where we recall that $\bar{P}^{\mathrm{AP},0}_{ij}$ are the color stripped tree-level Altarelli Parisi splitting functions and $\bar{P}^{\mathrm{AP},1}_{ij}$ are their one loop abelianized counterpart (see Ref. [119]). We then find[4]

$$\begin{aligned} 2s \cdot d\hat{\sigma}^{q\bar{q}}_{\mathrm{pdf},g\gamma} = & -2\,\frac{\alpha}{2\pi}\frac{\alpha_s(\mu)}{2\pi}\Bigg\{ \frac{Q_q^2\,C_F}{2\epsilon^2} \times \\ & \times \sum_{i=1}^{2} \int_0^1 dz \left[\bar{P}^{\mathrm{AP},0}_{qq} \otimes \bar{P}^{\mathrm{AP},0}_{qq} \right](z) \left\langle F^{(i)}_{\mathrm{LM}}(1_q, 2_{\bar{q}}, 3, 4; z) \right\rangle \\ & + \frac{Q_q^2\,C_F}{\epsilon^2} \int_0^1 dz_1\, dz_2\, \bar{P}^{\mathrm{AP},0}_{qq}(z_1)\, \bar{P}^{\mathrm{AP},0}_{qq}(z_2) \left\langle \frac{F_{\mathrm{LM}}(z_1\cdot 1, z_2 \cdot 2, 3, 4)}{z_1\, z_2} \right\rangle \Bigg\} \\ & + \frac{2s}{\epsilon} \cdot \Bigg\{ C_F\,\frac{\alpha_s(\mu)}{2\pi}\left[\bar{P}^{\mathrm{AP},0}_{qq} \otimes d\hat{\sigma}^{q\bar{q}}_{\mathrm{nlo,EW}} + d\hat{\sigma}^{q\bar{q}}_{\mathrm{nlo,EW}} \otimes \bar{P}^{\mathrm{AP},0}_{qq} \right] \\ & \quad + Q_q^2\,\frac{\alpha}{2\pi}\left[\bar{P}^{\mathrm{AP},0}_{qq} \otimes d\hat{\sigma}^{q\bar{q}}_{\mathrm{nlo,QCD}} + d\hat{\sigma}^{q\bar{q}}_{\mathrm{nlo,QCD}} \otimes \bar{P}^{\mathrm{AP},0}_{qq} \right] \Bigg\} \\ & + \frac{\alpha}{2\pi}\frac{\alpha_s(\mu)}{2\pi}\,\frac{Q_q^2\,C_F}{\epsilon} \sum_{i=1}^{2} \int_0^1 dz\, \bar{P}^{\mathrm{AP},1}_{qq}(z) \left\langle F^{(i)}_{\mathrm{LM}}(1_q, 2_{\bar{q}}, 3, 4; z) \right\rangle\,, \end{aligned} \tag{3.63}$$

where the NLO corrections $d\hat{\sigma}^{q\bar{q}}_{\mathrm{NLO,EW/QCD}}$ have been discussed in the previous section. The explicit expressions for the various color-stripped Altarelli-Parisi splitting functions and their convolutions appearing in Eq. (3.63) can be found in Appendix B. The analytic final result for the $q\bar{q}$ initiated partonic channel will be presented in

[4] To write this equation, we anticipate that we renormalize the weak coupling on-shell, and the strong coupling in $\overline{\mathrm{MS}}$. As a consequence, the former is a constant while the latter is scale-dependent.

Chapter 5. Here we conclude by stating that when Eqs. (3.63,3.61,3.58, 3.34,3.36, 3.47, 3.48, 3.49, 3.52, 3.56) are summed, the result is free from IR singularities.

3.4 A new perspective on the NSC: towards high multiplicity processes

Let us recap what we accomplished up to this point. We presented the subtraction of infrared singularities at NNLO in the context of the nested soft-collinear subtraction scheme by applying it to a relevant process whose phenomenological implications will be described in detail in Chapter 5. The scheme has also been successfully employed to compute NNLO QCD corrections to color singlet production [100] and decays [101], deep inelastic scattering (DIS) [102], as well as vector boson fusion (VBF) processes [125] and single top quark production [126]. Since at NNLO the soft and collinear radiation pattern is almost always localized on a single leg (collinear case) or dipole-like (soft case), these processes provide most of the building blocks for extending the framework to generic processes. Yet, a fully general formulation of the NSC, valid for arbitrary processes at NNLO is still challenging.

Significant improvements have been recently made, paving the way to the treatment of higher-multiplicity processes. In this section we want to elaborate on such efforts, although for a more thorough discussion we refer the reader to Refs. [103, 127, 128].

The original formulation of the NSC, as we have seen in our previous calculation of mixed QCD-EW corrections, can be summarized into three main steps:

- the identification of the real-emission subtraction terms;
- the analytic integration of the counterterms over the unresolved phase space, leading to explicit poles in the dimensional regulator;
- the combination of such poles with the ones coming from virtual contributions and renormalization of PDFs to yield a finite result.

This *modus operandi*, when applied to more complicated processes, as the production of a vector boson in association with jets, has shown some drawbacks: the bookkeeping becomes immediately cumbersome as the number of external particles increases, due to the large number of required subtraction terms. The separate calculation of each individual subtraction term may hide a number of simplifications that can occur before explicit evaluation. Moreover, the explicit use of color conservation relations in processes involving a small number of partons, which, allows to express all color correlations in terms of Casimir operators, may facilitate the intermediate steps, but leads to non-trivial generalisations in higher multiplicity processes.

Ideally we would like to search for universal structures early-on in the calculation. Indeed, for the sake of an example, consider a NLO soft limit versus a final state NLO collinear limit. Soft and collinear limits have very different properties: the former are sensitive to the color charges of *all* the partons involved in the process and therefore lead to color correlations, but they are not sensitive to the spin of the emitting parton. On the other hand, collinear limits are only sensitive to the color charge and momentum splitting of the emitter, so they are fully localized and do not lead to color correlations. They can however lead to spin correlations. It is therefore clear that the cancellation pattern for the two cases will be different. The key idea is then to assemble subtraction terms into universal operators that share common features, and can be inferred from the infrared structure of virtual corrections, which is known in full generality and independently on the hard scattering. This task becomes non-trivial at NNLO, where the singularity structures become more and more involved, although some progress can be made. In summary, one would like to construct the integrated subtraction terms by following the steps below

- Identify all the different singular configurations sharing common features (e.g. color correlations, spin correlations etc.);
- construct suitable operators, similar to the Catani's operators already introduced for the virtual singularities, encoding explicit divergences;

- find combination of operators that yield a finite result.

In doing so, the main difficulty is the inherited "asymmetry" in the treatment of virtual and real singularities. This is due to the fact that loop singularities are explicit, i.e. showing as a result of integration over the loop momenta, whereas real emission singularities only arise at the cross section level rather than at the amplitude level. Furthermore, real emission singularities often overlap and need phase space partitioning, as we have already explained in the previous section. Let us start by the calculation at NLO, where the construction of such operators is quite simple. This will set the stage for the more involved NNLO case, which we will treat in Section. 3.4.2.

3.4.1 NLO

Let us start with NLO, and see how this reorganization of the integrated subtraction terms takes place. As an example, we consider the production of an arbitrary number of gluons in $q\bar{q}$ annihilation plus a generic color singlet X, i.e. $q\bar{q} \to N\,g + X$. As already mentioned, we want to take inspiration from the virtual singularities, encoded in the Catani operator defined in Eq. (2.31), and that we report below written in a slightly different way for convenience [103]

$$\tilde{\boldsymbol{\mathcal{I}}}_1(\epsilon) = \frac{1}{2}\sum_{i\neq j}^{N_p} \frac{\mathcal{V}_i^{\text{sing}}(\epsilon)}{\mathbf{T}_i^2}\,(\mathbf{T}_i\cdot\mathbf{T}_j)\,e^{i\pi\lambda_{ij}\epsilon}e^{\epsilon L_{ij}}\,, \quad \mathcal{V}_i^{\text{sing}}(\epsilon) = \frac{\mathbf{T}_i^2}{\epsilon^2} + \frac{\gamma_i}{\epsilon}\,, \tag{3.64}$$

where γ_i are the quark and gluon anomalous dimensions related to the ones defined in Eq. (2.34)[5], $L_{ij} = \log(\mu^2/s_{ij})$, with $s_{ij} = 2p_i\cdot p_j$, and the parameters λ_{ij} are 1 if i and j are both incoming or outgoing partons and zero otherwise. Furthermore, $N_p = N + 2$ is the total number of partons in the process. We then write the virtual contribution to the cross section as

$$2s\; d\hat{\sigma}^V = [\alpha_s]\langle I_V(\epsilon)\cdot F_{\text{LM}}\rangle + \langle F_{\text{LV}}^{\text{fin}}\rangle\,, \qquad I_V(\epsilon) = \boldsymbol{\mathcal{I}}_1(\epsilon) + \boldsymbol{\mathcal{I}}_1^{\dagger}(\epsilon)\,, \tag{3.65}$$

[5]More specifically, the anomalous dimensions used here have an opposite sign and need to be multiplied by a factor of two (as a result of expanding in $\alpha_s/2\pi$ rather than $\alpha_s/4\pi$) in order to match the ones defined in Eq. (2.34).

where, as in the previous section, $[\alpha_s] = \alpha_s(\mu)e^{\epsilon\gamma_{\rm E}}/(2\pi\,\Gamma(1-\epsilon))$, and $F_{\rm LM}$ is the LO matrix element squared (including all the relevant symmetry factors). For the real-emission contribution, we organise the integrated subtraction terms into universal operators that are as close as possible to I_V, and have a specific structure in color space. In particular, we write [103]

$$\begin{aligned} 2s\; d\hat{\sigma}^{\rm R} = {}& [\alpha_s]\langle\Big[I_{\rm S}(\epsilon) + I_{\rm C}(\epsilon)\Big]\cdot F_{\rm LM}\rangle + \frac{[\alpha_s]}{\epsilon}\Big[\langle\mathcal{P}^{\rm gen}_{qq}\otimes F_{\rm LM}\rangle + \langle F_{\rm LM}\otimes\mathcal{P}^{\rm gen}_{qq}\rangle\Big] \\ & + \sum_{i=1}^{N_p}\Big\langle(I-S_{\mathfrak{m}})(I-C_{i\mathfrak{m}})\,\omega^{\mathfrak{m}i}\Delta^{(\mathfrak{m})}F_{\rm LM}(\mathfrak{m})\Big\rangle\,. \end{aligned} \tag{3.66}$$

In Eq. (3.66), the term on the last line is fully regulated and manifestly finite. The sum in this line runs over all the resolved partons of the process. Furthermore, $\Delta^{(\mathfrak{m})}$ is a damping factor that identifies $\mathfrak{m}$ as the only potential unresolved parton, and $F_{\rm LM}(\mathfrak{m})$ is proportional to squared matrix element for the process $pp \to X + N + \mathfrak{m}$. Details on how the damping factors are constructed can be found in Ref. [103]. The operator $I_{\rm S}$ in the first term in Eq. (3.66) encodes all the singularities of soft origin. It contains explicit singularities proportional to the color-correlated structures $\boldsymbol{T}_i\cdot\boldsymbol{T}_j$. It is quite easy to identify the form of the soft operator by looking at Eq. (3.9), replacing the EW charges with the color operators, and comparing it with $I_V(\epsilon)$. The $I_{\rm C}$ operator in Eq. (3.66) starts contributing at $\mathcal{O}(\epsilon^{-1})$ and is free of color correlations. It encodes all the singularities of collinear origin that are proportional to Born-like kinematics. Furthermore, it only depends on the energies and anomalous dimensions of the external partons. Next, the contribution in square brackets in Eq. (3.66) completes the divergent collinear content of $d\hat{\sigma}^{\rm R}$, with the symbol $\otimes$ identifying the convolution of the generalized splitting functions $\mathcal{P}^{\rm gen}$, whose expression is reported in Eq. (B.12), and the squared matrix element. This term is free of color correlations and features boosted kinematics. We note that the splitting function $\mathcal{P}^{\rm gen}$ is equal (up to a sign) to the LO Altarelli-Parisi splitting function at $\mathcal{O}(\epsilon^0)$. By summing $d\hat{\sigma}^{\rm R}$ and $d\hat{\sigma}^{V}$, the following combination arises

$$\Big\langle I_{\rm T}(\epsilon)\cdot F_{\rm LM}\Big\rangle = \Big\langle\Big[I_{\rm V}(\epsilon) + I_{\rm S}(\epsilon) + I_{\rm C}(\epsilon)\Big]\cdot F_{\rm LM}\Big\rangle = \mathcal{O}\Big(\epsilon^0\Big)\,. \tag{3.67}$$

The remaining singularities given by the hard-collinear component in squared brackets in Eq. (3.66) cancel against the PDFs collinear renormalisation contribution. The final expression of the NLO partonic cross section for the process $q\bar{q} \to X + N\,g$ reads

$$\begin{aligned} 2s\, d\hat{\sigma}^{\rm NLO} = [\alpha_s]\Big\langle I_{\rm T}^{(0)} \cdot F_{\rm LM}\Big\rangle + \langle F_{\rm LV}^{\rm fin}\rangle + [\alpha_s]\Big[\Big\langle \mathcal{P}_{qq}^{\rm NLO} \otimes F_{\rm LM}\Big\rangle \\ + \Big\langle F_{\rm LM} \otimes \mathcal{P}_{qq}^{\rm NLO}\Big\rangle\Big] + \Big\langle \mathcal{O}_{\rm NLO}\, \Delta^{(\mathfrak{m})} F_{\rm LM}(\mathfrak{m})\Big\rangle\,. \end{aligned} \tag{3.68}$$

Here $I_{\rm T}^{(0)}$ is the $\mathcal{O}(\epsilon^0)$ coefficient in the expansion of $I_{\rm T}(\epsilon)$, $\mathcal{O}_{\rm NLO} = \sum_{i=1}^{N_p}(I - S_{\mathfrak{m}})(I - C_{i\mathfrak{m}})\,\omega^{\mathfrak{m}i}$ is the subtraction operator for the fully-regulated real-emission contribution, and the finite NLO splitting function $\mathcal{P}^{\rm NLO}$ is given in Eq. (B.11).

Let us compare the final formula given above with the one obtained in the specific case of EW corrections to color singlet production, i.e. Eq. (3.26). The final term of Eq. (3.68) is the fully regulated one and it is equivalent to the first term of Eq. (3.26), provided we specify the process in the case of the general formula (we will give details on how to obtain the EW case from the general case in the next paragraph). The second and third terms of the general case final formula are also equivalent to the second and third terms of the specialized EW case, again upon applying the general formula to the specific case of EW corrections to color singlet production. Let us focus instead on the last term of Eq. (3.26). It corresponds exactly to what one would obtain by taking the first term of Eq. (3.68) and applying it to the specific case of EW corrections, i.e. expanding the operator $I_{\rm T}$. Note, however, that in the "old-fashioned" approach (the one discussed in Section 3.2), by the end of the calculation, one has lost all the physical intuition on the origin of the different terms appearing in the structure $\mathcal{G}_{\rm EW}$ reported in Eq. (3.27), since all the individual terms were first evaluated and then added together. In the new approach, instead, the final formula is written in terms of fully general operators with clear physical origin (since they are written in terms of anomalous dimensions and generalised splitting functions), i.e. $I_{\rm S}, I_{\rm V}, I_{\rm C}$, so that it is clear how to generalize it to any other process one may be interested in.

Indeed, starting from Eq. (3.68), it is straightforward to obtain the NLO EW corrections to the Drell-Yan process described in Section 3.2. Indeed, it is sufficient

to perform a few simple substitutions: first, set $N_p = 2$ in the upper bound of the sum appearing in the definition of the $I_{\mathrm{T}}^{(0)}$ operator, substitute the strong coupling with the electroweak one, substitute the color charge operators with electric charge operators and abelianize the relevant splitting functions, i.e. send $C_F \to Q_q^2$. This proves the power of this more general approach, since we are able to write the final formula for the cross section in a very general and flexible way.

3.4.2 NNLO

We now move to NNLO, and the strategy will be to try to iterate these $I-$operators as much as possible. We will only give a taste of the reorganization of the subtraction terms, focusing on the color correlated structures; the complete discussion can be found in Ref. [103]. As done at NLO, we will be guided by the virtual contributions to identify corresponding IR structures in the real emission terms. We begin by analysing the double-virtual component $d\hat{\sigma}^{\mathrm{VV}}$. Following Refs [20, 21, 129], we write

$$\begin{aligned} d\hat{\sigma}^{\mathrm{VV}} = {} & [\alpha_s]^2 \left\langle \left[\frac{1}{2} I_{\mathrm{V}}^2(\epsilon) - \frac{\Gamma(1-\epsilon)}{e^{\epsilon\gamma_{\mathrm{E}}}} \left(\frac{\beta_0}{\epsilon} I_{\mathrm{V}}(\epsilon) - \left(\frac{\beta_0}{\epsilon} + K \right) I_{\mathrm{V}}(2\epsilon) \right) \right] \cdot F_{\mathrm{LM}} \right\rangle \\ & + [\alpha_s]^2 \left\langle \left[-\frac{1}{2} \left[\tilde{\boldsymbol{\mathcal{I}}}_1(\epsilon), \tilde{\boldsymbol{\mathcal{I}}}_1{}^{\dagger}(\epsilon) \right] + \mathcal{H}_{2,\mathrm{tc}} + \mathcal{H}_{2,\mathrm{tc}}^{\dagger} + \mathcal{H}_{2,\mathrm{cd}} + \mathcal{H}_{2,\mathrm{cd}}^{\dagger} \right] \cdot F_{\mathrm{LM}} \right\rangle \\ & + [\alpha_s] \left\langle I_{\mathrm{V}}(\epsilon) \cdot F_{\mathrm{LV}}^{\mathrm{fin}} \right\rangle + \left\langle F_{\mathrm{LV}^2}^{\mathrm{fin}} \right\rangle + \left\langle F_{\mathrm{VV}}^{\mathrm{fin}} \right\rangle . \end{aligned} \tag{3.69}$$

In Eq. (3.69), K is a constant, and $F_{\mathrm{LV}^2}^{\mathrm{fin}}$, $F_{\mathrm{VV}}^{\mathrm{fin}}$ are the finite remainders of the NNLO matrix element squared. The two quantities $\mathcal{H}_{2,\mathrm{tc}}^{\dagger}$ and $\mathcal{H}_{2,\mathrm{cd}}^{\dagger}$ are triple color-correlated and color-diagonal contributions respectively, and were explicitly computed in Refs. [21, 129]. In the expression of $d\hat{\sigma}^{\mathrm{VV}}$ four different color structures appear:

- *color-uncorrelated* terms, arising for instance from $\mathcal{H}_{2,\mathrm{cd}} + \mathcal{H}_{2,\mathrm{cd}}^{\dagger} \sim I$;
- *color-correlated* terms, arising from $I_{\mathrm{V}} \sim \boldsymbol{T}_i \cdot \boldsymbol{T}_j$;
- *quartic color-correlated* terms, arising from $I_{\mathrm{V}}^2 \sim (\boldsymbol{T}_i \cdot \boldsymbol{T}_j)(\boldsymbol{T}_k \cdot \boldsymbol{T}_l)$;
- *triple color-correlated* terms, arising from $[\overline{I}_1, \overline{I}_1^{\dagger}]$ and $\mathcal{H}_{2,\mathrm{tc}} + \mathcal{H}_{2,\mathrm{tc}}^{\dagger} \sim f_{abc} T_k^a T_i^b T_j^c$.

Each of the structures listed above has to cancel independently. Here, we only give some comments regarding the cancellation of these structure, although we will not give any proof, and refer to Ref. [103] for a detailed discussion of their cancellation.

We first focus on terms proportional to $(\boldsymbol{T}_i \cdot \boldsymbol{T}_j)(\boldsymbol{T}_k \cdot \boldsymbol{T}_l)$. They arise from the first term in Eq. (3.69). Other terms that lead to similar color structures stem from the factorised contribution to the double-soft limit of the double-real matrix element squared. This contribution is indeed proportional to the product of two independent NLO-like soft currents, which, upon integration over the relevant phase space, returns $I_{\rm S}^2$. Moreover, the soft limit of the real-virtual correction yields the product of a soft current and a color-correlated, one-loop matrix element interfered with the LO one. This results in the product of Catani's operators and $I_{\rm S}$, and suggests that NNLO double color-correlated contributions can be rearranged in terms of the operator $I_{\rm T}$ found at NLO (see Eq. (3.67)). Such rearrangement would automatically guarantee that double color-correlated poles vanish. Indeed, as mentioned, $I_{\rm T}$ is of $\mathcal{O}(\epsilon^0)$. Since the definition of $I_{\rm T}$ involves also the collinear operator $I_{\rm C}$, it is crucial to identify it (and its combinations with $I_{\rm V}$ and $I_{\rm S}$) among the subtraction terms stemming from the double-real and the real-virtual limits. We find the following terms [127]

$$d\hat{\sigma}^{\rm VV} \supset Y_{\rm VV} = \frac{1}{2}\Big\langle I_{\rm V}^2 \cdot F_{\rm LM}\Big\rangle\,, \qquad d\hat{\sigma}^{\rm RR} \supset Y_{\rm RR}^{\rm (ss)} = \frac{1}{2}\Big\langle I_{\rm S}^2 \cdot F_{\rm LM}\Big\rangle\,, \tag{3.70}$$

$$d\hat{\sigma}^{\rm RR} \supset Y_{\rm RR}^{\rm (shc)} = \Big\langle I_{\rm S}\, I_{\rm C} \cdot F_{\rm LM}\Big\rangle\,, \qquad d\hat{\sigma}^{\rm RR} \supset Y_{\rm RR}^{\rm (cc)} = \frac{1}{2}\Big\langle I_{\rm C}^2 \cdot F_{\rm LM}\Big\rangle\,, \tag{3.71}$$

$$d\hat{\sigma}^{\rm RV} \supset Y_{\rm RV}^{\rm (s)} = \frac{1}{2}\Big\langle \Big[I_{\rm V}\, I_{\rm S} + I_{\rm S}\, I_{\rm V}\Big] \cdot F_{\rm LM}\Big\rangle\,, \quad d\hat{\sigma}^{\rm RV} \supset Y_{\rm RV}^{\rm (shc)} = \Big\langle I_{\rm V}\, I_{\rm C} \cdot F_{\rm LM}\Big\rangle\,, \tag{3.72}$$

where the subscript shc stands for "soft hard-collinear", s for "soft", ss for double soft and cc for "double collinear". Once combined, these objects return

$$Y = \frac{1}{2}\Big\langle \Big[I_{\rm V} + I_{\rm S} + I_{\rm C}\Big]^2 \cdot F_{\rm LM}\Big\rangle = \frac{1}{2}\Big\langle I_{\rm T}^2 \cdot F_{\rm LM}\Big\rangle\,. \tag{3.73}$$

Eq. (3.73) is precisely the square of the structure found at NLO (see Eq. (3.67)) and collects all the double color-correlated contributions into the operator $I_{\rm T}^2$, which is finite in ϵ by construction.

In order to extract the $Y_{\rm VV,RV,RR}$ functions as in Eqs (3.70)-(3.72), we have systematically expressed the double-virtual contribution and the soft limit of the real-virtual correction through the $I_{\rm V}$ operator, instead of $\overline{I}_1$ and $\overline{I}_1^\dagger$. In doing so, we obtain various commutators of the operators $\tilde{\boldsymbol{\mathcal{I}}}_1$, $\tilde{\boldsymbol{\mathcal{I}}}_1{}^\dagger$ and $I_{\rm S}$. These "remnants" give rise to different color structures, namely to triple color-correlated contributions proportional to $\langle\mathcal{M}_0|\, f_{abc}T_k^aT_i^bT_j^c\,|\mathcal{M}_0\rangle$. Such terms have to cancel against other sources of triple-color correlations, i.e. the operator $\mathcal{H}_{2,\rm tc}+\mathcal{H}_{2,\rm tc}^\dagger$ in the second line of Eq. (3.69). Interestingly, explicit triple-color correlations also arise from the non-factorised component of the soft limit of the real-virtual correction, provided that we have a large enough number of partons involved in the process ($N_p\geq 4$). The integration of this term over the unresolved phase space is non-trivial, and it has been computed using Mellin-Barnes techniques. We report the computation in Appendix E. We label the resulting integrated counterterm as $I_{\rm tri}^{\rm RV}$. Combining all the relevant terms, we find

$$\Sigma_N^{\rm tri}=[\alpha_s]^2\,\left\langle\left(I_{\rm tri}^{\rm RV}+I_{\rm tri}^{\rm (cc)}\right)\cdot F_{\rm LM}\right\rangle\,, \tag{3.74}$$

where $I_{\rm tri}^{\rm (cc)}$ is defined as

$$\begin{aligned} I_{\rm tri}^{\rm (cc)}&=-\left[I_+,I_-\right]+\left[2I_++I_{\rm S},I_-\right]+\mathcal{H}_{2,\rm tc}+\mathcal{H}_{2,\rm tc}^\dagger\,,\\ I_\pm(\epsilon)&=1/2\left(\tilde{\boldsymbol{\mathcal{I}}}_1(\epsilon)\pm\tilde{\boldsymbol{\mathcal{I}}}_1{}^\dagger(\epsilon)\right). \end{aligned} \tag{3.75}$$

To proceed, we need to compute the commutators of the various I-operators that appear in Eq. (3.75). Once all the technical details have been sorted out (see Ref. [103]), we obtain

$$\begin{aligned} I_{\rm tri}^{\rm (cc)}(\epsilon)=\frac{\pi}{2}\sum_{(ijk)}^{N_p} f_{abc}\,T_k^a\,T_i^b\,T_j^c\Bigg[&\frac{2L_{kj}\,\lambda_{ij}}{\epsilon^2}-\frac{4\phi_{jk}\lambda_{ij}}{\epsilon}\\ &+\left(\delta_{ij}^-+\delta_{ji}^-\right)\left(\delta_{kj}^++\delta_{jk}^+-2\phi_{jk}\right)\Bigg]+\mathcal{O}(\epsilon)\,, \end{aligned} \tag{3.76}$$

where $F^{(kij)}=f_{abc}\,T_k^a\,T_i^b\,T_j^c$ and

$$\begin{aligned} \delta_{ij}^+&=\frac{1}{2}L_{ij}^2+\frac{\gamma_i}{\boldsymbol{T}_i^2}\,L_{ij}-\frac{1}{2}\pi^2\lambda_{ij}^2\,,\qquad \delta_{ij}^-=\frac{\gamma_i}{\boldsymbol{T}_i^2}\,\lambda_{ij}+L_{ij}\,\lambda_{ij}\,,\\ \phi_{ij}&=-2\log\left(\frac{2E_{\rm max}}{\mu}\right)\log(\eta_{ij})-\frac{1}{2}\log^2(\eta_{ij})-{\rm Li}_2(1-\eta_{ij})\,. \end{aligned} \tag{3.77}$$

First, we notice that for a process with only outgoing (or only incoming) partons, we have $\lambda_{ij} = 1$ for all i, j and hence the triple color-correlated poles in Eq. (3.76) vanish, due to the contraction of the antisymmetric tensor $F^{(kij)}$ with the symmetric functions L_{kj} and ϕ_{jk}. Similarly, the ϵ-poles in $I^{\mathrm{RV}}_{\mathrm{tri}}$ also vanish if all resolved partons are in the final state. If both incoming and outgoing partons are present, it is convenient to write λ_{ij} in the following way

$$\lambda_{ij} = 1 - \delta_{i1} - \delta_{i2} - \delta_{j1} - \delta_{j2} + 2\delta_{i1}\,\delta_{j2} + 2\delta_{i2}\,\delta_{j1}\,, \tag{3.78}$$

where 1 and 2 label the initial-state partons. Using this representation we obtain

$$\begin{aligned} I^{(\mathrm{cc})}_{\mathrm{tri}} = \sum_{k\neq 1,2}^{N_p} F^{(k12)} \Bigg[&- \frac{2\pi}{\epsilon^2} \log\left(\frac{\eta_{2k}}{\eta_{1k}}\right) - \frac{2\pi}{\epsilon}\left(2\log\left(\frac{4E^2_{\max}}{\mu^2}\right)\log\left(\frac{\eta_{1k}}{\eta_{2k}}\right)\right. \\ &\left. + \log^2\eta_{1k} - \log^2\eta_{2k} + 2\,\mathrm{Li}(1-\eta_{1k}) - 2\,\mathrm{Li}(1-\eta_{2k})\right)\Bigg] + \mathcal{O}\Big(\epsilon^0\Big)\,. \end{aligned} \tag{3.79}$$

Comparing this result with the expression for $I^{\mathrm{RV}}_{\mathrm{tri}}$ in Eq. (H.15) of Ref. [103], we find that Eq. (3.74) is finite, and therefore all the triple color-correlated objects contributing to $d\hat{\sigma}^{\mathrm{NNLO}}$ are of $\mathcal{O}(\epsilon^0)$.

We stress that the issue of triple-color correlation is due to the non-abelian nature of QCD: the NNLO correction cannot be reduced to a double copy of the NLO case, as it would be in QED, or in the case of mixed QCD-EW corrections that we discussed in Section 3.3. Furthermore, Eq. (3.69) contains also color-uncorrelated terms that are diagonal in color space, and that can be written as combinations of Casimir operators of external partons. They have to be combined with the hard-collinear contributions contained within $d\hat{\sigma}^{\mathrm{RV}}$, $d\hat{\sigma}^{\mathrm{RR}}$ and $d\hat{\sigma}^{\mathrm{pdf}}$. The computation of these objects is conceptually simple but tedious (see Sec. 5 of Ref. [103]). What is worth underlining, however, is that even for these color-uncorrelated contributions it is possible to show the analytic cancellation of the poles for the production of an arbitrary number of gluons in $q\bar{q}$ annihilation. This is the first important step towards the generalization of the NSC scheme to arbitrary processes.

This chapter ends the "Craft" part of this thesis, since we have now briefly covered all the necessary theoretical tools needed to describe the hard process

of a high-energy scattering. The next two chapters are devoted to two different interesting processes where radiative corrections play an important role. More specifically, in Chapter 4 we will study interference effects in Higgs physics and we will see how one can use them to constrain the Higgs boson decay width. For this study, a simplified approach to a NNLO calculation will give us reliable results. In Chapter 5, instead, we will study dilepton production at the LHC in the high invariant mass region and in that case we will argue that the more sophisticated tools learnt so far will become crucial. Let the Art begin.

4

Bounding the Higgs width at the LHC

Contents

4.1 Motivation 95
4.2 Interference effects in $H \to \gamma\gamma$ 99
4.2.1 Theoretical background 99
4.2.2 Higher-order QCD calculation and results 104
4.3 Interference effects in $H \to Z\gamma$ 118
4.3.1 The $gg \to Z\gamma$ process 119
4.3.2 Interference effects at NLO QCD 122

4.1 Motivation

About two years ago we celebrated the tenth-year anniversary of the Higgs boson discovery at the CERN LHC [2, 3]. Since then, enormous efforts both from the theory and the experimental communities have been devoted to a precise determination of the Higgs boson properties such as its mass, decay width and couplings to other SM particles as part of the LHC precision physics program. Indeed, an in-depth exploration of the Higgs sector is one of the main goals of the current and future LHC runs [130].

The predominant mechanism of Higgs boson production at the LHC is gluon

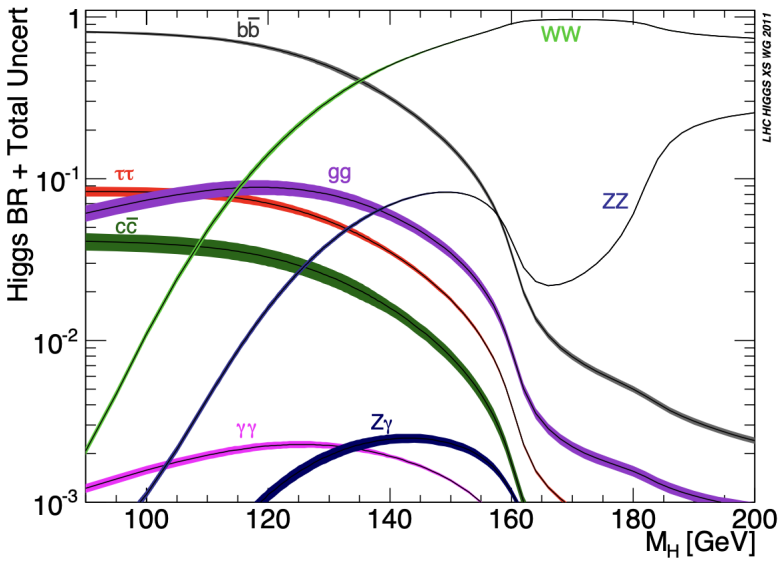


Figure 4.1: Higgs branching ratios [131]

fusion, as we mentioned in Chapter 1. The Higgs boson is an unstable particle, with a lifetime of $\mathcal{O}(10^{-22})s$, and it decays to both SM fermions and bosons. The Higgs branching ratios are reported in Figure 4.1. The $H \to \gamma\gamma$ and $H \to ZZ^* \to 4l$ decay channels, despite having small branching ratios, provide a very clean environment for the study of Higgs-boson properties. Measurements in the diphoton channel allowed for a determination of the Higgs boson mass with an uncertainty of 140 MeV [132]. The ZZ channel also allows for a precise determination, thanks to a very good experimental control on the final-state leptons. Indeed, in this channel the Higgs boson mass has been measured with an accuracy of about 180 MeV [133], mostly dominated by statistics. Combining the two channels leads to an uncertainty of about 110 MeV [134].

Measuring the Higgs boson total decay width Γ_H is more elusive, because of the extremely narrow nature of the Higgs resonance. Indeed, the predicted SM value of roughly 4 MeV has to be confronted with an experimental sensitivity of the order of $1 - 2$ GeV [135, 136]. Therefore, one has to resort to indirect analysis to extract bounds on the Higgs boson width. One option is to perform a global fit of SM parameters, e.g. within the context of the Standard Model Effective theory [137–139]. However, it has also been pointed out in the literature that one can

harness the sensitivity of specific observables on the Higgs width to constrain the latter. One proposal is to exploit the peculiarities of the off-shell Higgs cross-section in the four-lepton channel [140–142], which allows one to probe values of Γ_H as small as the SM one [143, 144]. However, such a technique relies on some underlying theoretical assumptions, see e.g. Refs [145–147].[1] Another proposal is to exploit signal-background interference effects in the diphoton channel [149, 150]. Such effects are expected to shift the Higgs invariant mass distribution peak by a value that depends on the Higgs boson width. In the SM, the shift turns out to be quite small. Initial theoretical analyses estimated it to be of about $50-100$ MeV [150, 151]. A more robust estimate that took into account realistic experimental conditions was conducted by the ATLAS collaboration who found a somewhat smaller mass-shift of about 40 MeV [152]. The predicted experimental sensitivity on the mass-shift at the LHC is of about few hundreds MeV [136, 153], which translates to an upper bound on the Higgs width of about $5-30$ times the SM value [150, 151, 154, 155]. While such bounds are not as constraining as the ones obtained from the off-shell method, they do not suffer from the same model dependence and as such they provide important complementary information.

For a reliable extraction of the Higgs boson width from the mass-shift, one needs a good theoretical control on the latter. The preliminary LO studies of Ref. [149], which considered the dominant $gg \to \gamma\gamma$ channel, showed that the apparent mass-shift could be of $\mathcal{O}(100-200)$ MeV for typical collider energies and setup. This LO analysis was later refined in Ref. [151] via the inclusion of $q(\bar{q})g$ and $q\bar{q}$ initiated processes, which account for a shift of $\mathcal{O}(30)$ MeV, carrying an opposite sign with respect to the gg case. The impact of higher-order QCD correction was soon after addressed in Ref. [150], which also explicitly noted that a measurement of the mass-shift could be used to put indirect bounds on Γ_H. The results of Ref. [150] were later confirmed in Ref. [155]. Additionally, the impact of small-p_T resummation [154] and extra hard QCD radiation [156] on the mass-shift were also studied. One of the main outcome of Ref. [150], is that NLO QCD corrections account for a large $\mathcal{O}(40\%)$

[1] The model-dependence of this approach can be alleviated by combining results in the gluon fusion and VBF channels [148].

effect on the mass shift, hence highlighting the relevance of higher-order corrections. Furthermore, the bulk of the effect comes from the low $p_{T,\gamma\gamma}$ region [150, 156, 157].

In this thesis we want to present an improvement on the current predictions for the mass-shift and extend the analysis beyond NLO QCD. For a long time, this was prevented by the lack of the relevant multi-loop amplitudes for the $gg \to \gamma\gamma$ continuum production. This bottleneck has recently been removed thanks to the latest advances in the calculation of QCD scattering amplitudes. In particular, the three-loop helicity amplitudes for $gg \to \gamma\gamma$ [158], as well as the two-loop ones for $\gamma\gamma + j$ production [57, 159] were recently computed. In principle, this – together with the well-known analogous results for the $gg \to H \to \gamma\gamma$ signal – allows for a complete NNLO evaluation of the signal-background interference and hence the mass-shift. In practice however, such an endeavour is non trivial as it requires the evaluation of two-loop 5-point scattering amplitudes in soft-collinear regions, as well as a very good numerical control on the latter. Here we want to present a first step towards the full NNLO calculation and work in the so-called *soft-virtual* approximation. Within this approximation, one retains the full information of virtual corrections and soft real emissions, but neglects the impact of hard radiation. Since the bulk of the interference is dominated by the region where the $\gamma\gamma$ pair has a low transverse momentum [150, 156, 157], we expect this approximation to work quite well in this case.

In this chapter, we will elaborate on these concepts and present results for the interference effects in $H \to \gamma\gamma$. Then, we will perform a similar analysis for the more rare $H \to Z\gamma$ decay. These two analyses here are based on the publications [160] and [161] respectively. The latter is motivated by the recent announcement by the ATLAS and CMS collaborations at CERN of evidence for this rare decay [162]. In this publication they present a signal yield of $\mu = 2.2 \pm 0.7$ times the SM expectation. Although the statistics is still low, it is interesting to gain better control on the SM prediction by including the interference effects with the background process $gg \to Z\gamma$.

4.2 Interference effects in $H \to \gamma\gamma$

4.2.1 Theoretical background

In this section, we briefly review the main aspects of signal-background interference for Higgs-mediated diphoton production at the LHC. For the sake of illustration, we discuss the main features of the interference at LO, focusing on the gluon-fusion channel. The higher order analysis will be presented in Section 4.2.2.

We consider diphoton production at the LHC in the gluon-fusion channel. At order α_s^2 in the SM two main mechanisms contribute: the Higgs-mediated process $gg \to H \to \gamma\gamma$ and the continuum process $gg \to \gamma\gamma$. We refer to the former as our "signal" and to the latter as our "background". Schematically, we write the scattering amplitude for this process as

$$\mathcal{M}_{gg\to\gamma\gamma} = \frac{\mathcal{M}_{\rm sig}}{m_{\gamma\gamma}^2 - m_H^2 + i\Gamma_H m_H} + \mathcal{M}_{\rm bkg}, \tag{4.1}$$

where $m_{\gamma\gamma}$ is the diphoton invariant mass and where we have explicitly factored out the Higgs-boson propagator. In order to improve readability, we dropped helicity labels, which are understood. It is helpful to further separate the real and imaginary parts of $\mathcal{M}_{\rm sig,bkg}$, i.e.

$$\mathcal{M}_{\rm sig,bkg} = {\rm Re}\mathcal{M}_{\rm sig,bkg} + i\,{\rm Im}\mathcal{M}_{\rm sig,bkg}\,. \tag{4.2}$$

Since we will be ultimately interested in the diphoton invariant-mass distribution, we need to consider the square of the amplitude in Eq. (4.1), which reads

$$\begin{aligned}|\mathcal{M}_{gg\to\gamma\gamma}|^2 = &\frac{|\mathcal{M}_{\rm sig}|^2}{\left(m_{\gamma\gamma}^2 - m_H^2\right)^2 + \Gamma_H^2 m_H^2} + |\mathcal{M}_{\rm bkg}|^2 \\ &+ 2\,{\rm Re}\left(\frac{\mathcal{M}_{\rm sig}}{m_{\gamma\gamma}^2 - m_H^2 + i\Gamma_H m_H}\mathcal{M}_{\rm bkg}^\dagger\right).\end{aligned} \tag{4.3}$$

The invariant-mass distribution can then be schematically organised as follows

$$\frac{d\sigma}{dm_{\gamma\gamma}} \sim |S|^2 + |B|^2 + I\,, \tag{4.4}$$

where the three terms S, B and I are in one-to-one correspondence with those on the right-hand side of Eq. (4.3). The signal-background interference part is

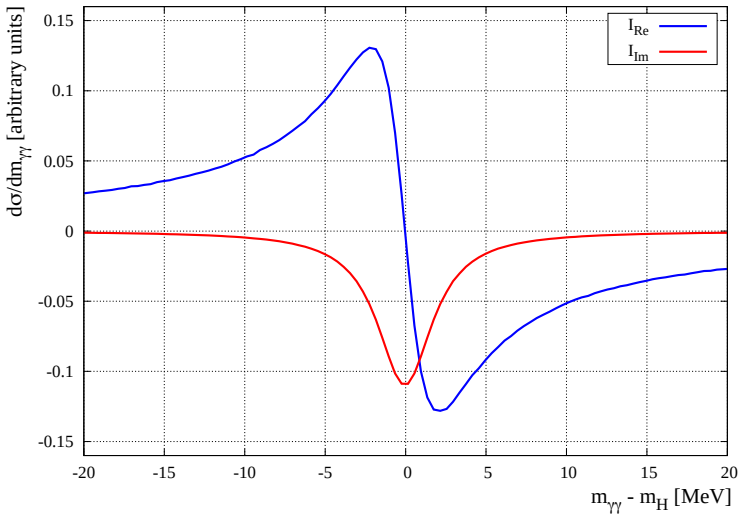


Figure 4.2: Real and imaginary parts of the signal-background interference terms, see text for details. This figure is just for illustration purposes. Our best prediction for these curves will be described in details in Sec. 4.2.2.

the last one in the equation above. One can get insight on the structure of the interference contribution by further separating it into a so-called "real part" $I_{\rm Re}$ and an "imaginary part" $I_{\rm Im}$ [163], i.e. $I = I_{\rm Re} + I_{\rm Im}$. These two components can be expressed through the actual real and imaginary parts of the amplitudes in Eq. (4.2) and are given by

$$I_{\rm Re} \propto \frac{2}{(m_{\gamma\gamma}^2 - m_H^2)^2 + \Gamma_H^2 m_H^2} \left(m_{\gamma\gamma}^2 - m_H^2\right) \times \\ \times \left[{\rm Re}\mathcal{M}_{\rm bkg}{\rm Re}\mathcal{M}_{\rm sig} + {\rm Im}\mathcal{M}_{\rm bkg}{\rm Im}\mathcal{M}_{\rm sig}\right], \tag{4.5}$$

$$I_{\rm Im} \propto \frac{2}{(m_{\gamma\gamma}^2 - m_H^2)^2 + \Gamma_H^2 m_H^2} \Gamma_H m_H \times \\ \times \left[{\rm Re}\mathcal{M}_{\rm bkg}{\rm Im}\mathcal{M}_{\rm sig} - {\rm Im}\mathcal{M}_{\rm bkg}{\rm Re}\mathcal{M}_{\rm sig}\right]. \tag{4.6}$$

It is clear from these equations that the real part of the interference is an antisymmetric function of the diphoton invariant mass $m_{\gamma\gamma}^2$ around the Higgs resonance, and therefore does not contribute to the total cross-section. This is not the case for the imaginary part, which is instead symmetric around the resonance. This is illustrated in Fig. 4.2, where we plot $I_{\rm Re}$ and $I_{\rm Im}$ in the gg channel up to NLO.

Naively, one may think that the relative impact of the interference on the Higgs total cross section could be quite sizeable, since the signal is a two-loop process

while the background starts at one loop. Because of this, one may expect a loop-enhancement factor of the interference with respect to the signal. However, a close inspection of Eq. (4.6) shows that the contribution to $I_{\rm Im}$ from the imaginary part of the background is strongly suppressed at leading order. This follows from the fact that the Higgs boson, being a scalar, only decays into a pair of photons with identical helicity. In turn, if the photons have equal helicities the imaginary part of the background at leading order vanishes, unless the process is mediated by a massive light quark. In our calculation we keep full dependence on the bottom quark at leading order but, since its contribution is mass-suppressed, the net effect is small and can be safely neglected at higher orders. Starting from two loops, the relevant background helicity amplitudes develop an imaginary part. This leads to $I_{\rm Im}$ having a destructive impact of around 1-2% [155, 164]. As far as the real part is concerned, there is no mass suppression at LO. Although such effect does not contribute to the total cross section, c.f. Eq. (4.6), it leads to a non-negligible shift of events around the diphoton invariant-mass peak, as was first noted in Ref. [149].

Moreover, it was observed in Ref. [150] that the integrated interference I has a different dependence on the Higgs boson production and decay couplings compared to the integrated signal. Specifically, if we schematically denote with λ_g and λ_γ the Higgs couplings to gluons and photons, we find that the signal is proportional to $\lambda_g^2\lambda_\gamma^2/\Gamma_H$, while the interference is only proportional to $\lambda_g\lambda_\gamma$. The main idea of Ref. [150] is to exploit this intertwined dependence on the Higgs boson couplings and its decay rate to extract information on Γ_H and to look for possible deviations from its SM value. Current experimental measurements constrain the Higgs-diphoton rate to be consistent with the SM prediction to within 10% [165–167]. At this level of accuracy, one can neglect the small impact of the destructive interference $I_{\rm Im}$ on the cross section. One then schematically writes this experimental observation as

$$\frac{\lambda_g^2\lambda_\gamma^2}{\Gamma_H} \approx \frac{\lambda_{g,\rm SM}^2\lambda_{\gamma,\rm SM}^2}{\Gamma_{H,\rm SM}}, \tag{4.7}$$

where λ_i, Γ_H are the "true" Higgs-boson couplings and width and $\lambda_{i,\rm SM}$, $\Gamma_{H,\rm SM}$ are their respective SM predictions. Eq. (4.7) holds in particular under appropriate

rescalings of $\lambda_{i,\mathrm{SM}}$ and $\Gamma_{H,\mathrm{SM}}$, e.g. $\lambda_i \to \kappa\lambda_{i,\mathrm{SM}}$ and $\Gamma_H \to \kappa^4\Gamma_{H,\mathrm{SM}}$, so it does not allow for a simultaneous direct extraction of couplings and width. However, if one supplements Eq. (4.7) with the observation that $I_{\mathrm{Re}} \propto \lambda_g\lambda_\gamma$, then one obtains

$$\frac{I_{\mathrm{Re}}}{I_{\mathrm{Re,SM}}} \propto \sqrt{\frac{\Gamma_H}{\Gamma_{H,\mathrm{SM}}}}. \tag{4.8}$$

Hence, a measurement of I_{Re} allows for an extraction of Γ_H, provided that the SM prediction $I_{\mathrm{Re,SM}}$ is under good theoretical and experimental control.

As mentioned before, the main effect of I_{Re} is to distort the Higgs invariant-mass distribution, effectively shifting the position of the peak. This translates into an apparent mass-shift with respect to the SM value [149]. A measurement of the mass-shift can then be used to constrain Γ_H, by e.g. comparing the measurement with the $4-$lepton Higgs decay channel, where the effect is supposed to very small (due, roughly speaking, to a *loop enhancement* present in the diphoton decay channel with respect to the 4-lepton case[2]). We now argue on how to extract the mass shift from the knowledge of the invariant mass distribution.

One first remark is that the Higgs resonance is extremely narrow, and therefore strongly smeared by the finite detector resolution. To properly take this into account, one should convolve theoretical prediction with a full detector simulation. However, such a study can only be carried out by experimental collaborations and it is outside the scope of this theoretical work. In this thesis we present an estimate of the mass-shift using two different, yet related, proxies for it that have been presented in the literature. Namely, we will consider the first moment of the diphoton invariant-mass distribution [149] and a full gaussian fit to it [150].

Before reviewing these techniques, we stress that they are inherently different, so one should not expect identical results for the mass shift. In other words, we can think of these procedures as a measurement of an observable that is strongly correlated, yet not identical, to the mass shift that experimentalists would measure.

[2]The interference is sensitive to the background to signal ratio, and the signal diagram in the diphoton channel is a two-loop diagram, whereas in the 4-lepton case it is a one loop diagram. In both cases, the background is a one loop diagram. Therefore the background over signal ratio, which controls the impact of the interference, is much smaller in the 4-lepton case. As a consequence, interference effects in the 4-lepton channel are entirely negligible.

Nevertheless, we may imagine that they capture similar physics, and hence they should receive comparable radiative corrections. In Section 4.2.2, we will see that this is indeed the case. This gives us confidence that, even if our theoretical predictions for the absolute values of the mass shift are inherently limited by our experimental modeling, our results for the QCD K-factors are quite robust.

We now describe the two methods in some detail. In both cases, we simulate detector effects by smearing the diphoton invariant-mass distribution using a Gaussian function with $\sigma = 1.7$ GeV [152]. The first-moment method [149] is based on the observation that, from the theoretical side, a very simple way to access the mass shift is to consider the first moment of the invariant-mass distribution, i.e.

$$\langle m_{\gamma\gamma} \rangle = \frac{1}{\sigma_{gg\to\gamma\gamma}} \int dm_{\gamma\gamma} m_{\gamma\gamma} \frac{d\sigma_{gg\to\gamma\gamma}}{dm_{\gamma\gamma}} \tag{4.9}$$

where $\sigma_{gg\to\gamma\gamma}$ is the fiducial cross-section. The mass shift is then defined as

$$\Delta m_{\gamma\gamma} = \langle m_{\gamma\gamma} \rangle_{\text{sig+int}} - \langle m_{\gamma\gamma} \rangle_{\text{sig}}. \tag{4.10}$$

The main advantage of this method is that it is theoretically very clean. Also, it is not very sensitive to overall normalisation issues, but rather focuses on the position of the peak. On the practical level however, it requires exquisite resolution on the invariant mass distribution which is very hard to achieve experimentally. It also strongly depends on the technical details of the theoretical analysis. For example, in Ref. [149] the author found that the mass-shift strongly depends on the choice of the upper and lower integration boundaries in Eq. (4.9). Indeed, a change of $\mathcal{O}(1\,\text{GeV})$ in such choice modifies the mass-shift estimate by almost 20% at leading order.

A different proposal that addresses at least some of the shortcomings of the first-moment method is to simply perform a Gaussian fit of the diphoton invariant mass distribution [150]. One then extracts the mass shift by comparing predictions obtained with and without including interference effects. It was argued in Ref. [150] that this method is more resilient against specific details of analysis with respect to the first-moment one.

These two methods predict a mass-shift of $\mathcal{O}(100)$ MeV at LO. More precisely, the first-moment technique gives results in the interval $\Delta m_{\gamma\gamma} \in \{-250, -150\}$ MeV depending on the integration window in Eq. (4.9) [149]. The likelihood fit of Ref. [150] instead predicts $\Delta m_{\gamma\gamma} = -120$ MeV. As we have stressed before, these two methods measure correlated yet slightly different observables, so one should not expect identical results.

4.2.2 Higher-order QCD calculation and results

We now discuss higher-order corrections to the interference. We start by describing LO predictions. At order α_s^2, we need to consider three different partonic channels, see Fig. 4.3 (top). We then write

$$\text{LO} = \text{LO}(\text{gg}) + \text{LO}(\text{qg}) + \text{LO}(\text{q}\bar{\text{q}})\,. \tag{4.11}$$

At this order, we compute the signal retaining the full top- and bottom- mass dependence. For the background, we neglect top-mediated contributions, since they are heavily suppressed. As we have explained in Section 4.2.1, the bottom-quark contributions are the only ones leading to a non-vanishing I_{Im} at this order [3]. We find the latter effect to be very small, so we neglect it at higher orders. Also, when computing (N)NLO corrections we consider Higgs production in the heavy-top effective theory, described by the Lagrangian in Eq. (1.78).

At higher-orders, we still treat the Higgs decay to photons at LO, with exact mass dependence. The explicit form of the Higgs decay amplitude, considering both quark and W-boson loops contributions, reads

$$\mathcal{A}_{H\gamma\gamma} = -\frac{\alpha_{em}}{4\pi v} m_{\gamma\gamma}^2 \Big[I_W\left(\frac{m_W^2}{m_{\gamma\gamma}^2}\right) + \sum_{q=b,t} N_c Q_q^2 I_q\left(\frac{m_q^2}{m_{\gamma\gamma}^2}\right) \Big]\,, \tag{4.12}$$

[3] Let us stress once again that the main reason for retaining the exact bottom-mass dependence at LO is to generate an imaginary part that would not be present otherwise. Beyond one-loop, the massless amplitude also develops an imaginary part so bottom-mass effects are subleading and can be safely discarded.

where Q_q^2 is the quark electric charge in units of the proton charge and

$$\begin{aligned} I_W(x) &= -2[6x+1+6x(2x-1)F(x)]\,, \quad I_q(x) = 4x[2+(4x-1)F(x)]\,, \\ F(x) &= \theta(1-4x)\frac{1}{2}\Big[\log\left(\frac{1+\sqrt{1-4x}}{1-\sqrt{1-4x}}\right) - i\pi\Big]^2 \\ &\quad - \theta(4x-1)2\left(\sin^{-1}\left(\frac{1}{2\sqrt{x}}\right)\right)^2\,, \end{aligned} \tag{4.13}$$

see e.g. [7] and references therein. Again in the case of exact top and bottom mass dependence, the expression for the Higgs production amplitude is

$$\mathcal{A}_{ggH} = -\frac{\alpha_s}{4\pi v}\frac{m_{\gamma\gamma}^2}{2}\sum_{q=b,t} Q_q^2 I_q\left(\frac{m_q^2}{m_{\gamma\gamma}^2}\right)\,. \tag{4.14}$$

As mentioned many times in this thesis, the gg channel is the dominant one for the signal process. For the interference, this statement is somehow weakened but still true. Indeed, the qg channel (see Fig. 4.3) accounts for about 30% of the result [151]. Here, we focus on higher order corrections to the gg channel only, i.e. we work in the large gluon-density approximation.

Strictly speaking, if we include only gluon-induced processes, NLO corrections are given by only the first three out of the four δNLO diagrams of Fig. 4.3. Of course, this would imply that one should evolve parton distribution functions (PDFs) in the same approximation. However, one can also retain formally subleading effects. In particular, the quark-induced contribution in the third row of Fig. 4.3 is linked to the gg channel through PDF evolution. One may then expect that its inclusion in the DGLAP evolution of the PDFs would alleviate the factorisation-scale dependence of the result. Therefore, following Ref. [150], in our analysis we use standard parton distributions and include the last diagram in the third row of Figure. 4.3. In what follows, we call 'δNLO' the contribution coming from the second and third rows of that figure. We stress that this is *not* the full NLO correction to the interference. It may also be instructive to consider only gluon-induced diagrams at this order. Indeed, comparing this against our default setup may give us a handle on the large gluon-density approximation, since δNLO and δNLO(gg) are formally of the same accuracy within this approximation. In what follows, we define corrections

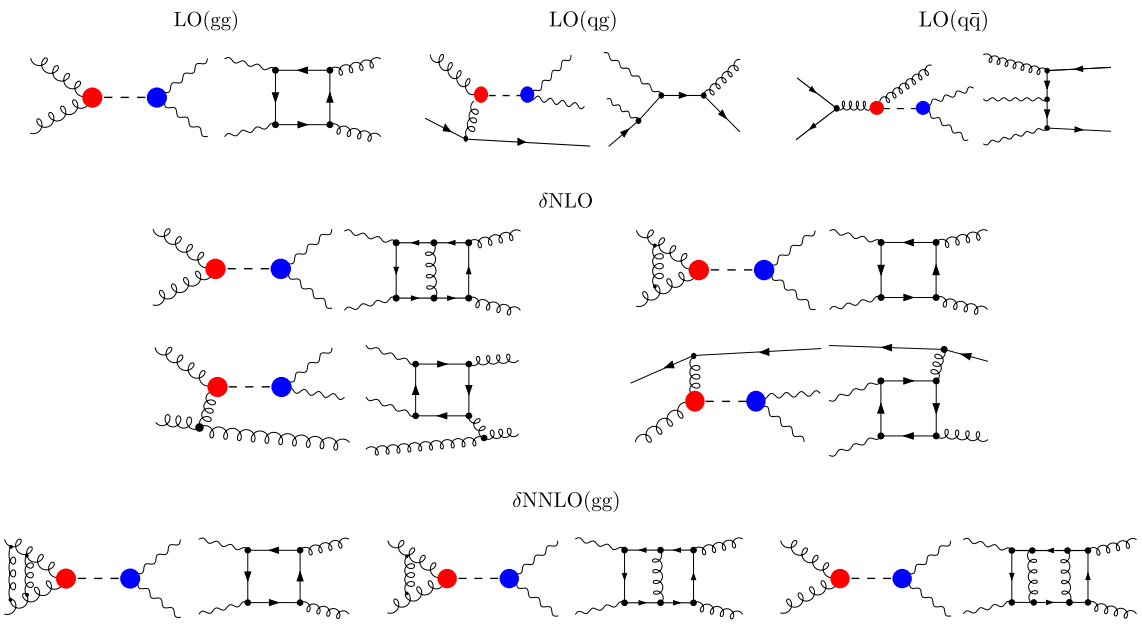


Figure 4.3: Representative diagrams contributing to the interference up to order α_s^4. The red dot denotes the effective vertex described through the Lagrangian in Eq. (1.78), while the blue dot denotes the Higgs decay via heavy quark loops and W boson, described in Eq. (4.12).

computed using only the first three diagrams of the block of diagrams (δNLO) in Fig. 4.3 as 'δNLO(gg)'. Correspondingly we call the the full NLO result

$$\text{NLO} = \text{LO} + \delta\text{NLO}, \quad \text{NLO}(gg) = \text{LO} + \delta\text{NLO}(gg), \tag{4.15}$$

with LO defined in Eq. (4.11).

We now consider NNLO corrections. As we have said, at this order we work in the soft-virtual approximation. This is justified by the fact that, at least at lower orders, interference effects are stronger in the region where the diphoton transverse momentum is small [150, 157]. The soft-virtual approximation and various refinements of it have been extensively adopted for Higgs predictions [168–172]. The main advantage of working in this limit is that the only process-dependent part is encoded in purely virtual contributions, see e.g. Ref. [173] for an explicit derivation.

Here we only sketch the structure of the soft-virtual approximation, and refer the reader to Ref. [173] for more details. Note that in the calculation of the inclusive

Higgs cross section that we performed in Chapter 1, the soft-virtual approximation would correspond to considering Eq. (1.110) and take the soft limit $z \to 1$. The only surviving structures, at leading power, would be the plus distributions and the coefficients of the delta function. In the case of the NNLO cross section, however, we perform the calculation directly in the soft limit. We write the fully-differential hadronic cross section for diphoton production in the gg channel as

$$\begin{aligned} d\sigma(\tau, y, \{\theta_i\}) = \int dx_1 dx_2 dz f_g(x_1, \mu_F) f_g(x_2, \mu_F) \\ \times \delta(\tau - x_1 x_2 z) d\hat{\sigma}\left(z, \hat{y}, \{\hat{\theta}_i\}, \alpha_s, \frac{Q^2}{\mu_R^2}, \frac{Q^2}{\mu_F^2}\right). \end{aligned} \tag{4.16}$$

In this equation, $\tau = Q^2/s_H$ with Q being the invariant mass of the diphoton system and s_H the square of the collider energy, y is the rapidity of the diphoton system in the laboratory frame and θ_i are a set of variable that fully describe the diphoton system (e.g. scattering angles). Variables with hats represent the corresponding partonic quantities. Eq. (4.16) is fully differential in the kinematics of the diphoton system, but retain no information on extra QCD radiation. We note that the partonic variables $\{\hat{\theta}_i\}$ depend on their hadronic counterparts $\{\theta_i\}$ and also on z, x_1, x_2. Finally, $\alpha_s = \alpha_s(\mu_R)$ is the renormalised QCD coupling constant evaluated at scale μ_R.

Major simplifications occur in the soft $z \to 1$ limit. First, in this case the rapidity dependence of Eq. (4.16) is entirely fixed by the inclusive cross section, up to power corrections [174–176]. The partonic cross section in Eq. (4.16) simplifies to

$$d\hat{\sigma}\left(z, \hat{y}, \{\hat{\theta}_i\}, \alpha_s, \frac{Q^2}{\mu_R^2}, \frac{Q^2}{\mu_F^2}\right) \approx d\hat{\sigma}_0(\{\hat{\theta}_i\}, \hat{y}, \alpha_s)\, z\, G\left(z, \alpha_s, \frac{Q^2}{\mu_R^2}, \frac{Q^2}{\mu_F^2}\right), \tag{4.17}$$

where we neglected power corrections in $(1-z)$ and we defined $d\hat{\sigma}_0(\{\hat{\theta}_i\}, \alpha_s)$ in such a way that $d\hat{\sigma}_0(\{\hat{\theta}_i\}, \alpha_s)\delta(1-z)$ is the Born cross section and G is an inclusive coefficient function in the soft limit, normalised such that $G = \delta(1-z) + \mathcal{O}(\alpha_s)$. In the soft limit, the diphoton kinematics is identical to the LO one, except that the partonic center-of-mass energy is rescaled by z. Such a rescaling factor can be absorbed by boosting an individual leg, i.e. by using the partonic momenta $x_{1,\text{Born}} \to z\, x_{1,\text{Born}}, x_{2,\text{Born}} \to x_{2,\text{Born}}$ (and vice versa). Alternatively, one can boost

both legs at the same time, i.e. $x_{i,\text{Born}} \to \sqrt{z}\, x_{i,\text{Born}}$, $i = 1, 2$. In the soft-limit, the two are formally equivalent and, in principle, one can consider both and treat their difference as an uncertainty. In practice, we expect this difference to be small [177], so for simplicity we always boost only one leg here.

If we write the perturbative expansion of the coefficient function as

$$G\left(z, \alpha_s\right) = \delta(1-z) + \sum_{n=1}^{\infty} \left(\frac{\alpha_s}{2\pi}\right)^n G^{(n)}(z), \tag{4.18}$$

then in the soft-virtual approximation the individual coefficients $G^{(n)}$ have the form

$$G^{(n)}\left(z, \frac{Q^2}{\mu_R^2}, \frac{Q^2}{\mu_F^2}\right) = c_0^{(n)} \delta(1-z) + \sum_{k=1}^{2n-1} c_k^{(n)} \mathcal{D}_k(z), \tag{4.19}$$

where $c_k^{(n)} = c_k^{(n)}(Q^2/\mu_R^2, Q^2/\mu_F^2)$ and $\mathcal{D}_k$ are the standard plus distributions defined in Eq. (1.106).

The result for the NLO and NNLO coefficients is given by

$$G^{(1)}(z) = \delta(1-z)\left(\frac{2}{3} N_c \pi^2 + \frac{\hat{\sigma}_{\text{fin}}^{1-\text{loop}}}{\hat{\sigma}_0}\right) + 8 N_c \mathcal{D}_1(z)\,, \tag{4.20}$$

and

$$\begin{aligned} G^{(2)}(z) = \Bigg\{ & \left[\frac{\hat{\sigma}_{\text{fin}}^{2-\text{loop}}}{\hat{\sigma}_0} + \frac{\hat{\sigma}_{\text{fin}}^{1-\text{loop}^2}}{\hat{\sigma}_0}\right] \delta(1-z) + \frac{\hat{\sigma}_{\text{fin}}^{1-\text{loop}}}{\hat{\sigma}_0} \times \Bigg[\delta(1-z)\frac{2}{3}\pi^2 N_c \\ & + 8\mathcal{D}_1(z) N_c\Bigg] + \Bigg[\delta(1-z)\left(\frac{11}{108} n_f^2 \pi^2 + N_c^2\left(\frac{607}{81} + \frac{517}{108}\pi^2 - \frac{\pi^4}{80} - \frac{407}{36}\zeta_3\right)\right. \\ & \left. + N_c n_f\left(\frac{37}{18}\zeta_3 - \frac{11}{8}\pi^2 - \frac{82}{81}\right)\right) + \mathcal{D}_0(z)\left(N_c n_f\left(\frac{56}{27} - \frac{4}{9}\pi^2\right)\right. \\ & \left. + N_c^2\left(78\zeta_3 - \frac{404}{27} + \frac{22}{9}\pi^2\right)\right) + \mathcal{D}_1(z)\left(-\frac{40}{9} N_c n_f + N_c^2\left(\frac{268}{9} - \frac{20}{3}\pi^2\right)\right) \\ & - 8 N_c \beta_0 \mathcal{D}_2(z) + 32 N_c^2 \mathcal{D}_3(z)\Bigg]\Bigg\}\,, \end{aligned} \tag{4.21}$$

where we have set $\mu_R = \mu_F = m_{\gamma\gamma}$ for simplicity. Furthermore, $\hat{\sigma}_{\text{fin}}^{1-\text{loop}}$, $\hat{\sigma}_{\text{fin}}^{1-\text{loop}^2}$ and $\hat{\sigma}_{\text{fin}}^{2-\text{loop}}$ represent the contributions due to the 1-loop times Born level amplitude finite remainder, 1-loop finite remainder squared and the interference of the 2-loop finite remainder with the Born amplitude, respectively. They are defined as the UV-renormalized 1-loop and 2-loop amplitudes, from which one subtracts the infrared

operators defined in Eq. (2.31). Note that, as expected, Eq. (4.20) agrees with the soft limit of the result presented in Eq. (1.110), provided that we make the one-loop finite remainder explicit in the former. We report the calculation of the double real emission matrix element in the soft limit in Appendix D.

The coefficients $c_k^{(n)}$ in Eq. (4.19) in principle depend on the process under consideration. However, Eq. (4.21) shows that the only process dependence arises from finite remainders of purely virtual contributions.

For our analysis, we also require the signal process at NNLO accuracy. In principle, computing this exactly does not pose significant challenges. Nevertheless, we expect the exact result to be very well described by a (refined) version of the soft-virtual approximation [168–171]. While the pure soft-virtual prediction provides a good approximation to the interference, this is not the case for the signal. We therefore employ a modified soft-virtual approximation to describe the latter. Specifically, we follow the approach of Ref. [170] which is known to reproduce the exact NNLO prediction to within few-percent accuracy. In practice, this amounts to modifying the plus distributions in Eqs. (4.20,4.21) according to [170]

$$\mathcal{D}_i(z) \to \mathcal{D}_i(z) + (2 - 3z + 2z^2)\frac{\ln^i \frac{1-z}{\sqrt{z}}}{1-z} - \frac{\ln^i(1-z)}{1-z}. \tag{4.22}$$

This modification captures soft emission at next-to-leading power, as well as part of the hard collinear emission. Such an approximation was already used for estimating signal-background interference effects for the $gg \to VV$ process [177]. In our case, we have specifically checked that for on-shell Higgs, within the fiducial volume used in our analysis, the soft-virtual approximation improved according to Eq. (4.22) agrees with the exact NNLO correction to within few percent. This is good enough for the kind of accuracy targeted in our analysis. In the following section, we will refer to this improved soft-virtual approximation as "NNLOsv′". The reason why we do not adopt such an improved approximation for the background is because it is currently unknown how to properly capture next-to-leading power soft term in this case. Indeed, a simple modification of emission off external legs works for the Higgs point-like interaction, but not for the background amplitude. Fortunately,

the interference seems to be dominated by low-p_T physics so the lack of such an improved approximation is less problematic than for the signal.

We now list the various ingredients of our calculation. The LO amplitudes, including the quark-mass effects, are well known, see e.g. Ref. [7] and references therein. At NLO, we took the one-loop amplitudes for the background from Refs. [57, 158, 178, 179], borrowing most of them from `MCFM` [180–182]. We note that the two-loop amplitude for $gg \to \gamma\gamma$ was first computed in Ref. [183]. NLO predictions were computed using FKS subtraction [88]. Finally, the three-loop $gg \to \gamma\gamma$ amplitude relevant for NNLO corrections was taken from Ref. [158]. All the tree- and one-loop results for the interference used in our calculation were cross-checked against a dedicated version of `OpenLoops2` [84, 184].

We are now ready to discuss the results or our calculation. We employ the so-called G_μ input scheme for the electroweak parameters and we use

$$G_F = 1.16639 \cdot 10^{-5}\ \text{GeV}^{-2}\,, m_W = 80.398\ \text{GeV}, \quad m_Z = 91.1876\ \text{GeV}\,,$$

which gives the electroweak coupling constant $\alpha = 1/132.338$. We set the Higgs mass to $m_H = 125$ GeV. Finally, we use $m_t = 173.2$ GeV and $m_b = 4.18$ GeV for the top and bottom mass, respectively. We use the `NNPDF31_nnlo_as_0118` [185] parton distribution functions as distributed through the `LHAPDF` library [186] and we use HOPPET [187] for various PDFs manipulations. The value of the strong coupling constant is extracted from the PDF set, with $\alpha_s(m_Z) = 0.118$. For the QCD factorisation and renormalisation scales, we choose the common value $\mu_F = \mu_R = m_{\gamma\gamma}/2$, where $m_{\gamma\gamma}$ is the invariant mass of the diphoton system. All of the results presented in this section have been derived for the 13.6 TeV LHC, i.e. proton-proton collisions. We define the fiducial region by imposing the following set of cuts on the final-state photons

$$\begin{aligned} p_{T,\gamma} > 20\,\text{GeV}, \qquad & \sqrt{p_{T,\gamma_1} p_{T,\gamma_2}} > 35\ \text{GeV}, \\ |y_\gamma| < 2.5, \qquad & \Delta R_{\gamma_1\gamma_2} > 0.4, \end{aligned} \tag{4.23}$$

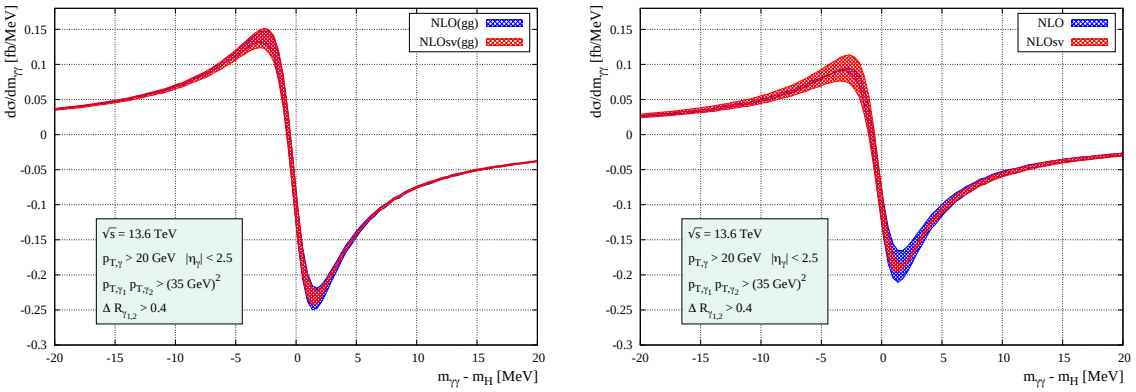


Figure 4.4: Left pane: comparison of the exact NLO calculation and the soft-virtual approximation in the gg channel. Right pane: complete NLO prediction, inclusive of all channels, compared to the corresponding soft-virtual approximation

which are designed to reduce sensitivity on infrared physics [188]. The cuts in Eq. (4.23) are different from the ones used in Refs. [150, 151]. Because of this, it is not immediate to compare our results with the ones presented there. Nevertheless, we have validated our LO and NLO calculations against Refs. [150, 151] in an equivalent setup. In particular, we have reproduced the results for the mass shift shown in Refs. [150, 151]. We have also used `MCFM` [180–182], together with in-house codes, to validate the signal and the reliability of the NNLOsv′ approximation.

We start the discussion of our results by assessing the validity of the soft-virtual approximation for the interference at NLO. We do this by first comparing the exact prediction including only the gg initiated process, which we dub NLO(gg), to the corresponding soft-virtual approximation, NLOsv(gg). This comparison is shown in the left pane of Fig. 4.4. Second, we compare the complete NLO calculation, i.e. including the qg and $\bar{q}g$ initiated channels [4] to the NLO soft-virtual approximation (NLOsv), which retains all LO contributions, but includes NLO corrections in the soft-virtual approximation for the gg channel only. This comparison is presented in the right pane of Fig. 4.4. The red and blue bands shown in both figures represent the envelope from a simultaneous rescaling of $\mu_{F,R}$ by a factor of two up and down with respect to the central value. We note that our result suggests

[4] We note that the impact of the $q\bar{q}$ channel is negligible.

that the uncertainty due to scale variations does not provide a reliable estimate of the actual error of the NLO prediction. This may be due to the fact that by introducing only the part of the qg channel that is relevant for PDF evolution, we have artificially decreased the N_f dependence. In the left pane of Fig. 4.4 one can see that the soft-virtual approximation does a remarkably good job in describing the dominant gg contribution. The shape of the interference is very well captured and the scale-variation bands almost perfectly match throughout the relevant interval of invariant mass. In the right side of Fig. 4.4 we notice a slight degrading of the approximation, mostly for what concerns the scale variation bands. This is because the soft-virtual approximation does not capture the full scale-compensation between different channels that happens at NLO. However, the shape, which is the relevant factor for the extraction of the mass-shift, is still described at a satisfactory degree.

This comparison gives us some confidence that the soft-virtual approximation can adequately describe higher-order QCD corrections to the signal-background interference. Furthermore, we note that the mass-shift extracted at NLO in the soft-virtual approximation differs from the exact value by 5%, whilst the genuine NLO correction is of $\mathcal{O}(30/40\%)$ and the theory uncertainty is $\mathcal{O}(10\%)$. The ability of the soft-virtual approximation to reproduce the interference effects can be better understood by keeping in mind that the predominant contributions come from the low $p_{T,\gamma\gamma}$ regions, as we already mentioned before. We point out that the fiducial setup adopted in Eq. (4.23), in particular with the choice of product cuts, plays a relevant role in the reliability of the soft-virtual approximation. We have indeed explicitly checked that imposing asymmetric cuts on the final-state photons, as is routinely done in Higgs analysis, breaks the quality of the approximation.

As already discussed, in order to get a more realistic picture of the interference effect at the detector level, we convolute the invariant mass distribution with a Gaussian function with a standard deviation of $\sigma = 1.7$ GeV [149, 152]. The invariant mass distribution arising from signal-background interference after the smearing is shown in Fig. 4.5. The LO features the well known antisymmetric behaviour around the peak coming from the real part of the interference, whereas the NLO

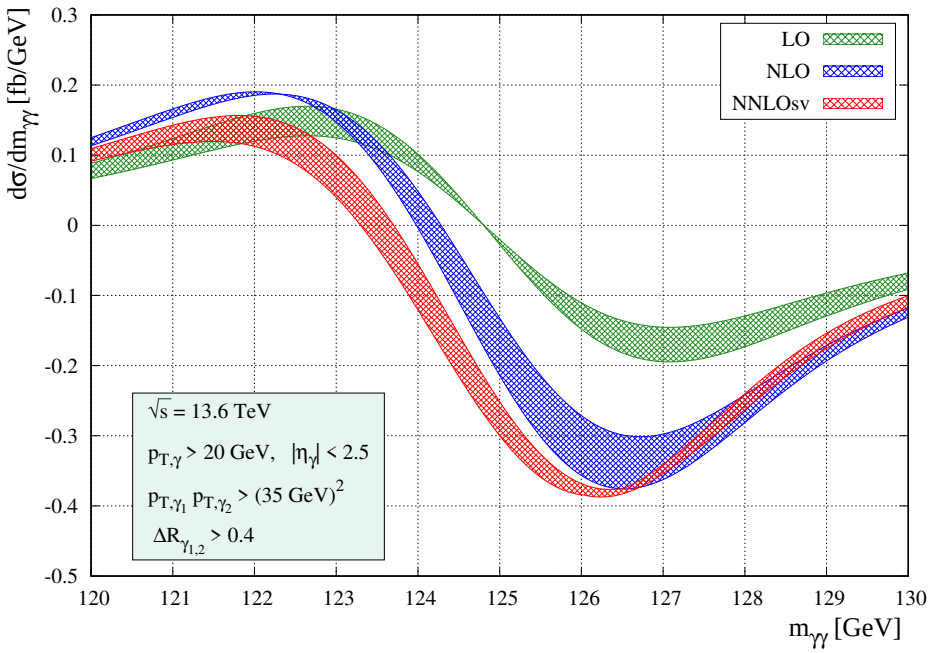


Figure 4.5: Signal-background interference contribution to the diphoton invariant mass distribution after Gaussian smearing. Bands represent the envelope given by the scale variation.

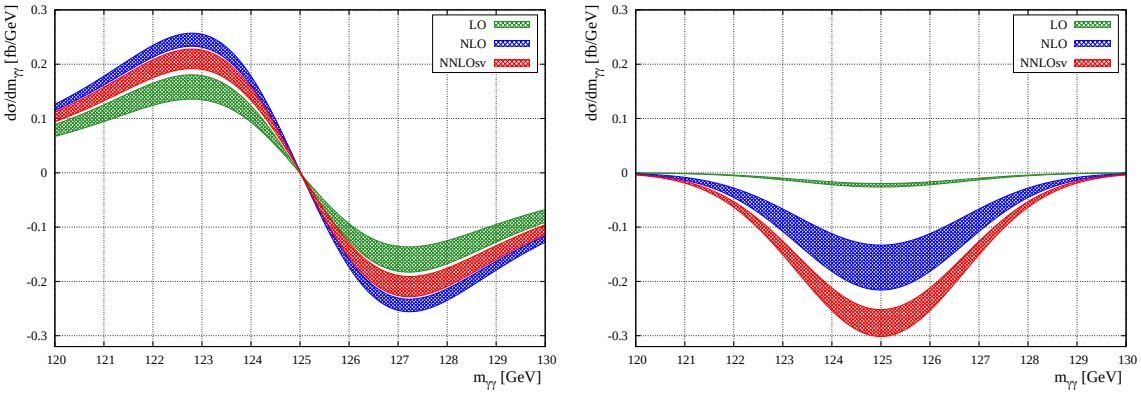


Figure 4.6: Real part (left pane) and imaginary part (right pane) of the interference at LO, NLO and NNLOsv after Gaussian smearing.

curve is shifted to the left and to the bottom, due to the impact of the imaginary part. In the same figure, we can appreciate for the first time the effect of the NNLO QCD corrections. The curve is further shifted down, thus depleting even more the number of events around the Higgs peak and softening the impact on the mass-shift. Moreover, from Fig. 4.5 one can see that the theory uncertainty, which arises almost

completely from renormalisation scale variations, gets generally reduced at NNLO, except in the region where the NLO band shrinks to zero. This behaviour can be understood keeping in mind that the interference is the sum of the real and imaginary parts which have different shapes, as discussed in Sec. 4.2.1. As shown in Fig. 4.6, scale-variation bands are separately reasonably well behaved for the real and imaginary parts, but on the left hand side of the Higgs boson peak a cancellation occurs, whereas on the right the two effects sum up (both negative in sign).

Before moving to our results for the mass shift, we briefly discuss the impact of the imaginary part of the interference to the total cross section in our fiducial region. As we have explained in Sec. 4.2.1, at LO this interference is very small because it only comes from contributions mediated by virtual bottom quarks, either in the signal or in the background. These are either mass (background) or Yukawa (signal) suppressed. The smallness of the LO imaginary part is indeed seen in Fig. 4.6. In our setup, we find

$$\sigma_S^{\rm LO} = 24.21^{+15\%}_{-14\%}\ \text{fb}, \qquad \sigma_I^{\rm LO} = -0.11^{+20\%}_{-17\%}\ \text{fb}. \tag{4.24}$$

Here and in the following the quoted uncertainties are obtained by coherently varying the renormalisation and factorisation scales by a factor of two around the central value $\mu = m_{\gamma\gamma}/2$. At LO, we find that more than 80% of the destructive interference quoted above comes from the imaginary part of the signal interfering with the real part of the background. This gives us confidence that neglecting mass effects in the background prediction does not significantly impact our result. Furthermore, as far as the signal goes, we note that the bulk (about 95%) of the imaginary part is generated by bottom-mass effects in the production amplitude. This is easy to understand just by looking at the relative importance of the top, bottom and W contributions to the production and decay amplitudes.

At higher orders however, a larger interference is generated by the imaginary part of the background, which no longer requires the presence of bottom quarks. Because of this, beyond LO we only compute radiative corrections in the infinite-top

approximation and drop any mass dependence in the background amplitudes. At NLO, we obtain

$$\sigma_S^{\rm NLO} = 58.12^{+20\%}_{-14\%}\ {\rm fb}, \qquad \sigma_I^{\rm NLO} = -0.72^{+27\%}_{-21\%}\ {\rm fb}. \tag{4.25}$$

These results are consistent with the analysis in Ref. [155]. Our best prediction beyond NLO is obtained within the soft-virtual approximation. We find

$$\sigma_S^{\rm NNLOsv'} = 72.21^{+8\%}_{-8\%}\ {\rm fb}, \quad \sigma_I^{\rm NNLOsv} = -1.21^{+7\%}_{-10\%}\ {\rm fb}, \tag{4.26}$$

hence the destructive interference reduces the total rate by 1.7%.[5] Given the theoretical [189] (see also Refs. [190, 191]) and experimental [166, 167] uncertainties on the Higgs total cross section, this effect is actually not negligible and it can be used to further constrain the Higgs width [155]. We do not pursue this line of investigation here, but we estimate that, with current uncertainties, one could already constrain the Higgs width to about 20-30 times the Standard Model.

We can finally present the main result of our study, i.e. the prediction for the mass-shift at NNLO. As discussed in Sec. 4.2.1, we adopt two different methods to estimate the mass-shift induced by the interference term. In Table 4.1 we show results obtained by performing a chi-squared fit of the smeared signal-plus-interference distribution with a Gaussian function of standard deviation $\sigma = 1.7\,{\rm GeV}$. The mass-shift is obtained as the difference between the obtained mean value and the input Higgs boson mass $m_H = 125$ GeV. In Table 4.2 instead we present results derived by computing the first moment of the signal-plus-interference distribution after smearing. In both tables we show predictions for different collider energies, but in the same fiducial region specified in Eq. (4.23). As mentioned earlier, the denoted ranges represent the theoretical uncertainty related to a change of the central scale $\mu = m_{\gamma\gamma}/2$ by a factor of two and a half. The entry NNLOsv indicates the result obtained by considering both signal and interference terms in the soft-virtual approximation. The NNLOsv′ entry instead, refers to the "improved" soft-virtual approximation discussed before. Specifically, in this case we still use

[5] We point out that the theory uncertainties for the signal cross section in Eq. (4.26) have been computed employing the exact NNLO QCD scale variations.

$\Delta m_{\gamma\gamma}$ [MeV]	7 TeV	8 TeV	13.6 TeV
LO	$-77.2^{+0.8\%}_{-1.0\%}$	$-79.5^{+0.6\%}_{-0.8\%}$	$-83.1^{+0\%}_{-0.3\%}$
NLO	$-56.2^{+13\%}_{-15\%}$	$-56.8^{+13\%}_{-14\%}$	$-55.2^{+12\%}_{-12\%}$
NNLOsv	$-46.3^{+15\%}_{-17\%}$	$-47.0^{+14\%}_{-16\%}$	$-46.0^{+11\%}_{-12\%}$
NNLOsv′	$-39.5^{+20\%}_{-24\%}$	$-39.7^{+19\%}_{-22\%}$	$-39.4^{+16\%}_{-17\%}$

Table 4.1: Mass-shift at different proton-proton collider energies with Gaussian fit method.

$\Delta m_{\gamma\gamma}$ [MeV]	7 TeV	8 TeV	13.6 TeV
LO	$-113.4^{+0.8\%}_{-1.0\%}$	$-116.7^{+0.6\%}_{-0.8\%}$	$-122.1^{+0.1\%}_{-0.3\%}$
NLO	$-82.6^{+13\%}_{-15\%}$	$-82.8^{+12\%}_{-14\%}$	$-81.2^{+12\%}_{-12\%}$
NNLOsv	$-68.1^{+15\%}_{-17\%}$	$-68.4^{+13\%}_{-15\%}$	$-67.7^{+11\%}_{-12\%}$
NNLOsv′	$-58.1^{+20\%}_{-23\%}$	$-59.2^{+18\%}_{-21\%}$	$-58.0^{+16\%}_{-17\%}$

Table 4.2: Mass-shift at different proton-proton collider energies with first-moment method.

the NNLOsv approximation for the interference, but compute the signal in the NNLOsv′ framework. As already explained, we expect this setup to be the most reliable one. Still, we find it useful to present numbers in both frameworks as a conservative way of estimating the uncertainties related to these approximations. In this respect, we note that the results obtained in the NNLOsv and NNLOsv′ approximations are compatible within their uncertainties.

We immediately notice that in both extraction methods, the estimated mass-shift is rather insensitive to the collider energy. Although a Gaussian fitting procedure and the evaluation of the first moment return different values for the mass-shift,

$\Delta m_{\gamma\gamma}/\Delta m_{\gamma\gamma}^{\rm LO}$	First moment	Gaussian Fit
$K_{\rm NLO}$	0.665	0.664
$K_{\rm NNLOsv}$	0.554	0.554
$K_{\rm NNLOsv'}$	0.475	0.474

Table 4.3: Comparison of K-factors, measured w.r.t. the LO value, for the mass-shift at $\sqrt{s} = 13.6$ TeV calculated via a gaussian fit method and via a first-moment method.

smaller for the former and larger for the latter, we notice that the K-factors relative to the corresponding LO prediction are almost identical. The results in Table 4.3 show that radiative corrections seem rather insensitive to the precise definition of the observable used to extract the mass shift. We stress that this is a welcome feature since our analysis does not include reliable detector simulation.

We also observe how the mass-shift gets systematically reduced in absolute value when including higher-order corrections. This is mainly because the K-factor for the signal turns out to be larger than the one for the interference, thus leading to a reduction of the mass-shift. This trend, already observed at NLO [150], seems to persist at NNLO (at least in the NNLOsv approximation).

Finally, we study how the bounds on Γ_H are affected by higher-order QCD corrections. The results at NLO and NNLOsv′ (i.e. our best prediction) are shown in Fig. 4.7. We note that the two curves do not overlap. This is a direct consequence of the analogous feature for the interference shown in Fig. 4.5. As explained in the discussion of that figure, this is at least partially due to competing effects coming from real and imaginary part of the interference, see Fig. 4.6. Furthermore, similar to the Higgs-signal case, the interference receives rather large corrections as well. Finally, we note that the NNLO soft-virtual curve lies above the NLO one, thus loosening potential bounds on Γ_H. For instance, assuming an error on the mass-shift of roughly 150 MeV, one could exclude values of Γ_H larger than

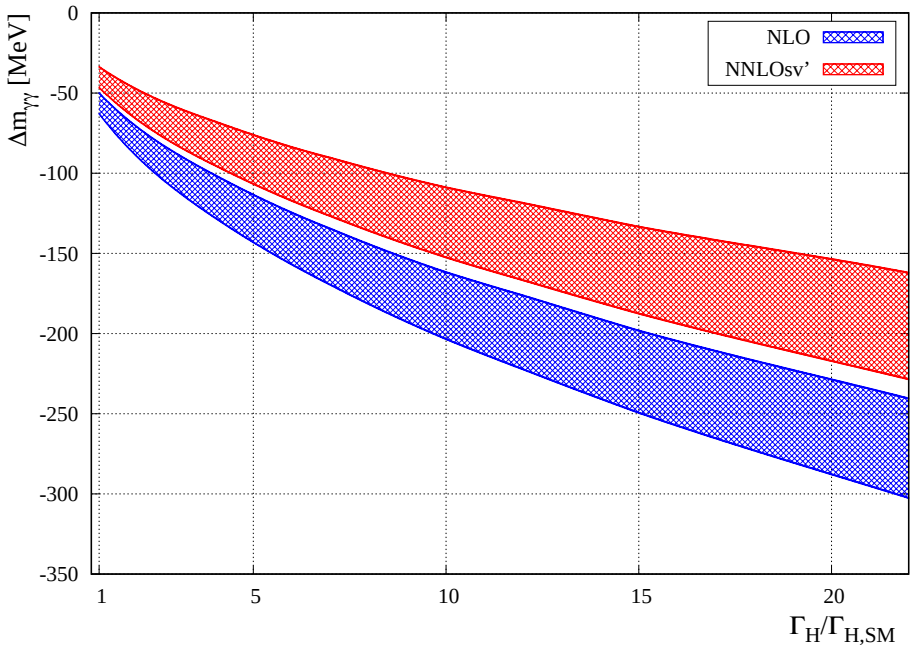


Figure 4.7: Mass-shift as a function of the Higgs boson width

10–20 times the SM prediction. This has to be compared with the corresponding bound at NLO of $\Gamma_H < (6\text{–}9)\Gamma_{H,\mathrm{SM}}$.

4.3 Interference effects in $H \to Z\gamma$

We are now in the position to discuss interference effects in the rare decay channel $H \to Z\gamma$. The $H \to Z\gamma$ decay mode [192] is of particular interest for several reasons. It is unique among the Higgs decays observed to date in that the final state is neither a pair of identical particles (such as $\gamma\gamma$) nor a particle-antiparticle pair (such as $b\bar{b}$). Moreover, as a loop-induced process, the $H \to Z\gamma$ decay can yield a non-trivial check of the SM at the quantum level, providing constraints on the structure of the Higgs boson and its possible couplings to heavy particles [193, 194]. This process is thus complementary to those from Higgs decays into two photons $H \to \gamma\gamma$ [195] and the gluon fusion production mechanism $gg \to H$ [196] which also proceed through loops of heavy particles, see e.g. Refs. [197–201]. For this reason, it is intriguing that the 3.4σ signal reported by ATLAS and CMS has a strength that is somewhat

higher than the SM value, leaving some space for possible physics beyond the SM, though such an apparent excess is not statistically significant at this point.

In order to evaluate possible interpretations of the $pp \to H \to Z\gamma$ signal yield, it is important to have at hand the most accurate available calculation in the SM. As in the more studied $\gamma\gamma$ channel that we described in the previous section, the γZ final state originates not only from the signal process $gg \to H \to Z\gamma$ but also from the QCD background process $gg \to Z\gamma$ which proceeds through box diagrams involving SM light quarks. The interference of the two processes could modify not only the signal rate but also the resonance line-shape and the apparent mass of the Higgs boson, although this channel will not be competitive with respect to the diphoton and the 4-lepton channels for mass determination.

Here we want to study the dominant radiative corrections at NLO in perturbative QCD of the signal strength in the SM, including the interference with the QCD background $gg \to Z\gamma$. For the latter, we employ the same soft-virtual approximation discussed for the diphoton decay channel. Within this approximation, we find that the NLO corrections in this channel differ from the corresponding effects in the $gg \to \gamma\gamma$ process. The NLO corrections are not large. Consequently, they do not impact significantly the apparent tension between the SM prediction and the recent ATLAS and CMS measurements. We therefore await with interest the evolution of this measurement with the accumulation of LHC luminosity.

4.3.1 The $gg \to Z\gamma$ process

At LO, the SM diagram for the dominant Higgs production mechanism at the LHC, $gg \to H$ [196], followed by the $H \to Z\gamma$ decay [192], is shown in the left panel of Fig. 4.8. As far as the dominant QCD interactions are concerned, the higher-order corrections to $gg \to H$ are clearly identical to the ones described in the $H \to \gamma\gamma$ case. In the case of the $H \to Z\gamma$ decay, the NLO QCD corrections to the relevant top-quark loop have been found to be very small [202–204]. We note, moreover, that in the SM the W-boson loop contribution dominates by far over the top-loop contribution, while those of the b-quark and other fermions are negligible.

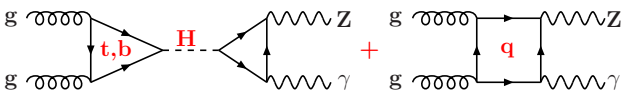


Figure 4.8: Feynman diagrams at leading order for the signal (left) and the background (right) in the process $gg \to Z\gamma$.

The $Z\gamma$ final state is also produced in pure QCD in gluon fusion, $gg \to Z\gamma$, through the box diagram shown in the right panel of Fig. 4.8. The cross section for this background process, which is dominated by light quark loops as heavy quarks decouple at large masses, has been given at LO in Refs. [205–207]. (We note that there is also a very large contribution to the background from the $q\bar{q} \to \gamma Z$ tree-level process, but we ignore it as it does not contribute to the interference which is our main concern here.) At NLO, the QCD corrections are analogous to those derived in the $gg \to \gamma\gamma$ case [178, 183, 208] and the relevant two-loop helicity amplitudes have been given in Ref. [209]. Note that, at NLO, we assume massless quarks in the background process, whereas the infinite top quark mass limit is assumed in the Higgs signal process.

As the Higgs signal and continuum background processes have the same initial and final states, they will interfere. The total amplitude for the $gg \to Z\gamma$ process including both contributions may be then written as

$$\mathcal{A} = -\frac{\mathcal{A}_{ggH}\mathcal{A}_{HZ\gamma}}{m_{Z\gamma}^2 - m_H^2 + im_H\Gamma_H} + \mathcal{A}_{ggZ\gamma}\,, \tag{4.27}$$

where $m_{Z\gamma}$ is the invariant mass of the $Z\gamma$ system and, in the first term, the denominator represents the propagator of the Higgs boson with mass m_H and total width Γ_H. The differential cross section for the full $gg \to \gamma Z$ process including the Higgs signal, the continuum background and their interference is given schematically by

$$\frac{\mathrm{d}\sigma(gg\to\gamma Z)}{\mathrm{d}m_{Z\gamma}} \propto \frac{S+I_{\mathrm{Re}}+I_{\mathrm{Im}}}{(m_{Z\gamma}^2-m_H^2)^2+m_H^2\Gamma_H^2}+B\,, \tag{4.28}$$

where the various components read

$$S = |\mathcal{A}_{ggH}\,\mathcal{A}_{HZ\gamma}|^2\,, \quad B = |\mathcal{A}_{ggZ\gamma}|^2\,, \tag{4.29}$$

$$I_{\rm Re} = -2{\rm Re}[\mathcal{A}_{ggH}\,\mathcal{A}_{HZ\gamma}\,\mathcal{A}^*_{ggZ\gamma}] \times (m^2_{Z\gamma} - m^2_H)\,, \tag{4.30}$$

$$I_{\rm Im} = -2{\rm Im}[\mathcal{A}_{ggH}\,\mathcal{A}_{HZ\gamma}\,\mathcal{A}^*_{ggZ\gamma}] \times m_H\Gamma_H\,. \tag{4.31}$$

Here, we refrain from giving explicit expressions for the various amplitudes and simply describe the relevant contributions. For the interference, its first component $I_{\rm Re} \propto m^2_{Z\gamma} - m^2_H$ is the real part of the interference discussed in the previous section. As we already said, it does not contribute to the cross section but it distorts the resonance shape and shifts the position of the peak, changing the apparent mass of the resonance. On the other hand, the second interference term $I_{\rm Im}$ is the imaginary part of the interference. Its contribution to the cross section is suppressed by the small Higgs width Γ_H.

We have seen in the $H \to \gamma\gamma$ case that the interference $I_{\rm Im}$ requires an absorptive part in the amplitudes. For the light quarks with $m_q \ll M_{Z,H}$, the contribution of mass corrections to the imaginary part is suppressed by powers of $4m^2_q/m^2_{Z,H}$ relative to the value in the massless limit. The amplitudes for the induced ggH and $HZ\gamma$ couplings involve imaginary components when the particles circulating in the loops have masses below the kinematical threshold, i.e., $m^2_H \geq 4m^2_X$, which is the case for bottom quarks. In the case of the $HZ\gamma$ amplitude, the b–quark contribution is completely negligible. In turn, the b-quark contribution to the Hgg amplitude is sizeable and its interference with the dominant top contribution represents about 10% of the total amplitude (at LO) and it has a non-negligible imaginary component [193, 194].

Since our focus here is to see whether interference effects can be enhanced, we consider those contributions that could be responsible for an enhancement of the interference effects which go beyond a simple counting of the powers of α_s. Such effects are usually given by strong phases, e.g., absorptive contributions arising from light on-shell particles in the loops. It is clear that such phases, if present,

would come from virtual corrections, and are therefore correctly taken into account by the soft-virtual approximation described in the previous section.

4.3.2 Interference effects at NLO QCD

At next-to-leading-order in perturbative QCD, some generic Feynman diagrams that contribute to the $gg \to Z\gamma$ process are given in Fig. 4.9. The upper row shows some representative NLO diagrams for the signal process $gg \to H$ with the subsequent decay $H \to Z\gamma$, and the lower row shows some of the NLO ones that contribute to the SM background. The latter involve two-loop box diagrams with virtual gluon exchange and one-loop diagrams (including pentagons) accompanied by real gluon emission.

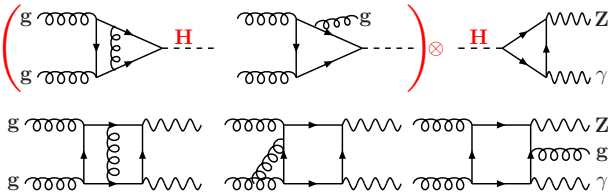


Figure 4.9: Generic Feynman diagrams in NLO QCD for the signal process $gg \to H$ with the decay $H \to Z\gamma$ (upper row) and for the background process $gg \to Z\gamma$ (lower row).

We report here the results of a simplified SM calculation at NLO in perturbative QCD that is expected to capture the most important features of the interference effects in this $gg \to Z\gamma$ search channel. We treat the interference term in the soft-virtual approximation, as we already did in the case of NNLO QCD corrections to the interference in the diphoton decay channel. Details on the soft-virtual approximation are given in Section 4.2.2 so we do not repeat them here. We stress however that the SM signal cross section is, instead, treated exactly through NLO in QCD, i.e., retaining the full dependence on the real radiation, both hard and soft.

Our NLO QCD prediction relies on the two-loop helicity amplitudes for the background process presented in Ref. [209]. The full helicity information allows us to incorporate the spin-correlated decay of the Z boson. In this paper we consider in particular its electron-positron decay channel, $Z \to e^-e^+$. In principle, the

complete $pp \to e^-e^+\gamma$ scattering process also includes a contribution where an off-shell photon decays to leptons, $pp \to \gamma^*(e^-e^+)\gamma$, and one where the Z boson decays to an e^-e^+ pair and the final-state photon is emitted off the leptons. However, both effects are negligible for the particular analysis we present here. The impact of the former is significantly reduced by the selection cuts we impose on the final-state leptons. The latter is expected to be small based on the fact that we focus on the Higgs-boson resonance region, which forces the invariant mass of the $e^-e^+\gamma$ system to be away from the Z resonance peak.

In choosing the selection criteria for the leptons and the photon, we were inspired by an analysis of the $H \to Z\gamma$ channel carried out by the ATLAS collaboration [210], and adopted analogous cuts used for the $Z \to e^+e^-$ decay mode. These cuts are rather inclusive and yield results that are qualitatively similar to the inclusive case. The difference is restricted to an overall normalisation and simply results in a small reduction of the cross section. Specifically, we require the e^-e^+ pair to have an invariant mass $m_{\ell\ell}$ in the range $50\text{ GeV} < m_{\ell\ell} < 101\text{ GeV}$, that all tagged final-state particles satisfy $p_{T,i} > 10$ GeV, with $i \in \{e^-, e^+, \gamma\}$, and finally that the rapidities are constrained by $|y_{e^\pm}| < 2.47$ and $|y_\gamma| < 2.37$.

The setup of our calculation is as follows. We adopt the G_μ scheme for the electroweak parameters and choose $m_Z = 91.1876$ GeV, $M_W = 80.398$ GeV, $\Gamma_Z = 2.4952$ GeV and $G_F = 1.16639 \cdot 10^{-5}$ GeV^2, which results in $\alpha = 1/132.277$. For the Higgs boson mass we choose $M_H = 125$ GeV. Our predictions are derived for a pp collider at a centre-of-mass energy of $\sqrt{s} = 13.6$ TeV, i.e. the current LHC operational mode. We use the `NNPDF31_nlo_as_0118` set [185] of parton distribution functions (PDFs) with the value $\alpha_s(M_Z) = 0.118$, and we make use of the `LHAPDF` [186] and HOPPET [187] programs for manipulation of the PDFs. For the QCD factorisation and renormalisation scales, we have chosen a common scale $\mu_F = \mu_R = \frac{1}{2}m_H$. Theory uncertainties for the signal process and for the LO interference are estimated by a simultaneous rescaling of the nominal value by factors 2 and 1/2. As for the interference at NLO, as described above, the spread is defined by the difference in the standard soft-virtual approximation and

its modification described in Eq. (4.22). We point out that the standard scale-variation uncertainty on the interference term is accidentally small and is contained within our more conservative estimate.

Fig. 4.10 displays our main findings. It shows the signal and interference (magnified by a factor of 10) line-shapes at LO and NLO as functions of the difference between the $Z\gamma$ invariant mass and the Higgs boson mass. The central values of the cross sections are obtained for the reference scale choice, while the bands stem from scale variations. The LO cross section for the signal, $gg \to H \to Z(e^-e^+)\gamma$, is shown as a blue band, and the NLO cross-section is shown as a green band. The ratio between the two is the well-known K factor of about $\simeq 2$ [211–213]. The red band shows the result of the calculation of the signal-background interference at LO and the orange band is the result of our NLO interference calculation in the soft-virtual approximation, i.e., including virtual contributions and the leading real contributions from soft-gluon emission.

We note that, already at LO, the interference tends to reduce the total cross section and shift the effective Higgs mass to higher values. However, both these effects are numerically very small (recall the factor of 10 of magnification in Fig. 4.10). The effects at NLO are qualitatively similar to those at the LO, and are larger numerically by a small factor that depends on the value of the invariant mass of the $Z\gamma$ system relative to the Higgs mass, as can be seen in Fig. 4.10. This differs from the large K factor for the non-interference term.

We observe that, if we restrict the invariant mass window of the $Z\gamma$ system to a very narrow window, $124 - 126$ GeV, the cross sections of the signal and interference terms in the fiducial volume outlined above are

$$\sigma_S^{\rm NLO} = 1.207^{+20\%}_{-15\%}\ {\rm fb},\ \sigma_I^{\rm NLO_{SV}} = -0.0344^{+12\%}_{-12\%}\ {\rm fb}, \tag{4.32}$$

where the label SV refers to the prediction in the soft-virtual approximation, and its central value is the mean of the results extracted in the two approaches (standard versus modified according to Eq. (4.22)) described above. The uncertainty is

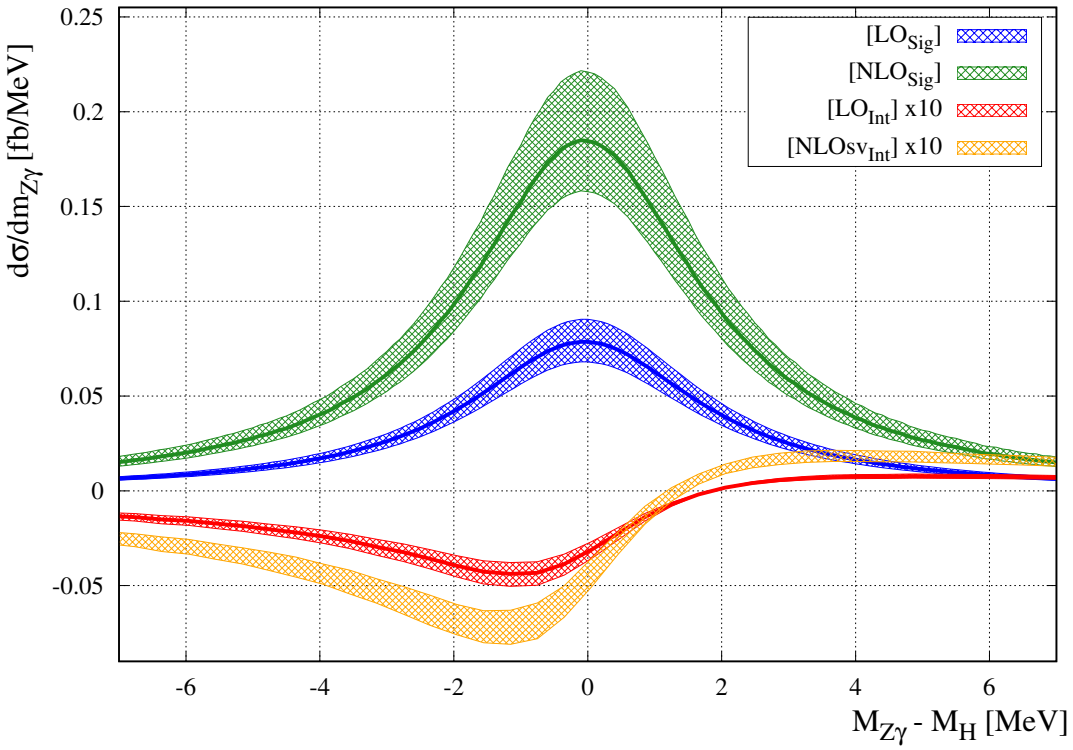


Figure 4.10: The $gg \to H \to Z\gamma$ signal cross section at LO (in blue) and at NLO in QCD (in green), and the interference with the $gg \to \gamma Z$ QCD background at LO (in red) and at NLO but in the soft-virtual approximation (in orange). The bands represent the scale variation, except for NLO_{SV} where the band shows the spread between two different soft-virtual approximations, see the text for details. The results are for the LHC with $\sqrt{s} = 13.6$ TeV, and the interference terms are magnified by a factor of 10 for visualisation purposes.

assessed as discussed for Fig. 4.10. Thus, we estimate that the interference has a destructive impact on the total rate of $\mathcal{O}(-3\%)$[6].

The NLO QCD corrections to the interference in the $gg \to Z\gamma$ process are small and do not modify substantially the signal rate in the Higgs $gg \to H \to Z\gamma$ production channel. These effects also do not modify significantly the effective Higgs mass measured in the $Z\gamma$ final state, which should be indistinguishable from that measured in the $\gamma\gamma$ and ZZ final states.

As a final remark, it is worth mentioning a few qualitative differences with respect to the more deeply investigated interference in the $\gamma\gamma$ decay channel. In the latter, as we already mentioned in the previous section, the Higgs boson decays to

[6]This number may be subject to small variations upon including large missing higher-order QCD corrections in the signal process.

a pair of massless spin-1 particles, and given the scalar nature of the Higgs, these photons must have identical helicities. In this configuration, the corresponding LO background amplitudes receive an imaginary contribution that is suppressed by the ratio m_q^2/m_H^2 where m_q is the mass of a light quark running in the loop, see, e.g., Fig. 4.8. Therefore, a noticeable destructive effect only arises at NLO [164]. In the $Z\gamma$ mode instead, such a helicity selection does not occur and an absorptive part is already manifest at LO. Furthermore, the real contribution $I_{\rm Re}$ has an opposite impact on the line shape than the one in $\gamma\gamma$, which induces a slight excess of events to right of the Higgs boson peak and not to the left as in $\gamma\gamma$.

To conclude, our analysis shows that interference effects beyond leading order are small, as was already the case for the leading-order QCD interference effects. They do not modify significantly the apparent tension between the SM prediction for the $gg \to H \to Z\gamma$ signal strength and that recently measured by the ATLAS and CMS collaborations, namely $\mu = 2.2 \pm 0.7$. As such, they leave space for alternative explanations of the apparent tension: either the speculative possibility of physics beyond the SM (see e.g. [214]) or, more plausibly, a statistical fluctuation.

5

Mixed QCD-EW corrections to dilepton production at the LHC

Contents

5.1 Introduction 127
5.2 Details of the calculation 130
5.2.1 Analytic results for the $q\bar{q}$ channel 130
5.2.2 Virtual contributions 132
5.3 Phenomenological results 136

5.1 Introduction

Let us briefly recap what we have achieved so far. In Chapter 1 we have highlighted the main bottlenecks of higher order calculations, namely scattering amplitudes and the appearance of infrared divergences, and we dealt with each of them in Chapters 2 and 3 respectively. In Chapter 4 we saw a phenomenological application where a full NNLO treatment was not strictly necessary as we were able to get reliable results in the soft-virtual approximation. In this chapter, we want to present another interesting phenomenological analysis where all the ingredients and tools that we learnt so far are necessary in full glory. This is the calculation

of mixed QCDxEW corrections to the neutral current Drell-Yan process in the high invariant mass region. It is the same process that we took as an example to explain how the NSC subtraction method works, so we rely on that for the infrared subtraction part of this calculation and we focus on its phenomenological implications here. Note that all the material that we present here is based on the analysis published in Ref. [119]. Let us now briefly highlight the relevance of this process for precision collider phenomenology.

The production of lepton pairs in hadron collisions, commonly referred to as the Drell-Yan (DY) process [215], continues to play an important role in tests of the SM of particle physics and in attempts to discover physics beyond it. In particular, many recent studies of the DY process [216, 217] have focused on the high invariant mass region of the lepton pair, where high-precision experimental results are becoming available.

Interest in the high invariant mass region stems from the fact that many extensions of the SM contain weakly-coupled states which can decay to lepton pairs. Even if such states are too heavy to be directly produced at the LHC, their presence can still be detected through searches for shape distortions in kinematic distributions.[1]

More generally, studies of dileptons with high invariant masses can be used to constrain heavy New Physics in a model-independent way, using the Standard Model Effective Field Theory (SMEFT) [219, 220]. In particular, the dilepton invariant mass distribution is affected by SMEFT operators that also impact the so-called *oblique parameters* [221] constrained within a few per mille precision using LEP data [222]. Since studies of the DY process in the high invariant-mass region are expected to reach only percent-level precision at the LHC, it may seem surprising that the LHC data could help to improve constraints on SMEFT operators. However, since such contributions are generated by dimension-6 operators, they grow quadratically with energy. Effectively, the higher energy of the LHC compensates for the limited precision, since the enhancement factor for $\sqrt{s} \simeq 1$ TeV is around 150 [223, 224]

[1] For a recent phenomenological study on this, see e.g. Ref. [218].

when compared to studies at $\sqrt{s} = m_Z$. Studies of dilepton pairs with high invariant mass may also help to elucidate the physical origin of flavour anomalies [225–228].

To achieve these goals, high-precision theoretical predictions within the SM are needed; in fact, to constrain the Wilson coefficients of SMEFT operators, percent-level precision is required. Since the strong coupling constant α_s is about 0.1, QCD corrections have to be accounted for through, at least, NNLO. At this perturbative order, both inclusive and fully-differential results are available [229–236]. Very recently, N^{3}LO QCD corrections to DY processes were calculated [237–242] and found to be close to a percent, motivating their inclusion at this level of precision. In addition to QCD corrections, EW contributions also need to be accounted for to achieve percent-level precision. The NLO EW corrections were calculated long ago [243–252], and found to be small, close to one percent for up to moderate values of the dilepton invariant mass. However, it is known that EW corrections are significantly enhanced at large invariant masses $\sqrt{s} \gg m_Z$ and can reach tens of percent in this region because of so-called *electroweak Sudakov logarithms* [253–256].

The enhancement of EW corrections at large dilepton invariant masses and the fact that QCD corrections can be as large as twenty percent at $\sqrt{s} \gg m_Z$, raise the question of the magnitude of mixed QCD-EW corrections and make it plausible that these corrections can reach $\mathcal{O}(1\%)$ at high invariant masses. If so, they become relevant for the many interesting phenomenological studies that were mentioned earlier. Although the impact of QCD and EW radiation has been studied using e.g. parton showers [257, 258], it is important to obtain predictions for the exact mixed QCD-EW corrections to DY, and their explicit computation is the goal of this chapter.

We note that mixed QCD-EW corrections have already been studied for *resonant* production of Z and W bosons [121, 123, 259–262] and were found to be small, close to one per mille. Although one may think that calculations of these corrections in the resonance region and in the high invariant mass region are technically similar, this is actually not the case. Indeed, in the resonance region, all contributions that connect initial and final states are suppressed by the ratio of the vector boson width

to its mass $\Gamma_V/m_V \sim 10^{-2}$ and can be neglected [263, 264]. Hence, when computing two-loop mixed QCD-EW corrections in such a case, it is sufficient to only consider corrections to the process $q\bar{q}' \to V$. However, in the high invariant mass region this is no longer the case and corrections to the full $q\bar{q}' \to \ell_1\bar{\ell}_2$ need to be considered.

This leads to two significant complications with respect to the resonant case. First, one has to deal with the full $q\bar{q}' \to \ell_1\bar{\ell}_2$ two-loop amplitude and compute Feynman integrals that include e.g. two-loop four-point functions with various internal and external masses. The relevant integrals and helicity amplitudes have been computed in Refs. [124, 265–269] and can be used to describe the mixed QCD-EW virtual corrections in the high invariant mass region. Second, as we already explained throughout this thesis, computing fully differential second-order corrections to the $q\bar{q}' \to \ell_1\ell_2$ process requires properly extracting soft and collinear singularities arising from real emission of partons from the initial *and* final state. This task has already been completed in Chapter 3. In this chapter, we briefly summarize the main features of our calculation, and discuss its phenomenological implications[2].

5.2 Details of the calculation

Since the subtraction of infrared divergences for this process has already been treated in Chapter 3, in this section we will only quote the analytic results for the integrated subtraction terms in the dominant $q\bar{q}$ channel. The analytic results for the other relevant partonic channels can be found in Ref. [119]. We will also give some details on the virtual amplitudes involved in this process.

5.2.1 Analytic results for the $q\bar{q}$ channel

Following the discussion in Chapter 3, we obtain a finite partonic cross section $d\hat{\sigma}^{q\bar{q}}_{\text{mix},g\gamma}$ defined in Eq. (3.31). We find it convenient to write it as a combination of

[2]We point out that an independent calculation of the mixed QCD-EW corrections to the production of massive dileptons was performed in Ref. [270]. In the high invariant-mass region, Ref. [270] observed percent-level effects. Although a high-precision direct comparison of our results with the ones in Ref. [270] is not possible because this reference only performed studies in the so called "bare lepton" setup (i.e. without recombining leptons and photons), our analysis qualitatively confirms these findings.

four terms that describe processes with different multiplicities of resolved final-state particles and/or distinct kinematic configurations. We write

$$d\hat{\sigma}^{q\bar{q}}_{\mathrm{mix},g\gamma} = d\hat{\sigma}^{q\bar{q}}_{\mathrm{el},g\gamma} + d\hat{\sigma}^{q\bar{q}}_{\mathrm{bt},g\gamma} + d\hat{\sigma}^{q\bar{q}}_{\mathcal{O}_{\mathrm{nlo}},g\gamma} + d\hat{\sigma}^{q\bar{q}}_{\mathrm{reg},g\gamma} \tag{5.1}$$

For the sake of simplicity, we present results in the center-of-mass frame of the colliding partons and choose $E_{\max} = E_1 = E_2 \equiv E_c = \sqrt{s}/2$.

The last term in Eq. (5.1) corresponds to the fully-regulated contribution

$$2s \cdot d\hat{\sigma}^{q\bar{q}}_{\mathrm{reg},g\gamma} = \Big\langle (I - S_g)(I - S_\gamma)\, \Omega_1^{q\bar{q}}\, F_{\mathrm{LM}}(1_q, 2_{\bar{q}}, 3, 4|5_g, 6_\gamma) \Big\rangle\,, \tag{5.2}$$

with $\Omega_1^{q\bar{q}}$ defined in Eq. (3.43). It can be computed numerically in four dimensions without further ado.

The *elastic* cross section $d\hat{\sigma}^{q\bar{q}}_{\mathrm{el},g\gamma}$ contains all contributions with Born kinematics. It reads

$$\begin{aligned}
2s \cdot d\hat{\sigma}^{q\bar{q}}_{\mathrm{el},g\gamma} = {} & \Big\langle F^{(\mathrm{QCD}\times\mathrm{EW}),\,\mathrm{fin}}_{\mathrm{LVV+LV^2}}(1_q, 2_{\bar{q}}, 3, 4) \Big\rangle \\
& + [\alpha] \left\langle \left[\mathcal{G}_{\mathrm{EW}} + 3Q_q^2 \log\left(\frac{s}{\mu^2}\right) \right] F^{(\mathrm{QCD}),\,\mathrm{fin}}_{\mathrm{LV}}(1_q, 2_{\bar{q}}, 3, 4) \right\rangle \\
& + [\alpha_s]\, C_F \left[\frac{2}{3}\pi^2 + 3\log\left(\frac{s}{\mu^2}\right) \right] \Big\langle F^{(\mathrm{EW}),\,\mathrm{fin}}_{\mathrm{LV}}(1_q, 2_{\bar{q}}, 3, 4) \Big\rangle \\
& + [\alpha]\,[\alpha_s]\, C_F \left\langle \left\{ Q_q^2 \left[-\frac{4\pi^4}{45} + \Big(2\pi^2 + 32\zeta_3\Big) \log\left(\frac{s}{\mu^2}\right) \right.\right.\right. \\
& \left.\left.\left. + \left(9 - \frac{4\pi^2}{3}\right) \log^2\left(\frac{s}{\mu^2}\right) \right] + \mathcal{G}_{\mathrm{EW}} \left(\frac{2\pi^2}{3} + 3\log\left(\frac{s}{\mu^2}\right) \right) \right\} F_{\mathrm{LM}}(1_q, 2_{\bar{q}}, 3, 4) \right\rangle\,,
\end{aligned} \tag{5.3}$$

where the function $\mathcal{G}_{\mathrm{EW}}$ already appeared at NLO and was defined in Eq. (3.27), while $F^{(\mathrm{QCD}\times\mathrm{EW}),\,\mathrm{fin}}_{\mathrm{LVV+LV^2}}, F^{(\mathrm{QCD}),\,\mathrm{fin}}_{\mathrm{LV}}, F^{(\mathrm{EW}),\,\mathrm{fin}}_{\mathrm{LV}}$ were defined in Eq. (3.61).

The boosted contribution reads

$$\begin{aligned}
2s \cdot d\sigma^{q\bar{q}}_{\mathrm{bt},g\gamma} = {} & [\alpha]\,[\alpha_s]\, 2C_F\, Q_q^2 \\
& \times \int_0^1 dz_1 dz_2\, \tilde{P}^{\mathrm{NLO}}_{qq}(z_1, E_c) \left\langle \frac{F_{\mathrm{LM}}(z_1 \cdot 1, z_2 \cdot 2, 3, 4)}{z_1\, z_2} \right\rangle \tilde{P}^{\mathrm{NLO}}_{qq}(z_2, E_c) \\
& + \sum_{i=1}^{2} \int_0^1 dz\, \tilde{P}^{\mathrm{NLO}}_{qq}(z, E_c) \Big[[\alpha]\, Q_q^2 \Big\langle F^{(i),(\mathrm{QCD}),\,\mathrm{fin}}_{\mathrm{LV}}(1_q, 2_{\bar{q}}, 3, 4; z) \Big\rangle \\
& \qquad + [\alpha_s]\, C_F \Big\langle F^{(i),(\mathrm{EW}),\,\mathrm{fin}}_{\mathrm{LV}}(1_q, 2_{\bar{q}}, 3, 4; z) \Big\rangle \Big]
\end{aligned}$$

$$
\begin{aligned}
&+ [\alpha]\, Q_q^2 \sum_{i=1}^{2} \int_0^1 dz \left\langle \mathcal{O}^g_{\text{nlo}} \left[\tilde{P}^{\text{NLO}}_{qq}(z, E_c) \right.\right. \\
&\qquad\qquad \left.\left. + \tilde{\omega}^{\gamma i, gi}_{\gamma \| i}\, \log \eta_{i5}\, \bar{P}^{\text{AP},0}_{qq,R}(z) \right] F^{(i)}_{\text{LM}}(1_q, 2_{\bar{q}}, 3, 4 | 5_g; z) \right\rangle \\
&+ [\alpha_s]\, C_F \sum_{i=1}^{2} \int_0^1 dz \left\langle \mathcal{O}^{\gamma}_{\text{nlo}} \left[\tilde{P}^{\text{NLO}}_{qq}(z, E_c) \right.\right. \\
&\qquad\qquad \left.\left. + \tilde{\omega}^{\gamma i, gi}_{g \| i}\, \log \eta_{i5}\, \bar{P}^{\text{AP},0}_{qq,R}(z) \right] F^{(i)}_{\text{LM}}(1_q, 2_{\bar{q}}, 3, 4 | 5_\gamma; z) \right\rangle \\
&+ [\alpha]\, [\alpha_s]\, C_F \sum_{i=1}^{2} \int_0^1 dz \left\langle \left\{ Q_q^2\, P^{\text{NNLO}}_{qq}(z, E_c) + \tilde{P}^{\text{NLO}}_{qq}(z, E_c) \right.\right. \\
&\times \left.\left. \left[Q_e^2\, G_{e^2} + 2 Q_q Q_e \left(G^{(1,2)}_{eq} + (-1)^i \log\left(\frac{s_{i3}}{s_{i4}} \right) \log(z) \right) \right] \right\} F^{(i)}_{\text{LM}}(1_q, 2_{\bar{q}}, 3, 4; z) \right\rangle .
\end{aligned}
\tag{5.4}
$$

Finally, the $\mathcal{O}_{\text{nlo}}$ term reads

$$
\begin{aligned}
2s \cdot d\sigma^{q\bar{q}}_{\mathcal{O}_{\text{nlo}}, g\gamma} &= \left\langle \mathcal{O}^g_{\text{nlo}}\, F^{(\text{EW}),\,\text{fin}}_{\text{LV}}(1_q, 2_{\bar{q}}, 3, 4 | 5_g) \right\rangle \\
&+ \left\langle \mathcal{O}^{\gamma}_{\text{nlo}}\, F^{(\text{QCD}),\,\text{fin}}_{\text{LV}}(1_q, 2_{\bar{q}}, 3, 4 | 5_\gamma) \right\rangle \\
&+ [\alpha] \left\langle \mathcal{O}^g_{\text{nlo}} \left[Q_q^2 \left(\frac{2}{3}\pi^2 + 3 \log\left(\frac{s}{\mu^2} \right) \right) + 2 Q_q Q_e\, G^{(1,2)}_{eq} + Q_e^2\, G_{e^2} \right] F_{\text{LM}}(1_q, 2_{\bar{q}}, 3, 4 | 5_g) \right\rangle \\
&+ [\alpha_s]\, C_F \left[\frac{2}{3}\pi^2 + 3 \log\left(\frac{s}{\mu^2} \right) \right] \left\langle \mathcal{O}^{\gamma}_{\text{nlo}}\, F_{\text{LM}}(1_q, 2_{\bar{q}}, 3, 4 | 5_\gamma) \right\rangle .,
\end{aligned}
\tag{5.5}
$$

where $\tilde{P}^{\text{NLO}}_{qq}(z, E)$ and $\bar{P}^{\text{AP},0}_{qq,R}(z)$ are reported in Eq. (B.9), while $P^{\text{NNLO}}_{qq}(z, E_c)$ is defined in Eq. (B.10). Finally, the functions G_{eq} and G_{e^2} in Eq. (5.4) and Eq. (5.5) are given by

$$
\begin{aligned}
G^{(i,j)}_{eq} =& \,\text{Li}_2(1 - \eta_{i3}) - \text{Li}_2(1 - \eta_{i4}) - \text{Li}_2(1 - \eta_{j3}) + \text{Li}_2(1 - \eta_{j4}) \\
&+ \left[\frac{3}{2} - \log\left(\frac{E_3}{E_c} \right) \right] \log\left(\frac{\eta_{i3}}{\eta_{j3}} \right) - \left[\frac{3}{2} - \log\left(\frac{E_4}{E_c} \right) \right] \log\left(\frac{\eta_{i4}}{\eta_{j4}} \right) , \\
G_{e^2} =& \, 13 - \frac{2}{3}\pi^2 + \log^2\left(\frac{E_3}{E_4} \right) + \left[3 - 2 \log\left(\frac{E_3 E_4}{E_c^2} \right) \right] \log(\eta_{34}) + 2\text{Li}_2(1 - \eta_{34}) .
\end{aligned}
\tag{5.6}
$$

5.2.2 Virtual contributions

In Chapter 3 we discussed the infrared singularity structure of virtual corrections but did not explain how to obtain the finite remainders, cf. Eqs. (3.22, 3.59, 3.61). In this section we briefly outline their computation, focusing especially on how the two-loop amplitudes presented in Ref. [124, 267] can be adapted to our subtraction framework and implemented in a numerical code.

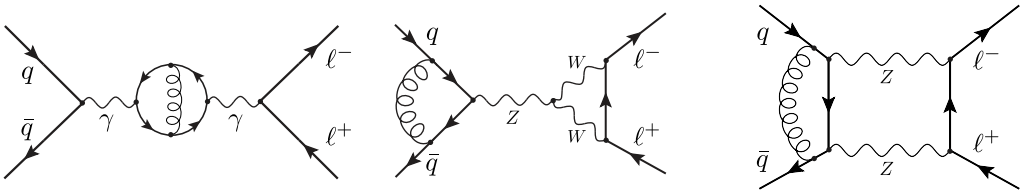


Figure 5.1: Examples of Feynman diagrams that contribute to two-loop amplitude: left: two-loop non-factorizable fermionic corrections, middle: factorizable corrections, right: bosonic non-factorizable corrections.

The complete calculation of mixed QCD-EW corrections to dilepton production requires the computation of various one- and two-loop contributions. We need one-loop QCD and electroweak corrections to the partonic process $q\bar{q} \to \ell^-\ell^+$, one-loop QCD corrections to the process $q\bar{q} \to \ell^-\ell^+ + \gamma$ and one-loop electroweak corrections to the process $q\bar{q} \to \ell^-\ell^+ + \text{jet}$ (and their crossings), as well as two-loop mixed QCD-EW corrections to the $q\bar{q} \to \ell^-\ell^+$ amplitude.

We first discuss one-loop contributions. Using the definition of infrared divergent and finite contributions described in Chapter 3, we obtain the finite part of the one-loop QCD correction

$$\left\langle F_{\text{LV}}^{(\text{QCD}),\,\text{fin}}(1_q, 2_{\bar{q}}, 3, 4)\right\rangle = \mathcal{C}^{\text{QCD}}\left\langle F_{\text{LM}}(1_q, 2_{\bar{q}}, 3, 4)\right\rangle, \quad \mathcal{C}^{\text{QCD}} = -8C_F\,\frac{\alpha_s(\mu)}{2\pi}\,. \quad (5.7)$$

The one-loop QCD amplitudes for the process $q\bar{q} \to \ell^-\ell^+ + \gamma$ are obtained from the well-known QCD amplitudes for the $q\bar{q} \to Z + j$ process [271]. For our code, we borrow the MCFM [180] implementation of these amplitudes. The one-loop electroweak corrections to the processes $q\bar{q} \to \ell^-\ell^+$ and $q\bar{q} \to \ell^-\ell^+ + g$ are instead computed using OpenLoops2 [84, 184, 272]. It is simple to obtain the infrared finite part of all these amplitudes, following the discussion in Chapter 3.

The double-virtual corrections to the process $q\bar{q} \to \ell^-\ell^+$ are calculated starting from the two-loop amplitudes presented in Refs. [124, 267]. We note, however, that in that reference only bosonic contributions to the amplitudes were considered, see middle and right diagrams in Fig. 5.1 for examples. Thus, we have calculated the additional terms arising from closed fermionic loops, see diagram in Fig. 5.1 left for an example. We note that fermionic corrections to dilepton production

in both the charged- and neutral-current cases were studied earlier in Ref. [273]. We have performed an independent calculation and checked our analytic results against those in Refs. [273, 274]. We also note that these contributions are the only ones relevant for the on-shell renormalization of the electroweak coupling α, and they are the only diagrams that make the extension of the complex mass scheme to $\mathcal{O}(\alpha\alpha_s)$ non-trivial, see Ref. [273] for further details.

In our implementation, we find it convenient to separate virtual corrections into a factorizable and a non-factorizable part. We define the former as the product of the one-loop EW contribution and the QCD K-factor Eq. (5.7):

$$\left\langle F^{\text{fact}}_{\text{LVV+LV}^2}(1_q, 2_{\bar{q}}, 3, 4)\right\rangle \equiv \mathcal{C}^{\text{QCD}} \left\langle F^{(\text{EW}),\text{fin}}_{\text{LV}}(1_q, 2_{\bar{q}}, 3, 4)\right\rangle . \tag{5.8}$$

Also, we separate the non-factorizable contribution into a bosonic part – extracted from Ref. [124] – and a fermionic part which accounts for closed fermion loops. In summary, we write the finite two-loop contribution to the cross section as

$$\begin{aligned}\left\langle F^{(\text{QCD}\times\text{EW}),\,\text{fin}}_{\text{LVV+LV}^2}(1_q, 2_{\bar{q}}, 3, 4)\right\rangle &= +\left\langle F^{\text{non-fact,ferm}}_{\text{LVV}}(1_q, 2_{\bar{q}}, 3, 4)\right\rangle \\ &+ \left\langle F^{\text{fact}}_{\text{LVV+LV}^2}(1_q, 2_{\bar{q}}, 3, 4)\right\rangle + \left\langle F^{\text{non-fact,bos}}_{\text{LVV}}(1_q, 2_{\bar{q}}, 3, 4)\right\rangle ,\end{aligned} \tag{5.9}$$

To avoid confusion, we note that the non-factorizable fermionic term only contains 1PI contributions similar to the leftmost diagram in Fig. 5.1. Indeed, it is easy to convince oneself that all reducible terms involving closed fermion loops are included in the factorizable part. A representative diagram for each of the three terms on the right-hand side of Eq. (5.9) is shown in Fig. 5.1.

The reason for separating the two-loop virtual corrections into factorizable and non-factorizable parts is that the former should be dominant at high-energy since they contain leading Sudakov logarithms. Indeed, we have checked that the non-factorizable contribution to the cross section is typically an order of magnitude smaller than the factorizable one. This happens across the entire high invariant mass phase space that we have investigated. The practical advantage of this observation is that the non-factorizable contribution – whose numerical evaluation is CPU expensive – can be determined to a much smaller accuracy to obtain the cross section with a target precision. We also note that the separation of two-loop virtual

corrections shown in Eq. (5.9) allows us to capture the bulk of the contribution coming from virtual top quarks, as we now explain. Computing such contributions exactly for the full two-loop amplitude is beyond the reach of current technology. As a consequence, they were dropped in Ref. [124]. Here, we neglect them in the bosonic non-factorizable term but include them in all the other contributions. Since bosonic non-factorizable contributions should be subdominant, this approach indeed allows us to capture the leading top-quark effects in a relatively simple way.

We now discuss how to obtain the bosonic non-factorizable contributions from the results of Ref. [124]. This reference presents the result in terms of infrared subtracted finite helicity remainders, referred to as "hard functions". Hard functions that describe $\mathcal{O}(\alpha^i \alpha_s^j)$ corrections to the scattering amplitude are denoted as $\mathcal{H}^{(i,j)}$.[3] We stress that the $\mathcal{H}^{(i,j)}$ finite remainders do not include contributions arising from closed fermion loops. We also note that in Ref. [124] wave functions and masses are renormalized in the on-shell scheme but both the QCD and EW couplings are renormalized in the $\overline{\text{MS}}$ scheme. In contrast, here we renormalize the EW coupling on-shell, so in principle we should perform a scheme change. However, it is easy to convince oneself that such change does not affect the bosonic non-factorizable contribution. Hence, we can take the amplitudes from Ref. [124] as they are.

To obtain $F_{\text{LVV}}^{\text{non-fact,bos}}$, we first define the non-factorizable hard function

$$\mathcal{H}_{\text{non-fact}}^{(1,1)} = \mathcal{H}^{(1,1)} - \frac{\mathcal{H}^{(1,0)}\mathcal{H}^{(0,1)}}{\mathcal{H}^{(0,0)}}, \tag{5.10}$$

and then use it to compute a non-factorizable K-factor

$$K_{\text{LVV}}^{\text{non-fact,bos}} = \frac{1}{2}\frac{\sum\limits_{\text{spin,color}} \text{Re}\left[\mathcal{H}^{(0,0)*}\mathcal{H}_{\text{non-fact}}^{(1,1)}\right]}{\sum\limits_{\text{spin,color}} |\mathcal{H}^{(0,0)}|^2} + \Delta\mathcal{H}(\mu^2, s), \tag{5.11}$$

where

$$\begin{aligned}\Delta\mathcal{H}(\mu^2, s) =& Q_q^2\, C_F \left[-\frac{1}{8} + 29\zeta_2 - 30\zeta_3 - 22\zeta_4 \right. \\ & \left. - \left(\frac{3}{2} - 12\zeta_2 + 24\zeta_3\right) \log\left(\frac{\mu^2}{s}\right) \right].\end{aligned} \tag{5.12}$$

[3] We note that compared to Ref. [124] we have dropped the helicity labels to simplify the notation.

The non-factorizable bosonic contribution to the cross section then reads

$$\left\langle F_{\rm LVV}^{\rm non-fact,bos}(1_q,2_{\bar{q}},3,4)\right\rangle = \frac{\alpha_s(\mu)}{2\pi}\frac{\alpha}{2\pi}\left\langle K_{\rm LVV}^{\rm non-fact,bos}F_{\rm LM}(1_q,2_{\bar{q}},3,4)\right\rangle . \tag{5.13}$$

We note that the $\Delta\mathcal{H}$ term in Eq. (5.12) appears because the definition of the two-loop finite remainders in Ref. [124] is slightly different from ours, cf. Eq. (3.61). We also note that the $\Delta\mathcal{H}$ term is the only source of explicit scale dependence in the double-virtual finite contribution to the cross section $\left\langle F_{\rm LVV+LV^2}^{\rm (QCD\times EW),\,fin}\right\rangle$.

We conclude this section by briefly discussing numerical implementation of these results. We have developed an efficient `C++` code for the numerical evaluation of the finite remainders of the non-factorizable two-loop bosonic corrections computed in Ref. [124] where results are are given in terms of complicated rational functions multiplying Goncharov polylogarithms. We have minimized the set of rational functions by finding $\mathbb{Q}$-linear relations among them [56, 275, 276], performed a partial fraction decomposition with minimal denominators powers [56] using the package `MultivariateApart` [124], and identified common subexpressions to optimize the performance. For the evaluation of the Goncharov polylogarithms we employ the HANDYG library [277].[4] The total evaluation time of the double-virtual contributions for a single phase-space point is, on average, about 0.7 s. We have also performed an independent MATHEMATICA implementation of Eq. (5.13) and found perfect agreement with the `C++` result for a random kinematic configuration.

5.3 Phenomenological results

We are now in position to perform a phenomenological study of dilepton production at high invariant mass. We begin by specifying the renormalization scheme and the input parameters. As we have mentioned, wave functions, masses and the electric charge are renormalized on-shell. The strong coupling and parton distribution functions are instead renormalized in the $\overline{\rm MS}$ scheme. We use the G_μ input scheme (already employed in Chapter 4) for the EW parameters. We

[4] As a cross-check, we have also used the `PolyLogTools` package of Ref. [278], which employs GINAC [279, 280] for the numerical evaluation of Goncharov polylogarithms, to compute the two-loop amplitudes. We found perfect agreement with the results obtained with HANDYG.

also employ the complex-mass scheme [281] and its extension to $\mathcal{O}(\alpha\alpha_s)$ case as described in Ref. [273].

We consider proton-proton collisions at 13.6 TeV center-of-mass energy. We use the `NNPDF31_nnlo_as_0118_luxqed` [185] parton distribution functions, available through the `LHAPDF` [186] library, for *all* computations reported in this section. We use the strong coupling constant α_s as provided by the PDF set; numerically, $\alpha_s(m_Z) = 0.118$. For the electroweak input parameters, the following values are used $m_Z = 91.1876$ GeV, $\Gamma_Z = 2.4952$ GeV, $m_W = 80.398$ GeV, $\Gamma_W = 2.1054$ GeV, $m_H = 125$ GeV, $\Gamma_H = 4.165$ MeV, $m_t = 173.2$ GeV and $G_F = 1.16639 \cdot 10^{-5}$ GeV^{-2}. With these input parameters, the fine structure constant reads $\alpha = 1/132.277$.

We note that since we work with massless leptons, their momenta are not collinear-safe quantities. For this reason, we cluster photons and leptons into "lepton jets", that are often referred to as "dressed leptons" in the literature. We do that if the separation between leptons and photons $R_{\ell\gamma} = \sqrt{(y_\ell - y_\gamma)^2 + (\varphi_\ell - \varphi_\gamma)^2}$ is smaller than R_{cut}, which we choose to be $R_{\text{cut}} = 0.1$. We recombine momenta in the so-called E scheme, i.e. to obtain the dressed-lepton momentum we sum the four-momenta of the clustered leptons and photons. For numerical computations, we take the renormalization scale μ_R and the factorization scale μ_F to be equal, and we choose the invariant mass of the (dressed) dilepton system divided by two i.e. $\mu_F = \mu_R = \mu = m_{\ell\ell}/2$ as the central value. Scale uncertainty is estimated by increasing or decreasing the scale μ by a factor of two.

Following the ATLAS analysis in the high invariant mass region [282], we define the fiducial region by requiring

$$m_{\ell\ell} > 200\,\text{GeV}\,, \quad p_{T,\ell^\pm} > 30\,\text{GeV}\,, \quad \sqrt{p_{T,\ell^-} p_{T,\ell^+}} > 35\,\text{GeV}\,, \quad |y_{\ell^\pm}| < 2.5\,. \tag{5.14}$$

We note, however, that in variance to Ref. [282] we do not impose asymmetric cuts on the lepton transverse momenta but we adopt the product cuts proposed in Ref. [188] and already employed in Chapter 4. We also note that all quantities that appear in Eq. (5.14), are defined in terms of dressed leptons. This applies

σ[fb]	$\sigma^{(0,0)}$	$\delta\sigma^{(1,0)}$	$\delta\sigma^{(0,1)}$	$\delta\sigma^{(2,0)}$	$\delta\sigma^{(1,1)}$
$q\bar{q}$	1561.42	340.31	−49.907	44.60	−16.80
$\gamma\gamma$	59.645		3.166		
qg		0.060		−32.66	1.03
$q\gamma$			−0.305		−0.207
$g\gamma$					0.2730
gg				1.934	
sum	1621.06	340.37	−47.046	13.88	−15.71

Table 5.1: Results for fiducial cross sections, in femtobarns, for central value of the renormalization and factorization scales. Contributions of different partonic channels are shown separately. Selection cuts for final-state leptons and jets are are given in Eq. (5.14). See text for further details.

to leptons' transverse momenta and rapidities $p_{T,\ell}$ and y_ℓ, respectively, as well as to the dilepton invariant mass $m_{\ell\ell}$.

To discuss the impact of the various higher-order corrections, we find it convenient to introduce the following notation for the differential cross section $d\sigma$, and its integrated counterpart $\delta\sigma$

$$d\sigma = \sum_{i,j=0} d\sigma^{(i,j)}\,, \qquad \delta\sigma^{(i,j)} = \int d\sigma^{(i,j)} \quad \text{with} \quad \sigma^{(0,0)} \equiv \delta\sigma^{(0,0)}\,. \tag{5.15}$$

In the above equation, $d\sigma^{(0,0)}$ and $\sigma^{(0,0)}$ represent the LO cross sections while $d\sigma^{(i,j)}$ and $\delta\sigma^{(i,j)}$ with $i,j>0$ stand for contributions to cross sections at order $\mathcal{O}(\alpha_s^i\alpha^j)$.

The results for fiducial cross sections are summarized in Table 5.1. We note that we have compared our NLO QCD and EW results against `Sherpa` [283] and `MoCaNLO+Recola` [284]. We have found perfect agreement for all the channels listed in Table 5.1. We observe that NLO QCD corrections increase the leading order cross section by about twenty percent, the NNLO QCD corrections change it by about 0.9%, and NLO electroweak corrections reduce it by about 3%. We note that numerical results reported in Table 5.1 are consistent with expectations based on the magnitude of the respective coupling constants, although the NNLO QCD corrections are slightly smaller than could have been anticipated. In particular, NLO EW corrections are compatible with a naive power counting $\delta^{\rm EW} \sim \alpha/\sin^2\theta_W \sim 0.03$, where θ_W is the weak mixing angle.

An interesting feature of the results shown in Table 5.1 is that the contribution of the diphoton channel at leading order, where dileptons are produced directly in collisions of photon "partons" that originate from the proton, is quite large, about 3.6% of the total cross section. The reason for that is the enhancement of this contribution by a logarithm $\ln\left(m^2_{\ell\ell}/p^2_{T,\ell^\pm}\right) \sim 5$. We also note that there is a strong cancellation between this contribution and the NLO electroweak corrections.

We observe that the NLO QCD correction does not show the cancellation between $q\bar{q}$ and qg partonic channels that is observed in the resonant region; in fact, we see that at high invariant masses, QCD corrections to the $q\bar{q}$ channel are the dominant ones with the qg channel playing only a minor role. The picture changes if we consider scales $\mu = m_{\ell\ell}/4$ or $\mu = m_{\ell\ell}$, in which case the contributions of the qg channels are of the same order as the $q\bar{q}$ ones. At NNLO QCD, there is a strong cancellation between these two partonic channels making this correction even smaller than the NLO EW one. This, of course, illustrates the unphysical nature of individual partonic channels at higher orders.

It follows from Table 5.1 that mixed QCD-EW corrections are quite large and decrease the fiducial cross section by about -1.0%, whereas an estimate based on power counting suggests that $\mathcal{O}(\alpha\alpha_s)$ corrections should be at the per mille level. In fact, the mixed QCD-EW corrections are about 30% of the electroweak corrections and *larger* than the NNLO QCD ones. These corrections receive dominant contribution from the $q\bar{q}$ partonic channel; all other channels affect fiducial cross sections by a much smaller amount.

It is also instructive to compare the magnitude of the mixed QCD-EW corrections with the theoretical uncertainty. To estimate it, we increase and decrease the central scale $\mu = m_{\ell\ell}/2$ by a factor of two and also choose a different input scheme for the electroweak parameters. In particular, we consider the so-called $\alpha(m_Z)$-scheme where $\alpha(m_Z) = 1/128$ is an input parameter, and the other input parameters are kept fixed.[5] We then take the envelope of these results as a proxy for the theoretical uncertainty. We find that the uncertainty of the leading order cross section is $+12\%$

[5]For a comprehensive discussion of electroweak input schemes see e.g. Ref. [285].

and -6%. If the cross section is computed through NNLO QCD and NLO EW, but the mixed QCD-EW corrections are neglected, we find

$$\sigma^{(0,0)} + \delta\sigma^{(1,0)} + \delta\sigma^{(0,1)} + \delta\sigma^{(2,0)} = 1928.3^{+1.8\%}_{-0.15\%} \text{ fb}. \tag{5.16}$$

We note that the main source of the theoretical uncertainty in Eq. (5.16) is the input-scheme change which, however, is reduced from about 6% at leading order to about two percent when NLO EW contributions are accounted for. The mixed QCD-electroweak corrections are about -1% and, thus, comparable in size to the theoretical uncertainty in Eq. (5.16). Upon including them, the central value of the fiducial cross section and its uncertainty decrease. We obtain

$$\sigma_{\text{QCD}\times\text{EW}} \equiv \sigma^{(0,0)} + \delta\sigma^{(1,0)} + \delta\sigma^{(0,1)} + \delta\sigma^{(2,0)} + \delta\sigma^{(1,1)} = 1912.6^{+0.65\%}_{-0.04\%} \text{ fb}. \tag{5.17}$$

The main reason behind the reduction of uncertainty with respect to Eq. (5.16) is that now the mixed QCD-EW corrections remove a large source of input-scheme dependence coming from the NLO QCD contribution.

It is well-known that at high invariant masses, EW corrections are dominated by the universal Sudakov logarithms. This implies that the mixed QCD-electroweak corrections should be well described by the product of QCD and electroweak corrections, at least inasmuch as the leading logarithms are concerned. Although it is not clear when this, "factorized", approximation becomes a good representation of the full result, it is easy to check its efficacy by comparing exact and approximate results for mixed QCD-EW corrections at various values of $m_{\ell\ell}$. To this end, we consider four invariant-mass windows defined as follows

$$\begin{aligned}
&\Phi^{(1)}: \ 200 \text{ GeV} < m_{\ell\ell} < 300 \text{ GeV}, \\
&\Phi^{(2)}: \ 300 \text{ GeV} < m_{\ell\ell} < 500 \text{ GeV}, \\
&\Phi^{(3)}: \ 500 \text{ GeV} < m_{\ell\ell} < 1.5 \text{ TeV}, \\
&\Phi^{(4)}: \ 1.5 \text{ TeV} < m_{\ell\ell} < \infty.
\end{aligned} \tag{5.18}$$

For each of these windows, we apply the $m_{\ell\ell}$-independent kinematic cuts described in Eq. (5.14). To compare the quality of the factorized approximation in each of

σ [fb]	$\sigma^{(0,0)}$	$\delta\sigma^{(1,0)}$	$\delta\sigma^{(0,1)}$	$\delta\sigma^{(2,0)}$	$\delta\sigma^{(1,1)}$	$\delta\sigma^{(1,1)}_{\text{fact.}}$	$\sigma_{\text{QCD}\times\text{EW}}$
$\Phi^{(1)}$	1169.8	254.3	−30.98	10.18	−11.11	−6.734	$1392.3^{+0.77\%}_{-0.04\%}$
$\Phi^{(2)}$	368.29	71.91	−11.891	2.85	−4.06	−2.321	$427.1^{+0.41\%}_{-0.02\%}$
$\Phi^{(3)}$	82.08	14.31	−4.094	0.691	−1.013	−0.7137	$91.97^{+0.15\%}_{-0.14\%}$
$\Phi^{(4)} \times 10$	9.107	1.577	−1.124	0.146	−0.2064	−0.1946	$9.500_{-0.97\%}$

Table 5.2: Fiducial cross sections in the invariant mass windows specified through Eq. (5.18). We show the LO predictions, $\sigma^{(0,0)}$ and the higher-order ones, $\delta\sigma^{(i,j)}$. In order to improve readability, we multiply the fiducial cross sections in the $\Phi^{(4)}$ phase space by a factor 10. In the next-to-last column we quote the result of the factorized approximation defined in Eq. (5.19). In the last column we show our best predictions obtained by including all the higher-order corrections considered in this manuscript, cf. Eq. (5.17).

the four mass regions, we define approximate mixed corrections as follows

$$\delta\sigma^{(1,1)}_{\text{fact}} = \delta^{(1,0)}_{\text{NLO}}\, \delta^{(0,1)}_{\text{NLO}}\, \sigma^{(0,0)}, \tag{5.19}$$

where

$$\delta^{(1,0)}_{\text{NLO}} = \frac{\delta\sigma^{(1,0)}}{\sigma^{(0,0)}}, \qquad \delta^{(0,1)}_{\text{NLO}} = \frac{\delta\sigma^{(0,1)}}{\sigma^{(0,0)}}. \tag{5.20}$$

The approximate mixed corrections are compared to their exact counterparts in Table 5.2. We find that $\delta\sigma^{(1,1)}_{\text{fact}}$ captures the main features of the mixed corrections but it does underestimate them for lower invariant masses. At high invariant masses $m_{\ell\ell} \gtrsim 1$ TeV the situation changes and the quality of the factorized approximation improves. For the highest invariant-mass window the factorized approximation captures more than 90% of the exact result. This behavior is not surprising since, as we already mentioned, the factorized approximation correctly reproduces the leading Sudakov logarithms that are expected to provide the dominant contribution at large invariant masses. In this table, we also show our predictions for the quantity $\sigma_{\text{QCD}\times\text{EW}}$ defined in Eq. (5.17), i.e. including NLO QCD, NLO EW, NNLO QCD and mixed QCD-EW corrections, in the four invariant mass windows. We observe that the theoretical uncertainty, estimated by a simultaneous variation of scales and input scheme, is below the percent level across the different windows considered.

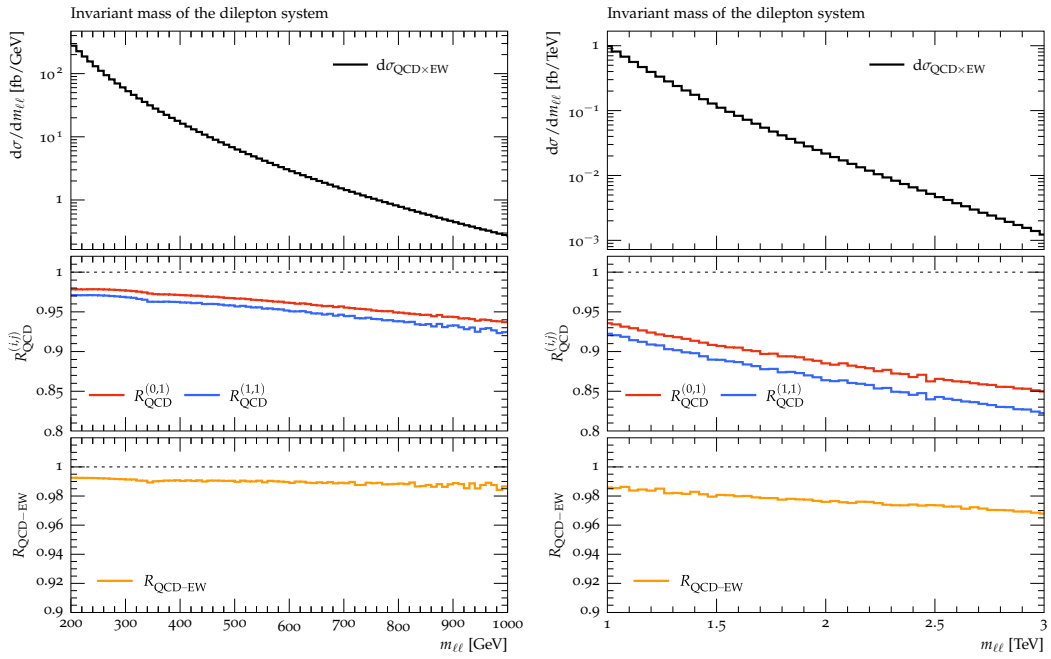


Figure 5.2: Dilepton invariant mass distribution for the Drell-Yan process $pp \to \ell^-\ell^+$ at the 13.6 TeV LHC. The upper pane shows our best prediction for $d\sigma$ which included NLO QCD, NNLO QCD, NLO EW, and mixed QCD-EW corrections. The middle pane shows the impact of the NLO EW and mixed QCD-EW corrections, see Eq. 5.22 for the definition of the ratios. The lower pane shows the ratio of mixed QCD-EW corrections to a result which includes both QCD and EW NLO corrections, but not NNLO QCD and mixed QCD-EW ones. The left plot shows results in the range 200 GeV $< m_{\ell\ell} <$ 1 TeV, the right plot shows the range 1 TeV $< m_{\ell\ell} <$ 3 TeV. See text for details.

We now turn to the discussion of kinematic distributions. The dilepton invariant mass distribution is shown in Fig. 5.2. There, the distributions in the upper panes include all corrections considered in this analysis

$$d\sigma_{\mathrm{QCD\times EW}} = d\sigma^{(0,0)} + d\sigma^{(1,0)} + d\sigma^{(0,1)} + d\sigma^{(2,0)} + d\sigma^{(1,1)}, \tag{5.21}$$

middle panes show the impact of the NLO EW and mixed QCD-EW corrections on the results computed through NLO QCD, and lower panes show the impact of the mixed QCD-EW corrections on cross sections computed through NLO QCD

and NLO EW accuracy. To this end, we define the following quantities

$$\begin{aligned} R^{(0,1)}_{\rm QCD} &= \frac{d\sigma^{(0,0)} + d\sigma^{(1,0)} + d\sigma^{(0,1)}}{d\sigma^{(0,0)} + d\sigma^{(1,0)}}, \\ R^{(1,1)}_{\rm QCD} &= \frac{d\sigma^{(0,0)} + d\sigma^{(1,0)} + d\sigma^{(0,1)} + d\sigma^{(1,1)}}{d\sigma^{(0,0)} + d\sigma^{(1,0)}}, \\ R_{\rm QCD-EW} &= R^{(1,1)}_{\rm QCD}/R^{(0,1)}_{\rm QCD} = \frac{d\sigma^{(0,0)} + d\sigma^{(1,0)} + d\sigma^{(0,1)} + d\sigma^{(1,1)}}{d\sigma^{(0,0)} + d\sigma^{(1,0)} + d\sigma^{(0,1)}}, \end{aligned} \tag{5.22}$$

and plot them in Fig. 5.2 as a function of the dilepton invariant mass. It follows from Fig. 5.2 that NLO EW corrections grow from $\mathcal{O}(-2\%)$ at $m_{\ell\ell} = 200$ GeV to $\mathcal{O}(-20\%)$ at 3 TeV, and that the mixed QCD-EW corrections follow the shape of the NLO EW ones. Nevertheless, $R_{\rm QCD-EW}$ is not entirely flat over the range of invariant masses that we consider; indeed, it slowly decreases from $\mathcal{O}(-1.5\%)$ at $m_{\ell\ell} \approx 200$ GeV to $\mathcal{O}(-4\%)$ at $m_{\ell\ell} \approx 3$ TeV. These results are consistent with those presented in Table 5.2 and are indicative of the presence of Sudakov logarithms in the virtual EW corrections, as mentioned previously. We note that the small dip in the middle pane at $m_{\ell\ell} \approx 340$ GeV originates from the $t\bar{t}$ thresholds in closed fermion loops that modify the propagators of the electroweak bosons.

While the magnitude of mixed QCD-electroweak corrections at large invariant masses is fairly easy to understand, their size at lower values of $m_{\ell\ell}$ is more puzzling as they seem to be enhanced relative to naive expectations. Indeed, it follows both from Table 5.1 and Table 5.2 that mixed QCD-EW corrections are only three times smaller than the EW corrections themselves and it is unclear why this is the case, given that one does not expect large Sudakov logarithms at such energy scales. One possibility is that the n_f-dependent terms, arising from quark loop insertions into massive vector boson propagators, are enhanced leading to a larger contribution from mixed QCD-EW corrections, as discussed in Ref. [273]. On the other hand, one should also keep in mind that NLO QCD corrections to leading order cross section are twenty percent whereas mixed QCD-EW corrections are thirty percent of the NLO EW contribution which implies that the difference is not too large. Hence, it can also be that these fairly large effects at small invariant masses are just the result of a numerical interplay of various contributions and that the observed enhancement is more or less accidental.

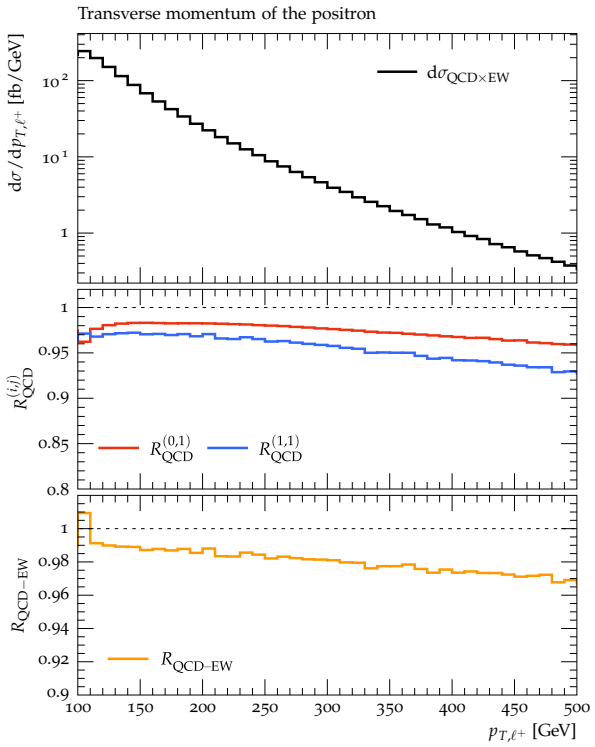


Figure 5.3: Transverse momentum distribution of the positively charged lepton. See the caption in Fig. 5.2 and the text for details.

We continue with the discussion of other observables. In Fig. 5.3 we show the transverse momentum distribution of the positively-charged lepton. Since at leading order the lepton transverse momentum $p_{T,\ell}$ is always smaller than $m_{\ell\ell}/2$, there is a correlation between the $p_{T,\ell}$ and the $m_{\ell\ell}$ distributions. Indeed, it follows from Fig. 5.3 that corrections to the transverse momentum distribution are similar to the ones to the $m_{\ell\ell}$ distribution, in that NLO EW corrections are negative and quite large, while the relative QCD-EW corrections are unusually large at low values of $p_{T,\ell}$, which give the largest contribution to the fiducial cross section. Mixed QCD-EW corrections largely follow the pattern of the NLO EW corrections. Nevertheless, the impact of the QCD-EW corrections does become slightly more important at higher values of $p_{T,\ell}$, amounting to around -3% on top of the NLO QCD and EW result at $p_{T,\ell} = 500\,\text{GeV}$.

Another interesting class of observables are rapidities and angular distributions. In left panes of Fig. 5.4 we show the rapidity of the dilepton system. We observe that

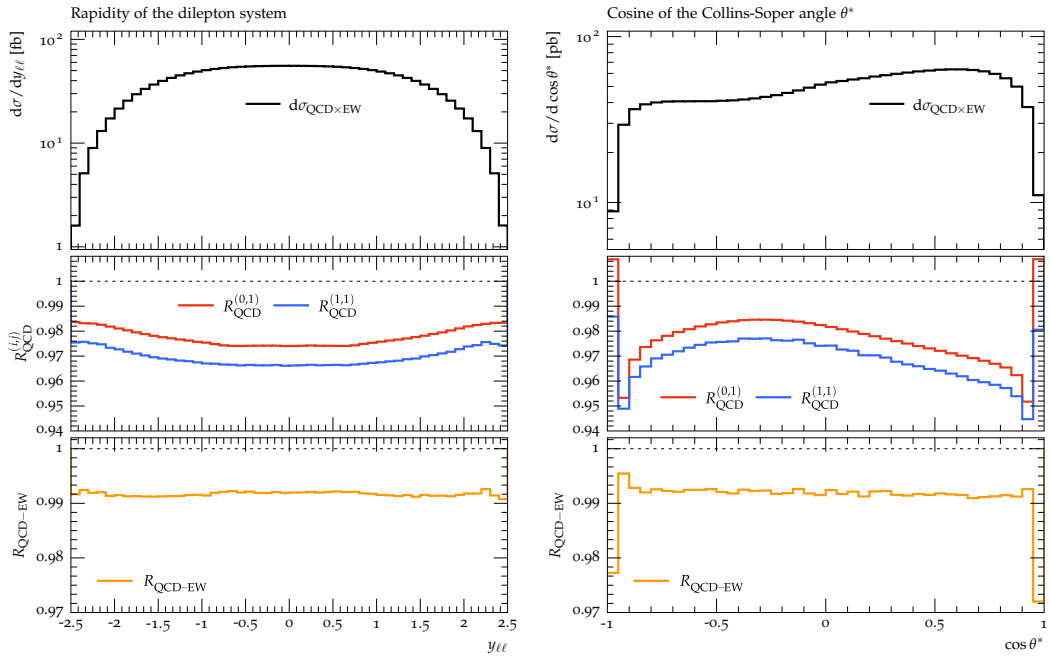


Figure 5.4: Distributions of the rapidity of the dilepton system and the cosine of the Collins-Soper angle. See the caption in Fig. 5.2 and the text for details.

both the NLO EW corrections and the mixed QCD-EW corrections are flat over the considered rapidity range and amount to $\mathcal{O}(-3\%)$ and $\mathcal{O}(-1\%)$, respectively. As the fiducial cross sections are dominated by low values of $m_{\ell\ell} \approx 200$ GeV, the corrections that we see in the rapidity distribution correspond to those shown in Table 5.1.

Angular distributions can be used to analyze the structure of the currents that facilitate the transition from quarks to leptons both within and beyond the Standard Model. Although these angular distributions can be computed in full generality, it is simpler to discuss an integrated quantity – the forward-backward asymmetry of a lepton relative to the direction of an incoming quark. A convenient variable that allows one to study such an asymmetry is the Collins-Soper angle [286], defined as follows

$$\cos\theta^* = \frac{p^+_{\ell^-} p^-_{\ell^+} - p^-_{\ell^-} p^+_{\ell^+}}{m\sqrt{m^2 + p^2_{\ell\ell,\perp}}} \times \mathrm{sgn}(p_{\ell\ell,z}) \,. \tag{5.23}$$

In Eq. (5.23), $p_i^{\pm} = E_i \pm p_{z,i}$ and $p_{\ell\ell} = p_{\ell^-} + p_{\ell^+}$. We show the $\cos\theta^*$ distribution for events in the fiducial volume Eq. (5.14) in the right panel of Fig. 5.4. Similar to the dilepton rapidity distribution, both the NLO EW and mixed QCD-EW

corrections to the Collins-Soper angle are flat and are comparable to corrections to the fiducial cross section, cf. Table 5.1.

It is clear from Fig. 5.4 that the distribution of the Collins-Soper angle is not symmetric and that there are more events with $\cos\theta^* > 0$ than with $\cos\theta^* < 0$. To quantify this effect, we consider the forward-backward asymmetry

$$A_{\rm FB} = \frac{\sigma_F - \sigma_B}{\sigma_F + \sigma_B}, \tag{5.24}$$

where

$$\sigma_F = \int\limits_0^1 \mathrm{d}\cos\theta^* \, \frac{\mathrm{d}\sigma(pp \to \ell^-\ell^+)}{\mathrm{d}\cos\theta^*}, \qquad \sigma_B = \int\limits_{-1}^0 \mathrm{d}\cos\theta^* \, \frac{\mathrm{d}\sigma(pp \to \ell^-\ell^+)}{\mathrm{d}\cos\theta^*}. \tag{5.25}$$

We calculate the forward-backward asymmetry for the fiducial phase space defined in Eq. (5.14) including all corrections computed in this thesis and find

$$A_{\rm FB} = 0.1580^{+0.15\%}_{-0.07\%} \,, \tag{5.26}$$

where the uncertainties are estimated from a simultaneous scale and input-scheme variations as described above. Omitting the mixed QCD-EW corrections changes the prediction in Eq. (5.26) by about 2 per mille which is again comparable with the uncertainty on the central value.

It is well-known that the forward-backward asymmetry increases with the invariant mass of dileptons. For this reason, it is instructive to study the forward-backward asymmetry and mixed QCD-electroweak corrections to it in the four $m_{\ell\ell}$ windows defined in Eq. (5.18). The results are shown in Table 5.3. There we display predictions for the forward-backward asymmetry that includes all corrections considered in this paper as well as the prediction for the forward-backward asymmetry without the mixed QCD-EW correction. We refer as $A_{FB}^{(2,0)+(1,1)}$ to the former and as $A_{FB}^{(2,0)}$ to the latter. We observe that the mixed QCD-EW corrections impact the value of $A_{\rm FB}$ below the percent level in the lower invariant mass windows, and reach -1.3% at high $m_{\ell\ell}$. To put these numbers into context, we note that if one considers a combined ATLAS+CMS luminosity of 6 ab^{-1}, one gets a few percent statistical uncertainty in the highest invariant mass region.

$A_{\rm FB}$	$A_{FB}^{(2,0)}$	$A_{FB}^{(2,0)+(1,1)}$
$\Phi^{(1)}$	$0.1442^{+0.05\%}_{-0.31\%}$	$0.1439^{+0.15\%}_{-0.08\%}$
$\Phi^{(2)}$	$0.1852^{+0.08\%}_{-0.40\%}$	$0.1847^{+0.10\%}_{-0.17\%}$
$\Phi^{(3)}$	$0.2401^{+0.13\%}_{-0.64\%}$	$0.2388^{+0.06\%}_{-0.45\%}$
$\Phi^{(4)}$	$0.3070^{+0.49\%}_{-1.5\%}$	$0.3030^{+0.19\%}_{-1.2\%}$

Table 5.3: Forward-backward asymmetry $A_{\rm FB}$ in the invariant mass windows specified through Eq. (5.18). We label as $A_{FB}^{(2,0)}$ the predictions including the LO contribution and higher order corrections from NLO-QCD, NLO-EW and NNLO-QCD, whereas $A_{FB}^{(2,0)+(1,1)}$ further includes the mixed QCD-EW correction.

6
Conclusions

In this thesis we covered the Arts and Crafts of particle phenomenology that allow us to describe the hard process of a high-energy scattering event at the LHC. In Chapter 1 we gave a brief overview on the theory of fundamental interactions that we rely upon when performing calculations: the Standard Model of particle physics. We summarized salient features of both the EW and strong sectors of the SM, including a brief discussion of the Higgs mechanism that ensures the consistency of the theory. We then moved to discussing perturbative methods in the SM and reviewed concepts such as asymptotic freedom, confinement, running coupling and renormalization group equations. These concepts are crucial in the context of higher order calculations, which are in turn needed to test the SM as the theory that describes nature. In the same chapter, we tried to argue that %-level precision physics is important in order to stress-test the SM and possibly get a handle on New Physics effects. In order to reach such a precision, higher-order calculations play a pivotal role.

We did this by considering a concrete example, Higgs production in gluon fusion at the LHC. By considering this example we were able to introduce many concepts that are the main characters of the rest of the thesis. Indeed in order to compute the cross section we needed to compute scattering amplitudes, immediately realizing how divergences come into play, especially divergences related to soft and collinear

configurations both in loop diagrams and in phase space integrals of real emission matrix elements. Scattering amplitudes and infrared divergences make up the "Crafts" part of this thesis, i.e. the part where we discussed the techniques that are needed to perform higher-order calculations. They were discussed in detail in Chapters 2 and 3 respectively.

In Chapter 2, we focused on scattering amplitudes. After briefly reviewing how they emerge as fundamental objects in QFT, we focused on the perturbative techniques that are nowadays used in multiloop calculations. We have done so by presenting one specific calculation, the calculation of five-points two loop scattering amplitudes in massless QCD. In this way, we were able to both present the techniques and also apply them to a state-of-the-art cutting-edge case. We argued how, in order to explore interesting QCD phenomena related to IR and high-energy physics, it is important to go beyond the large-N_c limit, and presented the main difficulties that one encounters when doing so. As an example, we gave details on the calculation of the four-quarks one-gluon amplitude. We computed it by summing up the Feynman diagrams, and dividing the amplitude into simpler building blocks that make the computation more accessible. We discussed the projection to scalar integrals via a tensor decomposition, the IBP reduction procedure and simplifications of the intermediate expressions. We arrived at expressions for the helicity amplitudes, UV renormalized and IR subtracted, which encode all the non-trivial physical information.

IR singularities were the main characters of Chapter 3. We argued that in order to obtain predictions for differential quantities one needs to be able to extract and cancel the divergences without integrating over the phase space of resolved final state particles. We described how subtraction schemes do this, and we considered one particular subtraction scheme, the NSC, focusing on the issues that arise at NNLO. Once again, we did this by means of a specific example, the subtraction of singularities in the case of mixed QCD-EW corrections to dilepton production at the LHC. This example is particularly instructive since it allowed us to introduce most of the concepts that are needed to perform NNLO subtraction but still working in

a simplified context. Indeed, in this case the double-soft radiation is completely factorized into the product of two eikonal currents, whereas the triple collinear configuration retains most of its NNLO complexity. This example is also useful for the analysis presented in Chapter 5, where the phenomenological implications of this process where considered. We also devoted the last two sections of Chapter 3 to a generalization of the NSC to the treatment of higher multiplicity processes. This concluded the "Crafts" part of the thesis.

The "Art" began in Chapter 4. There, we saw an application of the techniques learnt in the previous chapters, where, however, a simplified approach was enough in order to obtain sensible results. Indeed, we performed a NNLO analysis of interference effects in $H \to \gamma\gamma$ by employing the soft-virtual approximation. We argued that these effects are important since they can be used to constrain the Higgs boson decay width at hadron colliders. Indeed, we split the interference contribution into a real and an imaginary part, the former having the property of shifting the invariant mass distribution, and the latter to contribute to the total cross section. We then reviewed how the mass shift in the diphoton invariant mass can then be used to put a bound on the Higgs decay width. In passing, we were also able to provide an approximate NNLO prediction for the interference contribution to the total cross section, which amounts to almost -2%. In the last part of the Chapter we extended the interference studies to the rare decay channel $H \to Z\gamma$.

Finally, in Chapter 5, we presented another applications of the tools discussed in the "Crafts" part of this thesis. In this case, a full NNLO analysis was required. In particular we presented the calculation of mixed NNLO QCD-EW corrections to the neutral current Drell-Yan process in the high invariant mass region. The high invariant mass region is interesting since there the effects of electroweak corrections are enhanced due to the presence of Sudakov logarithms. For the subtraction part of the analysis, we relied on the method and results presented in Chapter 3. We observed how the mixed NNLO corrections are higher than what is expected by naive power counting, reaching the %-level impact.

Although tremendous concentrated community effort has been made in all the topics that we presented in this thesis, progress can still be made. On the scattering amplitude side, it would be interesting to see whether unitarity techniques can be pushed beyond one loop level, in order to avoid the Feynman diagram approach that we instead adopted. Furthermore, it would also be interesting to study various kinematic limits of the five points two loops amplitude presented, such as its behaviour in the limit where one external gluon becomes soft, or in the high energy limit. Doing this will give us a handle on soft and high energy factorization theorems at higher orders. On the subtraction side, there is work in progress toward its complete generalization to higher multiplicity processes. Phenomenological analysis can also be improved. For instance, in the case of interference effects in $H \to \gamma\gamma$ it would be nice to perform a full NNLO analysis in order to assess whether the soft-virtual is doing a good job or whether there are effects that are not being properly captured and that need the full NNLO machinery that we described throughout this thesis. In the case of mixed QCD-EW corrections, it would be interesting to perform a thorough study of Sudakov effects. We therefore hope to continue the exploration of these topics in the near future.

Appendices

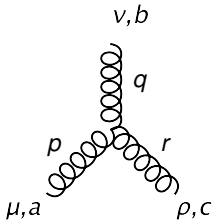
A
Feynman rules

In this appendix we collect the QCD and heavy-top EFT Feynman rules used for the calculations presented throughout this thesis. Note that we choose the Feynman gauge. The curly lines represent gluons, dotted lines represent ghosts and solid lines represent fermions. All particles are taken to be incoming.

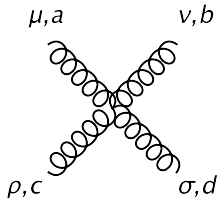
Propagators

$$
\begin{aligned}
&\mu,a \quad p \quad \nu,b = -i\,\delta^{ab} g^{\mu\nu} \frac{1}{p^2 + i\epsilon}\,, \\
&a \quad p \quad b = \delta^{ab} \frac{i}{p^2 + i\epsilon}\,, \\
&a,i \quad p \quad b,j = i\,\delta^{ab} \frac{\left(\not{p} + m\right)_{ji}}{p^2 - m^2 + i\epsilon}
\end{aligned}
\tag{A.1}
$$

QCD Vertices

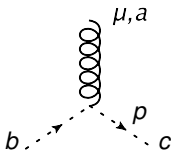


$$= -g_s f^{abc} \left[(p-q)^\rho g^{\mu\nu} + (q-r)^\mu g^{\nu\rho} + (r-p)^\nu g^{\rho\mu} \right] ,$$

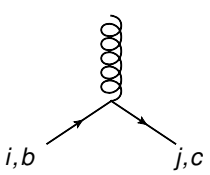


$$= -i\, g_s^2 \Big[f^{xac} f^{xbd} \left(g^{\mu\nu} g^{\rho\sigma} - g^{\mu\sigma} g^{\nu\rho} \right)$$

$$+ f^{xad} f^{xbc} \left(g^{\mu\nu} g^{\rho\sigma} - g^{\mu\rho} g^{\nu\sigma} \right) + f^{xab} f^{xcd} \left(g^{\mu\rho} g^{\nu\sigma} - g^{\mu\sigma} g^{\nu\rho} \right) \Big] , \tag{A.2}$$



$$= -g_s f^{abc} p^\mu ,$$



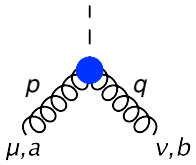
$$= -i\, g_s T^a_{bc} \left(\gamma^\mu \right)_{ji}$$

Heavy top mass EFT Vertices

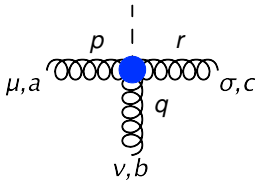
In the following, dashed lines represent scalar particles. We recall the lagrangian of the heavy-top EFT, given by

$$\mathcal{L} = -\frac{\lambda}{4} H\, G^a_{\mu\nu} G^{\mu\nu,a} , \tag{A.3}$$

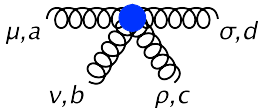
where H and $G^a_{\mu\nu}$ are the Higgs field and the gluon field strength tensor.



$$= -i\,\lambda\,\delta^{ab}\,(p^\nu q^\mu - g^{\mu\nu} p\cdot q)\ ,$$



$$= -\lambda\, g_s\, f^{abc}\,[g^{\mu\nu}(p-q)^\sigma + g^{\nu\sigma}(q-r)^\mu + g^{\sigma\mu}(r-p)^\nu]\ , \tag{A.4}$$



$$= -i\,\lambda\, g_s^2 \Big[f^{xac} f^{xbd}\,(g^{\mu\nu} g^{\rho\sigma} - g^{\mu\sigma} g^{\nu\rho})$$

$$+ f^{xad} f^{xbc}\,(g^{\mu\nu} g^{\rho\sigma} - g^{\mu\rho} g^{\nu\sigma}) + f^{xab} f^{xcd}\,(g^{\mu\rho} g^{\nu\sigma} - g^{\mu\sigma} g^{\nu\rho}) \Big]\ .$$

B
Splitting functions

In this section we collect the splitting functions that we have introduced in Chapters 3 and 5.

The splitting functions $P_{qq}^{\rm NLO}$ are defined as follows

$$\begin{aligned} P_{qq}^{\rm NLO}(z,L_i) &= \left[(1-z)^{-2\epsilon}P_{qq}(z) + \frac{1}{\epsilon}\,e^{-2\epsilon L_i}\,\delta(1-z)\right], \\ P_{qq}^{\rm NLO}(L_i) &= \gamma_{ee}^{22} + \frac{1}{\epsilon}\left(1-e^{-2\epsilon L_i}\right), \end{aligned} \tag{B.1}$$

where

$$\gamma_{ee}^{22} = -\int_0^1 dz\left\{\Big[z(1-z)\Big]^{-2\epsilon}P_{qq}\Big(z\Big) - 2\,\frac{(1-z)^{-2\epsilon}}{1-z}\right\}. \tag{B.2}$$

The triple-collinear splitting $P_{qq}^{TC}(z)$ is given by

$$\begin{aligned} P_{qq}^{TC}(z) = {}& \frac{1}{\epsilon}\left[\frac{3}{2}(1-z) + z\log(z) + \frac{3+z^2}{4(1-z)}\,\log^2(z)\right] + (1-z)\left[\frac{11}{2} - 6\log(1-z)\right] \\ & - \frac{2\pi^2\,z}{3} - \frac{z}{2}\,\log^2(z) - \frac{19+9z^2}{12(1-z)}\,\log^3(z) + 4z\,\mathrm{Li}_2(z) \\ & - \log(z)\left[z + \frac{\pi^2\,(5+3z^2)}{3(1-z)} + \frac{2(1+z^2)}{1-z}\,\mathrm{Li}_2(z)\right] \\ & + \frac{2(5+3z^2)}{1-z}\Big(\mathrm{Li}_3(z) - \zeta_3\Big) + \mathcal{O}(\epsilon)\,. \end{aligned} \tag{B.3}$$

The LO colour-stripped Altarelli-Parisi splitting functions that we have used are

$$\begin{aligned}
\bar{P}_{qq}^{\mathrm{AP},0}(z) &= 2\mathcal{D}_0(z) - (1+z) + \frac{3}{2}\,\delta(1-z)\,, \\
\bar{P}_{\bar{q}g}^{\mathrm{AP},0}(z) &= (1-z)^2 + z^2\,. \\
\bar{P}_{q\gamma}^{\mathrm{AP},0}(z) &= \frac{1+(1-z)^2}{z}\,.
\end{aligned} \tag{B.4}$$

In order to describe the single-collinear limits of the $q\bar{q} \to \ell^-\ell^+(g\gamma)$ we compute

$$\begin{aligned}
\left[\bar{P}_{qq}^{\mathrm{AP},0} \otimes \bar{P}_{qq}^{\mathrm{AP},0}\right](z) = {} & 6\mathcal{D}_0(z) + 8\mathcal{D}_1(z) + \left(\frac{9}{4} - \frac{2\pi^2}{3}\right)\delta(1-z) - \frac{\left(3z^2+1\right)\log(z)}{1-z} \\
& - z - 4(z+1)\,\log(1-z) - 5\,,
\end{aligned} \tag{B.5}$$

where $\otimes$ stands for the standard convolution product

$$\left[f \otimes g\right](z) = \int_0^1 dx\, dy\, f(x) g(y) \delta(z - xy)\,. \tag{B.6}$$

The NLO Altarelli-Parisi splitting function for the process $q \to qg$ reads (see e.g. Ref. [7])

$$\begin{aligned}
\bar{P}_{qq}^{\mathrm{AP},1}(z) = {} & 2 - \frac{9}{2}z + 2\log(1-z) - \frac{(1-4z)\log(z)}{2} - \frac{(1-2z)\log^2(z)}{2} \\
& + \left(z^2 + (1-z)^2\right)\left[5 - \frac{\pi^2}{3} - 2\log\left(\frac{1-z}{z}\right) + \log^2\left(\frac{1-z}{z}\right)\right].
\end{aligned} \tag{B.7}$$

We used the following real-virtual splitting function is

$$\begin{aligned}
\mathcal{P}_{qq}^{\mathrm{loop},\,RV}(z) = {} & \frac{1}{\epsilon}\frac{1+z^2}{1-z}\,\log z \\
& - \frac{1+z^2}{1-z}\Big(\mathrm{Li}_2(1-z) + 3\log(1-z)\log z\Big) - \frac{z}{2} - (1-z)\log z \\
& - \Bigg[\frac{1}{2}\Big(1 + z - 3z\log(1-z)\Big) - (1-z)\Big(3\log(1-z)\,\log z \\
& + \mathrm{Li}_2(1-z)\Big) - \frac{1}{2}\,\frac{1+z^2}{1-z}\Big(9\log^2(1-z)\,\log z \\
& + 6\log(1-z)\,\mathrm{Li}_2(1-z) - 2\mathrm{Li}_3(1-z)\Big)\Bigg]\epsilon + \mathcal{O}(\epsilon^2)\,.
\end{aligned} \tag{B.8}$$

To express the finite contributions to the $q\bar{q} \to \ell^-\ell^+(\gamma g)$ channel partonic cross sections we have introduced the NLO splitting functions

$$\begin{aligned}
\tilde{P}_{qq}^{\mathrm{NLO}}(z,E) &= 4\mathcal{D}_1(z) - 2(1+z)\log(1-z) + (1-z) + \bar{P}_{qq,R}^{\mathrm{AP},0}(z)\,\log\left(\frac{4E^2}{\mu^2}\right), \\
\bar{P}_{qq,R}^{\mathrm{AP},0}(z) &= 2\mathcal{D}_0(z) - (1+z)\,.,
\end{aligned} \tag{B.9}$$

The finite contributions to the different partonic channels depend on collinear functions that multiply boosted matrix elements. For the $q\bar{q} \to \ell^-\ell^+(\gamma g)$ channel we have

$$
\begin{aligned}
P_{qq}^{\rm NNLO}(z,E_c) =& \mathcal{D}_0(z)\Big[48\log^2\left(\frac{2E_c}{\mu}\right) - \frac{16}{3}\log^3(z) + 32\zeta_3\Big] + \log\left(\frac{2E_c}{\mu}\right)\Big[48\mathcal{D}_1(z) \\
&- 8(z+1){\rm Li}_2(z) - \frac{8(z^2+1){\rm Li}_2(1-z)}{z-1} - 20z + \frac{4}{3}\pi^2(z+1) + 24\Big] \\
&- 16(-2\mathcal{D}_1(z) + z + 2)\log^2\left(\frac{2E_c}{\mu}\right) + \mathcal{D}_2(z)\Big(48\log\left(\frac{2E_c}{\mu}\right) - 16\log(z)\Big) \\
&+ \log^2(z)\Big[-8\mathcal{D}_1(z) + 2(z+1)\log\left(\frac{2E_c}{\mu}\right) - z + 2\Big] \\
&+ 16\mathcal{D}_3(z) + \log(1-z)\Big[-\frac{\log(z)}{1-z}\Big(8(z^2+1)\log\left(\frac{2E_c}{\mu}\right) \\
&- 2(5z^2+2z+5)\Big) - 16(z+1)\log^2\left(\frac{2E_c}{\mu}\right) - 16(z+2)\log\left(\frac{2E_c}{\mu}\right) \\
&- \frac{6(z^2+1){\rm Li}_2(1-z)}{z-1} - 8(z+1){\rm Li}_2(z) - 9z + \frac{4}{3}\pi^2(z+1) \qquad \text{(B.10)} \\
&+ 4(z+1)\log^2(z) + 12\Big] + \log(z)\Big[\frac{4(3z^2+1)\log^2\left(\frac{2E_c}{\mu}\right)}{z-1} \\
&- \frac{8(z^2+z+1)\log\left(\frac{2E_c}{\mu}\right)}{z-1} - \frac{4(z^2+1){\rm Li}_2(z)}{z-1} + \frac{\pi^2(8z^2+8)}{3-3z} - 9z + 5\Big] \\
&+ \log^2(1-z)\Big[-24(z+1)\log\left(\frac{2E_c}{\mu}\right) + \frac{(5z^2+13)\log(z)}{1-z} + 4(z-1)\Big] \\
&+ \frac{(10-6z^2){\rm Li}_3(1-z)}{z-1} + \frac{4(3z^2+5){\rm Li}_3(z)}{z-1} + (2-2z){\rm Li}_2(1-z) \\
&+ 4(z-1){\rm Li}_2(z) - \frac{4(7z^2+1)\zeta_3}{z-1} + \frac{(13z^2+47)\log^3(z)}{6-6z} - \frac{10}{3}\pi^2(z-1) \\
&+ 2(8z-9) - 8(z+1)\log^3(1-z)\,.
\end{aligned}
$$

The splittings for the other partonic channels can be found in Ref. [119].

Finally, we have also defined the following generalized splitting functions

$$
\begin{aligned}
\mathcal{P}_{qq}^{\rm NLO}(z,\widetilde{L}_i) =& C_F\Big[(1-z) + 4\mathcal{D}_1(z) + \Big[4\mathcal{D}_0(z) + 3\delta(1-z)\Big]\widetilde{L}_i \\
&- 2(1+z)\Big[\widetilde{L}_i + \log(1-z)\Big]\Big]\,.,
\end{aligned}
\qquad \text{(B.11)}
$$

$$
\mathcal{P}_{qq}^{\rm gen}(z,E_i) = \left[\left(\frac{2E_i}{\mu}\right)^{-2\epsilon}\frac{\Gamma^2(1-\epsilon)}{\Gamma(1-2\epsilon)}\right]\Big[-\hat{P}_{qq}^{(0)}(z) + \epsilon\,\mathcal{P}_{qq}^{\rm fin}(z)\Big]\,. \qquad \text{(B.12)}
$$

$$
\mathcal{P}_{qq}^{\rm fin}(z) = \frac{1}{\epsilon}\left[2\sum_{n=1}^{\infty}\frac{(-1)^n(2\epsilon)^n}{n!}\mathcal{D}_n(z) + (1-z)^{-2\epsilon}P_{qq}^{\rm reg}(z) + (1-z)\right], \qquad \text{(B.13)}
$$

$$P_{qq}^{\mathrm{reg}}(z) = -\Big[(1+z) + \epsilon(1-z)\Big] \,, \tag{B.14}$$

$$\hat{P}_{qq}^{(0)}(z) = C_F \left[2\mathcal{D}_0(z) - (1+z) + \frac{3}{2}\delta(1-z)\right] \,. \tag{B.15}$$

C

Spinor helicity formalism

In this appendix we want to give a brief overview on the spinor helicity formalism, that we used extensively in Chapter 2. We recall the left and right projectors defined in Eq. (1.1)

$$P_{L,R} \equiv \frac{1 \mp \gamma_5}{2} \tag{C.1}$$

which have to property to project Dirac spinors onto either the left subspace $SU(2)_L$ or the right one $SU(2)_R$. More, in the so-called Weyl basis, one has

$$P_L = \begin{pmatrix} \mathbb{1} & 0 \\ 0 & 0 \end{pmatrix} \quad P_R = \begin{pmatrix} 0 & 0 \\ 0 & \mathbb{1} \end{pmatrix} \quad u = \begin{pmatrix} u_- \\ u_+ \end{pmatrix} \tag{C.2}$$

so that

$$P_L u = \begin{pmatrix} u_- \\ 0 \end{pmatrix} \quad P_R u = \begin{pmatrix} 0 \\ u_+ \end{pmatrix}. \tag{C.3}$$

We now introduce the following notation (equivalent to Eq. (2.19))

$$\begin{aligned} u_-(p) &= |p\rangle \quad u_+(p) = |p] \\ \overline{u_+}(p) &= \langle p| \quad \overline{u_-}(p) = [p| \end{aligned} \tag{C.4}$$

where $p^2 = 0$ is understood. The helicity spinors defined as in Eq.(C.4) obey the following properties:

- $\langle p|q] = [q|p\rangle = 0$;
- $[p\,q] = -\,[q\,p] \implies \langle p\,p\rangle = [p\,p] = 0$;
- $\langle p\,q\rangle\,[q\,p] = 2\,p\cdot q$;
- $\not{p} = |p\rangle\,[p| + |p]\,\langle p|$;
- Fierz identity: $\langle p_1\,\gamma^\mu\,p_2]\,\langle p_3\,\gamma_\mu\,p_4] = 2\,\langle p_1\,p_3\rangle\,[p_4\,p_2]$;
- Schouten identity: $\langle p_1\,p_2\rangle\,\langle p_3\,p_4\rangle + \langle p_1\,p_3\rangle\,\langle p_4\,p_2\rangle + \langle p_1\,p_4\rangle\,\langle p_3\,p_2\rangle = 0$;
- for real momenta $\langle p\,q\rangle = [q\,p]^*$,

where $p_i^2 = q^2 = 0$ is always understood. It is straightforward to prove these properties by exploiting the left and right handed projection operators properties and plugging in the explicit form of Dirac spinors. Note that the fourth property relates a spin-one object to two spin-$\frac{1}{2}$ objects, therefore allowing the description of spin-one massless particles by means of the spinor helicity formalism, i.e. in terms of representations of $SU(2)_L \times SU(2)_R$.

We now turn to the discussion of a powerful tool within the helicity spinor formalism, known as *z-scaling*. It is well known that the S-matrix is Lorentz invariant and therefore that s_{ij} defined as the usual Mandelstam variable (in the massless case) $s_{ij} = 2\,p_i\cdot p_j$ needs to be a constant under the action of the Lorentz group. We saw from the properties listed above that $s_{ij} = \langle p_i\,p_j\rangle\,[p_j\,p_i]$, so that we can consider the following scaling

$$|p_i\rangle \to z\,|p_i\rangle\,, \quad |p_i] \to \frac{1}{z}\,|p_i] \tag{C.5}$$

where z is a boost related parameter. Indeed, an amplitude involving an outgoing left spinor with momentum p_i will scale as $\mathcal{A} \to z_i\mathcal{A}$, whereas an amplitude involving a right handed spinor with momentum p_j will scale as $\mathcal{A} \to \frac{1}{z_j}\mathcal{A}$.

We now want to construct spin-one object and more specifically their polarization vectors. Whatever their form may be within this formalism, they need to possess

the following properties:

$$\begin{aligned} &\epsilon_\mu(p)\, p^\mu = 0 \quad \epsilon_\mu(p)\, n^\mu = 0 \\ &\epsilon(p)^2 = -1 \\ &\sum_\lambda \epsilon\epsilon^* = -g^{\mu\nu} + \frac{p^\mu n^\nu + p^\nu n^\mu}{p\cdot n} \end{aligned} \tag{C.6}$$

where n^μ is a generic four vector that satisfies $n^2 = 0$. We now want to represent polarization vectors in a helicity-definite basis. To this end we introduce the left and right handed polarization vectors, that we denote as ϵ_- and ϵ_+ respectively. We define them as follows

$$\epsilon_+(p,n) = \frac{1}{\sqrt{2}}\frac{\langle p\,\gamma^\mu\, n]}{[p\,n]}, \quad \epsilon_-(p,n) = -\frac{1}{\sqrt{2}}\frac{[p\,\gamma^\mu\, n\rangle}{\langle p\,n\rangle}. \tag{C.7}$$

The z-scaling of the above objects read $\epsilon_+(p) \to z_p^{-2}\epsilon_+(p)$ and $\epsilon_-(p) \to z_p^2\epsilon_-(p)$. Note that the definition in Eq. (C.7) has all the desired properties listed in Eq.(C.6). Moreover, $\epsilon_\pm(p,n) - \epsilon_\pm(p,n') \propto p^\mu$, as required by gauge invariance.

D

RR contribution to the SV cross section

In this appendix we present details on the calculation of the double real emission contribution to the diphoton production cross section in gluon fusion. We perform this calculation in the limit where both emitted partons are soft. This calculation is the most non-trivial ingredient for the soft-virtual NNLO cross section for diphoton production that we have discussed in Chapter 4.

We begin with the calculation of the three body phase space, since it will be necessary for the phase space integration of the double soft current, that will be discussed in Section D.2.

D.1 Three body phase space

In this section we show how to calculate the three-body phase space Φ_3 for a process $p_1 p_2 \to p_3 p_4 q$ with $q^2 Q^2$ fixed. We use the reverse unitarity method already introduced in Chapter 1 to write

$$\int d\Phi_3 = 2\mathrm{Im}(I_{\mathrm{loop}}) \tag{D.1}$$

with

$$
\begin{aligned}
I_{\text{loop}} &= \int \frac{d^d k_1}{(2\pi)^d} \int \frac{d^d k_2}{(2\pi)^d} \frac{1}{k_1^2} \frac{1}{k_2^2} \frac{1}{(k_1 - k_2 - p_{12})^2 - Q^2} = \\
&= \int \frac{d^d k}{(2\pi)^d} \int \frac{d^d k_1}{(2\pi)^d} \frac{1}{k_1^2} \frac{1}{(k - k_1)^2} \frac{1}{(k - p_{12})^2 - Q^2} = \\
&= \mathcal{N}(\epsilon) \int \frac{d^d k}{(2\pi)^d} \frac{1}{(-k^2)^\epsilon} \frac{1}{(k - p_{12})^2 - Q^2} \,,
\end{aligned}
$$

with $p_{12} = p_1 + p_2$ and where in the second line we performed the change of variable $k = k_1 - k_2$ and we exploited the fact that

$$
\int \frac{d^d k_1}{(2\pi)^d} \frac{1}{k_1^2} \frac{1}{(k - k_1)^2} = \mathcal{N}(\epsilon)(-k^2)^{-\epsilon} \tag{D.2}
$$

with

$$
\mathcal{N}(\epsilon) = i(4\pi)^{\epsilon-2} \frac{\Gamma(\epsilon)\Gamma^2(1-\epsilon)}{\Gamma(2-2\epsilon)}. \tag{D.3}
$$

We then need to solve the following integral

$$
\begin{aligned}
I_{2,\text{loop}} &= \int \frac{d^d k}{(2\pi)^d} \frac{1}{(-k^2)^\epsilon} \frac{1}{(k - p_{12})^2 - Q^2} = \\
&= - \int \frac{d^d k}{(2\pi)^d} \frac{\Gamma(1+\epsilon)}{\Gamma(\epsilon)} \int_0^1 dx_1 \int_0^1 dx_2 \delta(1 - x_1 - x_2) \\
&\times \frac{x_1^{\epsilon-1}}{(x_1(-k^2) - x_2((k - p_{12})^2 - Q^2))^{1+\epsilon}} \\
&= -\epsilon \int_0^1 dx \int \frac{d^d k}{(2\pi)^d} \frac{x^{\epsilon-1}}{(x(-k^2) - (1-x)((k - p_{12})^2 - Q^2))^{1+\epsilon}}
\end{aligned}
$$

where we employed the standard Feynman parametrization for loop integrals. If we now shift integration variable $l = k - (1-x)p_{12}$, we obtain

$$
I_{2,\text{loop}} = -\epsilon \int_0^1 dx x^{\epsilon-1} \int \frac{d^d l}{(2\pi)^d} \frac{1}{(-l^2 + M^2)^{1+\epsilon}} \tag{D.4}
$$

with

$$
M^2 = (1-x)(Q^2 - xs), \qquad s = (p_1 + p_2)^2. \tag{D.5}
$$

We now perform a Wick's rotation. We define $l_E^0 = il^0$ and $|\mathbf{l}| = |\mathbf{l}_E|$, so that we get

$$\begin{aligned} I_{2,\text{loop}} &= -i\epsilon \int_0^1 dx\, x^{\epsilon-1} \int \frac{d^d l_E}{(2\pi)^d} \frac{1}{(l_E^2 + M^2)^{1+\epsilon}} \\ &= -i \frac{\Omega_d}{2(2\pi)^d} \epsilon \int_0^1 dx x^{\epsilon-1} \int_0^{+\infty} dl_E^2 \frac{(l_E^2)^{\frac{d}{2}-1}}{(l_E^2 + M^2)^{1+\epsilon}} \\ &= i\epsilon 2^{2\epsilon-4} \pi^{\epsilon-2} \frac{\Gamma(2\epsilon-1)}{\Gamma(1+\epsilon)} (Q^2)^{1-2\epsilon} \int_0^1 dx x^{\epsilon-1} (1-x)^{1-2\epsilon} (1-\frac{x}{z})^{1-2\epsilon} \\ &= i\epsilon 2^{2\epsilon-4} \pi^{\epsilon-2} \frac{\Gamma(2\epsilon-1)\Gamma(\epsilon)\Gamma(2-2\epsilon)}{\Gamma(1+\epsilon)\Gamma(2-\epsilon)} (Q^2)^{1-2\epsilon} F_{21}\left(2\epsilon-1, \epsilon, 2-\epsilon, \frac{1}{z}\right), \end{aligned} \tag{D.6}$$

where we defined $z = Q^2/s$[1], and F_{21} is the standard hypergeometric function. If we now multiply by the factor defined in Eq.(D.3) we obtain

$$I_{\text{loop}} = (4\pi)^{-4+2\epsilon} (Q^2)^{1-2\epsilon} \frac{\epsilon\, \Gamma^2(1-\epsilon)\Gamma^2(\epsilon)\Gamma(-1+2\epsilon)}{\Gamma(2-\epsilon)\Gamma(1+\epsilon)} F_{21}(\epsilon, -1+2\epsilon, 2-\epsilon, \frac{1}{z}). \tag{D.7}$$

We now notice that the hypergeometric function has a branch-cut in the physical region, i.e. when $0 < z < 1$. We need to extract it in order to evaluate the imaginary part. To this purpose we write

$$\begin{aligned} F_{21}\left(\epsilon, -1+2\epsilon, 2-\epsilon, \frac{1}{z}\right) = &\left(-\frac{1}{z}\right)^{-\epsilon} \frac{\Gamma(2-\epsilon)\Gamma(-1+\epsilon)}{\Gamma(2-2\epsilon)\Gamma(-1+2\epsilon)} F_{21}(\epsilon, -1+2\epsilon, 2-\epsilon, z) \\ &+ \left(-\frac{1}{z}\right)^{1-2\epsilon} \frac{\Gamma(2-\epsilon)\Gamma(1-\epsilon)}{\Gamma(3-3\epsilon)\Gamma(\epsilon)} F_{21}\left(-1+2\epsilon, -2+3\epsilon, \epsilon, z\right) \end{aligned} \tag{D.8}$$

so that now the branch cut is entirely contained in the two factors $(-\frac{1}{z})^{-\epsilon}$ and $(-\frac{1}{z})^{1-2\epsilon}$. More specifically, recalling that $z \to z - i\eta$ (see previous footnote), we have

$$\begin{aligned} \left(-\frac{1}{z}\right)^{-\epsilon} &\to z^{\epsilon} e^{i\pi\epsilon} \\ \left(-\frac{1}{z}\right)^{1-2\epsilon} &\to -z^{2\epsilon-1} e^{i2\pi\epsilon} \end{aligned}$$

so that the integral acquires an imaginary part. If we now apply the optical theorem, i.e. we take $2\text{Im}(I_{\text{loop}})$ and make further simple manipulations we end up with

$$\begin{aligned} \int d\Phi_3 = &2^{-5+4\epsilon} \pi^{-3+2\epsilon} (Q^2)^{1-2\epsilon} \frac{\Gamma^2(2-\epsilon)}{(1-\epsilon)\Gamma(5-4\epsilon)} (1-z)^{3-4\epsilon} z^{\epsilon} \\ &\times F_{21}(3-3\epsilon, 2-2\epsilon, 4-4\epsilon, 1-z), \end{aligned} \tag{D.9}$$

[1]Following the Feynman prescription, we assign a small positive imaginary part to Q^2 and a small negative one to s, which implies that z has a small negative imaginary part.

which in the soft limit $z \to 1$ becomes

$$\int d\Phi_3 = 2^{-5+4\epsilon}\pi^{-3+2\epsilon}(Q^2)^{1-2\epsilon}\frac{\Gamma^2(2-\epsilon)}{(1-\epsilon)\Gamma(5-4\epsilon)}(1-z)^{3-4\epsilon}. \tag{D.10}$$

D.2 Double real cross section in the soft limit

We are now ready to move to the calculation of the double real emission contribution to the NNLO soft-virtual cross section for gluon-induced color singlet production. For definiteness, we consider the gluon-induced diphoton production process described in Chapter 4. We start with the double gluon emission process

$$g(p_1) + g(p_2) \to \gamma(p_3) + \gamma(p_4) + g(p_5) + g(p_6). \tag{D.11}$$

Since we are computing these corrections in the soft-virtual approximation, we only care about the emission of two soft gluons. In this limit, the cross section factorises as follows

$$\frac{d\sigma_{gg}}{dQ^2} = \frac{1}{2\pi}\sigma_0 \int d\Phi^{2\to 1+2\,\text{soft}}\text{Eik}(p_1,p_2,p_5,p_6)\,, \tag{D.12}$$

where $\sigma_0$is defined so that $\sigma_0\,\delta(1-z)$ is the leading order cross section, Q^2 is the invariant mass of the diphoton system, and

$$\begin{aligned}&\text{Eik}(p_1,p_2,p_5,p_6)\\ &= 4N_c^2 S_{12}(p_5)S_{12}(p_6) + N_c^2\left[2S_{12}(p_5,p_6) - S_{11}(p_5,p_6) - S_{22}(p_5,p_6)\right]\,.\end{aligned} \tag{D.13}$$

The soft functions are defined as follows [112]

$$\begin{aligned}&S_{ij}(k) = \frac{p_i\cdot p_j}{(p_i\cdot k)(p_j\cdot k)},\\ &S_{ij}(k_1,k_2) = S_{ij}^{so}(k_1,k_2) + \frac{p_i\cdot k_1 p_j\cdot k_2 + p_i\cdot k_2 p_j\cdot k_1}{p_i\cdot(k_1+k_2)p_j\cdot(k_1+k_2)}\\ &\times\left[\frac{1-\epsilon}{(k_1\cdot k_2)^2} - \frac{1}{2}S_{ij}^{so}(k_1,k_2)\right] - 2\frac{p_i\cdot p_j}{k_1\cdot k_2 p_i\cdot(k_1+k_2)p_j\cdot(k_1+k_2)},\end{aligned} \tag{D.14}$$

with

$$S_{ij}^{so}(k_1,k_2) = \frac{p_i\cdot p_j}{k_1\cdot k_2}\left(\frac{1}{p_i\cdot k_1 p_j\cdot k_2} + \frac{1}{p_i\cdot k_2 p_j\cdot k_1}\right) - \frac{(p_i\cdot p_j)^2}{p_i\cdot k_1 p_j\cdot k_1 p_i\cdot k_2 p_j\cdot k_2}. \tag{D.15}$$

In order to integrate the eikonal factor over the double unresolved phase space, we employ the method of reverse unitarity, that was already introduced in Chapter 1. First, we write the above integral as a loop integral, transforming delta functions into cut propagators.

More specifically, starting with the non-factorizable contribution, i.e. the second term of Eq.(D.13), we have

$$\begin{aligned}
&\int d\Phi^{2\to 1+2\,\mathrm{soft}}\left[2S_{12}(p_5,p_6)-S_{11}(p_5,p_6)-S_{22}(p_5,p_6)\right]\to\\
&\to\int\frac{d^dp_5}{(2\pi)^d}\frac{d^dp_6}{(2\pi)^d}\frac{1}{(p_5^2)_c}\frac{1}{(p_6^2)_c}\frac{1}{((p_1+p_2-p_5-p_6)^2-Q^2)_c}\\
&\times\left[2S_{12}(p_5,p_6)-S_{11}(p_5,p_6)-S_{22}(p_5,p_6)\right],
\end{aligned}\tag{D.16}$$

where the subscript c stands for cut propagators. Note that the denominators are not linearly independent. After resolving the linear relations between the different denominators, we use the package FIRE [287] to perform IBP reduction and we are able to express the loop integral as a sum of two master integrals as follows

$$\begin{aligned}
&\int\frac{d^dp_5}{(2\pi)^d}\frac{d^dp_6}{(2\pi)^d}\frac{1}{(p_5^2)_c}\frac{1}{(p_6^2)_c}\frac{1}{((p_1+p_2-p_5-p_6)^2-Q^2)_c}\\
&\times\left[2S_{12}(p_5,p_6)-S_{11}(p_5,p_6)-S_{22}(p_5,p_6)\right]=AG_1+BG_2
\end{aligned}\tag{D.17}$$

with

$$\begin{aligned}
G_1&=\int d\Phi_3\,,\\
G_2&=\int\frac{d^dp_5}{(2\pi)^d}\frac{d^dp_6}{(2\pi)^d}\frac{1}{(p_5^2)_c}\frac{1}{(p_6^2)_c}\frac{1}{((p_1+p_2-p_5-p_6)^2-Q^2)_c}\frac{1}{p_1\cdot p_5}\frac{1}{p_2\cdot p_6}\frac{1}{p_5\cdot p_6}\,,
\end{aligned}\tag{D.18}$$

and

$$A=\frac{16(-3+4\epsilon)(-1+4\epsilon)(-3+19\epsilon-11\epsilon^2)}{s_{12}^2\epsilon^3(-3+2\epsilon)(1-z)^4},\qquad B=s_{12}\,,\tag{D.19}$$

where $s_{12}=2p_1\cdot p_2$. Note that G_1 is the three-body phase space that we calculated in the previous section. The result is reported in Eq. (D.10). We are then left with the calculation of G_2, whose expression reads

$$G_2=\int\frac{d^dp_5}{(2\pi)^d}\frac{d^dp_6}{(2\pi)^d}\delta(p_5^2)\delta(p_6^2)\delta(s_{12}-Q^2-2p_{12}\cdot p_{56})\frac{1}{(p_1\cdot p_5)(p_2\cdot p_6)(p_5\cdot p_6)}\,,\tag{D.20}$$

with $p_{12} = p_1 + p_2$ and $p_{56} = p_5 + p_6$. We compute this as a phase space integral rather than a loop integral and after simple manipulations we obtain

$$\begin{aligned} G_2 =& \frac{4}{\epsilon^2}(2\pi)\left(\frac{\Gamma^2(1-\epsilon)}{\Gamma(1-2\epsilon)}\right)^2 s_{12}^{-2(1+\epsilon)}(1-z)^{-4\epsilon-1}\frac{\Gamma^2(-2\epsilon)}{\Gamma(-4\epsilon)} \\ & \times F_{32}(1,1,-\epsilon;1-2\epsilon,1-\epsilon;1). \end{aligned} \tag{D.21}$$

We are then ready to move on to the factorizable contribution, i.e. the first term of Eq.(D.13). We compute this integral by means of the reverse unitarity method as we did for the previous contribution, even though one could in principle also compute it by brute force. In this case the integral reduces to the computation of one master integral only: the phase space integral G_1. More specifically, IBPs relations allow us to write

$$\begin{aligned} &\int \frac{d^d p_5}{(2\pi)^d}\frac{d^d p_6}{(2\pi)^d}\frac{1}{(p_5^2)_c}\frac{1}{(p_6^2)_c}\frac{1}{((p_1+p_2-p_5-p_6)^2-Q^2)_c}S_{12}(p_5)S_{12}(p_6) \\ &= CG_1 \end{aligned} \tag{D.22}$$

with

$$C = \frac{32(-1+2\epsilon)(-3+4\epsilon)(-1+4\epsilon)}{\epsilon^3 s_{12}^2(1-z)^4}. \tag{D.23}$$

Finally, by adding up the two contributions, we can write the double real contribution to the inclusive cross section in the soft limit as

$$\begin{aligned} \frac{d\sigma_{gg}}{dQ^2} =& \sigma_0[\alpha_{s,b}]^2 N_c^2 s_{12}^{-1-2\epsilon}(1-z)^{-1-4\epsilon}\left(\frac{6(-3+4\epsilon)(-1+4\epsilon)(7-15\epsilon+7\epsilon^2)}{(-3+2\epsilon)}\right. \\ & \left.\times\frac{\Gamma^4(1-\epsilon)}{\epsilon^3\Gamma(4-4\epsilon)} + 2\frac{\Gamma^4(1-\epsilon)\Gamma^2(-2\epsilon)}{\epsilon^2\Gamma^2(1-2\epsilon)\Gamma(-4\epsilon)}F_{32}(1,1,-\epsilon;1-2\epsilon,1-\epsilon;1)\right), \end{aligned} \tag{D.24}$$

where we recall that

$$[\alpha_{s,b}] \equiv \frac{g_s^2}{8\pi^2}\frac{(4\pi)^\epsilon}{\Gamma(1-\epsilon)}. \tag{D.25}$$

Note that in order to calculate NNLO corrections to diphoton production through gluon fusion, we also need to consider the emission of a $q\bar{q}$ pair, i.e. the cross section relative to the following process

$$g(p_1) + g(p_2) \to \gamma(p_3) + \gamma(p_4) + q(p_5) + \bar{q}(p_6). \tag{D.26}$$

The calculation is almost identical to the double gluon emission case. The eikonal factor that we need to integrate over three-body phase space takes the form [112]

$$\mathrm{Eik}_{q\bar{q}}(p_1,p_2,p_5,p_6) = I_{11}(p_5,p_6) + I_{22}(p_5,p_6) - 2I_{12}(p_5,p_6)\,, \tag{D.27}$$

where

$$I_{ij}(k_1,k_2) = -\frac{2(p_i\cdot p_j)(k_1\cdot k_2) + [p_i\cdot(k_1-k_2)][p_j\cdot(k_1-k_2)]}{2(k_1\cdot k_2)^2[p_i\cdot(k_1+k_2)][p_j\cdot(k_1+k_2)]}. \tag{D.28}$$

The integral we need to compute is therefore

$$\begin{aligned}&\frac{d\sigma_{q\bar{q}}}{dQ^2} = \\ &\int \frac{d^dp_5}{(2\pi)^d}\frac{d^dp_6}{(2\pi)^d}\frac{1}{(p_5^2)_c}\frac{1}{(p_6^2)_c}\frac{1}{((p_1+p_2-p_5-p_6)^2-Q^2)_c}\mathrm{Eik}_{q\bar{q}}(p_1,p_2,p_5,p_6)\,.\end{aligned} \tag{D.29}$$

After IBP reduction, it leads to the following expression

$$\frac{d\sigma_{q\bar{q}}}{dQ^2} = \frac{32(-1+\epsilon)(-3+4\epsilon)(-1+4\epsilon)}{\epsilon^2(-3+2\epsilon)}s_{12}^{-2}(1-z)^{-4}G_1 \tag{D.30}$$

with G_1 the usual three-body phase space, as defined in Eq. (D.18). The result therefore yields

$$\frac{d\sigma_{q\bar{q}}}{dQ^2} = \sigma_0[\alpha_{s,b}]^2N_cn_fT_R\frac{8(\epsilon-1)(4\epsilon-3)(4\epsilon-1)s_{12}^{-2\epsilon-1}(1-z)^{-4\epsilon-1}\Gamma(1-\epsilon)^4}{\epsilon^2(2\epsilon-3)\Gamma(4-4\epsilon)}\,, \tag{D.31}$$

where we find the factor n_f arising by summing over different $q\bar{q}$ pair flavors. To complete the calculation of the SV cross section, one would also need to compute the real-virtual, double virtual and PDFs contributions. However, these are straightforward since they involve at most one extra radiated soft particle, which makes it immediate to obtain the respective contribution to the cross section by direct phase space integration. We do not report their calculation here. Once all the ingredients are combined, we obtained the formula in Eq. (4.21).

E

Phase space integration of the triple color-correlated one-loop soft current

In this appendix we discuss the computation of the triple color-correlated component arising from the integrated soft limit of the real-virtual contribution to the $q\bar{q} \to N\, g$ cross section. This contribution has been considered in Chapter 3 and more specifically in the context of the generalization of the NSC to high multiplicity processes. Indeed, in order to have such triple color correlations one needs to consider processes with at least four partons at leading order.

We start by recalling that at one-loop the emission of a soft gluon leads to a factorized expression that can be written, in the notation of Chapter 3, as [113, 114]

$$\begin{aligned}
&S_{\mathfrak{m}}\, F_{\mathrm{RV}}(\mathfrak{m}) \\
=& -g_{s,b}^2 \sum_{(ij)}^{N_p} \Bigg\{ 2\, S_{ij}(p_{\mathfrak{m}})\ (\boldsymbol{T}_i \cdot \boldsymbol{T}_j) \cdot F_{\mathrm{LV}} - \frac{\alpha_s(\mu)}{2\pi}\, \frac{\beta_0}{\epsilon}\, 2\, S_{ij}(p_{\mathfrak{m}})\ (\boldsymbol{T}_i \cdot \boldsymbol{T}_j) \cdot F_{\mathrm{LM}} \\
&- 2\, \frac{[\alpha_s]}{\epsilon^2}\, C_A\, A_K(\epsilon) \left(S_{ij}(p_{\mathfrak{m}}) \right)^{1+\epsilon} (\boldsymbol{T}_i \cdot \boldsymbol{T}_j) \cdot F_{\mathrm{LM}} \\
&- [\alpha_s]\, \frac{4\pi\, \Gamma(1+\epsilon)\Gamma^3(1-\epsilon)}{\epsilon\, \Gamma(1-2\epsilon)} \sum_{\substack{k=1 \\ k\neq i,j}}^{N_p} \kappa_{ij}\, S_{ki}(p_{\mathfrak{m}}) \left(S_{ij}(p_{\mathfrak{m}}) \right)^{\epsilon} f_{abc}\, T_k^a\, T_i^b\, T_j^c\, F_{\mathrm{LM}} \Bigg\}\,,
\end{aligned} \tag{E.1}$$

where $\kappa_{ij} \equiv \left(\lambda_{ij} - \lambda_{i\mathfrak{m}} - \lambda_{j\mathfrak{m}} \right) = +1$ when both i and j are incoming momenta and $\kappa_{ij} = -1$ otherwise, and $S_{ij}(p)$ is defined in the first line of Eq. (D.14).

We point out that κ_{ij} is symmetric under the exchange $i \leftrightarrow j$. Moreover, we have introduced the constant

$$A_K(\epsilon) = \frac{\Gamma^3(1+\epsilon)\,\Gamma^5(1-\epsilon)}{\Gamma(1+2\epsilon)\,\Gamma^2(1-2\epsilon)} = 1 + \mathcal{O}\Big(\epsilon^2\Big)\,. \tag{E.2}$$

In this appendix we focus on the following term

$$S^{\rm tri}_{\mathfrak{m}}\,F_{\rm RV}(\mathfrak{m}) = -[\alpha_s]\,\frac{4\pi\,\Gamma(1+\epsilon)\Gamma^3(1-\epsilon)}{\epsilon\,\Gamma(1-2\epsilon)}\sum_{\substack{k=1\\k\neq i,j}}^{N_p}\kappa_{ij}\,S_{ki}(p_{\mathfrak{m}})\,\Big(S_{ij}(p_{\mathfrak{m}})\Big)^{\epsilon}\,F^{(kij)}_{\rm LM}\,, \tag{E.3}$$

where we have used the notation

$$F^{(kij)}_{\rm LM} = \Big\langle \mathcal{M}^{(0)}\Big| f_{abc}\,T^a_k\,T^b_i\,T^c_j\,\Big|\mathcal{M}^{(0)}\Big\rangle \tag{E.4}$$

to indicate the triple-color correlated matrix element. Note that, if we only had three or less partons involved in the leading order process, we could use color conservation to obtain the following identity

$$f_{abc}\,T^a_1\,T^b_2\,T^c_3\,\Big|\mathcal{M}^{(0)}\Big\rangle = -f_{abc}\,T^a_1\,T^b_2\,\Big(T^c_1+T^c_2\Big)\,\Big|\mathcal{M}^{(0)}\Big\rangle = 0\,. \tag{E.5}$$

Our goal is to integrate Eq. (E.3) over the phase space of the soft gluon with momentum $p_{\mathfrak{m}}$. We begin by integrating over the energy $E_{\mathfrak{m}}$ and obtain

$$\Big\langle S^{\rm tri}_{\mathfrak{m}}\,F_{\rm RV}\Big\rangle = -[\alpha_s]^2\,\frac{4\pi^{3-\epsilon}\,2^{\epsilon}\,\Gamma(1+\epsilon)\Gamma^4(1-\epsilon)}{\epsilon^2\,\Gamma(1-2\epsilon)}\left(\frac{4E^2_{\rm max}}{\mu^2}\right)^{-2\epsilon}\sum_{(ijk)}\kappa_{ij}\;G^{kij}\;F^{(kij)}_{\rm LM}, \tag{E.6}$$

where (ijk) labels triplets with different i, j and k. In Eq. (E.6) we have defined

$$G^{kij} = \int\frac{d\Omega^{(d-1)}_{\mathfrak{m}}}{2(2\pi)^{d-1}}\frac{\rho_{ki}}{\rho_{k\mathfrak{m}}\rho_{i\mathfrak{m}}}\left(\frac{\rho_{ij}}{\rho_{i\mathfrak{m}}\rho_{j\mathfrak{m}}}\right)^{\epsilon}, \tag{E.7}$$

which is a function of the angular variables ρ_{ij}, ρ_{ik} and ρ_{jk}[1]. We note that since κ_{ij} is a symmetric tensor and $F^{(kij)}_{\rm LM}$ is fully anti-symmetric, only the anti-symmetric contribution $G^{kij}-G^{kji}$ can contribute to the sum, whereas the symmetric part drops out. We will use this result when writing intermediate expressions for $\Big\langle S^{\rm tri}_{\mathfrak{m}}\,F_{\rm RV}(\mathfrak{m})\Big\rangle$.

[1]We recall that we define $\rho_{ij} = 1-\cos\theta_{ij}$, where θ_{ij} denotes the angle between the i and j directions.

To perform the remaining integration over the soft-gluon angle, we employ the Mellin-Barnes representation of d-dimensional angular integrals (see e.g. Ref. [288]), and write the integral as

$$\begin{aligned} G^{kij} &= \int \frac{d\Omega_{\mathfrak{m}}^{(d-1)}}{2(2\pi)^{d-1}} \frac{\rho_{ki}}{\rho_{k\mathfrak{m}}\rho_{i\mathfrak{m}}} \left(\frac{\rho_{ij}}{\rho_{i\mathfrak{m}}\rho_{j\mathfrak{m}}}\right)^{\epsilon} \\ &= \rho_{ki}\,(\rho_{ij})^{\epsilon} \int_{-i\infty}^{+i\infty} \frac{dz_{ij}\,dz_{jk}\,dz_{ki}}{(2\pi i)^3}\, \frac{\pi^{-2+\epsilon}}{2^{4+2\epsilon}}\, \Gamma(-z_{ij})\Gamma(-z_{ki})\Gamma(-z_{jk}) \\ &\quad \times \Gamma(1+\epsilon+z_{ij}+z_{ki})\Gamma(-1-3\epsilon-z_{ij}-z_{ki}-z_{jk})\Gamma(\epsilon+z_{ij}+z_{jk}) \\ &\quad \times \Gamma(1+z_{ki}+z_{jk}) \frac{1}{\Gamma(-4\epsilon)\Gamma(\epsilon)\Gamma(1+\epsilon)}\, \eta_{ij}^{z_{ij}}\, \eta_{ki}^{z_{ki}}\, \eta_{jk}^{z_{jk}} \ . \end{aligned} \tag{E.8}$$

In the above equation we have introduced the three complex Mellin-Barnes variables z_{ij}, z_{ki}, z_{jk}, and $\eta_{ij} = \rho_{ij}/2$. The integration contour has to be chosen in such a way that the poles of $\Gamma(... + x)$ are separated from the poles of $\Gamma(... - x)$, with x being a generic integration variable. In order to resolve the singularity structure in ϵ we employ the packages `MBresolve` [289] and `MB` [290], which allow us to express our original integral as a linear combination of integrals that can be safely expanded in ϵ under the integration sign, and whose integration contours are straight vertical lines.

We can then expand in ϵ and use the residue theorem to compute the integrals. Upon doing so, it is possible to express the function G^{kij} up to $\mathcal{O}(\epsilon^0)$ in terms of classical and generalized polylogarithms (GPLs) [291, 292] up to weight three. It is convenient to write the final result for the angular integral as follows

$$G^{kij} = \int \frac{d\Omega_{\mathfrak{m}}^{(d-1)}}{2(2\pi)^{d-1}} \frac{\rho_{ki}}{\rho_{k\mathfrak{m}}\rho_{i\mathfrak{m}}} \left(\frac{\rho_{ij}}{\rho_{i\mathfrak{m}}\rho_{j\mathfrak{m}}}\right)^{\epsilon} = -\frac{\epsilon^2}{4\pi^2}\left[\frac{2^{-\epsilon}\pi^{\epsilon}\,\Gamma(1-\epsilon)}{\Gamma(1-4\epsilon)\Gamma^2(1+\epsilon)}\right] \overline{G}^{kij} \ , \tag{E.9}$$

where

$$\begin{aligned} \overline{G}^{kij} &= \frac{3}{4\epsilon^3} + \frac{1}{2\epsilon^2}\Big[\log(\eta_{ij}) - 3\log(\eta_{ik}) - \log(\eta_{jk})\Big] + \frac{1}{\epsilon}\Big[\frac{1}{2}\log^2(\eta_{ij}) \\ &\quad + \log(\eta_{ij})\,(-\log(\eta_{ik}) - \log(\eta_{jk})) + \log(\eta_{ik})\,(\log(\eta_{jk}) - 2\log(1-\eta_{ik})) \\ &\quad - 2\,\mathrm{Li}_2(\eta_{ik}) + \frac{3}{2}\log^2(\eta_{ik}) + \frac{1}{2}\log^2(\eta_{jk}) + \pi^2\Big] + \mathcal{O}(\epsilon^0) \ . \end{aligned} \tag{E.10}$$

The $\mathcal{O}(\epsilon)$ term, required for our result, is quite lengthy so we do not report it here. We will present the final result that contributes to the physical cross section at the

end of this appendix. Note that the ϵ-dependent prefactor in Eq. (E.9) starts at $\mathcal{O}(\epsilon^2)$, so that the whole angular integral is effectively $\mathcal{O}(\epsilon^{-1})$, as expected.

Inserting the result for G^{kij} into Eq. (E.6) we get the following final result for the triple-color correlated contribution to the real-virtual counterterm

$$\left\langle S_{\mathfrak{m}}^{\text{tri}}\, F_{\text{RV}} \right\rangle = [\alpha_s]^2\, \frac{\pi\Gamma^5(1-\epsilon)}{\Gamma(1-2\epsilon)\Gamma(1-4\epsilon)\Gamma(1+\epsilon)} \left(\frac{4E_{\text{max}}^2}{\mu^2}\right)^{-2\epsilon} \sum_{(ijk)} \left\langle \kappa_{ij}\, \overline{G}^{kij}\, F_{\text{LM}}^{(kij)} \right\rangle . \tag{E.11}$$

To proceed further it is convenient to split the function $\overline{G}^{kij}$ into contributions using its symmetry properties under the $i \leftrightarrow j$ permutations. We write

$$\overline{G}^{kij} = \overline{G}_s^{kij} + \overline{G}_r^{kij} \,, \tag{E.12}$$

with

$$\overline{G}_s^{kij} = \frac{3}{4}\frac{1}{\epsilon^3} + \frac{1}{2\epsilon^2}\log\left(\frac{\eta_{ij}}{\eta_{jk}\eta_{ik}}\right) + \frac{1}{\epsilon}\left[\frac{2\pi^2}{3} + \frac{1}{2}\log^2\left(\frac{\eta_{ij}}{\eta_{jk}\eta_{ik}}\right)\right] + \mathcal{O}(\epsilon^0) \tag{E.13}$$

and

$$\overline{G}_r^{kij} = -\frac{\log\eta_{ik}}{\epsilon^2} + \frac{1}{\epsilon}\Big[\log^2\eta_{ik} + 2\,\text{Li}_2(1-\eta_{ik})\Big] + \mathcal{O}(\epsilon^0) \,. \tag{E.14}$$

The function $\overline{G}_s^{kij}$ is symmetric under $i \leftrightarrow j$ permutations; hence, it does not contribute to $\left\langle S_{\mathfrak{m}}^{\text{tri}}\, F_{\text{RV}}(\mathfrak{m}) \right\rangle$ and can be dropped. Note also that the function $\overline{G}_r^{kij}$, up to $\mathcal{O}(\epsilon^{-1})$, is symmetric under the $i \leftrightarrow k$ permutation. It follows that $\left\langle S_{\mathfrak{m}}^{\text{tri}}\, F_{\text{RV}}(\mathfrak{m}) \right\rangle$ is free of poles for decays of a colour-singlet heavy particle, as in this case we have $\kappa_{ij} = -1$.

For a hadron collider process with two incoming and any number of outgoing partons, the function κ_{ij} reads

$$\kappa_{ij} = -1 + 2\delta_{i1}\delta_{j2} + 2\delta_{i2}\delta_{j1} \,, \tag{E.15}$$

from which it follows that

$$\begin{aligned} \sum_{(ijk)} \left\langle \kappa_{ij}\, \overline{G}^{kij}\, F_{\text{LM}}^{(kij)} \right\rangle &= \sum_{(ijk)} \left\langle \kappa_{ij}\, \overline{G}_r^{kij}\, F_{\text{LM}}^{(kij)} \right\rangle \\ &= 2 \sum_{k\neq 1,2} \left\langle \left(\overline{G}_r^{k12} - \overline{G}_r^{k21}\right) F_{\text{LM}}^{(k12)} \right\rangle . \end{aligned} \tag{E.16}$$

Using this result together with Eq. (E.14) and Eq. (E.11), we obtain the final formula for the poles in the triple color-correlated contribution to the soft limit of the real-virtual corrections. It reads

$$\left\langle S_{\mathfrak{m}}^{\text{tripole}} F_{\text{RV}} \right\rangle = [\alpha_s]^2 \sum_{k\neq 1,2} \left\langle F_{\text{LM}}^{(k12)} \left\{ \frac{2\pi}{\epsilon^2} \log \frac{\eta_{2k}}{\eta_{1k}} + \frac{2\pi}{\epsilon} \Bigg[\log^2 \eta_{1k} - \log^2 \eta_{2k} + 2 \log \left(\frac{4E_{\text{max}}^2}{\mu^2} \right) \log \left(\frac{\eta_{1k}}{\eta_{2k}} \right) + 2\,\text{Li}_2(1-\eta_{1k}) - 2\,\text{Li}_2(1-\eta_{2k}) \Bigg] + \mathcal{O}(\epsilon^0) \right\} \right\rangle . \tag{E.17}$$

We now present the formula for the $\mathcal{O}(\epsilon^0)$ terms of Eq. (E.10). We exploit once again the symmetry properties of the tripole contribution under the exchange of $i \leftrightarrow j$ indices and therefore only present results for the antisymmetric part. The result reads

$$\begin{aligned}
\overline{G}_{r,\text{fin}}^{kij} = {} & \text{Li}_2(\eta_{ij}) \log \left(\frac{\eta_{ik}}{\eta_{jk}} \right) - \text{Li}_2(\eta_{ik}) \log \left(\frac{\eta_{jk}}{\eta_{ij}\eta_{ik}} \right) + \text{Li}_2(\eta_{jk}) \log \left(\frac{\eta_{ik}}{\eta_{ij}\eta_{jk}} \right) \\
& + \log(\eta_{ik})\,\text{Li}_2 \left(-\frac{\eta_{ik}-\eta_{jk}}{1-\eta_{ik}} \right) + \log(\eta_{ik})\,\text{Li}_2 \left(-\frac{\eta_{ik}-\eta_{jk}}{\eta_{jk}} \right) + 3\,\text{Li}_3(1-\eta_{ik}) \\
& - 3\,\text{Li}_3(1-\eta_{jk}) + \text{Li}_2 \left(\frac{1-\eta_{jk}}{1-\eta_{ik}} \right) \log(\eta_{ik}\eta_{jk}) + \text{Li}_2 \left(\frac{\eta_{ik}}{\eta_{jk}} \right) \log(\eta_{ik}\,\eta_{jk}) \\
& - \log(\eta_{jk})\,\text{Li}_2 \left(-\frac{\eta_{jk}-\eta_{ik}}{\eta_{ik}} \right) - \log(\eta_{jk})\,\text{Li}_2 \left(-\frac{\eta_{jk}-\eta_{ik}}{1-\eta_{jk}} \right) + \text{Li}_3(\eta_{ik}) \\
& - \text{Li}_3(\eta_{jk}) + \log^2(\eta_{ik}) \left[\frac{1}{2} \log \left(\frac{1-\eta_{jk}}{\eta_{ij}} \right) + \log \left(\frac{\eta_{jk}-\eta_{ik}}{\eta_{jk}} \right) \right] \\
& + \log(\eta_{ik}) \Bigg[-\frac{1}{2} \log^2(\eta_{ij}) + \log(1-\eta_{ij}) \log(\eta_{ij}) + \frac{1}{2} \log^2 \left(\frac{1-\eta_{jk}}{1-\eta_{ik}} \right) \\
& + \frac{1}{2} \log^2 \left(\frac{\eta_{ik}}{\eta_{jk}} \right) + \log(1-\eta_{jk}) \log(\eta_{jk}(\eta_{jk}-\eta_{ik})) + \log^2(\eta_{jk}) - \frac{13\pi^2}{6} \Bigg] \\
& + \log(1-\eta_{jk}) \Bigg[-\log(\eta_{jk}) \log \left(\frac{\eta_{ij}}{\eta_{jk}-\eta_{ik}} \right) - \log^2(\eta_{jk}) - \frac{\pi^2}{6} \Bigg] \\
& + \log(1-\eta_{ik}) \Bigg[\log(\eta_{ik}) \Bigg[\log \left(\frac{\eta_{ij}}{\eta_{jk}-\eta_{ik}} \right) - \log(1-\eta_{jk}) \Bigg] + \log^2(\eta_{ik}) \\
& - \log(\eta_{jk}) \log(\eta_{jk}-\eta_{ik}) - \frac{\log^2(\eta_{jk})}{2} + \frac{\pi^2}{6} \Bigg] + \frac{1}{2} \log(\eta_{ij}) \log^2(\eta_{jk}) \\
& + \frac{1}{2} \log^2(\eta_{ij}) \log(\eta_{jk}) - \log(1-\eta_{ij}) \log(\eta_{ij}) \log(\eta_{jk}) - \frac{1}{3} \log^3 \left(\frac{\eta_{ik}}{\eta_{jk}} \right) \\
& - \frac{1}{2} \log \left(\frac{1-\eta_{jk}}{1-\eta_{ik}} \right) \log^2 \left(\frac{\eta_{ik}}{\eta_{jk}} \right) - \frac{1}{2} \log^2 \left(\frac{1-\eta_{jk}}{1-\eta_{ik}} \right) \log \left(\frac{\eta_{ik}}{\eta_{jk}} \right)
\end{aligned} \tag{E.18}$$

$$
\begin{aligned}
&- \log^2(\eta_{jk})\log(\eta_{jk}-\eta_{ik}) + \frac{2}{3}\pi^2 \log\left(\frac{\eta_{ik}}{\eta_{jk}}\right) + \log\left(\frac{\eta_{ik}}{1-\eta_{ik}}\right) \\
&\times \left[\frac{\pi^2}{6} - \log(1-\eta_{jk})\log(\eta_{jk})\right] - \frac{1}{2}\log^3(\eta_{ik}) + \log^2(1-\eta_{ik})\log(\eta_{ik}) \\
&+ \frac{\log^3(\eta_{jk})}{2} - \log^2(1-\eta_{jk})\log(\eta_{jk}) + \frac{3}{2}\pi^2\log(\eta_{jk}) - \frac{1}{6}\pi^2\log\left(\frac{\eta_{jk}}{1-\eta_{jk}}\right) \\
&+ \log(\eta_{ij})\Big[G(\tilde{\eta}_{ik}, w^+, 1) - G(\tilde{\eta}_{jk}, w^+, 1) + G(\tilde{\eta}_{ik}, w^-, 1) - G(\tilde{\eta}_{jk}, w^-, 1)\Big] \\
&- G(\tilde{\eta}_{ik}, w^+, \tilde{\eta}_{jk}, 1) + G(\tilde{\eta}_{jk}, w^+, \tilde{\eta}_{ik}, 1) + G(\tilde{\eta}_{ik}, w^+, 1, 1) - G(\tilde{\eta}_{ik}, w^+, \tilde{\eta}_{ik}, 1) \\
&- G(\tilde{\eta}_{jk}, w^+, 1, 1) + G(\tilde{\eta}_{jk}, w^+, \tilde{\eta}_{jk}, 1) - G(\tilde{\eta}_{ik}, w^-, \tilde{\eta}_{jk}, 1) + G(\tilde{\eta}_{jk}, w^-, \tilde{\eta}_{ik}, 1) \\
&+ G(\tilde{\eta}_{ik}, w^-, 1, 1) - G(\tilde{\eta}_{ik}, w^-, \tilde{\eta}_{ik}, 1) - G(\tilde{\eta}_{jk}, w^-, 1, 1) + G(\tilde{\eta}_{jk}, w^-, \tilde{\eta}_{jk}, 1)
\end{aligned}
$$

where we defined

$$
w^{\pm} = \frac{2 - \eta_{ij} - \eta_{ik} - \eta_{jk} \pm \sqrt{(\eta_{ij} - \eta_{ik} - \eta_{jk})^2 - 4\eta_{ik}\eta_{jk}(1-\eta_{ij})}}{2\left(\eta_{ik}\eta_{jk} - \eta_{ik} - \eta_{jk} + 1\right)} \tag{E.19}
$$

and $\tilde{\eta}_{ab} = 1/(1-\eta_{ab})$.

The expression in Eq. (E.18) is well defined in the region $\eta_{ik} < \eta_{jk}$. However, this is enough to cover the entire phase space since the other region can be obtained by swapping indices i and j and therefore, thanks to the antisymmetry of the result under such exchange, it only amounts to an overall sign change.

References

[1] Franz Gross et al. "50 Years of Quantum Chromodynamics". In: *Eur. Phys. J. C* 83 (2023), p. 1125. arXiv: 2212.11107 [hep-ph].

[2] Georges Aad et al. "Observation of a new particle in the search for the Standard Model Higgs boson with the ATLAS detector at the LHC". In: *Phys. Lett. B* 716 (2012), pp. 1–29. arXiv: 1207.7214 [hep-ex].

[3] Serguei Chatrchyan et al. "Observation of a New Boson at a Mass of 125 GeV with the CMS Experiment at the LHC". In: *Phys. Lett. B* 716 (2012), pp. 30–61. arXiv: 1207.7235 [hep-ex].

[4] Wikipedia contributors. *Standard Model — Wikipedia, The Free Encyclopedia*. [Online; accessed 3-June-2024]. 2024. URL: https://en.wikipedia.org/w/index.php?title=Standard_Model&oldid=1224183186.

[5] C. S. Wu et al. "Experimental Test of Parity Conservation in Beta Decay". In: *Phys. Rev.* 105 (4 1957), pp. 1413–1415. URL: https://link.aps.org/doi/10.1103/PhysRev.105.1413.

[6] Michael E. Peskin and Daniel V. Schroeder. *An Introduction to quantum field theory*. Reading, USA: Addison-Wesley, 1995.

[7] R. Keith Ellis, W. James Stirling, and B. R. Webber. *QCD and collider physics*. Vol. 8. Cambridge University Press, Feb. 2011.

[8] *Particle Data Group — pdg.lbl.gov*. https://pdg.lbl.gov/2024/html/authors_2024.html. [Accessed 03-06-2024].

[9] P. A. Zyla et al. "Review of Particle Physics". In: *PTEP* 2020.8 (2020), p. 083C01.

[10] Guthrie Miller et al. "Inelastic electron-Proton Scattering at Large Momentum Transfers". In: *Phys. Rev. D* 5 (1972), p. 528.

[11] Paolo Nason and Giulia Zanderighi. "Fits of α_s using power corrections in the three-jet region". In: *JHEP* 06 (2023), p. 058. arXiv: 2301.03607 [hep-ph].

[12] Stefan Höche. "Introduction to parton-shower event generators". In: *Theoretical Advanced Study Institute in Elementary Particle Physics: Journeys Through the Precision Frontier: Amplitudes for Colliders*. 2015, pp. 235–295. arXiv: 1411.4085 [hep-ph].

[13] *Summary Plots for Heavy Particle Searches and Long-lived Particle Searches - March 2023*. Tech. rep. All figures including auxiliary figures are available at https://atlas.web.cern.ch/Atlas/GROUPS/PHYSICS/PUBNOTES/ATL-PHYS-PUB-2023-008. Geneva: CERN, 2023. URL: https://cds.cern.ch/record/2853754.

[14] John C. Collins, Davison E. Soper, and George F. Sterman. "Factorization of Hard Processes in QCD". In: *Adv. Ser. Direct. High Energy Phys.* 5 (1989), pp. 1–91. arXiv: hep-ph/0409313.

[15] Gerard 't Hooft and M. J. G. Veltman. "Regularization and Renormalization of Gauge Fields". In: *Nucl. Phys. B* 44 (1972), pp. 189–213.

[16] M. Beneke and Vladimir A. Smirnov. "Asymptotic expansion of Feynman integrals near threshold". In: *Nucl. Phys. B* 522 (1998), pp. 321–344. arXiv: hep-ph/9711391.

[17] Jonathan Grigo, Kirill Melnikov, and Matthias Steinhauser. "Virtual corrections to Higgs boson pair production in the large top quark mass limit". In: *Nucl. Phys. B* 888 (2014), pp. 17–29. arXiv: 1408.2422 [hep-ph].

[18] T. Kinoshita. "Mass singularities of Feynman amplitudes". In: *J. Math. Phys.* 3 (1962), pp. 650–677.

[19] T. D. Lee and M. Nauenberg. "Degenerate Systems and Mass Singularities". In: *Phys. Rev.* 133 (1964). Ed. by G. Feinberg, B1549–B1562.

[20] Stefano Catani. "The Singular behavior of QCD amplitudes at two loop order". In: *Phys. Lett. B* 427 (1998), pp. 161–171. arXiv: hep-ph/9802439.

[21] Thomas Becher and Matthias Neubert. "On the Structure of Infrared Singularities of Gauge-Theory Amplitudes". In: *JHEP* 06 (2009). [Erratum: JHEP 11, 024 (2013)], p. 081. arXiv: 0903.1126 [hep-ph].

[22] Stefano Catani and Massimiliano Grazzini. "Collinear factorization and splitting functions for next-to-next-to-leading order QCD calculations". In: *Phys. Lett. B* 446 (1999), pp. 143–152. arXiv: hep-ph/9810389.

[23] Charalampos Anastasiou and Kirill Melnikov. "Higgs boson production at hadron colliders in NNLO QCD". In: *Nucl. Phys. B* 646 (2002), pp. 220–256. arXiv: hep-ph/0207004.

[24] R. E. Cutkosky. "Singularities and discontinuities of Feynman amplitudes". In: *J. Math. Phys.* 1 (1960), pp. 429–433.

[25] Guido Altarelli and G. Parisi. "Asymptotic Freedom in Parton Language". In: *Nucl. Phys. B* 126 (1977), pp. 298–318.

[26] Bakul Agarwal et al. "Five-Parton Scattering in QCD at Two Loops". In: (Nov. 2023). arXiv: 2311.09870 [hep-ph].

[27] Ruth Britto et al. "Direct proof of tree-level recursion relation in Yang-Mills theory". In: *Phys. Rev. Lett.* 94 (2005), p. 181602. arXiv: hep-th/0501052.

[28] Nima Arkani-Hamed, Freddy Cachazo, and Jared Kaplan. "What is the Simplest Quantum Field Theory?" In: *JHEP* 09 (2010), p. 016. arXiv: 0808.1446 [hep-th].

[29] R. E. Cutkosky. "Singularities and Discontinuities of Feynman Amplitudes". In: *Journal of Mathematical Physics* 1.5 (Sept. 1960), pp. 429–433. eprint: https://pubs.aip.org/aip/jmp/article-pdf/1/5/429/19167756/429_1_online.pdf. URL: https://doi.org/10.1063/1.1703676.

[30] Richard John Eden et al. *The analytic S-matrix*. Cambridge University Press, 2002.

[31] Zvi Bern et al. "One loop n point gauge theory amplitudes, unitarity and collinear limits". In: *Nucl. Phys. B* 425 (1994), pp. 217–260. arXiv: hep-ph/9403226.

[32] R. Keith Ellis et al. "Masses, fermions and generalized D-dimensional unitarity". In: *Nucl. Phys. B* 822 (2009), pp. 270–282. arXiv: 0806.3467 [hep-ph].

[33] R. Keith Ellis et al. "One-loop calculations in quantum field theory: from Feynman diagrams to unitarity cuts". In: *Phys. Rept.* 518 (2012), pp. 141–250. arXiv: 1105.4319 [hep-ph].

[34] Samuel Abreu et al. "Planar Two-Loop Five-Gluon Amplitudes from Numerical Unitarity". In: *Phys. Rev. D* 97.11 (2018), p. 116014. arXiv: 1712.03946 [hep-ph].

[35] Sidney Coleman. *Aspects of Symmetry: Selected Erice Lectures*. Cambridge, U.K.: Cambridge University Press, 1985.

[36] Georges Aad et al. "Measurement of multi-jet cross sections in proton-proton collisions at a 7 TeV center-of-mass energy". In: *Eur. Phys. J. C* 71 (2011), p. 1763. arXiv: 1107.2092 [hep-ex].

[37] Serguei Chatrchyan et al. "Measurement of the Ratio of the Inclusive 3-Jet Cross Section to the Inclusive 2-Jet Cross Section in pp Collisions at $\sqrt{s} = 7$ TeV and First Determination of the Strong Coupling Constant in the TeV Range". In: *Eur. Phys. J. C* 73.10 (2013), p. 2604. arXiv: 1304.7498 [hep-ex].

[38] Vardan Khachatryan et al. "Measurement of the inclusive 3-jet production differential cross section in proton–proton collisions at 7 TeV and determination of the strong coupling constant in the TeV range". In: *Eur. Phys. J. C* 75.5 (2015), p. 186. arXiv: 1412.1633 [hep-ex].

[39] Georges Aad et al. "Measurement of three-jet production cross-sections in pp collisions at 7 TeV centre-of-mass energy using the ATLAS detector". In: *Eur. Phys. J. C* 75.5 (2015), p. 228. arXiv: 1411.1855 [hep-ex].

[40] A. Gehrmann-De Ridder et al. "Triple Differential Dijet Cross Section at the LHC". In: *Phys. Rev. Lett.* 123.10 (2019), p. 102001. arXiv: 1905.09047 [hep-ph].

[41] Michał Czakon et al. "Single-jet inclusive rates with exact color at $\mathcal{O}(\alpha_s^4)$". In: *JHEP* 10 (2019), p. 262. arXiv: 1907.12911 [hep-ph].

[42] Michal Czakon, Alexander Mitov, and Rene Poncelet. "Next-to-Next-to-Leading Order Study of Three-Jet Production at the LHC". In: *Phys. Rev. Lett.* 127.15 (2021). [Erratum: Phys.Rev.Lett. 129, 119901 (2022), Erratum: Phys.Rev.Lett. 129, 119901 (2022)], p. 152001. arXiv: 2106.05331 [hep-ph].

[43] X. Chen et al. "NNLO QCD corrections in full colour for jet production observables at the LHC". In: *JHEP* 09 (2022), p. 025. arXiv: 2204.10173 [hep-ph].

[44] Manuel Alvarez et al. "NNLO QCD corrections to event shapes at the LHC". In: *JHEP* 03 (2023), p. 129. arXiv: 2301.01086 [hep-ph].

[45] Vladimir N. Gribov. *Strong interactions of hadrons at high emnergies: Gribov lectures on Theoretical Physics*. Ed. by Yuri L. Dokshitzer and Julia Nyiri. Cambridge University Press, Oct. 2012.

[46] Neelima Agarwal et al. "The infrared structure of perturbative gauge theories". In: *Phys. Rept.* 994 (2023), pp. 1–120. arXiv: 2112.07099 [hep-ph].

[47] Dmitry Chicherin and Vasily Sotnikov. "Pentagon Functions for Scattering of Five Massless Particles". In: *JHEP* 20 (2020), p. 167. arXiv: 2009.07803 [hep-ph].

[48] Giuseppe De Laurentis et al. "Double-Virtual NNLO QCD Corrections for Five-Parton Scattering: The Gluon Channel". In: (Nov. 2023). arXiv: 2311.10086 [hep-ph].

[49] Giuseppe De Laurentis, Harald Ita, and Vasily Sotnikov. "Double-Virtual NNLO QCD Corrections for Five-Parton Scattering: The Quark Channels". In: (Nov. 2023). arXiv: 2311.18752 [hep-ph].

[50] Paulo Nogueira. "Automatic Feynman graph generation". In: *J.Comput.Phys.* 105 (1993), pp. 279–289.

[51] Tiziano Peraro and Lorenzo Tancredi. "Physical projectors for multi-leg helicity amplitudes". In: *JHEP* 07 (2019), p. 114. arXiv: 1906.03298 [hep-ph].

[52] Tiziano Peraro and Lorenzo Tancredi. "Tensor decomposition for bosonic and fermionic scattering amplitudes". In: *Phys. Rev. D* 103.5 (2021), p. 054042. arXiv: 2012.00820 [hep-ph].

[53] J.A.M. Vermaseren. "New features of FORM". In: (2000). arXiv: math-ph/0010025 [math-ph].

[54] Ben Ruijl, Takahiro Ueda, and Jos Vermaseren. "FORM version 4.2". In: (July 2017). arXiv: 1707.06453 [hep-ph].

[55] T. Gehrmann, J.M. Henn, and N.A. Lo Presti. "Pentagon functions for massless planar scattering amplitudes". In: *JHEP* 10 (2018), p. 103. arXiv: 1807.09812 [hep-ph].

[56] Bakul Agarwal et al. "Two-loop leading colour QCD corrections to $q\bar{q} \to \gamma\gamma g$ and $qg \to \gamma\gamma q$". In: *JHEP* 04 (2021), p. 201. arXiv: 2102.01820 [hep-ph].

[57] Bakul Agarwal et al. "Two-Loop Helicity Amplitudes for Diphoton Plus Jet Production in Full Color". In: *Phys. Rev. Lett.* 127.26 (2021), p. 262001. arXiv: 2105.04585 [hep-ph].

[58] S. Laporta. "High-precision calculation of multiloop Feynman integrals by difference equations". In: *Int. J. Mod. Phys. A* 15 (2000), pp. 5087–5159. arXiv: hep-ph/0102033.

[59] Philipp Maierhöfer, Johann Usovitsch, and Peter Uwer. "Kira—A Feynman integral reduction program". In: *Comput. Phys. Commun.* 230 (2018), pp. 99–112. arXiv: 1705.05610 [hep-ph].

[60] Jonas Klappert et al. "Integral reduction with Kira 2.0 and finite field methods". In: *Comput. Phys. Commun.* 266 (2021), p. 108024. arXiv: 2008.06494 [hep-ph].

[61] Andreas von Manteuffel and Robert M. Schabinger. "A novel approach to integration by parts reduction". In: *Phys. Lett.* B744 (2015), pp. 101–104. arXiv: 1406.4513 [hep-ph].

[62] Andreas von Manteuffel and Robert M. Schabinger. "Quark and gluon form factors to four-loop order in QCD: the N_f^3 contributions". In: *Phys. Rev.* D95.3 (2017), p. 034030. arXiv: 1611.00795 [hep-ph].

[63] Tiziano Peraro. "Scattering amplitudes over finite fields and multivariate functional reconstruction". In: *JHEP* 12 (2016), p. 030. arXiv: 1608.01902 [hep-ph].

[64] Tiziano Peraro. "FiniteFlow: multivariate functional reconstruction using finite fields and dataflow graphs". In: (2019). arXiv: 1905.08019 [hep-ph].

[65] Matthias Heller and Andreas von Manteuffel. "MultivariateApart: Generalized partial fractions". In: *Comput. Phys. Commun.* 271 (2022), p. 108174. arXiv: 2101.08283 [cs.SC].

[66] S. Abreu et al. "Analytic Form of Planar Two-Loop Five-Gluon Scattering Amplitudes in QCD". In: *Phys. Rev. Lett.* 122.8 (2019), p. 082002. arXiv: 1812.04586 [hep-ph].

[67] Janusz Gluza, Krzysztof Kajda, and David A. Kosower. "Towards a Basis for Planar Two-Loop Integrals". In: *Phys. Rev. D* 83 (2011), p. 045012. arXiv: 1009.0472 [hep-th].

[68] Robert M. Schabinger. "A New Algorithm For The Generation Of Unitarity-Compatible Integration By Parts Relations". In: *JHEP* 01 (2012), p. 077. arXiv: 1111.4220 [hep-ph].

[69] Harald Ita. "Two-loop Integrand Decomposition into Master Integrals and Surface Terms". In: *Phys. Rev.* D94.11 (2016), p. 116015. arXiv: 1510.05626 [hep-th].

[70] Kasper J. Larsen and Yang Zhang. "Integration-by-parts reductions from unitarity cuts and algebraic geometry". In: *Phys. Rev.* D93.4 (2016), p. 041701. arXiv: 1511.01071 [hep-th].

[71] Janko Böhm et al. "Complete sets of logarithmic vector fields for integration-by-parts identities of Feynman integrals". In: *Phys. Rev. D* 98.2 (2018), p. 025023. arXiv: 1712.09737 [hep-th].

[72] Bakul Agarwal, Stephen P. Jones, and Andreas von Manteuffel. "Two-loop helicity amplitudes for $gg \to ZZ$ with full top-quark mass effects". In: *JHEP* 05 (2021), p. 256. arXiv: 2011.15113 [hep-ph].

[73] Wolfram Decker et al. SINGULAR *4-2-0 — A computer algebra system for polynomial computations*. http://www.singular.uni-kl.de. 2020.

[74] Costas G. Papadopoulos, Damiano Tommasini, and Christopher Wever. "The Pentabox Master Integrals with the Simplified Differential Equations approach". In: *JHEP* 04 (2016), p. 078. arXiv: 1511.09404 [hep-ph].

[75] Samuel Abreu, Ben Page, and Mao Zeng. "Differential equations from unitarity cuts: nonplanar hexa-box integrals". In: *JHEP* 01 (2019), p. 006. arXiv: 1807.11522 [hep-th].

[76] D. Chicherin et al. "Analytic result for the nonplanar hexa-box integrals". In: *JHEP* 03 (2019), p. 042. arXiv: 1809.06240 [hep-ph].

[77] Samuel Abreu et al. "The two-loop five-point amplitude in $\mathcal{N} = 4$ super-Yang-Mills theory". In: *Phys. Rev. Lett.* 122.12 (2019), p. 121603. arXiv: 1812.08941 [hep-th].

[78] D. Chicherin et al. “All Master Integrals for Three-Jet Production at Next-to-Next-to-Leading Order”. In: *Phys. Rev. Lett.* 123.4 (2019), p. 041603. arXiv: 1812.11160 [hep-ph].

[79] Johannes M. Henn. “Multiloop integrals in dimensional regularization made simple”. In: *Phys. Rev. Lett.* 110 (2013), p. 251601. arXiv: 1304.1806 [hep-th].

[80] Kuo-Tsai Chen. “Iterated path integrals”. In: *Bull. Am. Math. Soc.* 83 (1977), pp. 831–879.

[81] Alexander C. Edison and Stephen G. Naculich. “SU(N) group-theory constraints on color-ordered five-point amplitudes at all loop orders”. In: *Nucl. Phys. B* 858 (2012), pp. 488–501. arXiv: 1111.3821 [hep-th].

[82] Zvi Bern, Lance J. Dixon, and David A. Kosower. “One loop corrections to five gluon amplitudes”. In: *Phys. Rev. Lett.* 70 (1993), pp. 2677–2680. arXiv: hep-ph/9302280 [hep-ph].

[83] Zvi Bern, Lance J. Dixon, and David A. Kosower. “One loop corrections to two quark three gluon amplitudes”. In: *Nucl. Phys. B* 437 (1995), pp. 259–304. arXiv: hep-ph/9409393.

[84] Federico Buccioni et al. “OpenLoops 2”. In: *Eur. Phys. J. C* 79.10 (2019), p. 866. arXiv: 1907.13071 [hep-ph].

[85] S. Badger et al. “Analytic form of the full two-loop five-gluon all-plus helicity amplitude”. In: *Phys. Rev. Lett.* 123.7 (2019), p. 071601. arXiv: 1905.03733 [hep-ph].

[86] S. Abreu et al. “Leading-color two-loop QCD corrections for three-jet production at hadron colliders”. In: *JHEP* 07 (2021), p. 095. arXiv: 2102.13609 [hep-ph].

[87] https://zenodo.org/records/10227683.

[88] S. Frixione, Z. Kunszt, and A. Signer. “Three jet cross-sections to next-to-leading order”. In: *Nucl. Phys. B* 467 (1996), pp. 399–442. arXiv: hep-ph/9512328.

[89] S. Catani and M. H. Seymour. “A General algorithm for calculating jet cross-sections in NLO QCD”. In: *Nucl. Phys. B* 485 (1997). [Erratum: Nucl.Phys.B 510, 503–504 (1998)], pp. 291–419. arXiv: hep-ph/9605323.

[90] A. Gehrmann-De Ridder, T. Gehrmann, and E. W. Nigel Glover. “Antenna subtraction at NNLO”. In: *JHEP* 09 (2005), p. 056. arXiv: hep-ph/0505111.

[91] A. Gehrmann-De Ridder, T. Gehrmann, and E. W. Nigel Glover. “Gluon-gluon antenna functions from Higgs boson decay”. In: *Phys. Lett. B* 612 (2005), pp. 49–60. arXiv: hep-ph/0502110.

[92] A. Gehrmann-De Ridder, T. Gehrmann, and E. W. Nigel Glover. “Quark-gluon antenna functions from neutralino decay”. In: *Phys. Lett. B* 612 (2005), pp. 36–48. arXiv: hep-ph/0501291.

[93] Alejandro Daleo et al. “Antenna subtraction at NNLO with hadronic initial states: initial-final configurations”. In: *JHEP* 01 (2010), p. 118. arXiv: 0912.0374 [hep-ph].

[94] Radja Boughezal, Aude Gehrmann-De Ridder, and Mathias Ritzmann. “Antenna subtraction at NNLO with hadronic initial states: double real radiation for initial-initial configurations with two quark flavours”. In: *JHEP* 02 (2011), p. 098. arXiv: 1011.6631 [hep-ph].

[95] Thomas Gehrmann and Pier Francesco Monni. "Antenna subtraction at NNLO with hadronic initial states: real-virtual initial-initial configurations". In: *JHEP* 12 (2011), p. 049. arXiv: 1107.4037 [hep-ph].

[96] Aude Gehrmann-De Ridder, Thomas Gehrmann, and Mathias Ritzmann. "Antenna subtraction at NNLO with hadronic initial states: double real initial-initial configurations". In: *JHEP* 10 (2012), p. 047. arXiv: 1207.5779 [hep-ph].

[97] M. Czakon. "A novel subtraction scheme for double-real radiation at NNLO". In: *Phys. Lett. B* 693 (2010), pp. 259–268. arXiv: 1005.0274 [hep-ph].

[98] David Heymes. "General formulation of the sector-improved residue subtraction". In: *J. Phys. Conf. Ser.* 608.1 (2015). Ed. by L. Fiala, M. Lokajicek, and N. Tumova, p. 012073. arXiv: 1410.2696 [hep-ph].

[99] Fabrizio Caola, Kirill Melnikov, and Raoul Röntsch. "Nested soft-collinear subtractions in NNLO QCD computations". In: *Eur. Phys. J. C* 77.4 (2017), p. 248. arXiv: 1702.01352 [hep-ph].

[100] Fabrizio Caola, Kirill Melnikov, and Raoul Röntsch. "Analytic results for color-singlet production at NNLO QCD with the nested soft-collinear subtraction scheme". In: *Eur. Phys. J. C* 79.5 (2019), p. 386. arXiv: 1902.02081 [hep-ph].

[101] Fabrizio Caola, Kirill Melnikov, and Raoul Röntsch. "Analytic results for decays of color singlets to gg and $q\bar{q}$ final states at NNLO QCD with the nested soft-collinear subtraction scheme". In: *Eur. Phys. J. C* 79.12 (2019), p. 1013. arXiv: 1907.05398 [hep-ph].

[102] Konstantin Asteriadis et al. "Analytic results for deep-inelastic scattering at NNLO QCD with the nested soft-collinear subtraction scheme". In: *Eur. Phys. J. C* 80.1 (2020), p. 8. arXiv: 1910.13761 [hep-ph].

[103] Federica Devoto et al. "A fresh look at the nested soft-collinear subtraction scheme: NNLO QCD corrections to N-gluon final states in $q\bar{q}$ annihilation". In: *JHEP* 02 (2024), p. 016. arXiv: 2310.17598 [hep-ph].

[104] Matteo Cacciari et al. "Fully Differential Vector-Boson-Fusion Higgs Production at Next-to-Next-to-Leading Order". In: *Phys. Rev. Lett.* 115.8 (2015). [Erratum: Phys.Rev.Lett. 120, 139901 (2018)], p. 082002. arXiv: 1506.02660 [hep-ph].

[105] L. Magnea et al. "Local analytic sector subtraction at NNLO". In: *JHEP* 12 (2018). [Erratum: JHEP 06, 013 (2019)], p. 107. arXiv: 1806.09570 [hep-ph].

[106] Gloria Bertolotti et al. "NNLO subtraction for any massless final state: a complete analytic expression". In: *JHEP* 07 (2023), p. 140. arXiv: 2212.11190 [hep-ph].

[107] Gloria Bertolotti et al. "Local analytic sector subtraction for initial- and final-state radiation at NLO in massless QCD". In: *JHEP* 12 (2022), p. 042. arXiv: 2209.09123 [hep-ph].

[108] Lorenzo Magnea et al. "Strongly-ordered infrared counterterms from factorisation". In: (Mar. 2024). arXiv: 2403.11975 [hep-ph].

[109] Vittorio Del Duca et al. "Jet production in the CoLoRFulNNLO method: event shapes in electron-positron collisions". In: *Phys. Rev. D* 94.7 (2016), p. 074019. arXiv: 1606.03453 [hep-ph].

[110] Vittorio Del Duca et al. "Three-Jet Production in Electron-Positron Collisions at Next-to-Next-to-Leading Order Accuracy". In: *Phys. Rev. Lett.* 117.15 (2016), p. 152004. arXiv: 1603.08927 [hep-ph].

[111] Franz Herzog. "Geometric IR subtraction for final state real radiation". In: *JHEP* 08 (2018), p. 006. arXiv: 1804.07949 [hep-ph].

[112] Stefano Catani and Massimiliano Grazzini. "Infrared factorization of tree level QCD amplitudes at the next-to-next-to-leading order and beyond". In: *Nucl. Phys. B* 570 (2000), pp. 287–325. arXiv: hep-ph/9908523.

[113] Zvi Bern et al. "The infrared behavior of one loop QCD amplitudes at next-to-next-to leading order". In: *Phys. Rev. D* 60 (1999), p. 116001. arXiv: hep-ph/9903516.

[114] Stefano Catani and Massimiliano Grazzini. "The soft gluon current at one loop order". In: *Nucl. Phys. B* 591 (2000), pp. 435–454. arXiv: hep-ph/0007142.

[115] David A. Kosower and Peter Uwer. "One loop splitting amplitudes in gauge theory". In: *Nucl. Phys. B* 563 (1999), pp. 477–505. arXiv: hep-ph/9903515.

[116] B. I. Ermolaev and Victor S. Fadin. "Log - Log Asymptotic Form of Exclusive Cross-Sections in Quantum Chromodynamics". In: *JETP Lett.* 33 (1981), pp. 269–272.

[117] A. Bassetto, M. Ciafaloni, and G. Marchesini. "Jet Structure and Infrared Sensitive Quantities in Perturbative QCD". In: *Phys. Rept.* 100 (1983), pp. 201–272.

[118] Yuri L. Dokshitzer et al. "QCD Coherence in High-Energy Reactions". In: *Rev. Mod. Phys.* 60 (1988), p. 373.

[119] Federico Buccioni et al. "Mixed QCD-electroweak corrections to dilepton production at the LHC in the high invariant mass region". In: *JHEP* 06 (2022), p. 022. arXiv: 2203.11237 [hep-ph].

[120] Fabrizio Caola et al. "The double-soft integral for an arbitrary angle between hard radiators". In: *Eur. Phys. J. C* 78.8 (2018), p. 687. arXiv: 1807.05835 [hep-ph].

[121] Arnd Behring et al. "Mixed QCD-electroweak corrections to W-boson production in hadron collisions". In: *Phys. Rev. D* 103.1 (2021), p. 013008. arXiv: 2009.10386 [hep-ph].

[122] Maximilian Delto and Kirill Melnikov. "Integrated triple-collinear counter-terms for the nested soft-collinear subtraction scheme". In: *JHEP* 05 (2019), p. 148. arXiv: 1901.05213 [hep-ph].

[123] Maximilian Delto et al. "Mixed QCD⊗QED corrections to on-shell Z boson production at the LHC". In: (2019). arXiv: 1909.08428 [hep-ph].

[124] Matthias Heller et al. "Mixed EW-QCD two-loop amplitudes for $q\bar{q} \to \ell^+\ell^-$ and γ_5 scheme independence of multi-loop corrections". In: *JHEP* 05 (2021), p. 213. arXiv: 2012.05918 [hep-ph].

[125] Konstantin Asteriadis et al. "NNLO QCD corrections to weak boson fusion Higgs boson production in the H $\to$ b$\bar{b}$ and H $\to$ WW* $\to$ 4l decay channels". In: *JHEP* 02 (2022), p. 046. arXiv: 2110.02818 [hep-ph].

[126] Christian Brønnum-Hansen et al. "Non-factorisable contribution to t-channel single-top production". In: *JHEP* 06 (2022), p. 061. arXiv: 2204.05770 [hep-ph].

[127] Chiara Signorile-Signorile and Davide Maria Tagliabue. "Towards a general nested soft-collinear subtraction method for NNLO calculations". In: *PoS* EPS-HEP2023 (2024), p. 269.

[128] Chiara Signorile-Signorile and Davide Maria Tagliabue. "Advances in the nested soft-collinear subtraction scheme". In: *PoS* RADCOR2023 (2023), p. 075. arXiv: 2308.11982 [hep-ph].

[129] Thomas Becher et al. "Transverse-momentum spectra of electroweak bosons near threshold at NNLO". In: *JHEP* 02 (2014), p. 004. arXiv: 1309.3245 [hep-ph].

[130] M. Cepeda et al. "Report from Working Group 2: Higgs Physics at the HL-LHC and HE-LHC". In: *CERN Yellow Rep. Monogr.* 7 (2019). Ed. by Andrea Dainese et al., pp. 221–584. arXiv: 1902.00134 [hep-ph].

[131] A. Denner et al. "Standard Model Higgs-Boson Branching Ratios with Uncertainties". In: *Eur. Phys. J. C* 71 (2011), p. 1753. arXiv: 1107.5909 [hep-ph].

[132] Georges Aad et al. "Measurement of the Higgs boson mass with H $\to \gamma\gamma$ decays in 140 fb−1 of s=13 TeV pp collisions with the ATLAS detector". In: *Phys. Lett. B* 847 (2023), p. 138315. arXiv: 2308.07216 [hep-ex].

[133] "Measurement of the Higgs boson mass in the $H \to ZZ^* \to 4\ell$ decay channel using 139 fb^{-1} of $\sqrt{s} = 13$ TeV pp collisions recorded by the ATLAS detector at the LHC". In: (July 2022). arXiv: 2207.00320 [hep-ex].

[134] Georges Aad et al. "Combined Measurement of the Higgs Boson Mass from the H$\to\gamma\gamma$ and H$\to$ZZ*$\to 4\ell$ Decay Channels with the ATLAS Detector Using s=7, 8, and 13 TeV pp Collision Data". In: *Phys. Rev. Lett.* 131.25 (2023), p. 251802. arXiv: 2308.04775 [hep-ex].

[135] Albert M Sirunyan et al. "Measurements of properties of the Higgs boson decaying into the four-lepton final state in pp collisions at $\sqrt{s} = 13$ TeV". In: *JHEP* 11 (2017), p. 047. arXiv: 1706.09936 [hep-ex].

[136] "Measurement of the properties of Higgs boson production at $\sqrt{s} = 13$ TeV in the $H \to \gamma\gamma$ channel using 139 fb^{-1} of pp collision data with the ATLAS experiment". In: (July 2022). arXiv: 2207.00348 [hep-ex].

[137] Ilaria Brivio, Tyler Corbett, and Michael Trott. "The Higgs width in the SMEFT". In: *JHEP* 10 (2019), p. 056. arXiv: 1906.06949 [hep-ph].

[138] John Ellis et al. "Top, Higgs, Diboson and Electroweak Fit to the Standard Model Effective Field Theory". In: *JHEP* 04 (2021), p. 279. arXiv: 2012.02779 [hep-ph].

[139] Jacob J. Ethier et al. "Combined SMEFT interpretation of Higgs, diboson, and top quark data from the LHC". In: *JHEP* 11 (2021), p. 089. arXiv: 2105.00006 [hep-ph].

[140] Nikolas Kauer and Giampiero Passarino. "Inadequacy of zero-width approximation for a light Higgs boson signal". In: *JHEP* 08 (2012), p. 116. arXiv: 1206.4803 [hep-ph].

[141] Fabrizio Caola and Kirill Melnikov. "Constraining the Higgs boson width with ZZ production at the LHC". In: *Phys. Rev. D* 88 (2013), p. 054024. arXiv: 1307.4935 [hep-ph].

[142] John M. Campbell, R. Keith Ellis, and Ciaran Williams. "Bounding the Higgs Width at the LHC Using Full Analytic Results for $gg- > e^-e^+\mu^-\mu^+$". In: *JHEP* 04 (2014), p. 060. arXiv: 1311.3589 [hep-ph].

[143] Armen Tumasyan et al. "First evidence for off-shell production of the Higgs boson and measurement of its width". In: (Feb. 2022). arXiv: 2202.06923 [hep-ex].

[144] Morad Aaboud et al. "Constraints on off-shell Higgs boson production and the Higgs boson total width in $ZZ \to 4\ell$ and $ZZ \to 2\ell 2\nu$ final states with the ATLAS detector". In: *Phys. Lett. B* 786 (2018), pp. 223–244. arXiv: 1808.01191 [hep-ex].

[145] Christoph Englert and Michael Spannowsky. "Limitations and Opportunities of Off-Shell Coupling Measurements". In: *Phys. Rev. D* 90 (2014), p. 053003. arXiv: 1405.0285 [hep-ph].

[146] Heather E. Logan. "Hiding a Higgs width enhancement from off-shell gg(→h*)→ZZ measurements". In: *Phys. Rev. D* 92.7 (2015), p. 075038. arXiv: 1412.7577 [hep-ph].

[147] Aleksandr Azatov et al. "Off-shell Higgs Interpretations Task Force: Models and Effective Field Theories Subgroup Report". In: (Mar. 2022). arXiv: 2203.02418 [hep-ph].

[148] John M. Campbell and R. Keith Ellis. "Higgs Constraints from Vector Boson Fusion and Scattering". In: *JHEP* 04 (2015), p. 030. arXiv: 1502.02990 [hep-ph].

[149] Stephen P. Martin. "Shift in the LHC Higgs Diphoton Mass Peak from Interference with Background". In: *Phys. Rev. D* 86 (2012), p. 073016. arXiv: 1208.1533 [hep-ph].

[150] Lance J. Dixon and Ye Li. "Bounding the Higgs Boson Width Through Interferometry". In: *Phys. Rev. Lett.* 111 (2013), p. 111802. arXiv: 1305.3854 [hep-ph].

[151] Daniel de Florian et al. "A complete $O(\alpha_S^2)$ calculation of the signal-background interference for the Higgs diphoton decay channel". In: *Eur. Phys. J. C* 73.4 (2013), p. 2387. arXiv: 1303.1397 [hep-ph].

[152] "Estimate of the m_H shift due to interference between signal and background processes in the $H \to \gamma\gamma$ channel, for the $\sqrt{s} = 8$ TeV dataset recorded by ATLAS". In: (Apr. 2016).

[153] "A projection of the precision of the Higgs boson mass measurement in the diphoton decay channel at the High Luminosity LHC". In: (2022).

[154] Leandro Cieri et al. "Transverse-momentum resummation for the signal-background interference in the H→γγ channel at the LHC". In: *Phys. Rev. D* 96.5 (2017), p. 054003. arXiv: 1706.07331 [hep-ph].

[155] John Campbell et al. "Interference in the $gg \to h \to \gamma\gamma$ On-Shell Rate and the Higgs Boson Total Width". In: *Phys. Rev. Lett.* 119.18 (2017). [Addendum: Phys.Rev.Lett. 119, 199901 (2017)], p. 181801. arXiv: 1704.08259 [hep-ph].

[156] F. Coradeschi et al. "Interference effects in the $H(\to \gamma\gamma) + 2$ jets channel at the LHC". In: *Phys. Rev. D* 92.1 (2015), p. 013004. arXiv: 1504.05215 [hep-ph].

[157] Stephen P. Martin. "Interference of Higgs Diphoton Signal and Background in Production with a Jet at the LHC". In: *Phys. Rev. D* 88.1 (2013), p. 013004. arXiv: 1303.3342 [hep-ph].

[158] Piotr Bargiela et al. "Three-loop helicity amplitudes for diphoton production in gluon fusion". In: *JHEP* 02 (2022), p. 153. arXiv: 2111.13595 [hep-ph].

[159] Simon Badger et al. "Virtual QCD corrections to gluon-initiated diphoton plus jet production at hadron colliders". In: *JHEP* 11 (2021), p. 083. arXiv: 2106.08664 [hep-ph].

[160] Piotr Bargiela et al. "Signal-background interference effects in Higgs-mediated diphoton production beyond NLO". In: *Eur. Phys. J. C* 83.2 (2023), p. 174. arXiv: 2212.06287 [hep-ph].

[161] Federico Buccioni et al. "Interference effects in $\mathrm{gg} \to \mathrm{H} \to \mathrm{Z}\gamma$ beyond leading order". In: *Phys. Lett. B* 851 (2024), p. 138596. arXiv: 2312.12384 [hep-ph].

[162] Georges Aad et al. "Evidence for the Higgs Boson Decay to a Z Boson and a Photon at the LHC". In: *Phys. Rev. Lett.* 132.2 (2024), p. 021803. arXiv: 2309.03501 [hep-ex].

[163] Duane A. Dicus and Scott S. D. Willenbrock. "Photon Pair Production and the Intermediate Mass Higgs Boson". In: *Phys. Rev. D* 37 (1988), p. 1801.

[164] Lance J. Dixon and M. Stewart Siu. "Resonance continuum interference in the diphoton Higgs signal at the LHC". In: *Phys. Rev. Lett.* 90 (2003), p. 252001. arXiv: hep-ph/0302233.

[165] "Measurement of the total and differential Higgs boson production cross-sections at $\sqrt{s} = 13$ TeV with the ATLAS detector by combining the $H \to ZZ^* \to 4\ell$ and $H \to \gamma\gamma$ decay channels". In: (July 2022). arXiv: 2207.08615 [hep-ex].

[166] Georges Aad et al. "Measurements of the Higgs boson inclusive and differential fiducial cross-sections in the diphoton decay channel with pp collisions at $\sqrt{s} = 13$ TeV with the ATLAS detector". In: *JHEP* 08 (2022), p. 027. arXiv: 2202.00487 [hep-ex].

[167] "Measurement of the Higgs boson inclusive and differential fiducial production cross sections in the diphoton decay channel with pp collisions at $\sqrt{s} = 13$ TeV". In: (Aug. 2022). arXiv: 2208.12279 [hep-ex].

[168] Stefano Catani, Daniel de Florian, and Massimiliano Grazzini. "Higgs production in hadron collisions: Soft and virtual QCD corrections at NNLO". In: *JHEP* 05 (2001), p. 025. arXiv: hep-ph/0102227.

[169] S. Moch and A. Vogt. "Higher-order soft corrections to lepton pair and Higgs boson production". In: *Phys. Lett. B* 631 (2005), pp. 48–57. arXiv: hep-ph/0508265.

[170] Richard Ball et al. "Higgs production in gluon fusion beyond NNLO". In: *Nucl. Phys. B* 874 (2013), pp. 746–772. arXiv: 1303.3590 [hep-ph].

[171] D. de Florian et al. "Approximate $\mathrm{N^3LO}$ Higgs-boson production cross section using physical-kernel constraints". In: *JHEP* 10 (2014), p. 176. arXiv: 1408.6277 [hep-ph].

[172] Charalampos Anastasiou et al. “Higgs boson gluon–fusion production at threshold in N^{3}LO QCD”. In: *Phys. Lett. B* 737 (2014), pp. 325–328. arXiv: 1403.4616 [hep-ph].

[173] Daniel de Florian and Javier Mazzitelli. “A next-to-next-to-leading order calculation of soft-virtual cross sections”. In: *JHEP* 12 (2012), p. 088. arXiv: 1209.0673 [hep-ph].

[174] Paolo Bolzoni. “Threshold resummation of Drell-Yan rapidity distributions”. In: *Phys. Lett. B* 643 (2006), pp. 325–330. arXiv: hep-ph/0609073.

[175] Thomas Becher, Matthias Neubert, and Gang Xu. “Dynamical Threshold Enhancement and Resummation in Drell-Yan Production”. In: *JHEP* 07 (2008), p. 030. arXiv: 0710.0680 [hep-ph].

[176] Marco Bonvini, Stefano Forte, and Giovanni Ridolfi. “Soft gluon resummation of Drell-Yan rapidity distributions: Theory and phenomenology”. In: *Nucl. Phys. B* 847 (2011), pp. 93–159. arXiv: 1009.5691 [hep-ph].

[177] Marco Bonvini et al. “Signal-background interference effects for $gg ß H ß W^+W^-$ beyond leading order”. In: *Phys. Rev. D* 88.3 (2013), p. 034032. arXiv: 1304.3053 [hep-ph].

[178] John M. Campbell et al. “Predictions for diphoton production at the LHC through NNLO in QCD”. In: *JHEP* 07 (2016), p. 148. arXiv: 1603.02663 [hep-ph].

[179] Zvi Bern, Lance J. Dixon, and Carl Schmidt. “Isolating a light Higgs boson from the diphoton background at the CERN LHC”. In: *Phys. Rev. D* 66 (2002), p. 074018. arXiv: hep-ph/0206194.

[180] John M. Campbell and R. Keith Ellis. “An Update on vector boson pair production at hadron colliders”. In: *Phys. Rev. D* 60 (1999), p. 113006. arXiv: hep-ph/9905386.

[181] Radja Boughezal et al. “Color singlet production at NNLO in MCFM”. In: *Eur. Phys. J. C* 77.1 (2017), p. 7. arXiv: 1605.08011 [hep-ph].

[182] John Campbell and Tobias Neumann. “Precision Phenomenology with MCFM”. In: *JHEP* 12 (2019), p. 034. arXiv: 1909.09117 [hep-ph].

[183] Z. Bern, A. De Freitas, and Lance J. Dixon. “Two loop amplitudes for gluon fusion into two photons”. In: *JHEP* 09 (2001), p. 037. arXiv: hep-ph/0109078.

[184] Fabio Cascioli, Philipp Maierhofer, and Stefano Pozzorini. “Scattering Amplitudes with Open Loops”. In: *Phys. Rev. Lett.* 108 (2012), p. 111601. arXiv: 1111.5206 [hep-ph].

[185] Richard D. Ball et al. “Parton distributions from high-precision collider data”. In: *Eur. Phys. J. C* 77.10 (2017), p. 663. arXiv: 1706.00428 [hep-ph].

[186] Andy Buckley et al. “LHAPDF6: parton density access in the LHC precision era”. In: *Eur. Phys. J. C* 75 (2015), p. 132. arXiv: 1412.7420 [hep-ph].

[187] Gavin P. Salam and Juan Rojo. “A Higher Order Perturbative Parton Evolution Toolkit (HOPPET)”. In: *Comput. Phys. Commun.* 180 (2009), pp. 120–156. arXiv: 0804.3755 [hep-ph].

[188] Gavin P. Salam and Emma Slade. “Cuts for two-body decays at colliders”. In: *JHEP* 11 (2021), p. 220. arXiv: 2106.08329 [hep-ph].

[189] D. de Florian et al. "Handbook of LHC Higgs Cross Sections: 4. Deciphering the Nature of the Higgs Sector". In: 2/2017 (Oct. 2016). arXiv: 1610.07922 [hep-ph].

[190] G. Zanderighi. "Higgs physics 10 years after the discovery". In: (). Talk given at the Higgs 2022 conference.

[191] R. Harlander. "Higher-order predictions for Higgs processes". In: (). Talk given at the Higgs 2022 conference.

[192] L. Bergstrom and G. Hulth. "Induced Higgs Couplings to Neutral Bosons in e^+e^- Collisions". In: *Nucl. Phys. B* 259 (1985). [Erratum: Nucl.Phys.B 276, 744–744 (1986)], pp. 137–155.

[193] John F. Gunion et al. *The Higgs Hunter's Guide*. Vol. 80. 2000.

[194] Abdelhak Djouadi. "The Anatomy of electro-weak symmetry breaking. I: The Higgs boson in the standard model". In: *Phys. Rept.* 457 (2008), pp. 1–216. arXiv: hep-ph/0503172.

[195] John R. Ellis, Mary K. Gaillard, and Dimitri V. Nanopoulos. "A Phenomenological Profile of the Higgs Boson". In: *Nucl. Phys. B* 106 (1976), p. 292.

[196] H. M. Georgi et al. "Higgs Bosons from Two Gluon Annihilation in Proton Proton Collisions". In: *Phys. Rev. Lett.* 40 (1978), p. 692.

[197] A. Djouadi et al. "The Higgs photon - Z boson coupling revisited". In: *Eur. Phys. J. C* 1 (1998), pp. 163–175. arXiv: hep-ph/9701342.

[198] Cheng-Wei Chiang and Kei Yagyu. "Higgs boson decays to $\gamma\gamma$ and $Z\gamma$ in models with Higgs extensions". In: *Phys. Rev. D* 87.3 (2013), p. 033003. arXiv: 1207.1065 [hep-ph].

[199] Chian-Shu Chen et al. "New Scalar Contributions to $h \to Z\gamma$". In: *Phys. Rev. D* 87 (2013), p. 075019. arXiv: 1301.4694 [hep-ph].

[200] Aleksandr Azatov et al. "New Prospects for Higgs Compositeness in $h \to Z\gamma$". In: *Phys. Rev. D*88.7 (2013), p. 075019. arXiv: 1308.2676 [hep-ph].

[201] Qing-Hong Cao et al. "Signature of pseudo Nambu–Goldstone Higgs boson in its decay". In: *Phys. Lett. B* 789 (2019), pp. 233–237. arXiv: 1810.07661 [hep-ph].

[202] M. Spira, A. Djouadi, and P. M. Zerwas. "QCD corrections to the H Z gamma coupling". In: *Phys. Lett. B* 276 (1992), pp. 350–353.

[203] Thomas Gehrmann, Sam Guns, and Dominik Kara. "The rare decay $H \to Z\gamma$ in perturbative QCD". In: *JHEP* 09 (2015), p. 038. arXiv: 1505.00561 [hep-ph].

[204] R. Bonciani et al. "Next-to-leading order QCD corrections to the decay width H $\to$ Zγ". In: *JHEP* 08 (2015), p. 108. arXiv: 1505.00567 [hep-ph].

[205] L. Ametller et al. "Role of the QCD Induced Gluon - Gluon Coupling to Gauge Boson Pairs in the Multi - Tev Region". In: *Phys. Rev. D* 32 (1985), p. 1699.

[206] J. J. van der Bij and E. W. Nigel Glover. "PHOTON Z BOSON PAIR PRODUCTION VIA GLUON FUSION". In: *Phys. Lett. B* 206 (1988), pp. 701–704.

[207] K. L. Adamson, D. de Florian, and A. Signer. "Gluon induced contributions to $Z\gamma$ production at hadron colliders". In: *Phys. Rev. D* 67 (2003), p. 034016. arXiv: hep-ph/0211295.

[208] Stefano Catani et al. "Diphoton production at hadron colliders: a fully-differential QCD calculation at NNLO". In: *Phys. Rev. Lett.* 108 (2012). [Erratum: Phys.Rev.Lett. 117, 089901 (2016)], p. 072001. arXiv: 1110.2375 [hep-ph].

[209] Thomas Gehrmann, Lorenzo Tancredi, and Erich Weihs. "Two-loop QCD helicity amplitudes for $g\,g \to Z\,g$ and $g\,g \to Z\,\gamma$". In: *JHEP* 04 (2013), p. 101. arXiv: 1302.2630 [hep-ph].

[210] Georges Aad et al. "A search for the $Z\gamma$ decay mode of the Higgs boson in pp collisions at $\sqrt{s} = 13$ TeV with the ATLAS detector". In: *Phys. Lett. B* 809 (2020), p. 135754. arXiv: 2005.05382 [hep-ex].

[211] A. Djouadi, M. Spira, and P. M. Zerwas. "Production of Higgs bosons in proton colliders: QCD corrections". In: *Phys. Lett. B* 264 (1991), pp. 440–446.

[212] S. Dawson. "Radiative corrections to Higgs boson production". In: *Nucl. Phys. B* 359 (1991), pp. 283–300.

[213] M. Spira et al. "Higgs boson production at the LHC". In: *Nucl. Phys. B* 453 (1995), pp. 17–82. arXiv: hep-ph/9504378.

[214] Rafael Boto et al. "New physics interpretations for nonstandard values of $h \to Z\gamma$". In: (Dec. 2023). arXiv: 2312.13050 [hep-ph].

[215] S. D. Drell and Tung-Mow Yan. "Massive Lepton Pair Production in Hadron-Hadron Collisions at High-Energies". In: *Phys. Rev. Lett.* 25 (1970). [Erratum: Phys. Rev. Lett.25,902(1970)], pp. 316–320.

[216] Albert M Sirunyan et al. "Search for resonant and nonresonant new phenomena in high-mass dilepton final states at $\sqrt{s} = 13$ TeV". In: *JHEP* 07 (2021), p. 208. arXiv: 2103.02708 [hep-ex].

[217] Morad Aaboud et al. "Search for new high-mass phenomena in the dilepton final state using 36 fb^{-1} of proton-proton collision data at $\sqrt{s} = 13$ TeV with the ATLAS detector". In: *JHEP* 10 (2017), p. 182. arXiv: 1707.02424 [hep-ex].

[218] Simone Alioli et al. "Catching a New Force by the Tail". In: *Phys. Rev. Lett.* 120.10 (2018), p. 101801. arXiv: 1712.02347 [hep-ph].

[219] W. Buchmuller and D. Wyler. "Effective Lagrangian Analysis of New Interactions and Flavor Conservation". In: *Nucl. Phys. B* 268 (1986), pp. 621–653.

[220] B. Grzadkowski et al. "Dimension-Six Terms in the Standard Model Lagrangian". In: *JHEP* 10 (2010), p. 085. arXiv: 1008.4884 [hep-ph].

[221] Michael E. Peskin and Tatsu Takeuchi. "A New constraint on a strongly interacting Higgs sector". In: *Phys. Rev. Lett.* 65 (1990), pp. 964–967.

[222] Adam Falkowski and Kin Mimouni. "Model independent constraints on four-lepton operators". In: *JHEP* 02 (2016), p. 086. arXiv: 1511.07434 [hep-ph].

[223] Marco Farina et al. "Energy helps accuracy: electroweak precision tests at hadron colliders". In: *Phys. Lett. B* 772 (2017), pp. 210–215. arXiv: 1609.08157 [hep-ph].

[224] Sally Dawson and Pier Paolo Giardino. "New Physics Through Drell Yan SMEFT Measurements at NLO". In: (May 2021). arXiv: 2105.05852 [hep-ph].

[225] R. Aaij et al. "Test of lepton universality with $B^0 \to K^{*0}\ell^+\ell^-$ decays". In: *JHEP* 08 (2017), p. 055. arXiv: 1705.05802 [hep-ex].

[226] Roel Aaij et al. "Search for lepton-universality violation in $B^+ \to K^+\ell^+\ell^-$ decays". In: *Phys. Rev. Lett.* 122.19 (2019), p. 191801. arXiv: 1903.09252 [hep-ex].

[227] Roel Aaij et al. "Test of lepton universality in beauty-quark decays". In: (Mar. 2021). arXiv: 2103.11769 [hep-ex].

[228] Simone Bifani et al. "Review of Lepton Universality tests in B decays". In: *J. Phys. G* 46.2 (2019), p. 023001. arXiv: 1809.06229 [hep-ex].

[229] R. Hamberg, W.L. van Neerven, and T. Matsuura. "A Complete calculation of the order $\alpha - s^2$ correction to the Drell-Yan K factor". In: *Nucl.Phys.* B359 (1991), pp. 343–405.

[230] W. L. van Neerven and E. B. Zijlstra. "The $O(\alpha_s^2)$ corrected Drell-Yan K factor in the DIS and MS scheme". In: *Nucl. Phys. B* 382 (1992). [Erratum: Nucl.Phys.B 680, 513–514 (2004)], pp. 11–62.

[231] Robert V. Harlander and William B. Kilgore. "Next-to-next-to-leading order Higgs production at hadron colliders". In: *Phys. Rev. Lett.* 88 (2002), p. 201801. arXiv: hep-ph/0201206.

[232] Charalampos Anastasiou et al. "Dilepton rapidity distribution in the Drell-Yan process at NNLO in QCD". In: *Phys. Rev. Lett.* 91 (2003), p. 182002. arXiv: hep-ph/0306192 [hep-ph].

[233] Charalampos Anastasiou et al. "High precision QCD at hadron colliders: Electroweak gauge boson rapidity distributions at NNLO". In: *Phys. Rev.* D69 (2004), p. 094008. arXiv: hep-ph/0312266 [hep-ph].

[234] Kirill Melnikov and Frank Petriello. "Electroweak gauge boson production at hadron colliders through O(alpha(s)**2)". In: *Phys. Rev.* D74 (2006), p. 114017. arXiv: hep-ph/0609070 [hep-ph].

[235] Stefano Catani et al. "Vector boson production at hadron colliders: a fully exclusive QCD calculation at NNLO". In: *Phys. Rev. Lett.* 103 (2009), p. 082001. arXiv: 0903.2120 [hep-ph].

[236] Ryan Gavin et al. "FEWZ 2.0: A code for hadronic Z production at next-to-next-to-leading order". In: *Comput. Phys. Commun.* 182 (2011), pp. 2388–2403. arXiv: 1011.3540 [hep-ph].

[237] Claude Duhr, Falko Dulat, and Bernhard Mistlberger. "Drell-Yan Cross Section to Third Order in the Strong Coupling Constant". In: *Phys. Rev. Lett.* 125.17 (2020), p. 172001. arXiv: 2001.07717 [hep-ph].

[238] Claude Duhr, Falko Dulat, and Bernhard Mistlberger. "Charged current Drell-Yan production at N^{3}LO". In: *JHEP* 11 (2020), p. 143. arXiv: 2007.13313 [hep-ph].

[239] Claude Duhr and Bernhard Mistlberger. "Lepton-pair production at hadron colliders at N^{3}LO in QCD". In: (Nov. 2021). arXiv: 2111.10379 [hep-ph].

[240] Xuan Chen et al. "Dilepton Rapidity Distribution in Drell-Yan Production to Third Order in QCD". In: *Phys. Rev. Lett.* 128.5 (2022), p. 052001. arXiv: 2107.09085 [hep-ph].

[241] Stefano Camarda, Leandro Cieri, and Giancarlo Ferrera. "Drell-Yan lepton-pair production: q_T resummation at N^{3}LL accuracy and fiducial cross sections at N^{3}LO". In: (Mar. 2021). arXiv: 2103.04974 [hep-ph].

[242] X. Chen et al. "Third order fiducial predictions for Drell-Yan at the LHC". In: (Mar. 2022). arXiv: 2203.01565 [hep-ph].

[243] Stefan Dittmaier and Michael Krämer. "Electroweak radiative corrections to W boson production at hadron colliders". In: *Phys. Rev. D* 65 (2002), p. 073007. arXiv: hep-ph/0109062.

[244] U. Baur et al. "Electroweak radiative corrections to neutral current Drell-Yan processes at hadron colliders". In: *Phys.Rev.* D65 (2002), p. 033007. arXiv: hep-ph/0108274 [hep-ph].

[245] U. Baur and D. Wackeroth. "Electroweak radiative corrections to $p\bar{p} \to W^{\pm} \to \ell^{\pm}\nu$ beyond the pole approximation". In: *Phys. Rev. D* 70 (2004), p. 073015. arXiv: hep-ph/0405191.

[246] A. Arbuzov et al. "One-loop corrections to the Drell-Yan process in SANC. I. The Charged current case". In: *Eur. Phys. J. C* 46 (2006). [Erratum: Eur.Phys.J.C 50, 505 (2007)], pp. 407–412. arXiv: hep-ph/0506110.

[247] V. A. Zykunov. "Weak radiative corrections to Drell-Yan process for large invariant mass of di-lepton pair". In: *Phys. Rev. D* 75 (2007), p. 073019. arXiv: hep-ph/0509315.

[248] C. M. Carloni Calame et al. "Precision electroweak calculation of the charged current Drell-Yan process". In: *JHEP* 12 (2006), p. 016. arXiv: hep-ph/0609170.

[249] V. A. Zykunov. "Radiative corrections to the Drell-Yan process at large dilepton invariant masses". In: *Phys. Atom. Nucl.* 69 (2006), p. 1522.

[250] C.M. Carloni Calame et al. "Precision electroweak calculation of the production of a high transverse-momentum lepton pair at hadron colliders". In: *JHEP* 0710 (2007), p. 109. arXiv: 0710.1722 [hep-ph].

[251] A. Arbuzov et al. "One-loop corrections to the Drell–Yan process in SANC. (II). The Neutral current case". In: *Eur.Phys.J.* C54 (2008), pp. 451–460. arXiv: 0711.0625 [hep-ph].

[252] Stefan Dittmaier and Max Huber. "Radiative corrections to the neutral-current Drell-Yan process in the Standard Model and its minimal supersymmetric extension". In: *JHEP* 01 (2010), p. 060. arXiv: 0911.2329 [hep-ph].

[253] Johann H. Kuhn, A. A. Penin, and Vladimir A. Smirnov. "Summing up subleading Sudakov logarithms". In: *Eur. Phys. J. C* 17 (2000), pp. 97–105. arXiv: hep-ph/9912503.

[254] Marcello Ciafaloni, Paolo Ciafaloni, and Denis Comelli. "Enhanced electroweak corrections to inclusive boson fusion processes at the TeV scale". In: *Nucl. Phys. B* 613 (2001), pp. 382–406. arXiv: hep-ph/0103316.

[255] Ansgar Denner and Stefano Pozzorini. "One loop leading logarithms in electroweak radiative corrections. 1. Results". In: *Eur. Phys. J. C* 18 (2001), pp. 461–480. arXiv: hep-ph/0010201.

[256] Ansgar Denner and Stefano Pozzorini. "One loop leading logarithms in electroweak radiative corrections. 2. Factorization of collinear singularities". In: *Eur. Phys. J. C* 21 (2001), pp. 63–79. arXiv: hep-ph/0104127.

[257] Luca Barze et al. "Neutral current Drell-Yan with combined QCD and electroweak corrections in the POWHEG BOX". In: *Eur. Phys. J.* C73.6 (2013), p. 2474. arXiv: 1302.4606 [hep-ph].

[258] R. Frederix et al. "The automation of next-to-leading order electroweak calculations". In: *JHEP* 07 (2018). [Erratum: JHEP 11, 085 (2021)], p. 185. arXiv: 1804.10017 [hep-ph].

[259] Federico Buccioni et al. "Mixed QCD-electroweak corrections to on-shell Z production at the LHC". In: *Phys. Lett. B* 811 (2020), p. 135969. arXiv: 2005.10221 [hep-ph].

[260] Roberto Bonciani et al. "Next-to-Next-to-Leading Order Mixed QCD-Electroweak Corrections to on-Shell Z Production". In: *Phys. Rev. Lett.* 125.23 (2020), p. 232004. arXiv: 2007.06518 [hep-ph].

[261] Arnd Behring et al. "Estimating the impact of mixed QCD-electroweak corrections on the W-mass determination at the LHC". In: *Phys. Rev. D* 103.11 (2021), p. 113002. arXiv: 2103.02671 [hep-ph].

[262] Roberto Bonciani et al. "On-shell Z boson production through $\mathcal{O}(\alpha\alpha_s)$". In: *JHEP* 02 (2022), p. 095. arXiv: 2111.12694 [hep-ph].

[263] Stefan Dittmaier, Alexander Huss, and Christian Schwinn. "Mixed QCD-electroweak $\mathcal{O}(\alpha_s\alpha)$ corrections to Drell-Yan processes in the resonance region: pole approximation and non-factorizable corrections". In: *Nucl.Phys.* B885 (2014), pp. 318–372. arXiv: 1403.3216 [hep-ph].

[264] Stefan Dittmaier, Alexander Huss, and Christian Schwinn. "Dominant mixed QCD-electroweak $\mathcal{O}(\alpha_s)$ corrections to Drell-Yan processes in the resonance region". In: *Nucl. Phys.* B904 (2016), pp. 216–252. arXiv: 1511.08016 [hep-ph].

[265] Roberto Bonciani et al. "Two-Loop Master Integrals for the mixed EW-QCD virtual corrections to Drell-Yan scattering". In: *JHEP* 09 (2016), p. 091. arXiv: 1604.08581 [hep-ph].

[266] Andreas von Manteuffel and Robert M. Schabinger. "Numerical Multi-Loop Calculations via Finite Integrals and One-Mass EW-QCD Drell-Yan Master Integrals". In: *JHEP* 04 (2017), p. 129. arXiv: 1701.06583 [hep-ph].

[267] Matthias Heller, Andreas von Manteuffel, and Robert M. Schabinger. "Multiple polylogarithms with algebraic arguments and the two-loop EW-QCD Drell-Yan master integrals". In: *Phys. Rev. D* 102.1 (2020), p. 016025. arXiv: 1907.00491 [hep-th].

[268] Syed Mehedi Hasan and Ulrich Schubert. "Master Integrals for the mixed QCD-QED corrections to the Drell-Yan production of a massive lepton pair". In: *JHEP* 11 (2020), p. 107. arXiv: 2004.14908 [hep-ph].

[269] Tommaso Armadillo et al. "Two-loop mixed QCD-EW corrections to neutral current Drell-Yan". In: (Jan. 2022). arXiv: 2201.01754 [hep-ph].

[270] Roberto Bonciani et al. "Mixed strong−electroweak corrections to the Drell−Yan process". In: (June 2021). arXiv: 2106.11953 [hep-ph].

[271] Zvi Bern, Lance J. Dixon, and David A. Kosower. "One loop amplitudes for e+ e- to four partons". In: *Nucl. Phys. B* 513 (1998), pp. 3–86. arXiv: hep-ph/9708239.

[272] Federico Buccioni, Stefano Pozzorini, and Max Zoller. "On-the-fly reduction of open loops". In: *Eur. Phys. J. C* 78.1 (2018), p. 70. arXiv: 1710.11452 [hep-ph].

[273] Stefan Dittmaier, Timo Schmidt, and Jan Schwarz. "Mixed NNLO QCD×electroweak corrections of $\mathcal{O}(N_f\alpha_s\alpha)$ to single-W/Z production at the LHC". In: *JHEP* 12 (2020), p. 201. arXiv: 2009.02229 [hep-ph].

[274] A. Djouadi and P. Gambino. "Electroweak gauge bosons selfenergies: Complete QCD corrections". In: *Phys. Rev. D* 49 (1994). [Erratum: Phys.Rev.D 53, 4111 (1996)], pp. 3499–3511. arXiv: hep-ph/9309298.

[275] S. Abreu et al. "Analytic Form of the Planar Two-Loop Five-Parton Scattering Amplitudes in QCD". In: *JHEP* 05 (2019), p. 084. arXiv: 1904.00945 [hep-ph].

[276] Herschel A. Chawdhry et al. "NNLO QCD corrections to three-photon production at the LHC". In: *JHEP* 02 (2020), p. 057. arXiv: 1911.00479 [hep-ph].

[277] L. Naterop, A. Signer, and Y. Ulrich. "handyG —Rapid numerical evaluation of generalised polylogarithms in Fortran". In: *Comput. Phys. Commun.* 253 (2020), p. 107165. arXiv: 1909.01656 [hep-ph].

[278] Claude Duhr and Falko Dulat. "PolyLogTools — polylogs for the masses". In: *JHEP* 08 (2019), p. 135. arXiv: 1904.07279 [hep-th].

[279] Christian W. Bauer, Alexander Frink, and Richard Kreckel. "Introduction to the GiNaC framework for symbolic computation within the C++ programming language". In: (2000). arXiv: cs/0004015 [cs-sc].

[280] Jens Vollinga and Stefan Weinzierl. "Numerical evaluation of multiple polylogarithms". In: *Comput.Phys.Commun.* 167 (2005), p. 177. arXiv: hep-ph/0410259 [hep-ph].

[281] Ansgar Denner et al. "Electroweak corrections to charged-current e+ e- to 4 fermion processes: Technical details and further results". In: *Nucl.Phys.* B724 (2005), pp. 247–294. arXiv: hep-ph/0505042 [hep-ph].

[282] Georges Aad et al. "Measurement of the double-differential high-mass Drell-Yan cross section in pp collisions at $\sqrt{s} = 8$ TeV with the ATLAS detector". In: *JHEP* 08 (2016), p. 009. arXiv: 1606.01736 [hep-ex].

[283] Enrico Bothmann et al. "Event Generation with Sherpa 2.2". In: *SciPost Phys.* 7.3 (2019), p. 034. arXiv: 1905.09127 [hep-ph].

[284] Ansgar Denner, Jean-Nicolas Lang, and Sandro Uccirati. "Recola2: REcursive Computation of One-Loop Amplitudes 2". In: *Comput. Phys. Commun.* 224 (2018), pp. 346–361. arXiv: 1711.07388 [hep-ph].

[285] Ansgar Denner and Stefan Dittmaier. "Electroweak Radiative Corrections for Collider Physics". In: *Phys. Rept.* 864 (2020), pp. 1–163. arXiv: 1912.06823 [hep-ph].

[286] John C. Collins and Davison E. Soper. "Angular Distribution of Dileptons in High-Energy Hadron Collisions". In: *Phys. Rev. D* 16 (1977), p. 2219.

[287] A. V. Smirnov. "Algorithm FIRE – Feynman Integral REduction". In: *JHEP* 10 (2008), p. 107. arXiv: 0807.3243 [hep-ph].

[288] Gabor Somogyi. "Angular integrals in d dimensions". In: *J. Math. Phys.* 52 (2011), p. 083501. arXiv: 1101.3557 [hep-ph].

[289] A. V. Smirnov and V. A. Smirnov. "On the Resolution of Singularities of Multiple Mellin-Barnes Integrals". In: *Eur. Phys. J. C* 62 (2009), pp. 445–449. arXiv: 0901.0386 [hep-ph].

[290] M. Czakon. "Automatized analytic continuation of Mellin-Barnes integrals". In: *Comput. Phys. Commun.* 175 (2006), pp. 559–571. arXiv: hep-ph/0511200.

[291] Alexander B. Goncharov. "Multiple polylogarithms, cyclotomy and modular complexes". In: *Math. Res. Lett.* 5 (1998), pp. 497–516. arXiv: 1105.2076 [math.AG].

[292] A.B. Goncharov. "Multiple polylogarithms and mixed Tate motives". In: (2001). arXiv: math/0103059 [math.AG].